SAPIENZA
UNIVERSITÀ DI ROMA

Department of Chemical Engineering Materials Environment

Electrical, Materials and Nanotechnology Engineering (EMNE)

(XXX cycle)

Ph.D. Thesis

Modified aluminide coatings with reactive element for turbine blades protection

Virgilio Genova

Supervisor: Prof. Cecilia Bartuli

Lyst of acronyms

ATR-FTIR = Attenuated Total Reflectance Fourier Transform Infrared Spectroscopy
CVD = Chemical Vapor Deposition
DST = Dynamic Segregation Theory
René 108DS = Directionally Solidified
EDS = Energy Dispersive Spectroscopy
EDTA = Ethylendiaminotethracetic acid
ENL = External Nickel Layer
EPNP = Electroless Pure Nickel Plating
FE-SEM = Field Emission gun Scanning Electron Microscopy
GDOES = Glow Discharge Optical Emission Spectroscopy
HPC = High Pressure Combustor
HPT = High Pressure Turbine
HTHC = High Temperature Hot Corrosion
HTLA = High Temperature Low Activity
HRTEM = High Resolution Transmission Electron Microscopy
IDZ = Interdiffusion Zone
IPT = Intermediate Presurre Turbine
LPC = Low Pressure Combustor
LPT = Low Pressure Turbine
LTHA = Low Temperature High Activity
LTHC = Low Temperature Hot Corrosion
PN_A_ = Pure Nickel_solution A_
PN_Al_ = Pure Nickel_Aluminum_
RE = Reactive Element
SEAD = Selected Area Diffraction
TBC = Thermal Barrier Coating
TGO = Thermally Grown Oxide
VPA= Vapor Phase Aluminizing
XRD = X-Ray Diffraction

List of symbols

P_R = plating ratio
wt % = weight percentage
T = temperature
h = hours
x = mass or thickness of oxide
k_P = parabolic contant
(g) = gas phase
(l) = liquid phase
(s) = solid phase
ΔM = mass variation

INTRODUCTION

Increasing the maximum temperature of the gases introduced into the turbine increases both the efficiency and performance of a turbo-gas system; Switching from an input temperature of 900 ° C to 1250 ° C can result in a 30% increase in output power, leaving unchanged consumption. In order to ensure the structural integrity of components working in the hottest areas of the engine, research over the last decades has focused on the development of increasingly innovative technologies that aim to increase the efficiency of the system while at the same time increasing its operating life.

Turbine blades are one of the most critical components of this system because they not only work in a highly aggressive environment, but are also subject to strong mechanical stresses related to the rotation of turbochargers and aerodynamic loads. In addition to the presence of oxidation and hot corrosion mechanisms, high temperatures contribute to the degradation of the structural properties of the component and result in thermo-mechanical stress related to the temperature gradients and to the different coefficients of thermal expansion of the used materials.

In those applications where operating temperatures are compatible with the thermomechanical properties of the materials used, the turbine blades are coated to provide protection against high temperature oxidation and hot corrosion phenomena. If the operating temperatures are too high, multiple solutions are taken to reduce the temperature experienced by the component; the most important are: internal and external cooling techniques and the use of special coating systems (TBCs - Thermal Barrier Coating).
TBC coatings are a multilayer system consisting of a top ceramic layer (top coat) and an intermediate layer (bond coat) designed to protect the component from high operating temperatures and oxidation, respectively.

The aim of this work is to increase the performance of turbojet engines used in the aeronautical field, by appropriately modifying the bond coat formation processes. In order to achieve this, at the first part of this work, the change of processes already used in the industrial field was proceeded, while in the second part of the work an innovative and alternative method was proposed and studied to improve these processes.

CHAPTER 1

Gas Turbojet

Gas turbines have been used since 1791[1] in a wide variety of applications including aircraft propulsion, marine propulsion and power generation. Components of these engines experience very high stresses and temperatures in highly corrosive and oxidizing gases, and are required to maintain their mechanical properties for thousands of hours of service.

1.1 Principle of operation

The turbojet is a turbogas-based aeronautical propulsion. Figure 1.1 shows a section of a simple turbojet, where the various stages of the engine are illustrated.

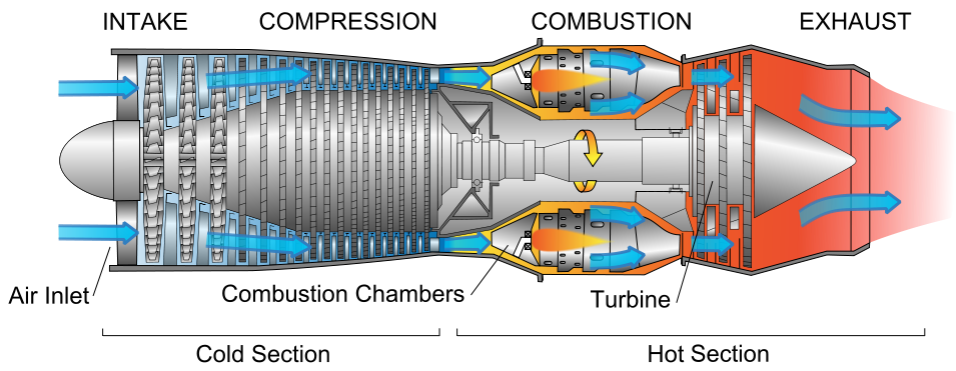

Figure 1.1: *Cross-section of a simple turbojet*

The dynamic intake moves air from outside and drives it into a compressor, where it slows down and compresses. The compressed air then enters in the combustion chamber at a pressure of about 30 ÷ 35 bar and at a temperature around 550 ÷ 625 ˚C. Combustion takes place here, with fuel injection in the compressed air stream. At this point, hot combustion gases are forced into the turbine, expanding them and having the role of providing the power needed to move the compressor. At the exit of this stage the gas is still at a higher pressure than the ambient temperature, and can therefore be accelerated in a nozzle. In this way, the propulsion fluid is ejected at a higher speed than the one with which it enters the engine, thus generating the thrust.

The excellent properties in terms of thrust, specific consumption, thrust / weight ratio, have imposed this family of propulsion as the most widely used in civil aviation as well as military.

The jet engine based on the gas turbine cycle was first patented by Frank Whittle in Great Britain in 1930, but only in 1939 was the first aircraft propelled by a turbojet. After the end of the Second World War it was established thanks to its high specific thrust (per unit weight of the engine) and the low-power specific at high speeds.

The simple turbojet is extremely efficient at high subsonic flight speeds. To extend the field of application of the turbojets and to improve their efficiency throughout the subsonic field, the turbofan was introduced, as shown in Figure 1.2

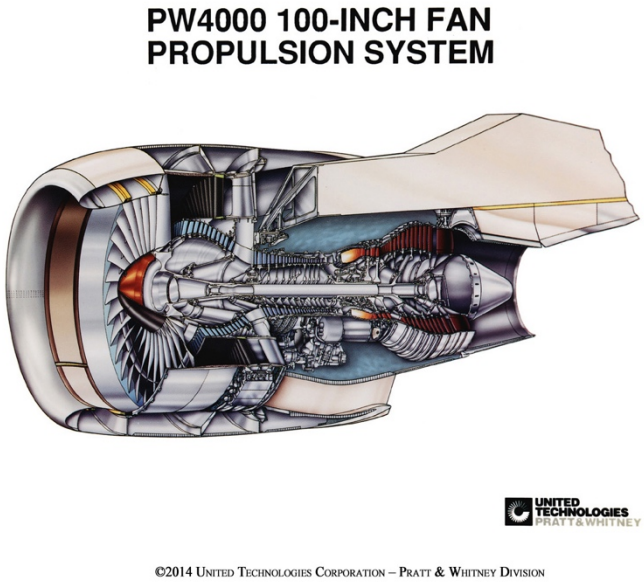

Figure 1.2: *Turbofan Pratt & Whitney PW4000*

1.2 Operating condition

Figure 1.3 shows a section of the Rolls-Royce Trent 800 reaction engine (Boeing 777 aircraft engine), and illustrates the various phases and pressure and temperature profiles along the engine, while Table 1.1 summarizes the operating conditions of each section:

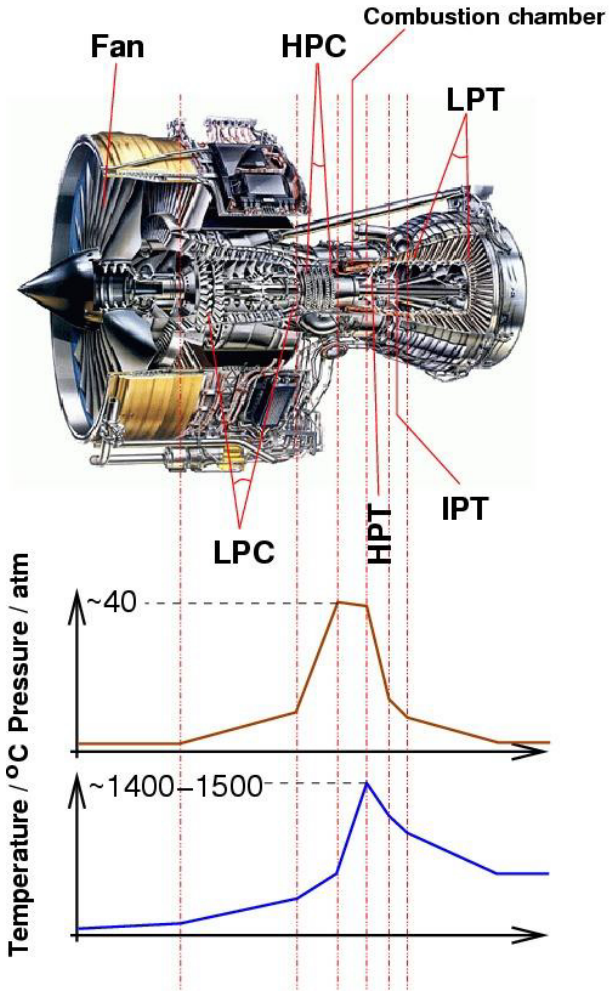

Figure 1.3: *Section of the Rolls-Royce Trent 800 engine with temperature and pressure profile for the different stages[2]*

Table 1.1: *Operating parameters for Rolls-Royce Trent 800*

Components	Material	Pressure [bar]	Temperature [°C]	Rotation speed [rpm]
FAN	Titanium	1	810	3500
LPC	Titanium	8	290	6800
HPC	Titanium	37	600	10200
COMBUSTOR	Ni-alloy	35	1500	-
HPT	Ni-alloy	35	1400	10200
LPT	Ni-alloy	14	900	6800
EXHAUST	Ni-alloy	6	860	3500

As can be seen from Table 1.1, the operating temperatures to which the various components are subjected are several, and this directly affects the choice of materials in the different engine sections (Figure 1.4)

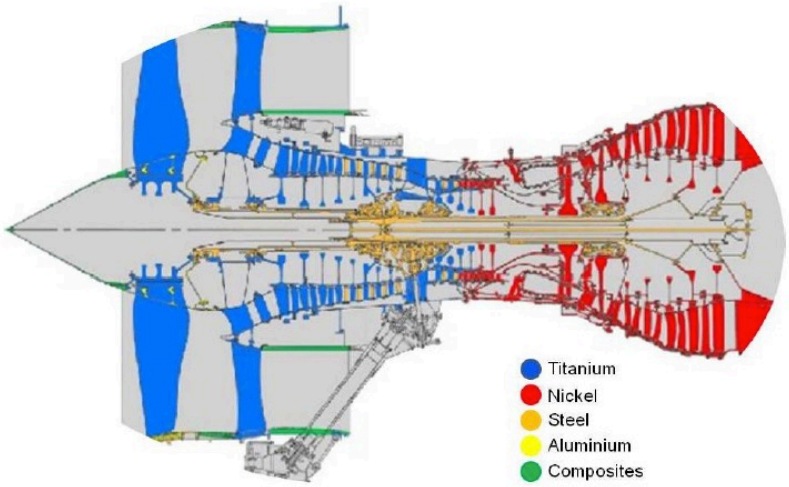

Figure 1.4: *Materials used in a Rolls-Royce Trent 800*

Finally, Table 1.1 also shows how high pressure turbine blades (HPTs) are the components operating in the most severe conditions in terms of temperature and pressure. They also experience high tension due to centrifugal forces, constant over time and rapid thermal transients during the flight cycle.

1.3 Design of a turbojet

The criterion on which the choice of materials is based is, once resistance specifications have been achieved, the performance improvement in terms of internal speed and temperature reached by the gas, while maintaining the entire lightweight system.

As mentioned in Section 1.2, the turbine is the most critical part of an aeronautical engine; For this reason, over the years, research has focused particularly on the study of materials that meet certain thermal and mechanical resistance requirements at high temperatures. From here on, attention will be focused on turbine blades, as it is the resistance to the thermal and mechanical stresses of these components that discriminates the maximum permissible temperature in the combustion chamber and consequently the performance of the entire engine.

From a mechanical point of view, the main factors to be taken into account during design are creep and thermal and mechanical fatigue, as well as the resistance requirement to the tested loads. The first

two phenomena mainly affect the first stage of turbines, while for the second stage the limiting factor is mainly creep.

In addition, the hot gases that invest the blades are highly oxidizing, and contain contaminants such as chlorides and sulphates, which can cause hot corrosion of the component; these gases may also contain erosive elements [3]. Erosion can be caused by the sand during take-off and landing.

Figure 1.5 shows the temperature profile of a HPT blade. Considering the gas temperature increases at the turbine entry these values are now considerably higher, although the temperature profile essentially remains the same.

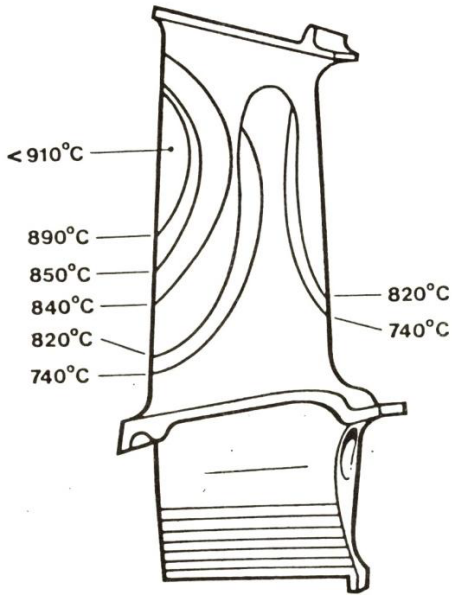

Figure 1.5: *Temperature profile for a blade of High Pressure Turbine (HPT)[4]*

Then, a turbine blade must have the following characteristics:

1. High mechanical resistance at high temperatures;
2. Resistance to creep, thermal fatigue and mechanical fatigue;
3. High microstructural stability;
4. Resistance to oxidation and hot corrosion;
5. Resistance to erosion.

In practice, it is not easy to collect all of these properties in a single material, and that is why superficial coatings that can meet the characteristics of the substrate are used in this kind of system.

1.4 Ni-based superalloy.

The word superalloy means a group of alloys developed for high performance applications at high temperatures, such as aircraft turbine engines [5].

As reported by Sims and Hegel [6], superalloy is defined as "an alloy developed for high temperature applications, generally based on elements of Group VIII-A, which have high mechanical strength and surface stability."

The superalloys can generally be divided into three classes, according to the main alloy element:

1. Nickel-based (Ni)
2. Cobalt-based (Co)
3. Iron-based (Fe)

Ni-based superalloy is the most commonly used for turbine blades manufacturing.

Figure 1.6 describes the turbine working temperature trend as a function of the materials that have been used for the realization of the turbines over the last sixty years; in particular, the monocrystalline Ni-based superalloys have been greatly developed over the last few years due to the growing demand for materials capable of delivering high mechanical performance at high temperatures. These alloys have a very high mechanical strength at high temperatures, allowing theoretical achievement of temperatures up to 1300°C without any damage. The high thermomechanical resistance is mainly due to the absence of discontinuities originating from grain boundaries and precipitate concentration sites, which in the polycrystalline superalloys represent the triggering and propagation zones of the cracks. Table 1.2 shows the characteristic temperatures at the compressor output and at the turbine intake from 1955 to the present.

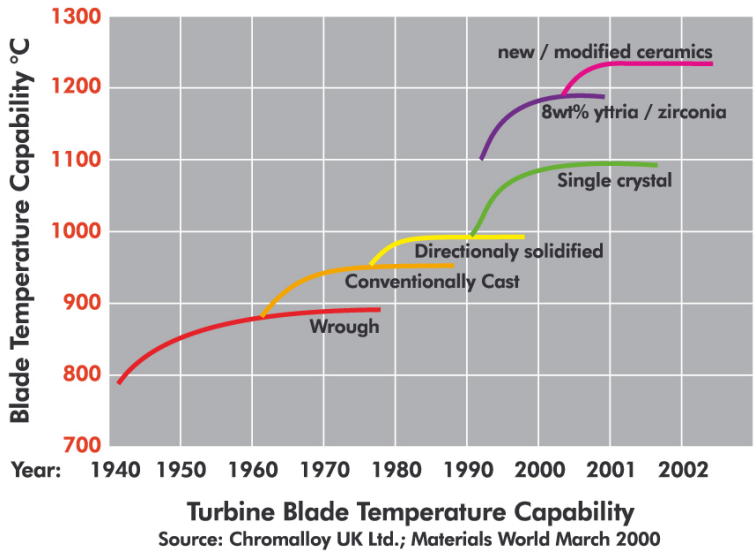

Figure 1.6: *Evolution of high temperature superalloys capacity for a period of 60 years after their appearance in 1940.*

Table 1.2: *Operating temperatures in the last 60 years*

Service year	Temperature [°C] Outlet compressor	Temperature [°C] Inlet turbine
1955	379	771
1965	427	938
1975	593	1343
1995	693	1427
2008	>700	>1500
2015	766	1760

Thanks to the availability of materials to withstand the increasing turbine gas entry temperatures, aircraft engines quadrupled (from the first Henkel turbine in 1939) their push / weight ratio with a specific consumption of approximately halved. Figure 1.7 shows the three types of superalloys used for the production of turbine blades and the improvements recorded according to the life time of each type of material as previously stated, having conventionally associated polycrystalline alloys with a value of 1.

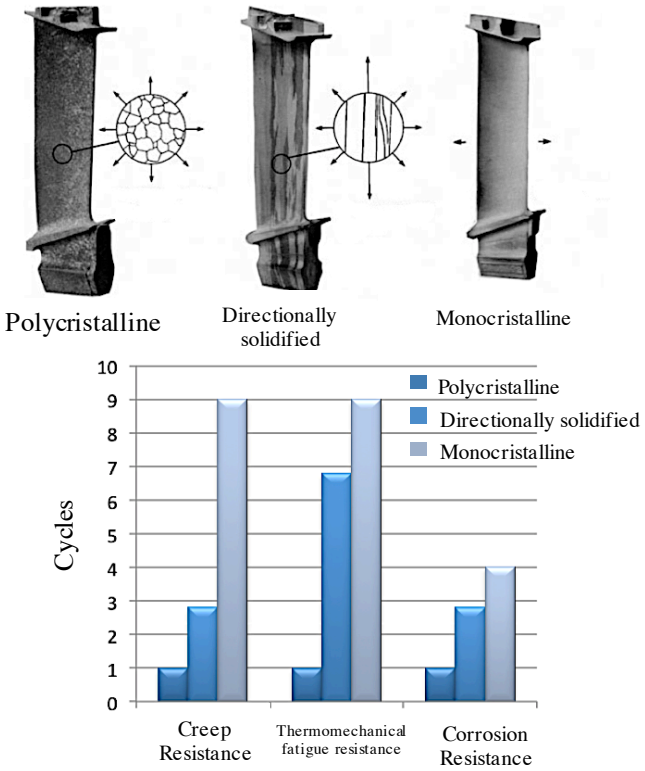

Figure 1.7: *Features of three different superalloy*

Ni-based super-alloys offer high performance:

1. High melting temperature
2. High resistance, which includes tensile strenght, creep and fatigue resistance
3. Ductility
4. Toughness
5. High temperature corrosion resistance

However, nickel does not have these properties, since pure metals, such as nickel, are generally too ductile and do not have sufficient resistance to the harsh environments, both mechanically and chemically. Therefore, these are rarely used without being reinforced by various mechanisms.

Nickel-based superalloys are generally reinforced by precipitation hardening or solid-solution strengthening, both of which are effective as reinforcing methods at high temperatures.

Precipitation hardening

In the precipitation hardening, soluble atoms participate in the creation of a second fine phase and highly dispersed. Traditionally, two thermal treatments are used for Ni-based superalloys. The first is the thermal treatment to homogenize the microstructure and reduce the effects of elemental segregation. The second is the aging to develop phase precipitates γ'- [Ni_3(Al, Ti)]. These precipitates, consistent with the matrix, and extremely stable in temperature, act as a barrier to the movement of the dislocations, greatly increasing the resistance to creep. Elements such as Al and Ti promote the creation of phase γ', by alloying with the phase γ-Ni. The size of this phase can be precisely controlled by means of thermal treatments. Generally, this type of hardening is used in turbine pallets.

Solid solution strenghtening

In this type of hardening, solute atoms (such as Al) randomly substitute solvent atoms (Ni, in this case) without altering the crystalline structure.

The continuous phase, characterized by a center-faced cubic lattice (cfc), forms the matrix of Ni-based alloys; this is hardening by the solid solution with several randomly distributed atomic species. Various metallic elements (Co, Cr, Mo, Fe, Ta, W, Re) are dissolved in the matrix by randomly replacing Ni atoms. Due to their different sizes than Ni, the solid solution causes local stresses that prevent the movement of the dislocations, interacting with the stress field caused by the dislocations themselves. In addition, solute atoms may also go to the interstices between the atoms of the matrix by anchoring the grain boundaries and thereby improving the sliding and migration resistance that would occur during the creep diffusion.

It is preferred to use this type of hardening in applications where high mechanical strength is required.

1.5 Degradation phenomena. Hot corrosion and oxidation at high temperature

Turbine blades, especially those in high pressure conditions (HPT), are subjected to high stresses and temperatures; according to the operating conditions, can trigger creep, hot corrosion, high temperature oxidation and surface erosion as mentioned in Section 1.4. All these aspects must necessarily be taken into consideration during the design process to ensure proper operation and useful life of the component. Figure 1.8 shows the complexity of the elemental composition of a Ni-based superalloy for aeronautical applications [7]. The complexity, in terms of chemical compositions, don't allow to obtain a material that can have some high mechanical properties with a high resistance to harsh environments.

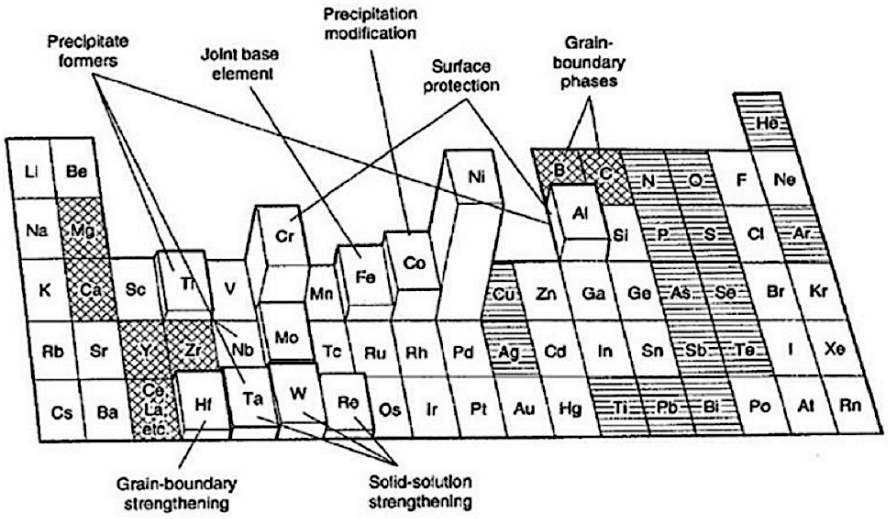

Figure 1.8: *Alloy elements present in Ni-based superalloys. The elements with lesser benefits are marked with a cross-hatch, while the harmful elements for the performance of the material are marked with a horizontal hatch [8].*

For this reason, it is simpler and more functional to use surface coatings. The idea of applying protective layers on the surface of turbine blades was practiced already in 1960 and found extensive applications. Since then, protective coatings are conventionally used for aeronautical engines and ground turbines. Corrosion phenomena can be divided into two types: uniform corrosion and localized corrosion.

Localized corrosion is particularly present at the root of the blade, exposed to temperatures around 620 to 760 ° C. These areas of damage can then expand and reach to the center of the component causing the failure. There is a close relationship between the damage and the characteristics of stresses and the environment: the higher the velocity of the flow that invests the blade, the less the

corrosion damage; the lower the quality of the fuel used and the more severe will be the corrosion; the longer the operating time, the more penetration depth of the corrosion products will be.
The uniform corrosion can be classified according to three different phenomena (Figure 1.11): high temperature oxidation (T> 1000 ° C); hot corrosion at high temperatures (Type I: T = 850 to 950 ° C); hot corrosion at low temperatures (Type II: T = 650 ÷ 800 ° C) [9].

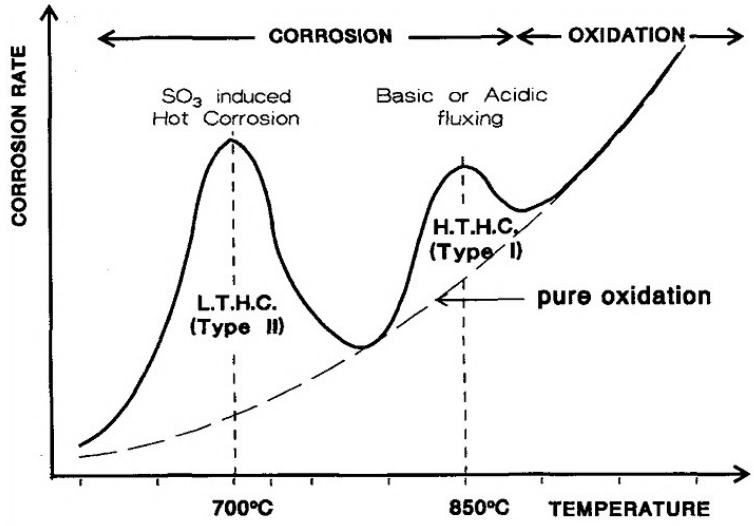

Figure 1.9: *Corrosion rate vs Temperature [10]*

High temperature oxidation is a phenomenon where metals and alloys exposed to oxygen or a gas containing oxygen, at high temperatures, convert a part or all of the metals into their corresponding oxide.
The oxide, if it is attached to the substrate, can give rise to a degree of protection and slow down the oxidation kinetics, or may become detached, exposing the underlying substrate to oxidation; In addition, for long exposure times, the phase responsible for selective oxidation can be exhausted in the substrate and thus initiate the oxidation of a different element / phase with formation of a smaller scale oxide, resulting in a sensible acceleration of the oxidative phenomenon.

The theory of Pilling-Bedworth (1923) tried to explain why some metals form a protective scale and others do not; this theory argues that the ability to protect the scale depends on the ratio between the molar volumes of the metal and its oxide. A general indicator of the protection of the oxide scale is given by the Pilling-Bedworth ratio (PBR) defined as:
For:

• PBR <1: the volume of oxide formed is less than the volume of metal consumed; porous, cracked and non-protective scale are formed;
• PBR> 1: layers of protective oxides are formed;
• PBR >> 2: the volume of oxide is much greater than the volume of the metal; so, the scale is very compressed.
However, this theory is not always verified, but there are some exceptions due to approximations that are adopted; these relate to the mechanism of oxide growth, geometry, the volatility of the oxide and the chemical effects of alloy elements. However, in general, it is a qualitative indication.

A metal is oxidized since the free energy variation ΔG_0, associated with the reaction, is negative. ΔG is influenced by a number of parameters such as:
• Temperature
• Partial oxygen pressure
• Composition
The effect on the ΔG_0 of the temperature and partial pressure of O_2 at the variation of the oxidized element is given in the Ellingham diagram (Figure 1.10):

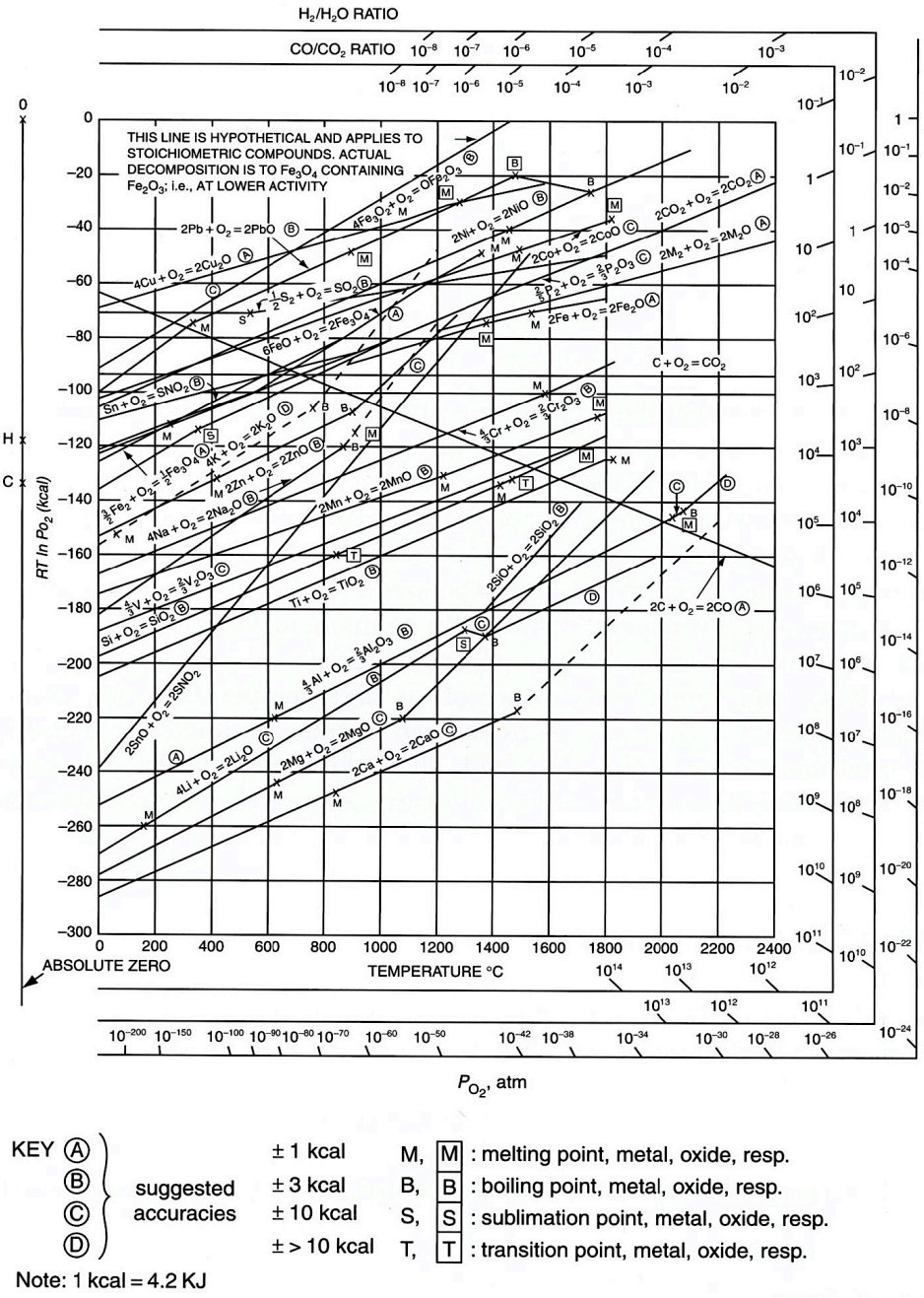

Figure 1.10: *Ellingham's diagram*

Figure 1.10 shows that noble metals are at the top of the diagram, indicating that they are less reactive. The Ellingham diagram allows:

1. to order oxides according to their greater or less metal reduction reaction,

2.to determine the partial pressure of oxygen in equilibrium with a metal at a certain temperature

3. to determine the degree of CO / CO_2 or H_2 / H_2O that cause the reduction of a metal oxide at a given temperature.

However, Ellingham's diagram does not allow predicting the rate of oxidation reactions and therefore does not account for kinetic aspects.

It has been experimentally observed that the growth of the oxide layer follows one of the following laws:

• Linear Growth: $x = k_L t$

• Parabolic Growth: $x^2 = \frac{k_P}{2} t$

• Logarithmic Growth: $x = k_e \log(at + 1)$

where x is the thickness of the oxide layer after exposure time t, k_L, k_P and k_e are growth rate indices, temperature functions T, and a is a constant.

Linear growth

If the metal surface is not protected by an oxide scale, the oxidation rate remains constant over time. In this growth mechanism is the reaction between metal and oxygen to control the degree of oxidation at the interface between oxide and metal scales, while the species transport process is not influential. The oxidation kinetics is described by:

$$\frac{dx}{dt} = k_L$$

$$x = k_L t$$

with x mass or thickness of oxide, considered zero at the initial moment (Figure 1.11).

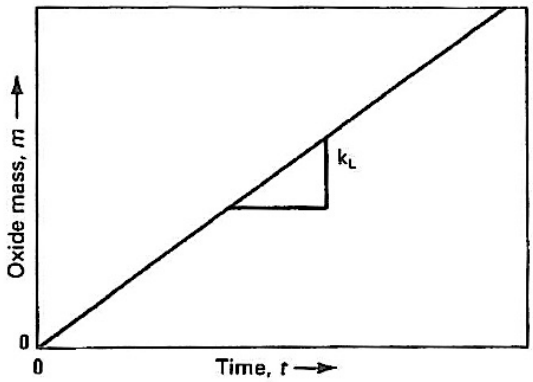

Figure 1.11: *Linear oxidation kinetic*

Oxidation never slows down. For sufficiently long exposure times the metal is consumed completely.
As mentioned, this phenomenon occurs when the RPB ratio is less than 1, or if the oxide is volatile or liquid.

Parabolic Growth

Many systems oxidize by following a parabolic pattern. Oxidation in these cases is thermally activated and the rate of growth is controlled by ion diffusion through the oxide layer, with driving force caused by a chemical potential gradient. The growth rate is inversely proportional to the thickness, and kinetics are described by:

$$\frac{dx}{dt} = k_P \frac{1}{x}$$

$$x^2 = \frac{k_P}{2} t$$

with x mass or thickness of oxide, considered zero at the initial moment (Figure 1.12).

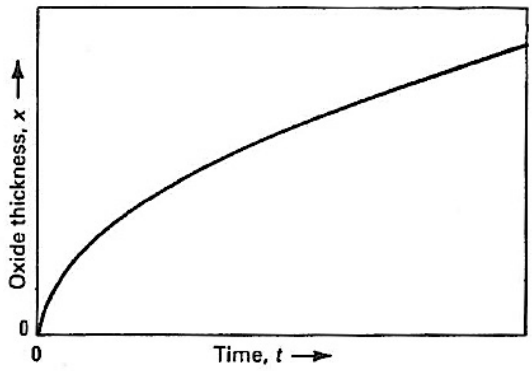

Figure 1.12: *Parabolic oxidation kinetic*

As the thickness of oxide increases, the diffusion distance increases and the kinetics thus slows down.

Logarithmic growth

The oxidation rate generally follows a logarithmic or reverse logarithmic law at low temperatures (below 400 ° C) when only a thin film (<200 nm) of oxide has formed [12]. The driving force that allow the growth is the formation of localized electric fields in the vicinity of the metal surface; absorbed oxygen atoms acquire electrons from metal atoms, creating large electric fields along the thin layer between positive metal ions and negative oxygen ions. Metal atoms are driven by the electric field through the oxide layer. The oxidation kinetics in the case of logarithmic kinetics is described by:

$$x = k_e \log(at + 1)$$

in the case, instead, of inverse logarithmic kinetics we have:

$$\frac{1}{x} = b - k_i \log t$$

with x mass or thickness of oxide, considered zero at the initial moment (Figure 1.13).

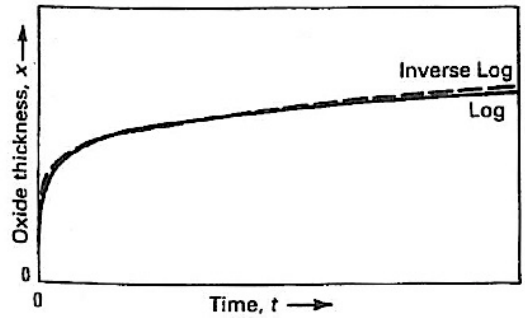

Figure 1.13: *Logarithmic and inverse logarithmic oxidation kinetic*

The metals that oxidize with this kinetics reach a thickness of oxide which oxidation apparently stops.

When metals and alloys, in a high temperature oxidizing environment, have the surface covered with a thin film of salts, accelerated oxidation can occur. This phenomenon is referred to as hot corrosion, and affects the ability to protect the substrate by the oxide scale. This type of attack is sensitive to a different number of variables such as composition and amount of deposit, gas composition, temperature, surface erosion, composition and alloy microstructure.
It has been shown that the aggressiveness of this type of attack, which can be catastrophic, consists of two phases:
1. Initial Stage: The alloy and the deposit are subject to alteration, such as the reduction of the element favoring the formation of the protective oxide scale, the incorporation of a deposit component into the alloy, the dissolution of oxides in the salts, the formation of cracks and / or channels in the scale. During this phase the corrosion rate is slow and similar to that in the absence of the deposit;
2. Propagation Phase: The salts enter through the damaged scale and propagate to the scale-alloy interface. When the deposit reaches low oxygen sites and meets the depleted zone of element alloy that create a protective oxide scale (such as Cr and Al), propagation occurs quickly.

Generally, corrosion that occur above the melting point of the salts is called type I hot-corrosion, while the one that occurs below the melting point of the individual constituents of the salts, unless they form eutectic, is called type II hot corrosion.

High Temperature Hot Corrosion (HTHC) Type II

The HTHC begins with the condensation of alkaline metal salts melted on the surface of the component. A number of subsequent chemical reactions cause the attack of the protective oxide scale with an acceleration of the oxidation phenomenon and the formation of a porous oxide scale.

Mainly, during the combustion, the salt formed is Na_2SO_4 starting from Na and S present in the atmosphere and in the fuel; this salt has a high thermodynamic stability. Other impurities contained in the fuel or atmosphere such as vanadium, phosphorus, lead and chlorides can be combined with sodium sulphate and form a mixture of salts with low melting temperature, thus expanding the area undergoing corrosive attack.

Potassium sulphate K_2SO_4 behaves in a similar way to sodium sulphate.

Vanadium is an inevitable contaminant in some fuels, especially in marine ones. In addition to its low melting point, vanadium compounds greatly increase the solubility of the oxide when mixed with Na_2SO_4.

This type of corrosion can generally be divided into four progressive stages, from initial start, up to component failure:

1. At the initial stage, a slight increase in surface roughness is observed, due to the growth and localized fracture of the oxide layer. However, neither the chromium impoverishment in the substrate nor the mechanical integrity loss of the component is observed;
2. At this stage, the roughness of the surface increases due to continuous breaks of the oxide layer. Chromium in the substrate begins to run out, but mechanical integrity is not affected yet;
3. The oxidation of the material reaches a considerable depth; Mechanical integrity is compromised and blades must be replaced. Also, at this stage, corrosion is able to proceed independently of the presence of sodium;
4. At this stage, the catastrophic attack of the material occurs. The failure of the component becomes very likely due to the loss of structural material.

From a macroscopic point of view, this type of corrosion is characterized by the material's peeling and significant changes in color (greenish tone resulting from the formation of NiO). Microscopically, morphology is characterized by the presence of sulphates and depleted regions under the porous, non-protective scale.

Figure 1.14 shows the components used in aeronautical field coated with alumina (Figure 1.14a)), subject to HTHC, which reveals the characteristics of the attack. In Figure 1.14b), sulfur attack is evident, which play an important role in the degradation process, while Figure 1.14 (c) is shown the penetration of the coating and exposure of the substrate to the attachment.

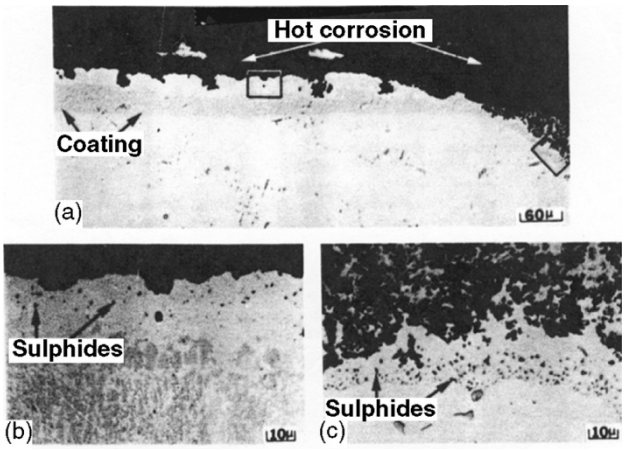

Figure 1.14: *Micrographs of the microstructural evolution during hot corrosio – a) Ni-base aluminized HTHC; b-c) cross-section microstructure, respectively, for the coating and the substrate [11]*

Low Temperature Hot Corrosion (LTHC) Type I

LTHC generally occurs below the melting point of pure salts, but may also occur above the melting temperature of the salt itself if the deposits form a eutectic with a melting point far lower than that of the individual constituents. This is the case of the Na_2SO_4 and V_2O_5 compound, characterized by a melting temperature significantly lower than the individual compounds (Figure 1.25).

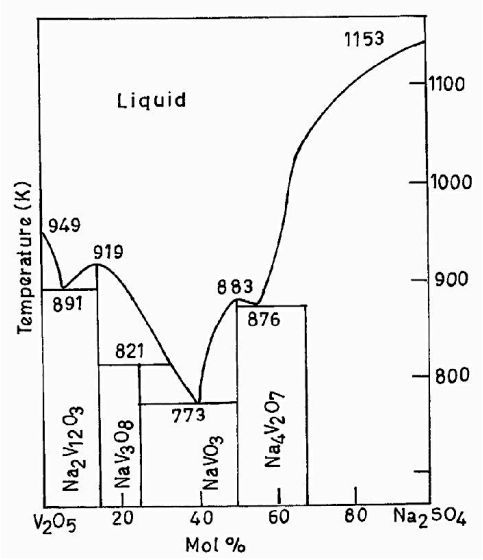

Figure 1.15: *Phase diagram of Na_2SO_4 and V_2O_5*

Similarly, nickel-based superalloys form a eutectic Na_2SO_4-$NiSO_4$. A high partial pressure of SO_3 in the gas phase is required to proceed with the reactions, as opposed to what happens in the HTHC. In addition, compared to Type I hot corrosion, no incubation period is observed in this type, nor is the sulphate presence and the depletion of reactive elements (Cr and Al) is generally observed. The LTHC typically causes pitting of the material (Figure 1.16).

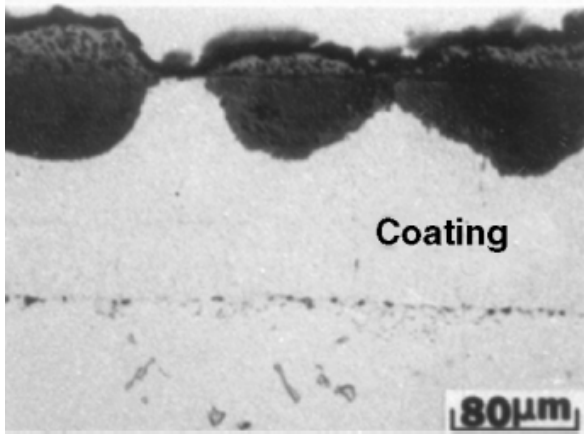

Figure 1.16: *Type II hot corrosion for a CoCrAlY after 4200h of test*

References

[1] A.M.Y. Razak, Industrial gas turbines: Performance and operability, CRC Press.

[2] Micheal Cervenka, Rolls-Royce Corporation.

[3] Driver, D.; Hall, D.W.; Meetham, G.W, ed. G.W. Meetham, Applied Science Publishers, 1981, pp. 1-30.

[4] C. Duret-Thual, R. Morbioli, and P. Steinmetz, Luxembourg, 1986.

[5] Bradley, E.F.; 'Superalloys, ASM International, 1988.

[6] Sims, C.T.; Hagel, W.C.; Preface, John Wiley & Sons, 1972.

[7] T. R. Pollock and S. Tin, *J. Propuls. power*, vol. 22, no. 2, pp. 361–374, 2006.

[8] Matthew.J. Donachie, Stephen.J. Donachie: Superalloys-A tecnical guide, 2nd Edition. Copyright by the Materials Information Society, 2002.

[9] Felix, P.C., High Temperature Alloys for Gas Turbines 1978, ed. D Coutsouradis et al, Applied Science Publishers, 1978, pp. 69-80.

[10] N. Eliaz et al., Engineering Failure Analysis, 9, 31-43, 2002.

[11] R. Streiff, J. De Physique IV.,Vol.3, 17-41, 1993.

[12] Briks N., G.H. Meier, F.S., 2006, Cambridge University Press.

CHAPTER 2

High temperature coatings

2.1 Coating requirements

Because of the extreme conditions experienced by the turbine blades, this is in the aeronautical field or in a power generation plant (heavy duty), protection against the harsh environmental effects is required in order to maintain the integrity of the components and to increase overall performance and useful life of the system. Surface engineering is intended to combine the mechanical properties of the substrate with the required surface protection.

Any coating deposited on a turbine blade must necessarily ensure protection within a specified period of useful life from the destructive attacks due to high-temperature corrosion, oxidation and erosion; a coating to be protective must meet the following requirements [1]:

1. Must resist corrosion, oxidation and erosion.
2. Must safely withstand the applied static and cyclic stresses on the surface of the turbine.
3. It must exhibit good microstructural stability.
4. Do not degrade the mechanical properties of the substrate.
5. Must be as compatible as possible with substrate alloy in terms of chemistry and thermal expansion coefficient (CTE).

The choice of a suitable coating for a given application depends on the complex interaction between surface and coating and the substrate properties.

2.2 Protection systems for harsh environments

The primary objective of a coating or surface treatment for high temperature working components is the ability to form a thermodynamically stable, slow growth superficial oxide capable of protecting the underlying alloy from the environment [3]. For this reason, most of the coatings contain the three key elements: aluminum, chrome and silicon. These, in part, are added between the alloy elements in small quantities because an excessive concentration of these elements causes the embrittlement of the superalloy.

The main limitation to improving the efficiency of aeronautical engines is the materials with which the turbine blades are made: in fact, the high inlet temperatures in the turbine are not compatible with

the thermo-mechanical properties of the materials used for blades. The superalloys also show a dramatic decay of their mechanical properties.

In practice, therefore, it is aimed at maximizing the operating temperature of the first stages of the turbine without affecting its mechanical properties; it is sought with appropriate methods to lower the temperature experienced by the turbine blades without affecting the temperature of the gas leaving the combustion chamber. This can be achieved in two different ways; the blades design includes [4]:

1. Installation of integrated cooling systems, in which the coolant is conveyed into some suitable holes or directly into the blade surface (Figure 2.1).

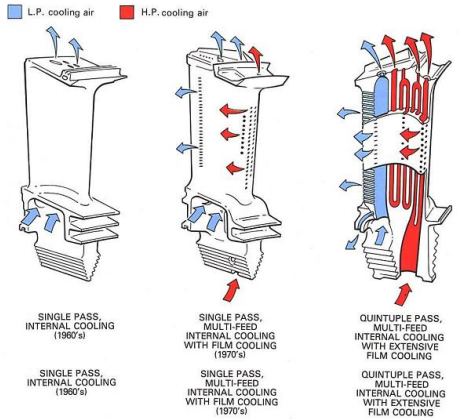

Figure 2.1: *Examples of cooling systems*

2. Protection with antioxidant coatings and thermal barrier coatings (Thermal Barrier Coatings - TBC)

An integrated cooling system has the advantage of not causing any weight gain and not affecting the useful life of the component; however, it has a negative effect on the overall engine yield, as it draws fluid from the cycle to use it for non-propulsion purposes; Moreover, from a technological point of view, the realization of this type of system entails greater complexity and cost of production.

Protective coatings have the advantages to be less expensive in terms of production costs. On the contrary, the use of thermal barrier coating implies a weight gain and a greater risk of sudden coating delamination caused by centrifugal forces.

However, it should be pointed out that the adoption of one and / or the other method becomes necessary when designing more powerful engines is required.

2.2.1 Thermal Barrier Coatings (TBCs)

Thermal barrier coating (TBCs) are able to break down the temperature experienced by the underlying alloy from high operating temperatures, but also to protect the turbine blades from the aggressive environment in which it operates.

TBCs are a multilayer system made by:

1. An insulating ceramic coating often about 100 ÷ 400 μm [2], called top coat, typically yttrium-partially stabilized zirconia (Y-PSZ)
2. A metallic bond coat between the substrate and the top coat, resistant to oxidation and corrosion, and with the task of promoting adhesion between the thermal barrier and the substrate, while also complying with the thermal expansion coefficients (CTE) between the substrate itself and the Y-PSZ coating.
3. Thermally Grown Oxide (TGO) is formed at the time of deposition of the ceramic layer which is interposed between bond coat and external ceramic coating. This layer continues to increase during exercise, due to the permeability of oxygen through zirconium oxide.

Figure 2.2 illustrates a schematic of the three elements that make up a TBC, while Figure 2.3 shows a section of a turbine blade covered by a thermal barrier and the temperature profile that the three layers experience up to the substrate.

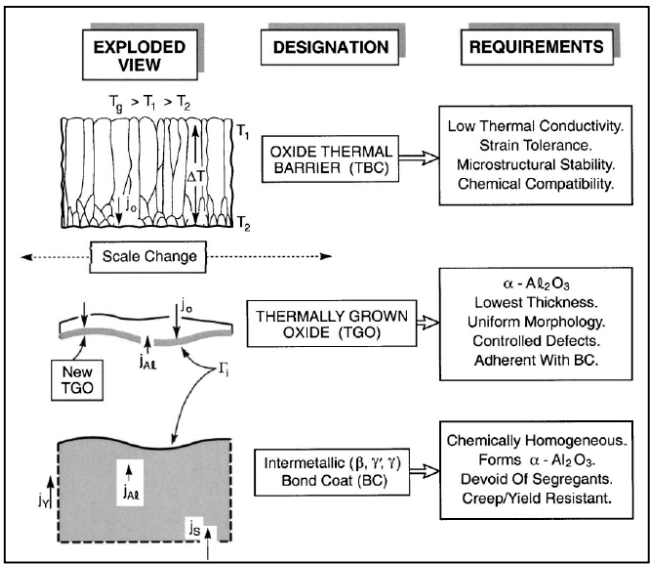

Figure 2.2: *TBC systems [5]*

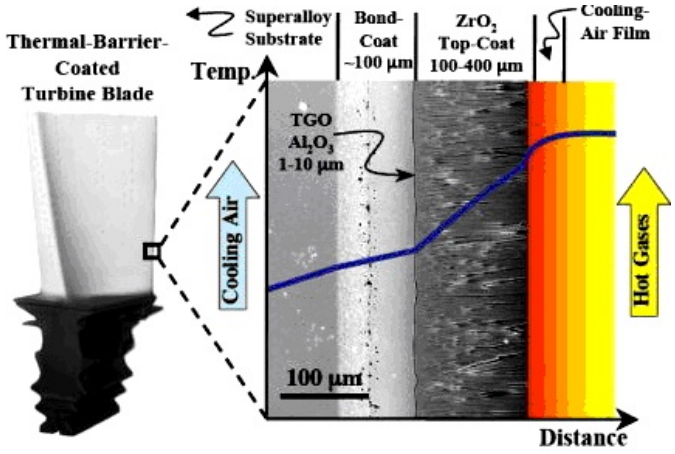

Figure 2.3: *Multilayer coatings schema*

The top coat is the most external layer of the system and, as seen in Figure 2.3, has a thermal shielding power of a few hundred degrees, which results in an elongation of the useful life of the blades; Furthermore, it allows less use of cooling systems, thus reducing the design difficulties and the realization of the cooling systems. Such coating allows to operate with higher temperature gas, resulting in improved efficiency and performance. It also provides protection from the erosion phenomena.

In this system, the oxidation protection is ensured by the bond coat, which is oxidized, giving a slow-growing oxide scale (TGO) which is opposed to the further diffusion of oxygen. This scale becomes thicker as the time of exposure to high temperatures becomes, as oxygen can easily diffuse through the very porous structure of the overlying ceramic coating (Figure 2.4).

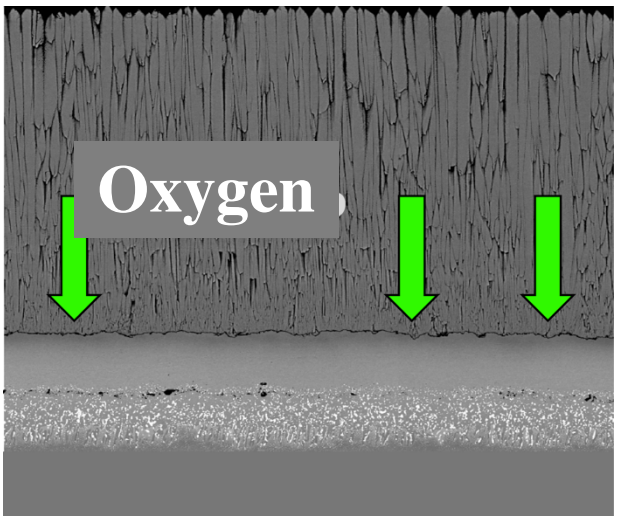

Figure 2.4: *TBC microstructure*

By their nature, top coat and substrate have a very different thermal expansion coefficient, which results in considerable thermal stresses during service and can cause coating failure, leading to exposure to the surface of the blade. The metallic bond coat has an intermediate thermal expansion coefficient between the two layers, ensuring continuity between alloy and ceramic, thus reducing this phenomenon.

2.2.2 Bond coat: state of the art

The bond coats are generally divided into two groups:

• Diffusion coatings: coatings made by diffusion of one or more elements in the surface of the metal to be protected. These are applied by thermochemical processes, in particular Pack Cementation and Chemical Vapor Deposition (CVD).

• Overlay coatings: coatings with a specific composition applied to the surface to be protected by thermal spray or physical vapor deposition (PVD). This category belongs to the MCrAlY systems, where M is usually nickel and / or cobalt.

Both coating classes are based on Al as oxidizing form α-Al_2O_3, characterized by excellent adhesion and a very low permeability to oxygen.

In the first type, the surface is enriched with elements capable of forming the protective scale, while in the second it overlaps the substrate with a predefined composition material capable of forming a protective scale. In diffusion coatings, therefore there is a chemical reaction, which changes the composition of the substrate; with overlay coatings simply goes to deposit a layer of a new material on it (Figure 2.5).

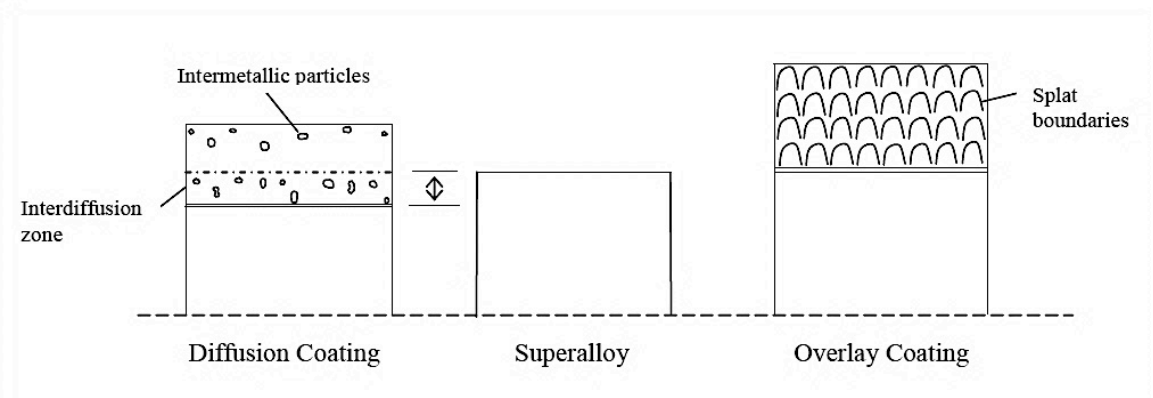

Figure 2.5: *Differences, in terms of microstructure, for a diffusion aluminide coating and an overlay [3]*

The main difference between the two protection systems is the adhesion of the coating; this aspect is fundamental: in a rotating turbine running at thousands of revolutions per minute, a leak of the coating will cause a damage to the system. In power generation applications, this results in an implant stop, and restoration of the naked component exposed to surface degradation phenomena. As far as aeronautical applications are concerned, having high-speed projected elements inside the engine can cause the engine to lock itself. Figure 2.6 describes properties and compositions of the typically used antioxidant coatings. It is to be noted that Al and / or Cr coatings have excellent oxidation behavior as they rapidly form a slow-growth protective oxide (Al_2O_3 and Cr_2O_3) scale; when Cr content increases, an improvement in corrosion resistance is observed;

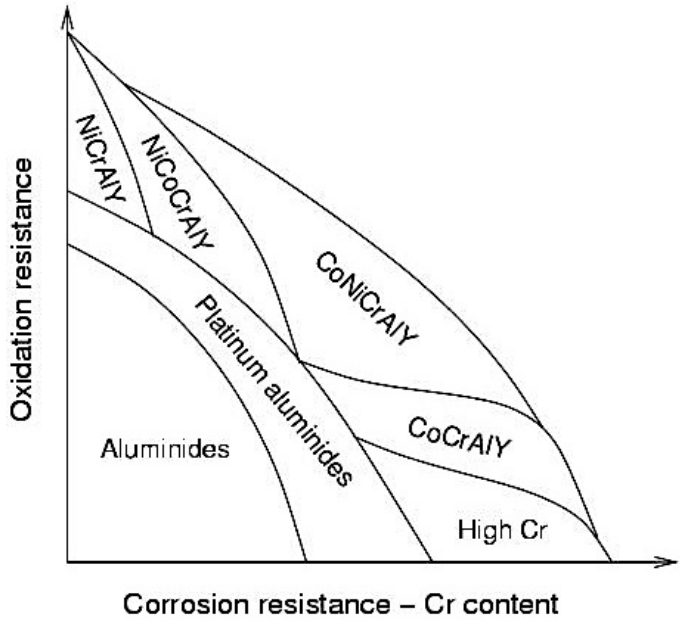

Figure 2.6:*Compositions and properties, in terms of oxidation and corrosion resistance, for several coatings [2]*

2.3 Diffusion aluminide coatings

In this type of protective coating, the surface is enriched with aluminum which, as said, is able to form a slow-growth protective oxide scale. Depending on the surface, Al reacts chemically with the substrate in Ni, forming a new phase called β-NiAl; it will be the aluminum present in this intermetallic to undergo oxidation by protecting the underlying substrate. Figure 2.7 shows the result of 2500 hours flight at low altitudes at sea level on a turbine blade. The macroscopic difference between a non-coated blade and a protected β-NiAl layer is evident.

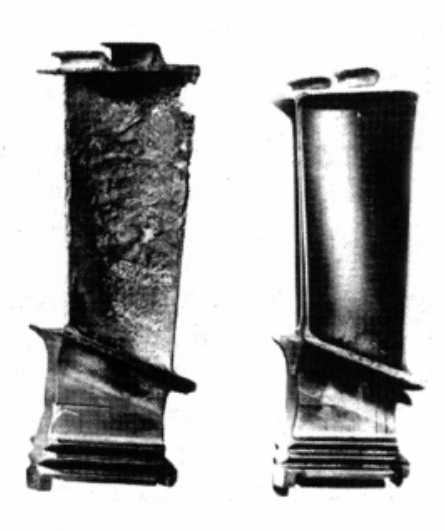

Figure 2.7: *Aluminized and not coated turbine blades*

In general, diffusive coatings can easily cover complex shapes and inner surfaces, which are generally complicated to coat; there is no substrate-coating interface, so there are no adhesion problems since the coating is contained in the component, there are no elements that can be detached. The process is very reproducible, as it is driven by thermodynamics, and finally the apparatus is economical.
Conversely, the diffusing coating that is formed cannot be different from the substrate composition, since from a chemical point of view the reaction takes place between the substrate and the gas containing the element that will diffuse inside. Another negative aspect is that the substrate to be coated should be exposed to high temperatures: superalloys undergo very complicated high temperature thermal treatments, and the risk is that by enriching the surface at temperatures comparable to those with which these treatments are performed, the resulting hardening may be lost and the substrate properties may be compromised.

Stages of equilibrium of Ni-Al alloy

Ni crystallizes in a cubic face centered structure (CFC). If Ni is allied with Al, there are many changes. Up to an approximately 4 wt% Al, there is no change in the Ni atomic structure, except for occasional random replacement of Al atoms against Ni; This phase is called γ phase and is characterized by CFC structure (Figure 2.8a).
By increasing the content of Al, it selectively begins to replace Ni atoms at the angles of the cell, while the atoms on the cube faces remain of Ni (Figure 2.8b). The ratio of the atoms to each cell is 1 every 3 Ni, giving the Ni_3Al composition, known as γ' phase.

If the alloying is increased up to 25 wt% Al, the crystalline structure changes, giving rise to an ordered biatomic cubic structure. The ratio between Al and Ni atoms is 1: 1, providing the NiAl composition, known as phase β, (Figure 2.8c).

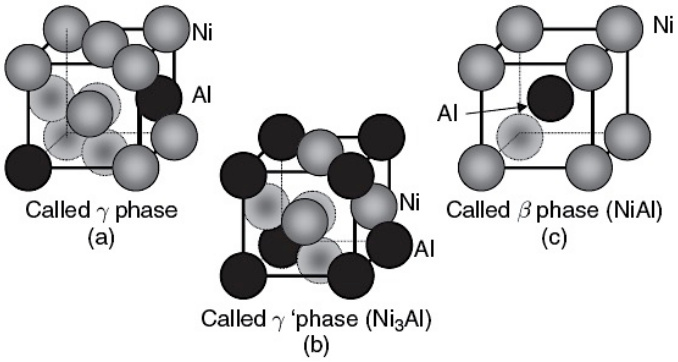

Figure 2.8:*Allotropic phases of NiAl*

The Ni-Al binary phase diagram, shown in Figure 2.9, may provide useful information on the phase that is characterized aluminide coating obtained by diffusion over Ni-based superalloys.

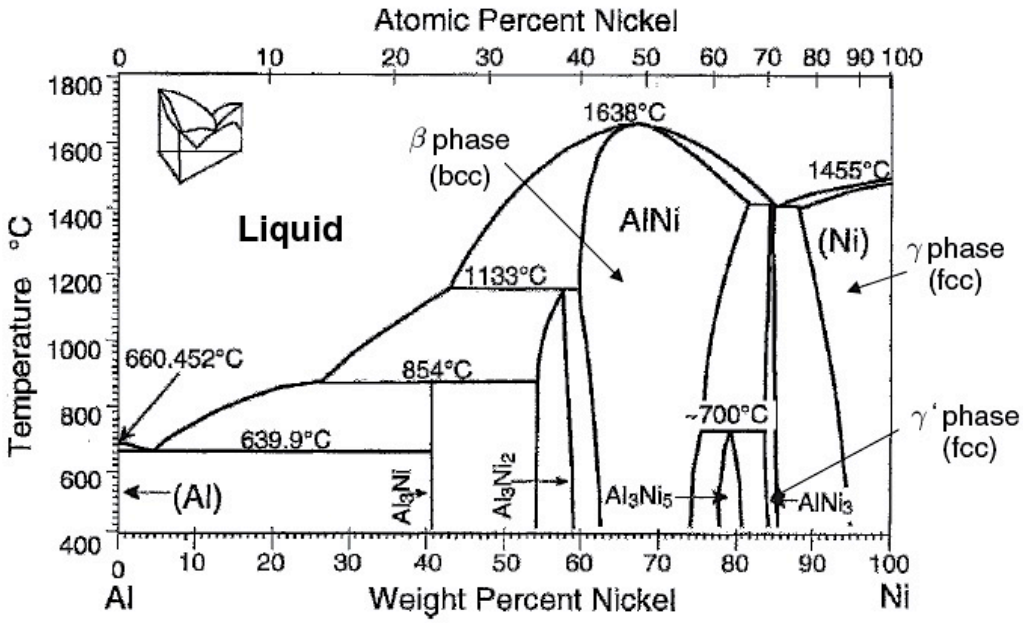

Figure 2.9: *Ni-Al diagram phase*

The field of the β phase is very wide, indicating that at this stage the concentration of Al can be very far from the stoichiometric NiAl composition. In addition, the melting point of the β phase is much higher than the pure Ni. These characteristics make the β phase very favorable for use in high temperature coatings.

2.4 Platinum modified aluminide coatings

The deposition of an electrolytic platinum layer before the aluminization, followed by a diffusion thermal treatment (at 1000 ÷ 1100 ° C, up to 5 hours at 10-7 torr) was initially designated to create a barrier against the diffusion of aluminum towards the substrate, delaying the decomposition of NiAl to Ni_2Al_3.Subsequent analyzes have shown that Pt does not act as a diffusion barrier, and a number of other mechanisms have been proposed to explain the effective role of Pt in increasing the oxidation and corrosion resistance of aluminide, because this element does not participate directly to the formation of the protective oxide scale. Figure 2.10 shows how the presence of Pt increase the performance of an aluminide in terms of hot corrosion resistance:

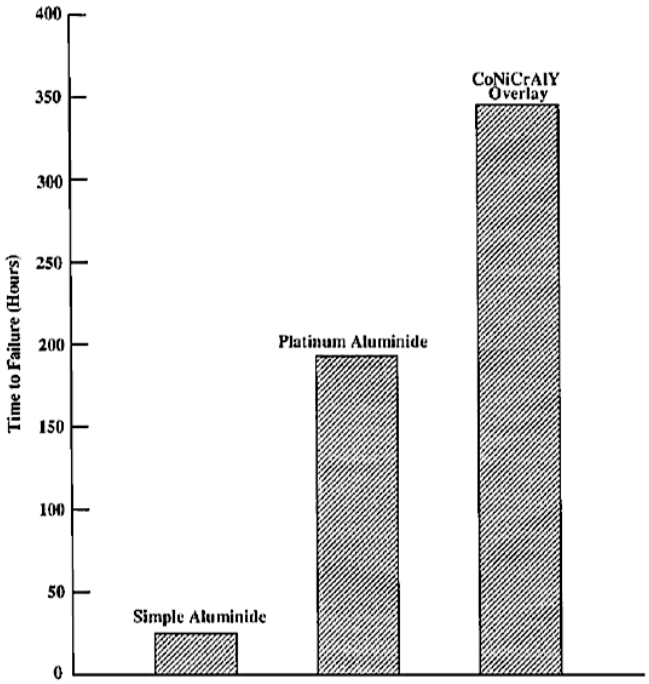

Figure 2.10: *Comparison of hot corrosion resistance for a simple aluminide coating, a platinum modified aluminide coating and a CoNiCrAlY overlay coating*

As mentioned, the mechanisms through which platinum acts on the bond coat properties are not clear. For example, it has been shown that the formation of the phase $PtAl_2$ increase the quantity of the aluminum inside the bond coat, with the consequent increasing of the selective oxidation of the Al [4]. This is essentially due to two factors:

1. No platinum oxide is formed at operating temperatures;
2. Al is very mobile in rich platinum phases.

This results in an alumina scale with increased purity and reduced growth rate. The efficacy with which platinum performs this action is related to an optimum concentration of Pt, which in excessive amounts would brittle the superalloy, and greatly increase the process costs.

In addition, it suppresses the precipitation of Cr rich phases inside the outer layer of the coating. In fact, Cr in solid solution increases the activity of the Al near the surface; this benefit is less in the presence of precipitates, which therefore results in a reduction in the oxidation resistance of the coating. Pt also suppresses the diffusion of refractory elements such as Mo, V and W from the alloy to the outer layer and improves the stability of the coatings against the inter-diffusion between the substrate and coating itself, preventing the phase transformation from β to Ni-richer phases [5]. Finally, it suppresses the formation of voids at the interface, thus increasing the adhesion of the scale to the coating [6].

2.5 Modified diffusion aluminide coating with reactive elements

It has been known for more than 70 years that the addition of small quantities of reactive elements (RE), generally transition elements such as Hf, Zr, Y, Si, La or Ce, has beneficial effects on the oxidation behavior of aluminide. They take the name of reactive elements because they themselves react in the coating during oxidation.
Pfeil in 1937 [7] was the first to report the beneficial effects of the RE; Since then, the scientific literature agrees on the best adhesion of the oxide and the reduction of the rate of growth of the scale in Ni-based superalloys [8].
Figure 2.11 clearly shows the benefits introduced by RE on oxidation rate. The k_P of a β-NiAl coating is compared with a Y, Y_2O_3 and Zr doped β-NiAl.

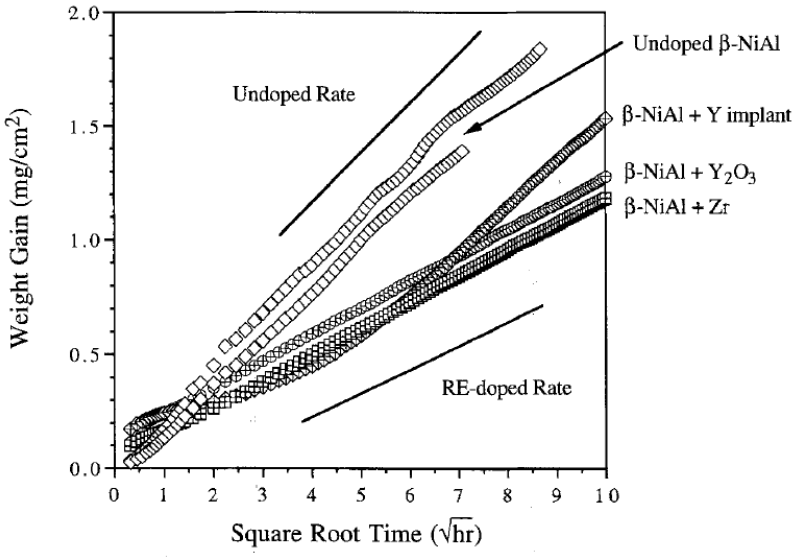

Figure 2.11: *RE effects on weight gain of β-NiAl doped*

The actual mechanisms that take place for the RE are a very controversial topic from a scientific point of view. In general, the mechanisms proposed were:

• REs segregate as ions along the polycrystalline oxide scale grain boundaries, significantly limiting the transport to the outside of aluminum and thus reducing the rate of growth of the oxide. From a combined contribution of both aluminum and oxygen in the absence of reactive elements, oxidation is mainly governed by oxygen transport. It has been experimentally observed that the rate of growth of the oxide scale is influenced differently depending on the element forming it: in Al_2O_3 there is a reduction in the speed of about 2-4 × while in Cr_2O_3 of a factor 10-100 ×.

• REs segregate as ions, but are not static, but spread outward during oxidation, driven by the Dyanamic Segregation Theory [10].

• REs occupy reticular vacations, causing decreasing of Kirkendall voids formation at bond coat / oxide scale interface: Al and Ni interdiffuse with different speeds, causing the formation and coalescence of voids, which reduces adhesion of the scale of oxide to the substrate [10],[11].

• REs cause the formation of oxide pegs in the substrate, which improve adhesion to the interface by means of a real mechanical anchorage: the reactive element oxides grow by internal oxidation below the scale. The distribution of these pegs is a function of solubility: reactive elements with higher solubility result in the formation of more thin oxide pegs than those with limited solubility [12].

• The REs bind to S, inhibiting its segregation to the oxide-substrate scale interface: in fact, the presence of S at the interface lowers the cavity formation energy, which would affect the adhesion of the oxide scale [13].

• The REs determine strong interactions with the oxide interface: Density Functional Theory (DFT) principles based on theoretical calculations indicate that the first transition elements, characterized by open electronic shells, are able to determine, added to bond coat, bond-to-bond interactions to the strongest interface.
In practice, it is believed that co-sharing of these mechanisms causes a beneficial effect on oxidation and hot corrosion resistance [14].

2.5.1 State of the art

It is preferred to use reactive elements with a high atomic radius such as Zr and Hf, because they can react more easily thanks to their atomic dimensions.
Guo et al [15] compared the behavior of some coatings after 100h of cyclic oxidation at 1200 ° C, showing that among all the compositions studied, indeed, doped aluminide with Hf, Zr and an Hf-Zr blend are those which presented a greater oxidation resistance (Figure 2.12) with a lower k_P.

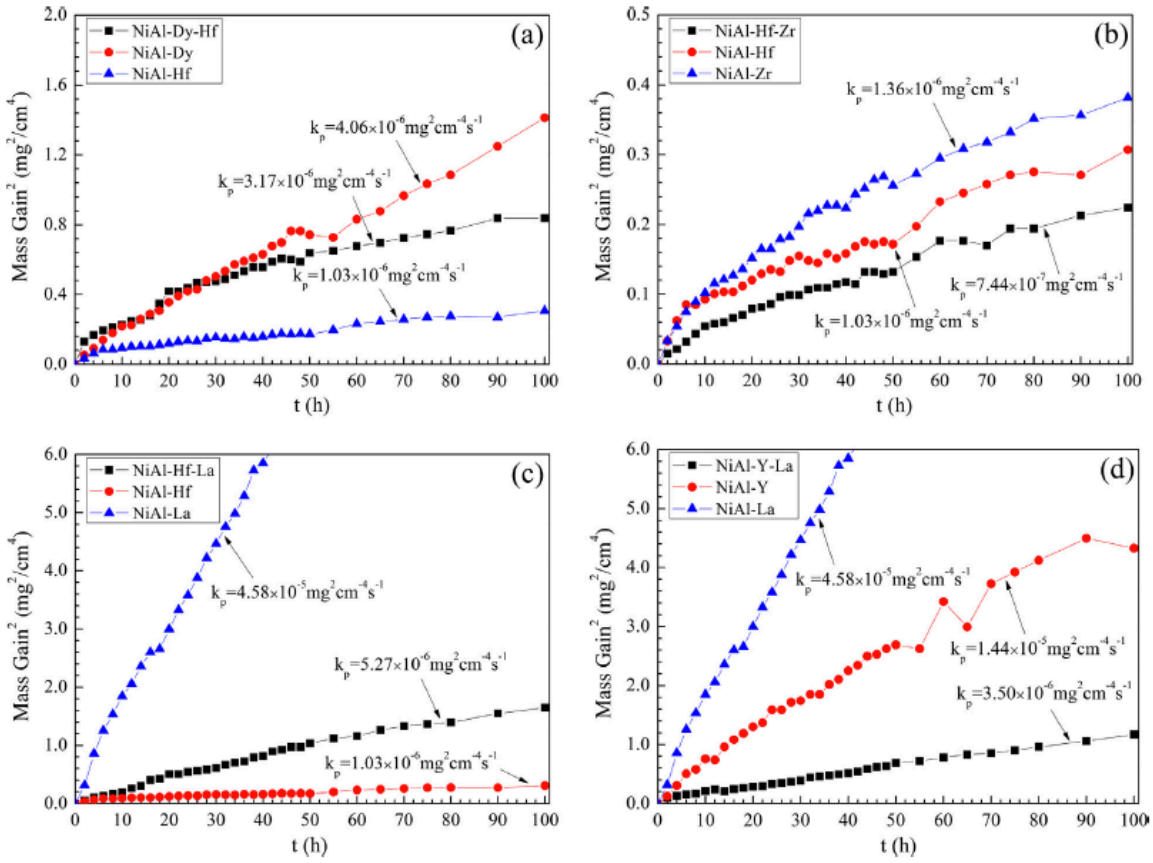

***Figure 2.12**: Square weight gain (sample + spalling) for NiAl with different amount of RE during 100h cycles at 1200°C in air: (a) NiAl–0.05%Dy–0.05%Hf, NiAl–0.05% Dy e NiAl–0.05 %Hf ; (b) NiAl–0.05%Hf–0.05% Zr, NiAl–0.05% Hf e NiAl–0.09% Zr ; (c) NiAl–0.05% Hf–0.05%La, NiAl–0.05% Hf e NiAl–0.09% La ; (d) NiAl–0.05% Y–0.05%La, NiAl–0.06% Y e NiAl–0.09% La*

Guo suggested that Hf and Zr cations segregate to the oxide grain boundaries by interacting with oxygen (Figure 2.13); Moreover, if deposited together, they form an ionic group that synergistically produces stronger interactions than the two individual ions.

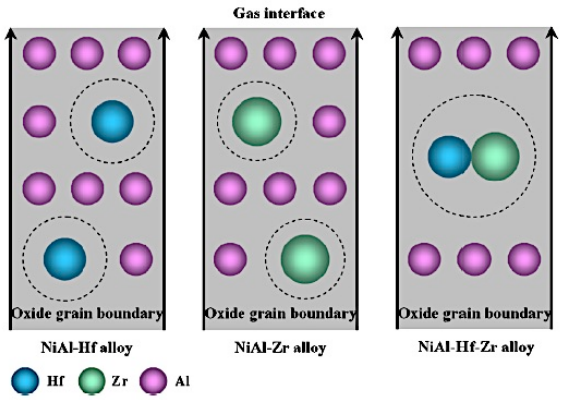

***Figure 2.13:** Zr and Hf doping of a modified aluminide coating*

Hamadi et al. [17] characterized a doped NiAl coating with Zr; Figure 2.14 shows the concentration profile of the Zr obtained by GDMS, in which it is noted that the RE moves to the interface between the interdiffusion zone and β-NiAl.

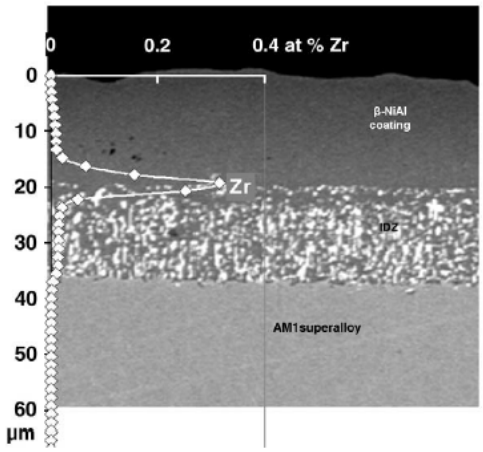

Figure 2.14: *Cross-section of the coating with the Zr profile*

The cyclic oxidation resistance of the AM1 / NiAl (Zr) system was compared to that of the AM1 / NiAl system to obtain the effect of Zr; In addition, the AM1 / (Ni, Pt) Al system has also been taken as an industrial reference. From the curves shown in Figure 2.15 it is shown that the behavior of the doped lining with Zr is absolutely comparable to Pt aluminum.

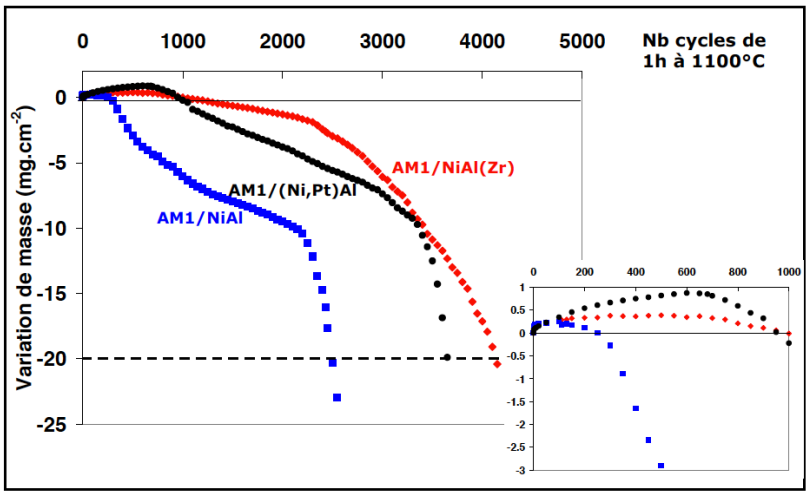

Figure 2.15: *Mass variation vs time for cyclic oxidation tests at 1100°C*

SEM (Figure 2.16) analysis also showed that after 250 cycles, spallation and oxidation phenomena are present on the coating surface of NiAl, while appearing on the surface of the modified coating only after 500 cycles. Moreover, in the case of NiAl, the spallation zones reveal the presence of

numerous cavities at the intermetallic-oxide interface; these cavities have not been observed in the doped coating

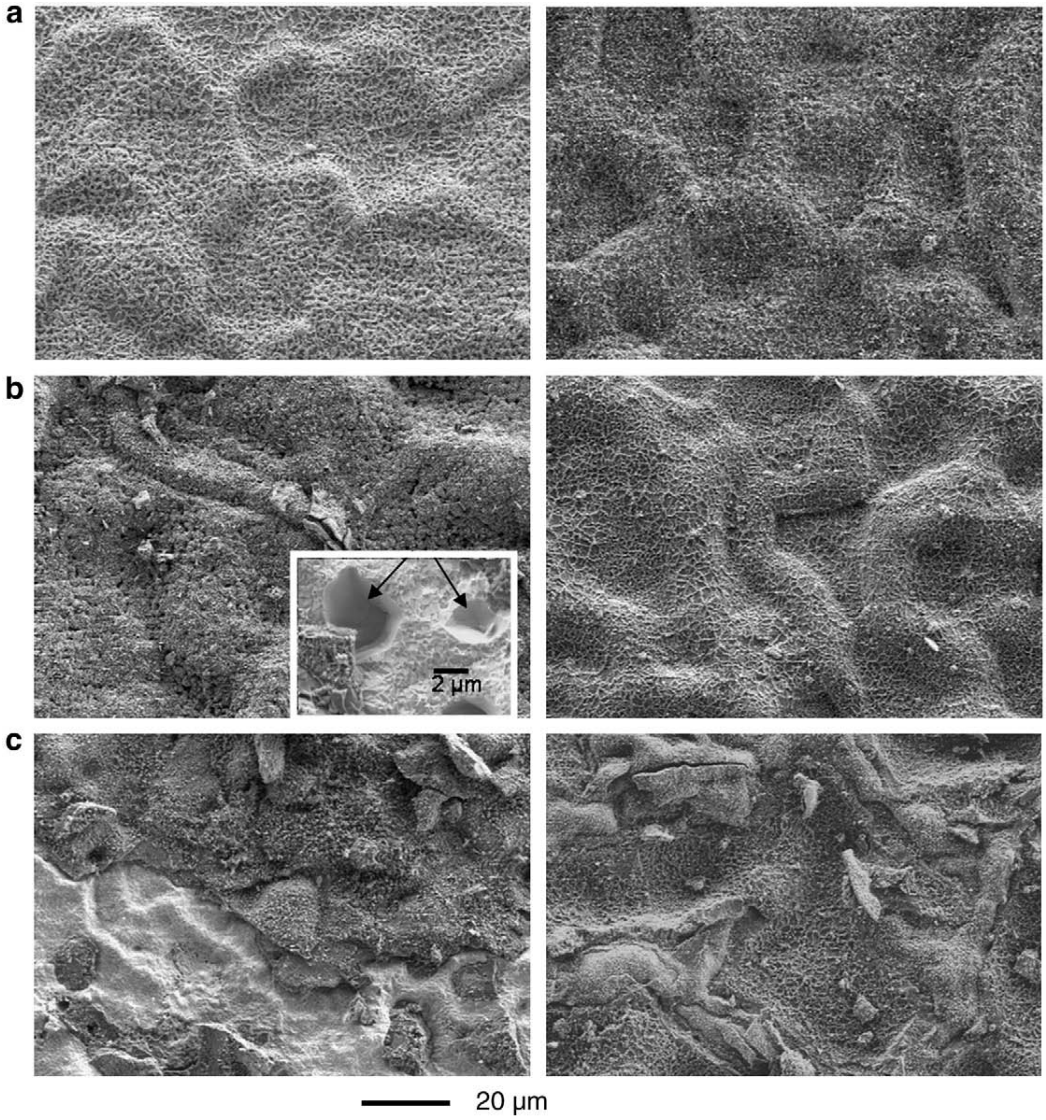

Figure 2.16: *Cross-section SEM micrographs of oxidized sample AM1/NiAl (on the left) and AM1/NiAl (Zr – on the right) after: a) 50 cycles; b) 250 cycles; c) 500 cycles of oxidation tests at 1100°C. In the figure b, the arrows indicate the cavities[18].*

Figure 2.17 compares the isothermal oxidation behavior of modified aluminide and simple aluminide coatings.

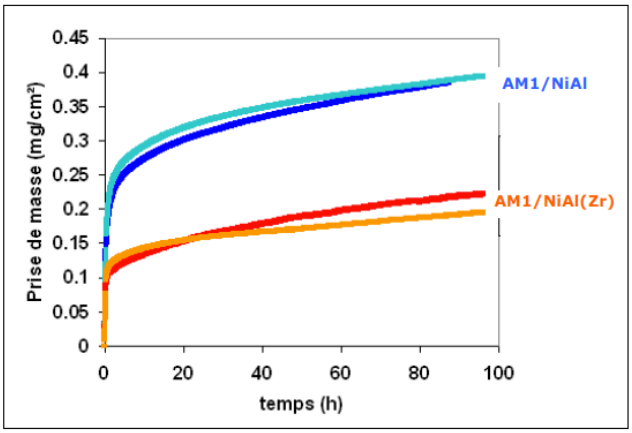

Figure 2.17: *Change in weight after 100h of isothermal oxidation at 1100 ° C of doped and standard NiAl coating.*

In the first 3h the gain by weight is significant, and corresponds to the transient oxidation regime; at this stage, oxides of all the constituents of the alloy are formed, provided that under such conditions the relative free energy variation is negative. By the progress of the oxidative process, it is expected that the thermodynamically stable oxide predominates with respect to the others. The metastable phases of the alumina (γ, δ, θ), do not have the same protective action as it guarantees the α-Al_2O_3. Therefore, avoiding or minimizing transient oxidation processes improves the protective action of the oxide scale.

Subsequently, oxide growth reaches a steady state. Between 20 and 100h the curves for both coatings have the same pattern and thus the same steady oxidation regime.

The data show that with Zr the transient oxidation phase is reduced by a factor of 2. This may be due to or to inhibition of the transport to the outside of the Al, which thus promotes anionic oxidation and the growth of α-Al_2O_3, or to the growth of θ-Al_2O_3 nucleation.

References

[1] Y. Tamarin, ASM International, Ohio, 2002.

[2] J.R. Nicholls, Journal of metals, 52 (1), pp. 28-35, 2000.

[3] N.P. Padture, M. Gell, and E.H. Jordan, Science, 296 pp. 280-284, 2002.

[4] J. R. Nicholls, “Designing Oxidation-Resistant Coatings,” no. January, 2000.

[5] A. G. Evans, D. R. Mumm, J. W. Hutchinson, G. H. Meier, and F. S. Pettit, ,” *Prog. Mater. Sci.*, vol. 46, no. 5, pp. 505–553, 2001.

[6] G. Evans et al., Progress in Materials Science ,46, 505-553, (2001).

[7] Tawancy H. M.; Sridhar N.; Abbas N. M., “Journal of Materials Science, 35 (2000), p. 3615-3629.

[8] G.W. Meetham, Mater. Sci. Eng. 2 (1986) 290.

[9] G.W. Goward, Surf. Coat. Technol. 108-109 (1998) 73-79.

[10] D. P. Whittle, J. Stringer, Phil. Trans. R. Soc. Lond. A, (1980) 295

[11] J.D. Kuenzly and D.L. Douglass: Oxid. Met. Vol. 8 (1974), p. 139

[12] R. Bianco and R. A. Rapp, J. Electrochem. Soc. (1993) vol. 140, issue 4, 1181-1190

[13] ee, W.Y., Wright, I.G., Pint, B.A. et al. Metall and Mat Trans A (1998) 29: 833

[14] B. A. Pint, Oxid. Met. 45 (1996) 1-37.

[15] B.A. Pint, Proc. of the J. Stringer Symposium, November 2001.

[16] M.W. Brumm, H.J. Grabke, Corros. Sci. 34, 547, 1993.

[17] H. Guo et al., Corrosion Science 88 (2014) 197–208.

[18] S. Hamadi et al., Surface & Coatings Technology 204 (2009) 756–760.

CHAPTER 3

Processes for production of diffusion aluminide coatings

3.1 Coating technique

Diffusion coatings are obtained from an alloy that is superficially enriched with elements capable of forming oxide scale such as Al, Cr, Si, or combinations [1], up to a depth of 10 ÷ 100 µm. These elements bind to the primary elements of the alloy, resulting in intermetallics. This type of coating can be obtained by various techniques, as shown in Figure 3.1:

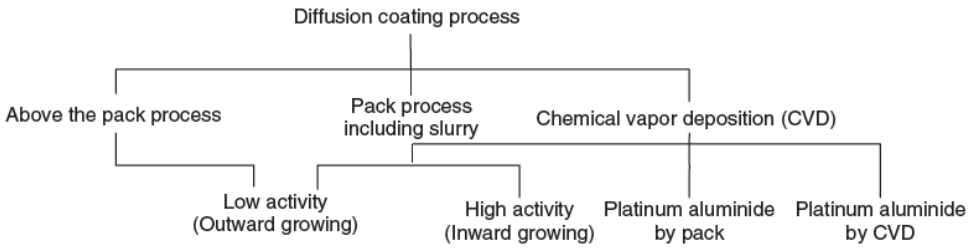

Figure 3.1: *Diffusion coating technique*

Figure 3.2 describes the process steps generally common to all techniques, which are:

• Generation of vapors, generally halide, containing the element that will form the protective oxide scale (Al, Cr or Si);

• Gas transport to the surface of the component, by a partial pressure gradient;

• Gas reaction with substrate followed by solid state diffusion processes within the alloy;

• Additional thermal treatments, if needed, to obtain the desired composition and coating properties.

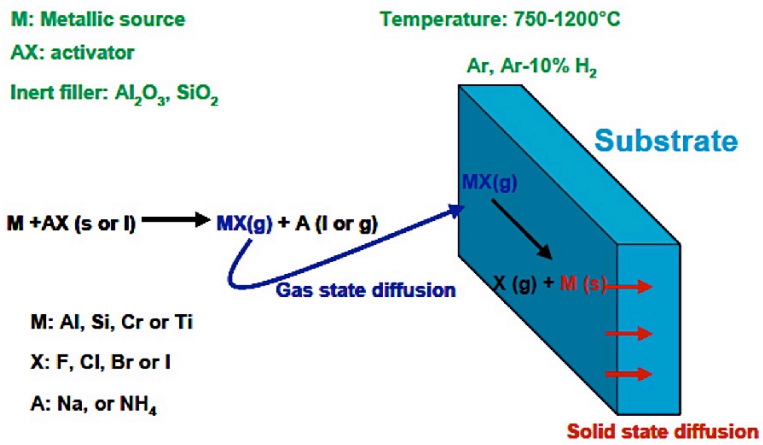

Figure 3.2: *Deposition mechanism of diffusion coating procedure by vapour phase process*

From a thermodynamic point of view, the most important chemical reactions are those related to the formation of volatile halide and its decomposition, and those related to solid state diffusion. There are therefore two crucial temperatures for the correct deposition of an element: the temperature that allows the formation of the gaseous halide and the one that activates the diffusion.
The microstructure, the activity of the Al (or Cr, Si) within the coating and the thickness of the coating depend on the alloy used as substrate, on the process parameters and on the following heat treatment selected.

3.2 Growing mechanism of diffusion coatings

There are two mechanisms for a diffusive coating formation, depending if the main diffusing species is aluminum inside the substrate or is the Ni diffusing outwardly. The two mechanisms lead to the achievement of different types of coatings, known as inward and outward coatings.

There are, therefore, two distinct process, which differ in the term of the Al activity in the gaseous phase and process temperatures:
• High Temperature, Low Activity HTLA
• Low Temperature, High Activity LHTA
The activity of a gaseous phase can be approximated, at low pressures, with the ratio between the partial pressure of the gas and the atmospheric pressure. High activity involves high partial pressure, which in the specific case indicates the availability of Al-gaseous halide.

3.2.1 High Temperature Low Activity Process

This method applies a high temperature (> 1000 ° C), for a time ranging from 3 to 4 hours, in the presence of a low activity of the Al (HTLA).
It is a "single-stage" method with the outward diffusion of the Ni and the subsequent reaction with Al to form the β-NiAl coating: the growth of this phase is therefore going outward. In practice, Al also diffuses into the substrate, resulting in coating growth in that direction, but this contribution is significantly lower than that due to the transport of the Ni ($D_{Ni} > D_{Al}$). Conversely, the diffusion of Ni to the outside causes the formation of a poor Ni area just below the original surface of the substrate; such a zone can be a phase precipitate rich in metal elements and is commonly referred to as interdiffusion zone (IDZ).

Figure 3.3 shows schematically the progressive stages that characterize the deposition. It is noted that, as compared to the surface of the substrate, the coating has grown outwardly.

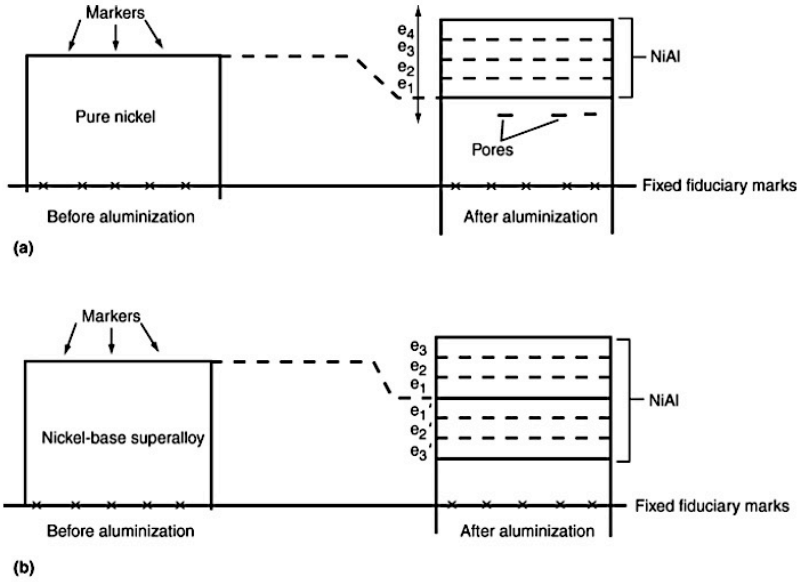

Figure 3.3: *Schema for the progressive stages of aluminization by HTLA pack cementation – a) Pure Ni (e_1 is formed firstly, then e_2,e_3 and so on); b) Ni-based super alloy (e_1 and e_1' are formed firstly, then the others) [2]*

As mentioned, the outside diffusion of the Ni is much faster than the diffusion of aluminum. This difference between the two speeds involves the voids, known as Kirkendall voids near the original interface (Figure 3.3a). The advancement of the process causes, in a Ni-based superalloy, a depletion of Ni in its respective areas within the alloy (Figure 3.3b). Thus, when a layer e1 is formed externally, a corresponding layer, depleted in Ni, forms inside the alloy, and so on. This technique therefore allows to obtain a β-NiAl coating, which is however accompanied by the presence of precipitates (such as TiCs) that are not soluble in the intermetallic matrix (Figure 3.4).

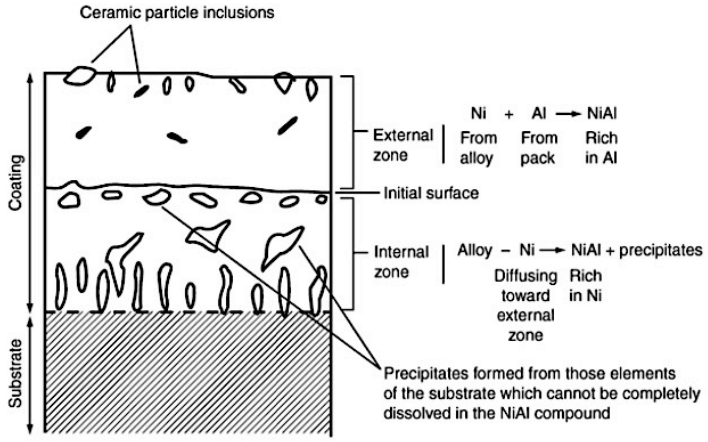

Figure 3.4: *Final microstructure of a Ni-based super alloy coated by HTLA pack cementation*

Figure 3.5 shows in section a sample aluminized by HTLA pack cemetation. It is noted that this coating is characterized by two areas, which are roughly the same thickness:

• External β-NiAl layer

• Intermediate area, poor in Ni with heavier element precipitates

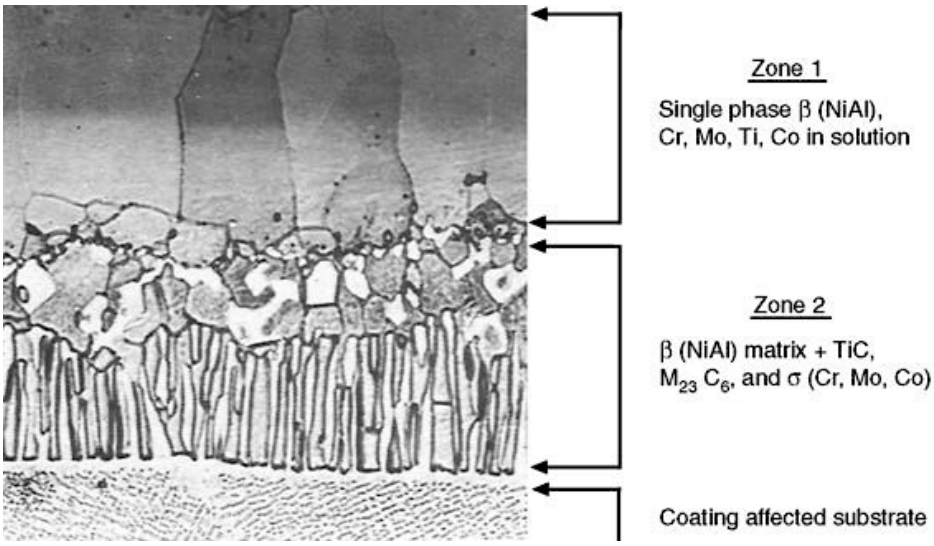

Figure 3.5: *Ni-based superalloy aluminized by HTLA pack cementation [3]*

3.2.2 Low Temperature High Activity Process

In this method the deposition takes place at low temperature (LTHA) and involves the execution of two steps: a low temperature deposition (700 - 850 ° C) followed by diffusion annealing at temperatures above 1000 ° C . Downstream of the first step, the coating is made up of an excessively rich phase in aluminum (δ-Ni_2Al_3 or δ-Ni_2Al_3 + β-NiAl rich in aluminum), carbides and precipitates of the various constituent elements. This microstructure is due to the diffusion into the interior of the inward diffusion, which causes an increase in the interior of the coating (D_{Al}> D_{Ni}). During the second stage (diffusion treatment), the Ni moves outwards leading to β-NiAl formation, quite similar to HTLA mode. This step is crucial, as the δ-Ni_2Al_3 phase is a fragile phase with mechanical properties much lower than β-NiAl. Again, in this case, the formation of an interdiffusion zone is provided at the interface between the coating and the substrate.

Figure 3.6 shows the first stage of deposition, the aluminization. It is noted that, as compared to the surface of the substrate, the coating is increased inward.

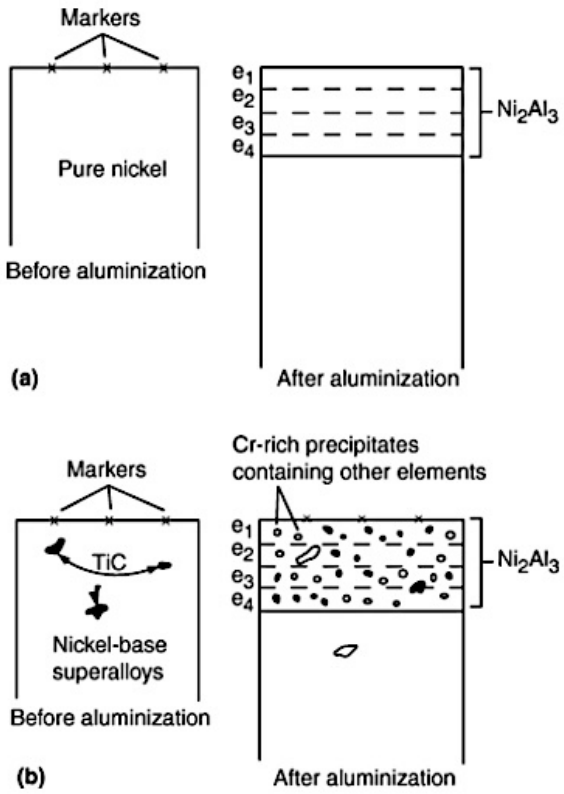

Figure 3.6: *Schema for the progressive stages of aluminization by LTHA pack cementation – a) Pure Ni (e_1 is formed firstly, then e_2,e_3 and so on); b) Ni-based super alloy (e_1 is formed firstly, then the others)*

Figure 3.7 shows the final microstructure; this consists of:

an outer layer of β-NiAl with carbides and precipitates of substrate elements that were formerly bonded to Ni, an intermediate layer of β-NiAl free of carbides and precipitates, and finally an interdiffusion area. In addition, it is noted that during the thermal treatment, following the aluminization, the coating is characterized by a portion of growth towards the outside, due to the activation of the Ni diffusion outwardly.

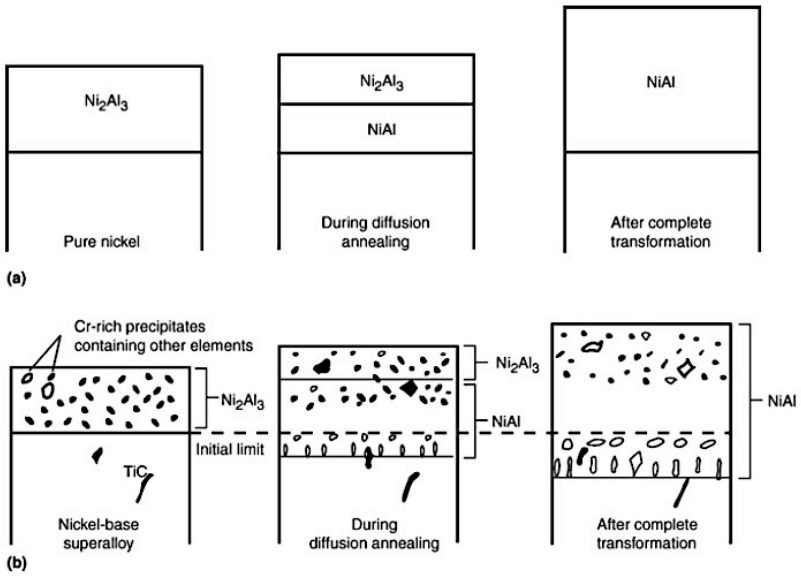

Figure 3.7: *Final structure of a Ni-based super alloy coated by LTHA pack cementation*

Figure 3.8 shows a section of an aluminized sample by pack cemetation LTHA. It is noted that the β-NiAl thickness is substantially larger than that of the interdiffusion zone.

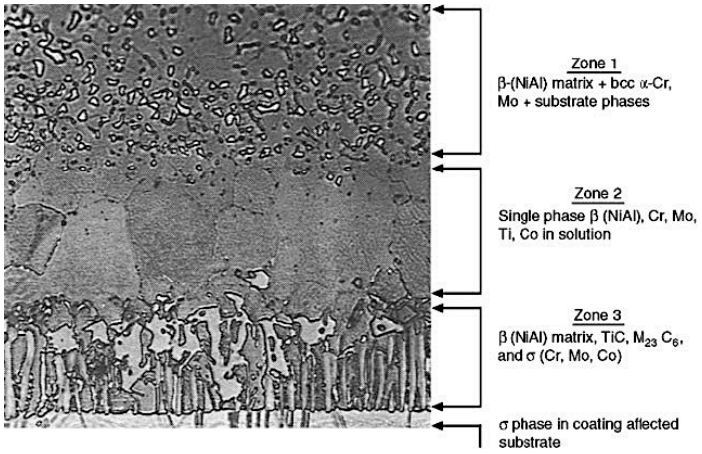

Figure 3.8: *Ni-based superalloy aluminized by LTHA pack cementation*

3.3 Pack Cementation

In this process, the components to be coated are first cleaned, generally by means of alumina blasting to remove oxides and contaminants from the surface. If necessary, the area of the component to be protected from deposition of the coating is masked with a material that can withstand the process temperatures without going against degradation. At this point, as shown in Figure 3.9, the components are buried in a mixture of powders (packs) inside a sealed (or semisealed) reactor. The reactor is then

inserted into a furnace and heated in an inert atmosphere (Ar or H2), in order to avoid the oxidation of the elements that will produce the coating in the pack.

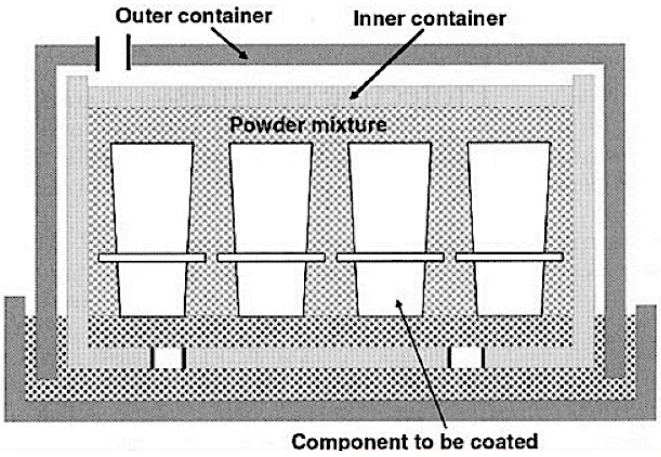

Figure 3.9: *Pack cementation process*

The reactor is composed of materials that do not degrade at process temperatures such as Inconel alloys and stainless steels 310, 321 and 347.

Powders contain:

• The aluminum source (or Cr, Si), generally called master alloy.

• An "activator" salt, usually an ammonium or sodium halide, which, by reaction with the source, will form the gaseous species containing aluminum and transport it to the surface to be coated.

• An inert filler, such as powdered alumina, designed to create interconnected porosity for gas transport and prevent sintering, which would occur at process temperatures.

The inert filler is not always indispensable; the choice depends on what type of Al source is used. Generally, in LTHA processes, it is preferred to use Al pure as a master alloy, which allows to cast more gas in the gas phase, resulting in a greater availability of the deposition elements. However, choosing a low-core element involves the need to adopt an inert filler that prevents the sintering of the pack. If this is not used, there will be difficulties in recovering the components.

In HTLA processes Al (Al-Cr, Al-Co) alloys are generally used as the source; The filler is not necessary, in this case, because of high melting point of the master alloy

A salt, to be suitable for activating a pack cementation, must be necessarily unstable, to react at the process temperatures. Salt selection guidelines are the following:

The anion is generally a halide. Concernign the cation, ammonium salts are preferred because they decompose to high T, producing H_2 that increase the reducting atmosphere.

The reaction that the activating salt has with the component depends on the type of salt used. In the case of NH4Cl, NH4Br and NH4I (Figure 3.10a), the halide stays in the gas phase even after reaction with the substrate and deposits only solid Al: there are no co-products that can be deposited on the surface of the component. The F is still used, despite the disadvantage of ist utilization, since it is characterized by high partial pressure, therefore forms AlF very easily. Finally, using Na-halides (Figure 3.10c), instead of solid precipitates, there are liquids on the surface.

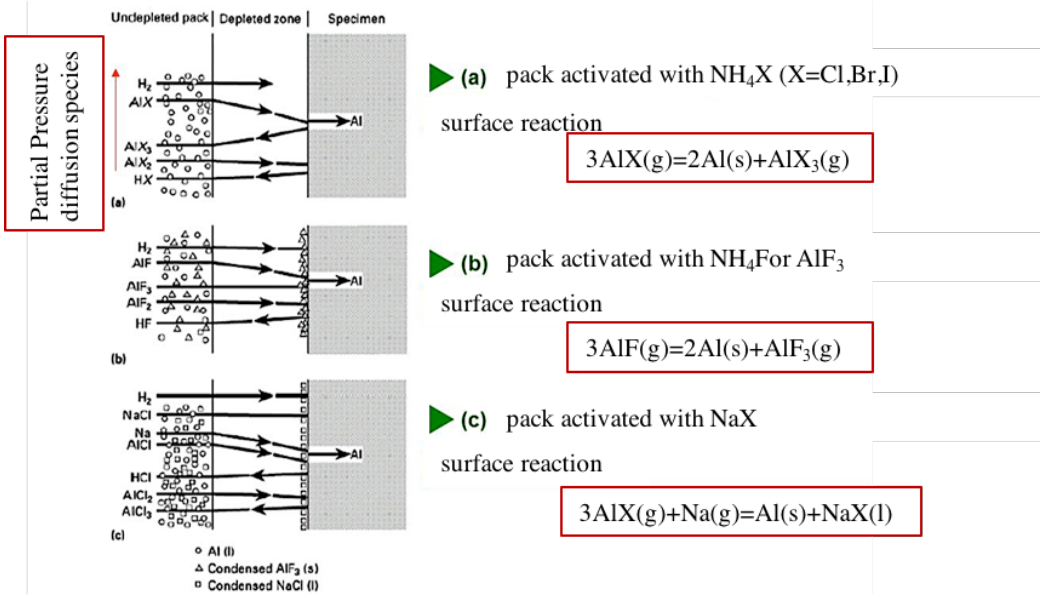

Figure 3.10: *Mechanism of reaction and diffusion for different activator salts*

The reactions between NH4X ammonium halide and a substrate in Ni-base super alloy are as follows:

- Decomposition of NH4X

$$NH_4X_{(s)}=NH_{3(g)}+HX_{(g)} \quad (3.1)$$

- Volatile Al halide formation

$$6HX_{(g)}+2Al_{pack}=2AlX_{3(g)}+3H_{2(g)} \quad (3.2)$$

$$2AlX_{3(g)}+2Al_{pack}=3AlX_{(g)} \quad (3.3)$$

- Al deposition on top of the substrate

$$2AlX_{(g)}+3Ni_{sub}=2NiAl_{alloy}+NiX_{2(g)} \quad (3.4)$$

$$3NiX_{2(g)}+5Al_{pack}=3NiAl_{alloy}+2AlX_{3(g)} \quad (3.5)$$

$$3AlX_{(g)}+2Ni_{sub}=2NiAl_{alloy}+AlX_{3(g)} \quad (3.6)$$

$$2AlX_{(g)}+2Ni_{sub}=2NiAl_{alloy}+X_{2(g)} \quad (3.7)$$

$$2AlX_{(g)}+H_{2(g)}+2Ni_{sub}=2NiAl_{alloy}+2HX_{(g)} \quad (3.8)$$

where reactions (3.4) and (3.5) are displacement reactions, disproportionation (3.6), decomposition (3.7), and finally reduction reaction (3.8).

The advantages of this technology are:

1. the exercise at atmospheric pressure;
2. the good reproducibility of the coating and
3. low plant costs, since the latter is essentially a furnace.

The main disadvantages concern the limited flexibility of the process in terms of coating composition and the length of the process for high thicknesses. In addition, pack particles may be trapped in the outer layer of the coating: this phenomenon is generally negative since such inclusions will prevent the formation of a continuous oxide scale.

3.1.1 Process above the pack

This process works very similar to that discussed in Section 3.3, with the exception that the components to be coated are placed above the powders containing Al.

Al transport from the pack to the substrate occurs by gas phase diffusion while the substrate surface inside for solid phase diffusion. The first type of diffusion increases the surface concentration of Al in the coating while the second decreases it to a steady state. In the vapor phase, the Al transport rate is much faster than solid phase diffusion within the substrate, which is therefore the deciding step for the deposition rate. Finally, there is the diffusion of reaction products from the substrate to the outside of the reactor, which controls the purity of the coating.

The diagram of an above the pack system is shown in Figure 3.11.

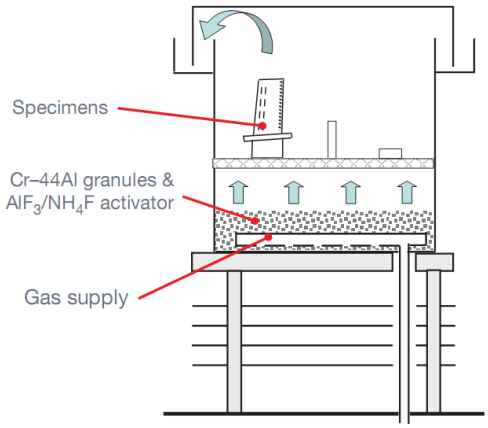

Figure 3.11: *Above the pack process*

A typical temperature profile of the above the pack aluminization process is shown in Figure 3.12:

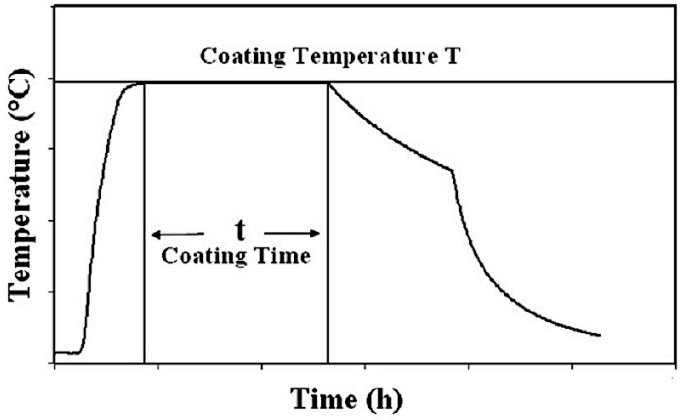

Figure 3.12: *Profile temperature in a out-of-pack process*

This method, as compared to standard pack cementation, simplifies the process of unpacking components from dust; Moreover, it allows for a much cleaner and homogenous coating, even for complex geometry components, without embedding of particles during the process.

Another variant, more technological than concept, is VPA (Vapour Phase Aluminizing); the only difference lies in the fact that no more dusts but pellets are used. The advantage is the simplification of the charge and discharge processes of Al source, since no volatile metallic dust is formed: this in fact provides for the most in-worker protection systems and under a certain dimension can become dangerous (pyrophoric phenomenon). Finally, it is easier to ignore the waste of the process: once depletion of Al under some concentration occurs, the source is exhausted and can be replaced and reloaded more easily.

3.4 Slurry aluminization

The coatings obtained by this technique offer a very similar chemical composition to that found in alluminide products by pack cementation. In this process, powders and activators are mixed with an organic binder (or an aqueous emulsion) to obtain a slurry. The coating is applied to the substrate by immersion or spraying at room temperature; then undergoes a low temperature treatment treatment, typically around 200 ° C. After this, the diffusion process of the Al is activated: the components are brought to temperature (650 ÷ 1100 ° C), which varies depending on the substrate to be coated and its final use.

With this technique, it is easy to restore if necessary parts of the coating, since it is possible to apply the slurry locally. However, it is less clean than above the pack as it introduces an interface between a solid precursor and the component; all those reactions between the gas and the surface become reactions between a solution and the component, which will then be covered with that part of the slurry that has not reacted. At the end of the treatment, you will need to clean up the residues present, which is not trivial when you want to cover the cavities.

References

[1] Z.D. Xiang, P.K. Datta, Mat. Sc. and Eng. A356 (2003) 136/144

[2] R. Pichoir, Corrosion, D.R. Holmes and A. Rahmel, Ed.,(1978) Applied Science Publishers Ltd., London p 271.

[3] G.W. Goward and D.H. Boone, Oxid. Metals, (1971),Vol 3, p 475

CHAPTER 4

Design of experimental activities

The substrate

The substrate used is a directionally solidified nickel-based superalloy, commercially known as René 108ds, whose composition is shown in Table 4.1. The alloy was supplied as bars with a diameter of 20 mm. These bars were cut in order to obtain the 5 ÷ 6 mm thick disks for the phase 1 and 1 ÷ 2 mm thick disk for the phase 2

Table 4.1: *Chemical composition of René 108ds, the substrate used in this work*

	Compositions (wt%)								
	Ni	Cr	Co	Al	Ti	Mo	W	Hf	Ta
Renè 108DS	Bal.	8,4	9,5	5,5	0,7	0,5	9,5	1,5	3

Coating requirements

Superalloys used in high-temperature applications are generally developed with optimized mechanical properties such as tensile, creep, and fatigue strength while maintaining microstructural stability over a wide temperature range. These properties come from the chemical modification of the superalloy. Despite of this mechanical resistance, the environmental protection has to be provided by coatings, which are not suitable with the thermal stress exposition during operating time. So, to design a performing material, some requirements are to be considered [1]:

Oxidation and corrosion resistance:

- Study of the formation of the protective coating
- Selective permeability of the oxygen to the oxide scale
- Tailored growth rate of protective surface scale
- Controlled doping of the protective coating by reactive elements

The coatings adopted within the turbine differ according to the considered rotor stage. From an industrial point of view the blades of the first stage at a higher temperature (HPT) are coated with an aluminide modified with Pt, which ensures high performance with very high production costs, both for the cost of the raw material and the cost of the electrodeposition process, despite the deposited layer being ≤ 10 μm. The third stage blades (LPTs) are coated with standard aluminide because of the low temperatures to which they are subjected. For IPT, industrial modified Pt aluminide coating is used: the performance and cost of this coating are oversized to the needs of the blades, but there are no other solutions that guarantee the same safety against a lower cost. For this reason, the first phase of this work was to find a good candidate, as doping element, to replace the Pt and reduce cost without losing the protective properties for the IPT.
The selected process for the coating formation is the aluminization by pack cementation which is an industrially well consolidated procedure. This first step of the work was performed in order to obtain a *know-how* to increase the coating characteristics. Then, as the best parameters for the standard process was evaluated, the doping with reactive element was introduced and studied by comparison with the standard coatings. This was an important step to understand deeply the mechanism of the oxidation and corrosion resistance increased by the introduction of the reactive element.

As it was said before, a protective coating can increase the environmental corrosion resistance despite the decreasing of mechanical properties of the component. This variation in mechanical properties can involve a damage to the component with the consequent failure which can have disastrous consequences in some applications. So, the performing material, with oxidation/corrosion resistance increased, has to respect some other requirements in terms of stability of the component:

Stability

- No undesired phase formation within the coating
- Compositional stability across interface
- Minimized brittle phase formation

The final microstructure of the coating is the result of the diffusion of chemical elements between the coating and the substrate during the aluminization. Consequently, as the interdiffusion zone is formed into the superalloy, the system can be described as a complex multilayer material (Figure 4.1). The microstructure of each layer evolves under service conditions due to the combined effect of high temperature and mechanical stresses. As a consequence of the high temperature, the materials are

subjected to a thermal expansion without any exception. Each phase has his thermal expansion with his coefficient; even if the properties of IDZ are unknown [2], it is evident that the thermal expansion of the three different phases can't be considered independent since the IDZ expansion, for example, is prohibited by the coating zone. This kind of stress can generate thermo-mechanical fatigue during the complex thermal and mechanical history for a typical cycle of operation.

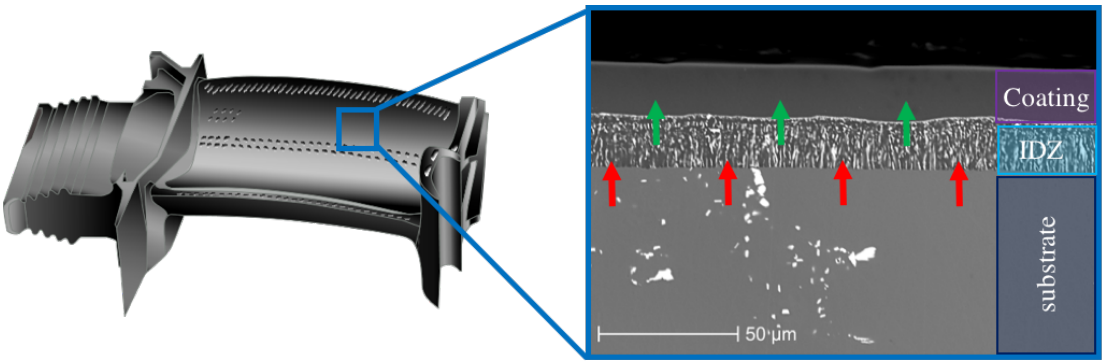

Figure 4.1: *Image of the multilayer system composed by: substrate, IDZ, protective coating. The arrows indicate the sense of thermal expansion*

According to the principle of outward diffusion in aluminization process, the Ni diffuses and reacts with Al to form the β-NiAl coating: the growth of this phase is therefore external. In practice, Al also diffuses into the substrate, resulting in coating growth in that direction, but this contribution is significantly lower than that due to the transport of the Ni ($D_{Ni} > D_{Al}$). As a consequence of this diffusion, the IDZ can be considered as a depleted zone of Ni in which the phases are rich in heavier elements of the superalloy. So, theoretically, the addition of an external nickel layer (ENL) onto the substrate could have several advantages:

- Control of chemical composition of the β-NiAl phase
- No IDZ formation
- Substrate-independent process

First of all, the possibilities to tailor the composition of the ENL could open the way to embed particles inside the diffusion coating with a consequent increasing of corrosion resistance. Then, the deposition of a nickel layer onto the substrate before the aluminization could play the role of a Ni source for the aluminization process, without modifying the composition of the superalloy. And finally, the possibilities to have a Ni reservoir for the diffusion coating formation could positively influence the choice of the chemical composition of the superalloy by freeing the presence of the Ni as based element instead of other elements that can influence the mechanical properties of the alloy.

About the possibilities to embed particles inside the ENL, it was already studied that the doping of the bond coat with some oxides particles could increase the oxidation resistance: Peng and

co-workers [3] added La_2O_3 particles into aluminide coatings using two steps: the first step is to electroplate a Ni-La_2O_3 composite film on Ni, and the second one is to aluminize on the as-deposited composite film. The oxidation results showed that the aluminide coatings with La_2O_3 particles exhibited better oxidation resistance compared to La_2O_3-free aluminide coatings. Similar technique was applied to manufacture aluminide coatings with CeO_2 or Y_2O_3 dispersion [4], [5].

Furthermore, it was reported that during the low activity aluminization, the filler Al_2O_3 [6] could be entrapped into the outer layer of aluminide coating, thus affecting the grain growth and oxidation behavior of the aluminide coatings [7]. The author works exhibited that the Al_2O_3-dispersed chromizing coating produced by chromizing an as-electrodeposited Ni-Al_2O_3 nanocomposite film exhibited an increased oxidation resistance. In this field, nanoparticles show some great properties because of their high reactivity but the dispersibility in a matrix is a fundamental parameter to have a positive influence on the bulk properties. The idea, developed in the phase 2 of this work, is to deposit a nickel-matrix n-Al_2O_3 nanocomposite onto the substrate in order to use the nanoparticles as reactive element and as nucleation grain to promote the rapid transition of the alumina through the various metastable phases up to phase α so as to form a protective and stable TGO. In order to incorporate nanoparticles into the coating, it was necessary to develop a production process capable of transporting the nanoparticles within the bond coat: if this is impossible in the case of vapor-phase processes such as CVD and pack cementation, it is possible in case of liquid deposition such as electrodeposition. In fact, particles could be conveyed by platinum electrodeposition, but this also requires a cost that is not indifferent even for the stack of blades that would not require a modified aluminide with platinum: it is therefore necessary to use a coating that is economical, both from the point of view of the materials, both from the point of view of the synthesis process.

In addition, the high complexity of blades geometry makes it difficult to handle electrolytic deposition, since the coatings produced with this technique are not homogeneous when complex geometries are present.

In summary, the coating has to meet these requirements:

1. Must be compatible with the CVD process used to form β-NiAl
2. Must be able to convey nanoparticles
3. It must have homogeneous thickness even on complex surfaces
4. Must be economical

The technique that could respond to these needs is that called autocatalytic or electroless deposition, which is, a deposition that operates in the absence of electrical current and which produces more homogeneous coatings than those obtainable by electrolytic depositions. As will be discussed later, however, this process has undergone modifications to produce a pure nickel layer.

Operatively, at first, the optimization of the solution formulation was achieved to reach the required thicknesses; Subsequently, the nanoparticles were introduced and the concentrations were optimized.

The third phase of this work has been about the aluminization process of the new electroless nickel plating samples. The introduction of an ENL was, theoretically, positive for the aluminide coating. However, there is no publications in literature about the application of an electroless nickel layer with the aluminization. So, it was necessary to select a technique that was easy to apply, economical and clean from a chemical point of view. Furthermore, the toxicity of the compounds used and the residues and process risks associated with the use of halogen activators make the pack cementation a process to replace. Slurry aluminization was the perfect candidate because the main benefit of the slurry compared to phase vapour deposition is the easier manufacturing and the lower cost especially for large parts. In collaboration with University of La Rochelle and the group of Professor F. Pedraza, the EPNP samples were aluminized by the slurry aluminization. In summary, in Figure 4.2, the scheme collects the idea of the phase 2 and 3.

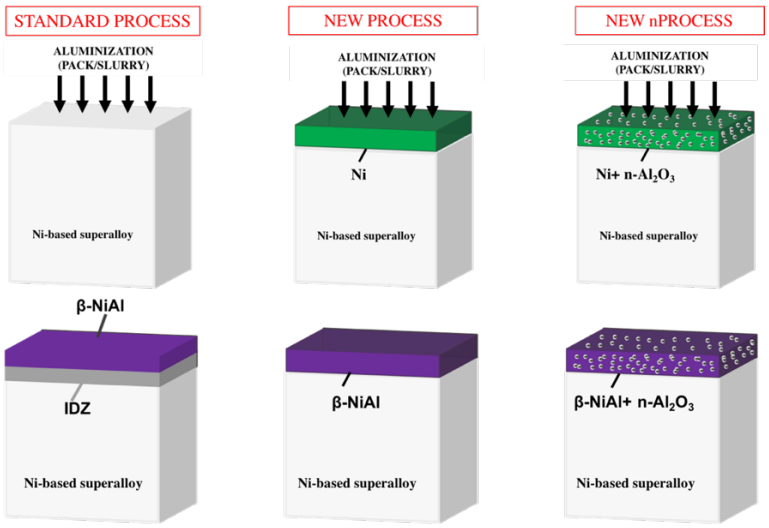

Figure 4.2: *Schema of the aluminization for the new electroless nickel plating substrate.*

4.1 Phase 1: Oxidation and hot corrosion resistance

4.1.1 Standard aluminide coatings

Standard diffusion aluminide coatings were obtained by a semi-sealed HTLA (High Temperature Low Activity) above-the-pack cementation in VPA configuration at Centro Sviluppo Materiali (CSM) S.p.A. (Figure 43).

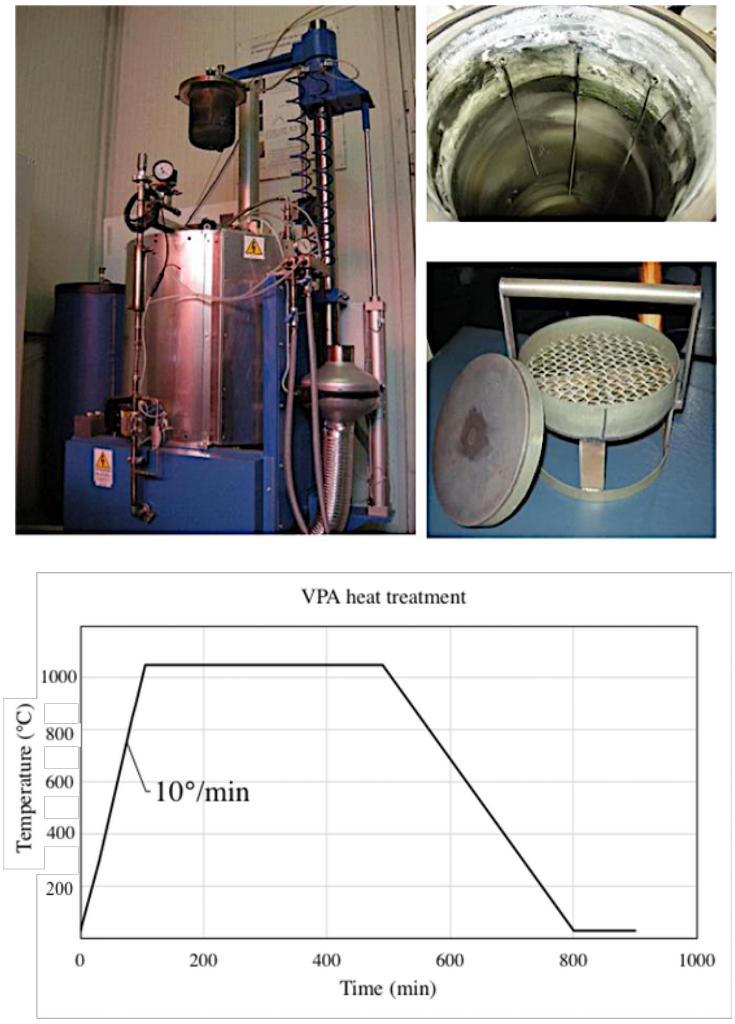

Figure 4.3: *Deposition plant for above the pack cementation (thanks to CSM S.p.a.); Heat treatment profile (below)*

The heat treatment profile, in Figure 43, have two plateaux, one at about 750°C and the other at about 1100°C. The heat treatment temperatures were chosen in order to follow the single steps of aluminization described in the paragraph 3.2.1 and respecting the temperature of the last heat treatment of the super alloy.

The samples were introduced in the furnace (Figure 4.4) and heated with a temperature profile shown in Figure 43. In order to avoid the atmosphere contamination, the aluminization was conducted under continuous flux of Ar. The activator salts powder (NH_4F pur. ≥99.99% and AlF_3 pur. ≥99.99%) and the master alloy (Al-Cr 60 wt%) were purchased from SIGMA-Aldrich and dried before the deposition at 80°C.

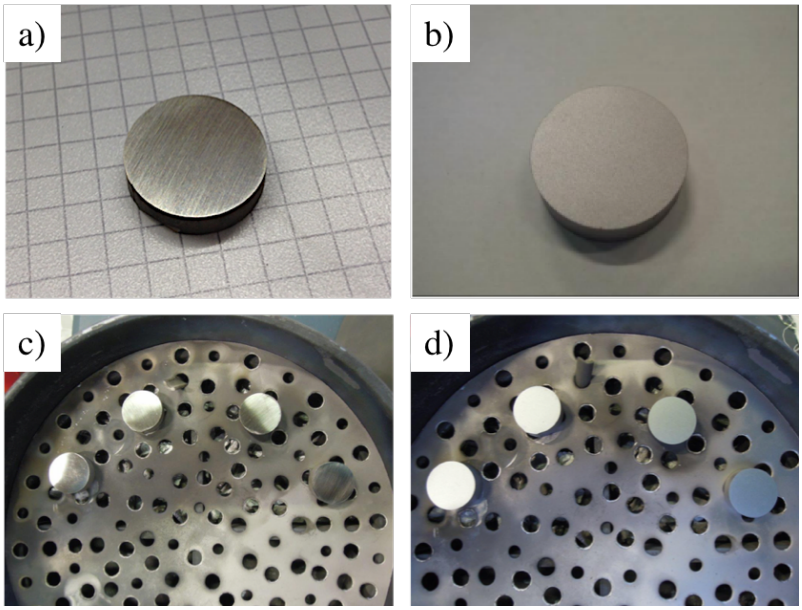

Figure 4.4: *Sample before (a) and after (b) aluminization; samples placed in the basket before (c) and after aluminization (d)*

The Ni-based super alloy rod was cut in cylinders (19.2mm of diameter and 6 mm of thickness), cleaned with acetone and polished with a P400 mesh SiC paper.

To determine the effect of activator salts in the coating, two different concentrations were chosen for each salt. In the

Table 4.3 concentrations in terms of wt% of the pack alloy and mole of fluoride are reported for NH_4F and AlF_3. In all the depositions, it was respected the *equi* molarity of fluoride.

Table 4.3

Concentrations of activator salts, respect to Al master alloy, for the series NF and AlF

Deposition	wt% of activator salt	mol of activator salt
NF1	0.050	0.0135
NF2	0.075	0.0202
AlF1	0.100	0.0135
AlF2	0.170	0.0202

4.1.2 Isothermal oxidation tests

High temperature oxidation tests were carried out in air into a Lenton Thermal Design Ltd tubular furnace, shown in Figure 4. .

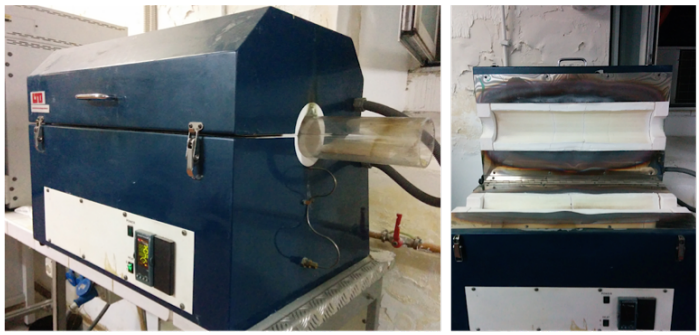

Figure 4.5: *Tubular furnace Lenton Thermal Design Ltd, with quartz reactor.*

The coated samples were placed on a substrate holder made with aluminum oxide, in order to avoid some interactions with the substrate. For each test, the samples were introduced in the furnace by the

heating zone, then slowly move close the hot zone (1050°C) and, after the test time, removed from the furnace with a slow cooling rate (Figure 4.). This operation was performed for alternating cycles of 7/14 hours for a total of 105 hours.

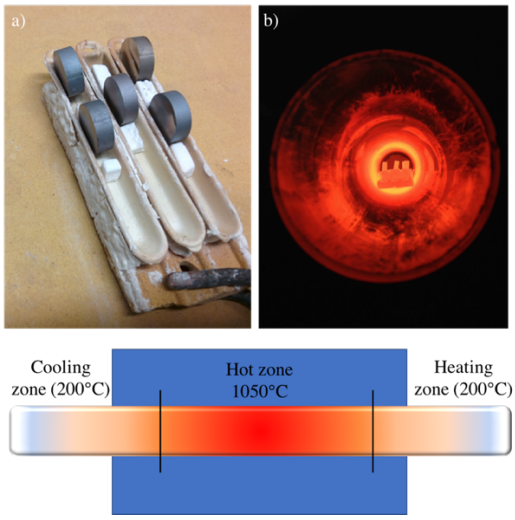

Figure 4.6: *Isothermal oxidation test: a) Sample holder; b) Example of a test at 1050°C. Below is represented the schema of the different zones inside the furnace*

It is noteworthy that the heating and cooling zone is a fundamental step of the oxidation tests: in fact, a sudden decreasing or increasing of temperature, mostly for the samples after the first hours of oxidation, could damage the oxide scale by thermal shock and compromise the test. Oxidation curves were obtained by measuring the weight gain for each cycle with an analytical balance.

4.1.3 Hot corrosion tests

Hot corrosion tests were performed in a high temperature furnace Lindberg. The alkaline salts chosen for the corrosion were Na_2SO_4 and NaCl in a ratio of 1/3. The procedure to perform the test was selected to be reproducible and significant for the operating conditions (temperature and quantity of corrosive agent). For this reason, the corrosive agent was added by mixing the salts with a minimum quantity of deionized water (20 wt%) in order to obtain a slurry that can easily be spread over the sample's surfaces (Figure 4.-left). Once the slurry was prepared, spread and weighed, water has been removed by heating in hot plate in order to obtain a film of salts mixture all over the surface of the samples.

Figure 4.8: *Hot corrosion test procedure: slurry application on a sample (left, red circle) and samples prepared for the heat treatment (right)*

Hot corrosion cycle tests were performed at 900°C with cycle of 10 hours for a total of 200 hours. Every cycle, the samples were washed in hot deionized water, in order to remove the un-reacted salts and the soluble corrosion products before measuring the mass variations. Once the mass variation is measured, the slurry was refilled with the same step described before. This can ensure the reproducibility of the process.

4.1.4 Modified aluminide coatings with Zr

Once the results of the standard aluminization have shown the best parameters in terms of yield of the process (thickness and quality of the coating) and in terms of oxidation and hot corrosion resistance, the modified aluminization was performed by adding Zr in the coating.

The aim of this operation is to obtain a modified coating with higher performance in terms of oxidation and corrosion resistance without modifying the plating process studied in the first part of this work. The reactive element chosen for the doping of the coating is the zirconium, that has an atomic dimension suitable for the interaction with oxygen anions and a relative low cost of production.

Modified coatings were obtained by adding ZrF_4 in the activator salts mixture. The concentration of the standard fluoride has been kept constant while the concentration of ZrF_4 was studied and the values selected for the aluminization were reported in Table 4.4. The presence of Zr, after the aluminization, has been studied by GDOES in collaboration with the group of Prof. Fedrizzi at University of Udine, Polytechnic Department of Engineering and Architecture.

Isothermal oxidations and hot corrosion tests were performed and compared with the results obtained for the standard coatings.

Table 4.4: *Concentrations of activator salt, respect to the Al master alloy, for the series ZrF*

Deposition	wt% of activator salt	mol of activator salt
ZrF1	0.121	0.0072
ZrF2	0.145	0.0087
ZrF3	0.165	0.0100
ZrF4	0.335	0.0201
ZrF5	0.670	0.0402

4.2 Phase 2: Electroless nickel plating

4.2.1 Principle of deposition

The term electroless plating refers to an autocatalytic deposition technique that is purely chemical, in the absence of electrical current. The first publications on this technique are by Brenner and Riddell [8] who first coined the term "electroless plating". The deposition occurs by selective reduction of metallic ions on the surface of the substrate, creating a catalytic layer, which is why the electroless deposition is also called autocatalytic [9].

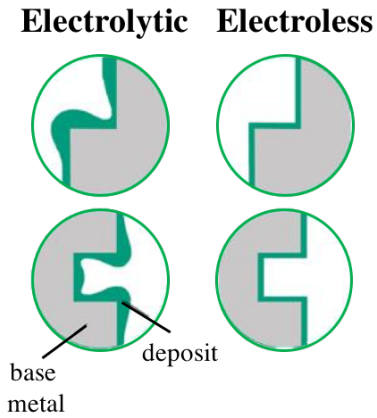

Figure 4.9: *Comparison between electrolytic and electroless plating: inhomogeneities for the coating electrolytic*

Operating in the absence of an electric power source, there is a need of a reducting agent within the solution which, when oxidized, is made available the electrons for the reduction of the metal ions. This results in a very uniform thickness coating, when compared to those obtained by electrolytic

deposition, which does not produce thickening near the edges, *i.e.* where the electric field is concentrated. In general, the process can be considered as a classical electrochemical reaction in which an anode reaction and a cathodic reaction occur [10] [11] [12]:

Anodic reaction (oxidation):

$$Re \rightarrow Ox + ne^{-}$$

Cathodic reaction (reduction):

$$mMe^{z+} + zme^{-} \rightarrow mMe^{0}$$

Where Re is the reducting agent and Ox is the oxidized form. Specifically, electroless deposition also provides a number of collateral reactions that differ in function of the reducting agent and the alkalinity or acidity of the solution. All the reactions that produce the coating can be universally described by a series of anodic and cathodic elemental reactions as claimed by Van Den Meerakker [13].

For alkali solutions the anode reactions are:

1. Dehydrogenation of the reducting agent:
2. Oxidation:
3. Recombination:
4. Oxidation

The cathode reactions are:

5. Metal Deposition / reduction:
6. Hydrogen evolution:

These reactions proceed under a thermodynamic push that is a function of the temperature, activity and the used species. This is driven by Gibbs' free energy which is related to the electrode potential. The electrode potential quantifies the tendency of a given chemical species to gain electrons, so to reduce itself: it corresponds to the electromotive force supplied by a galvanic cell consisting of a standard hydrogen electrode and an electrode of the material to be measured, and is expressed in Volt. Since it is virtually impossible to measure the potential of a single cell electrode, it is always referred to a standard configuration in which an electrode is hydrogen and the potential of the entire cell is measured at 298 ° K and the pressure of 1 atm. If redox occurs in a concentration and temperature

other than standard, the reduction potential can be calculated according to what is known as the Nernst equation. For a generic reduction reaction:

$$Me^{n+} + ne^{-} \rightarrow Me^{0}$$

Nernst equation can be expressed as follows:

$$E = E_0 + \frac{RT}{nF} \cdot \ln \frac{[Ox]}{[Red]} = E_0 + \frac{RT}{nF} \cdot \ln \frac{[Me^{2+}]}{[Me^{0}]}$$

Where:

$[Ox]$: Molar concentration of the species in oxidized form

$[Red]$: Molar concentration of the species in reduced form

E_0: Reduction standard potential

R: gas constant with value 8.314

T: absolute temperature in Kelvin

F: Faraday constant value 96485 C

n: the number of electrons transferred to the reaction

This equation is related to the free energy of Gibbs, which takes into account the thermodynamics of the reaction. For the generic oxidation reaction, the free energy variation is:

$$\Delta G = \Delta G^{0} + RT \ln \frac{a_{Me}}{a_{Me^{z+}}}$$

Where ΔG^{0} is the standard molar energy of formation, that is, the energy associated with the formation of a chemical species in the state of aggregation more stable under standard conditions. The relationship between free energy and reduction potential is:

$$\Delta G = -nFE$$

Where n represents the number of electrons per product moles and F is the faraday constant. explaining:

$$E = -\frac{\Delta G^{0}}{nF} - \frac{RT}{nF} \ln \frac{a_{Me}}{a_{Me^{z+}}}$$

From the sign of drift the spontaneity of the reaction:

•$\Delta G = 0$: The system is in balance

•$\Delta G < 0$: The reaction happens spontaneously

•$\Delta G > 0$: The reaction to progress requires an energy supply

The electroless plating technique requires the presence of a catalytic surface, specifically the almost all metals of the group VIII periodic table, *i.e.* Fe, Co, Rh, Pd, Pt and Ni. Ni, Co, Rh and Pd are considered as catalytic metals; instead, if the substrate metal is less electronegative than the metal to be deposited, a catalytic nickel layer is formed by the substrate according to the following reactions:
Example nickel on Iron [9]:

$$Fe^0 + Ni^{2+} \rightarrow Fe^{2+} + Ni^0_{cat}$$

Example nickel on aluminum:

$$2Al^0 + 3Ni^{2+} \rightarrow 2Al^{1+} + 3Ni^0_{cat}$$

Overall, the coating process can be divided into five steps:

1. Reagent transport on the surface
2. Adsorption of reagents on the surface
3. Redox reactions
4. Desorption of Redox reaction products from the surface
5. Redox reaction products transport away from the surface

The chemical reactions that occur are dependent on the composition of the solution, the nature of the reducing agent and the pH. As hypothesized by Brenner and Riddell [8], a fundamental role plays the ions H^+ and OH^- actually oxidises the reducting agent by providing electrons to the metallic ions. As the reaction proceeds, nucleation zones are formed that continue to grow in size until a continuous film is produced.

4.2.2 Plating solution compositions

Electroless nickel coatings are obtained by a reduction in aqueous solution of nickel ions on a catalytic surface. The deposit itself is catalytic for reduction, so the reaction continues until the surface is immersed. The solution consists of a Ni-soluble salt which acts as a Ni^{2+} reaction reservoir, a reducting agent that provides electrons for nickel-reducing, complexing agents that control the available nickel for the reaction, buffer solutions that inhibit pH variations, accelerators that increase reaction rate and stabilizers. The nature and quantity of these components determine the characteristics of the plating solutions and, therefore, of the deposit.
Below are discussed in detail all the components of the solution as well as the process parameters.

Reducting agents:

The most industrially used reducting agents are mainly four. These four reducting agents are structurally similar as they all contain two or more reactive hydrogens: in fact, the reduction of nickel occurs by catalytic dehydrogenation [12].

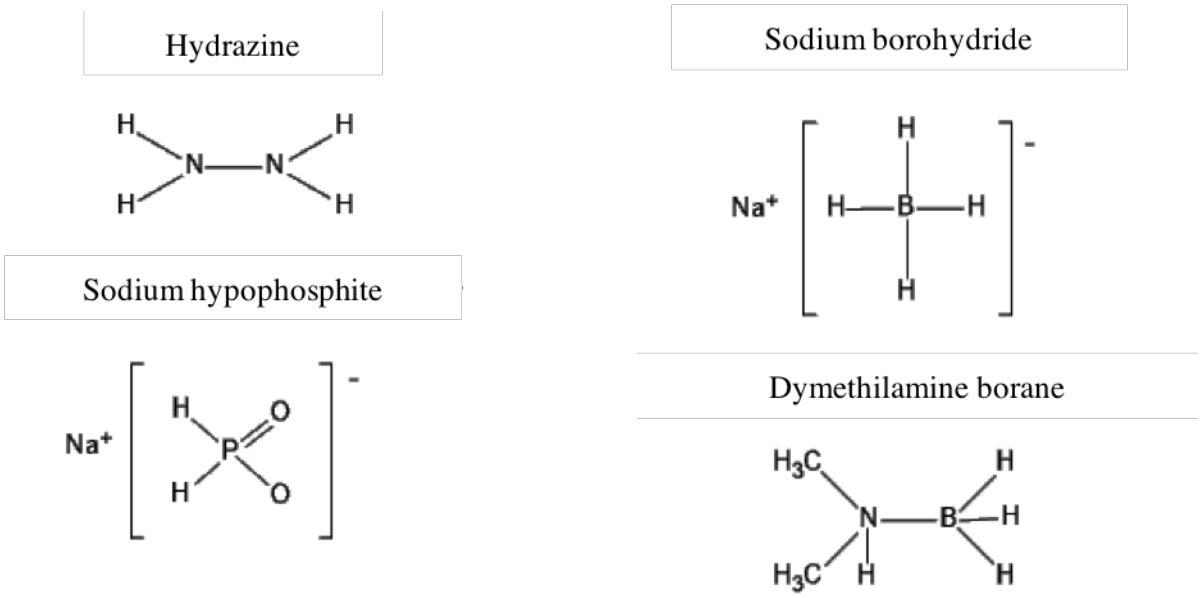

Figure 4.10: *Structural formulae for the reductng agents used in electroless plating*

The most used reducting agent is the sodium hypophosphite and the detailed electroless deposition mechanism can be summarized by four reactions:

$$H_2PO_2^- + H_2O \rightarrow H^+ + HPO_3^{2-} + 2H_{ads} \quad (1)$$

$$Ni_2^+ + 2H_{ads} \rightarrow Ni^+ + 2H^+ \quad (2)$$

$$H_2PO_2^- + H_{ads} \rightarrow H_2O + OH^- + P \quad (3)$$

$$H_2PO_2^- + H_2O \rightarrow H^+ + HPO_3^{2-} + H_2 \quad (4)$$

In reaction (1), hypophosphite ions oxidize into orthophosphite ions in the presence of sufficient energy and a catalytic surface. Part of the atomic hydrogen product is adsorbed by the substrate. The adsorbed hydrogen reduces Ni^{2+} ions in nickel metal (2) and reacts with hypophosphite ions producing water, hydroxyl ions and phosphorus (3). Also, part of the hypophosphite ions is oxidized into orthophosphite ions with molecular hydrogen formation (4). Below is the complete reaction (5)

$$Ni^{2+} + 4\,H_2PO_2^- + H_2O \rightarrow Ni^0 + 3H_2PO_3 + H^+ + P + {}^3/_2\,2H_2 \qquad (5)$$

The ions in solution migrate to the substrate by creating a diffusion flow from the solution to the surface of the sample to be coated. The same surface works as a catalyst by activating the electronic exchange and allowing the oxidation of the two-species present in the solution. The H^+ ions formed during the redox reaction combine to form molecular H_2 that bubble on the surface of the solution. Figure 4.11 shows the diffusion layer with the species present for a Ni-P deposition.

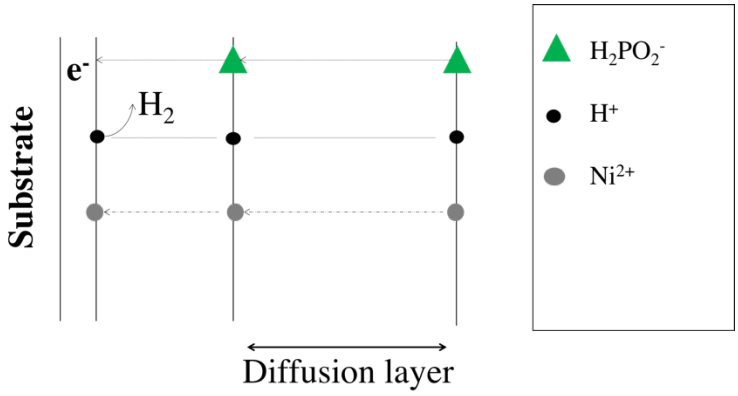

Figure 4.11: *Deposition Mechanism. Diffusion layer where ions migrate from the solution to the substrate, then reduce or oxidize*

Even if the properties of the co-deposited coatings (Ni-P and Ni-B) allow to use them in a wide range of applications such as fouling and wear resistance, the presence of the phosphorous and the boron in the alloys does not allow the utilization of this systems in applications involving high temperature conditions because of the high reactivity of the hetero-atoms. In order to avoid the co-deposition of the elements coming from the chemistry of the plating solution, hydrazine (N_2H_2) was already selected as reductive agent for the production of metallic nano-particles [14],[15],[16],[17], functional coating onto nanostructured systems[18],[19] and membrane[20],[21],[22],[23]. It is known [17] that hydrazine can oxidize, in basic conditions, by the following reaction:

The cathodic semi-reaction of Ni^{2+} reduction is the following:

$$2Ni^{2+} + 4e^- \rightarrow 2Ni^0 \qquad E_0 = -0.25\,V$$

By combining the two reactions, the reaction that produces the catalytic reduction of nickel on the substrate is the following:

$$2Ni^{2+} + N_2H_4 + 4OH^- \rightarrow 2Ni^0 + 4H_2O + N_2 \qquad E_0 = 0.91\,V$$

This is the reaction hypothesized for the reduction of nickel by hydrazine in the presence of a catalytic surface. Thus, considering an efficiency of 100% hydrazine oxidation, a mole of hydrazine is sufficient to reduce two moles of nickel. However, this reaction does not justify the formation of hydrogen which has been confirmed experimentally and above all the formation of precipitates in the absence of catalytic surface; such formation, in alkaline solutions, is justified by the reduction of hydrolyzed nickel directly from hydrazine according to the reactions:

$$Ni^{2+} + 2OH^- \rightarrow Ni(OH)_2^{2+}$$

$$Ni(OH)_2^{2+} + N_2H_4 \rightarrow Ni(OH)_{ad}^{+} + N_2H_3OH + H_{ads}$$

$$Ni(OH)_{ad}^{+} + N_2H_3OH \rightarrow Ni + N_2H_2(OH)_2 + H_{ads}$$

$$2H \rightarrow H_2$$

the overall reaction can therefore be written as follows:

$$Ni^{2+} + N_2H_4 + 2OH^- \rightarrow Ni^0 + N_2 + 2H_2O + H_2$$

In this case a molar amount of hydrazine is required to reduce a mole of nickel, hence a greater quantity than that described in the previous mechanism that does not envisage hydrogen evolution. They should then be considered some collateral reactions that see hydrazine decompose or react with other elements, such as oxygen [17]: in fact, hydrazine may decompose in both alkaline and acidic solutions according to the reaction:

$$3N_2H_4 \rightarrow N_2 + 4NH_3$$

Otherwise, hydrazine can react with oxygen by the following reaction:

$$N_2H_4 + O_2 \rightarrow N_2 + 2H_2O$$

As a result, the real efficacy of reducing nickel with hydrazine is to be considered less than 100%.

Nickel salts

The cation Ni^{2+} comes from the dissolution of a metal salt. Typically, the most used salts are sulfates, chlorides or acetates. Nickel sulphate is preferred for its higher solubility and lower cost. For chlorides, it has been found that chloride ion can disadvantage deposition on aluminum [1].

Complexing agents

Complexing agents are additives used to prevent the decomposition of the bath. These additives play three roles [10],[12]:

1. Reduce the concentration of free ions
2. Prevent the precipitation of nickel hydroxide
3. Help maintain pH stable

When nickel ions are in aqueous solution, they are bound to a precise number of water molecules: this number is called a coordinate number. The complexing agents, once introduced into the solution, are to replace the water molecules, by changing the properties of metal ions: in particular, the solubility and reduction potential are modified.

The binding agent that is put into solution replaces the water molecules so much more efficiently as the bond is stronger with the metal cation. A measure of this force is given by the constant of stability (or stability constants) of the complex, which is the function of all the sequential reactions that originate from the substitution of the individual molecules of water by the binding agents.

A n example of binding agent is ethylenediaminotetraacetic acid - EDTA, the structure of which is shown in Figure 4., which can form 6 coordinate bonds: 2 sites are represented by nitrogen atoms and 4 by the carboxylic groups -COOH.

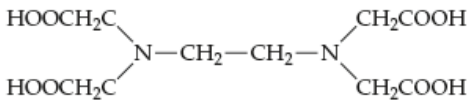

Figure 4.12: *Structural formula of ethylenediaminotetraacetic acid (EDTA)*

Although polydentate binding agents such as EDTA are able to make multiple bonds, they do not necessarily form all available bonds but are strongly influenced by the pH of the solution. The most common and stable Ni - EDTA complex is 1: 1 stechiometry obtained with EDTA in completely deprotonated form $EDTA^{4-}$. This form is present at high pHs, ranging from 10 to 14. By varying the

concentration and type of complexes within the solution, the rate of deposition, stability of the solution and coating quality can be changed.

Table 4.5 presents some of the most commonly used complexes in the electroless depositions, with relative equilibrium constants with nickel.

Table 4.5: *Binding agents for electroless nickel plating with stability constants for the complex*

Binding agent	**Structure**	**Chelating groups**	**pK_{stab} = - log K**
Acetic acid	CH_3COOH	1	1,5
Lactic acid	$CH_3CHOHCOOH$	1	2,2
Succinic acid	$HOOCCH_2CH_2COO^-$	1	2,2
Malonic acid	$^-OOCHCH_2COO^-$	2	4,2
ethylendiammine	$H_2NCH_2CH_2NH_2$	2	13,5
Citric acid	$HOOCCH_2(OH)C(COOH)COOH$	4	6,9
EDTA	$((HOOCCH_2)_2NCH_2)_2$	6	18,6

4.2.3 Plating solution parameters

The two fundamental parameters, in addition to the reagent concentrations, are the process temperature and the pH of the solution. As far as temperature is concerned, it has been found experimentally that the solutions with hydrazine begin deposition at 60°C, increasing the deposition rate by increasing the temperature until degradation to 95°C.

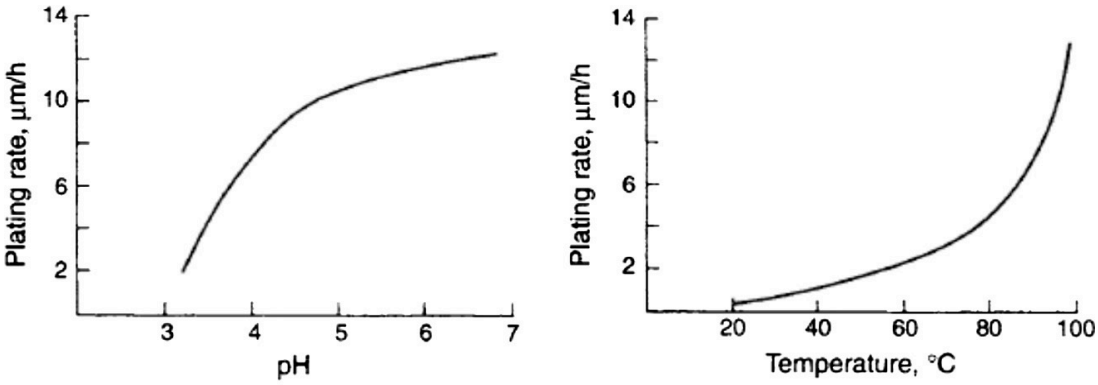

Figure 4.13: *Plating rate vs pH (left) and temperature (right) for Ni-P depositions.*

In fact, evaporation of the solution occurs at temperatures close to boiling temperature of the solvent, generating a variation of reagent concentrations within the solution, and thereby modifying the reaction stoichiometry and coating quality. This variation can also lead to the precipitation of nickel hydroxide $Ni(OH)_2$ following the increase in Ni^{2+} and OH^- ion concentrations beyond the hydroxide solubility product.

Such increase in deposition rate corresponds to a change in the morphology of the coating and its adhesion. Typically, increasing the temperature will result in porous deposits, while deposits with metallic appearance will be favored by low deposition rates. Adhesion varies because the density of nucleation sites on the substrate is changed, varying the stress condition of the coating.

As for the pH of the solution, solutions based on hydrazine requires a pH range of between 9 and 12. As in the case of temperature, changing the pH of the solution results in a modification of the morphology and adhesion of the coating. Since the hydrazine reduction reaction consumes ions, and since hydrogen production is a side-effect reaction, with the advancement of deposition there will be a decrease in pH: if this decrease is important it is necessary to use a pH correction or a buffer solution. A buffer solution is a substance capable of opposing a pH modification following addition of an acid or base: in general, it is a solution consisting of a weak base and its conjugated acid, or a weak acid and its conjugated base. The compound in the buffer varies the degree of dissociation depending on the pH variations that are produced in the solution. This allows to maintain bath reactions within an optimum pH window for redox reactions and complex formation during deposition.

4.2.4 Selected plating solution compositions and parameters

In the selection of plating solution chemical compositions, the analysis started from some publications relating to the production of coated membranes for gas separation and other publications related to the production of battery electrodes. After analyzing these publications, a composition was discarded due to the low declared deposition rates (20 μm in 8 hours) and the poor homogeneity of the coating as reported in Figure 4.

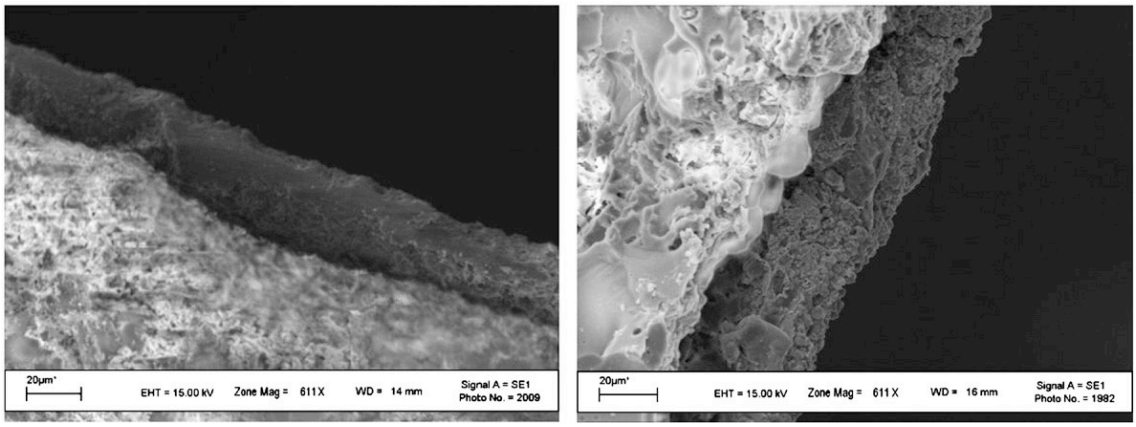

Figure 4.14: *Examples of coatings obtained by varying the reagent concentrations reported in the publications [24],[25]*

The two starting compositions selected for the phase 2 of this work are reported in (from now solution A and solution B)

Table 4.6: *Chemical compositions and parameters for the solution A and B*

		Solution A g/l (mol/l)	**Solution B g/l (mol/l)**
Nickel acetate	$Ni(OCOCH_3)_2 \cdot 4H_2O$	21,2 (0,08)	-
Nickel chloride	$NiCl_2 \cdot 6H_2O$	-	23,76 (0,1)
Hydrazine	$N_2H_4 \cdot H_2O$	20,02 (0,4)	32,56 (0,65)
Na_2EDTA	$Na_2EDTA \cdot 2H_20$	5,62 (0,016)	-
Lactic acid	$C_3H_6O_3$	13,5 (0,15)	-
Potassium carbonate	K_2CO_3	-	69,1 (0,5)
Potassium hydrogen carbonate	$KHCO_3$	-	45 (0,45)
Potassium hydrogen phosphate	K_3HPO_4	-	87,1 (0,45)
Sodium hydroxide	NaOH	9,87 (0,247)	-
Potassium hydroxide	KOH	-	9,78 (0,3)
pH		9,2	10,9
T		75°C	85°C

Solution A was initially formulated by Wen et al. to coat zirconium oxide powders and subsequently adopted by Haag et al. for functionalizing aluminum oxide membranes. Two different binders are used: EDTA forming a very high stability constant Ni-EDTA complex (pK=18.6) and lactic acid forming a complex with a modest stability constant (pK=2.2): experimentally it has been observed that coatings obtained using both complexes exhibit a higher deposition rate than the case of EDTA alone because of the two different stability constants. The plating solutions were prepared at room temperature, then placed on a heating plate equipped with a magnetic stirrer and heat to the deposition temperature (75 or 85 ° C). Only when the process T is reached the sample to be coated has been inserted.

During experimentation of solution A, the pH was increased to achieve industrially desirable deposition rates, bringing the pH to process T around the value of 9.2 and velocity in the order of 10. Subsequently, the concentrations of the two complexes were varied so that the coatings produced were adherent to the substrate and porous-free. Despite this, the coatings still have little adhesion, stress and porosity.

During experimentation of solution B, it was studied the complex named tris(hydrazine carboxylato-N',O) nickelate(1-) (called Ni complex from this moment) formation by varying the preparation of plating solution; briefly the nickel complex is formed by adding a solution of Ni^{2+} obtained by dissolving 7mmol of $NiCl_2$ hexahydrate in 100 ml of DW to the hydrazine carboxylate solution and stirred until complete mixing. Then a buffer solution of K_2HPO_4 was added and the pH was adjusted with KOH to a value of 11.5.

For both solutions (A and B), the plating solution was heated in a glass reactor with a magnetic stirrer IKA RET control-visc (sensitivity ±0,5°C) until the temperature was reached. During the deposition temperature and stirring was controlled by the magnetic stirrer and always stable while pH was constantly measured with a METTLER TOLEDO pHmeter S400 (Figure 4.).

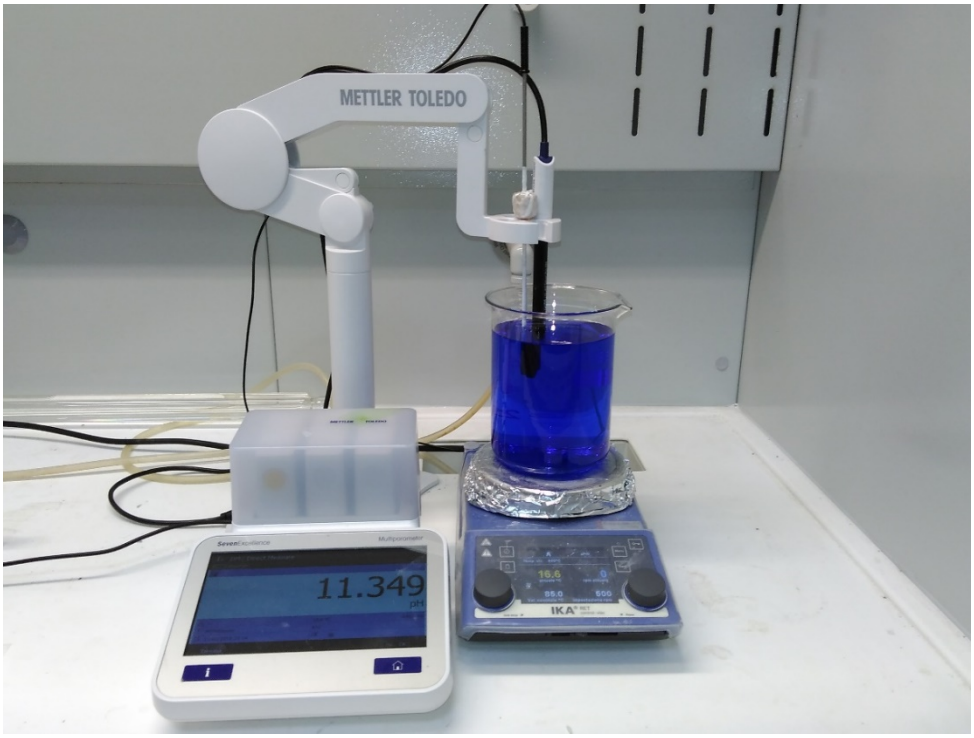

Figure 4.15: *Experimental set-up for plating deposition*

4.2.5 Nanocomposite coatings (Ni-nAl_2O_3)

The choice to use electroless deposition as a vehicle for nanoparticles dispersion, resides essentially in the fact that the metal deposition mechanism itself allows the incorporation of finely dispersed particles into solution. The ion diffusion flow in solution to the substrate allows the capture of particles that are embedded within the metal matrix (Figure 4.).

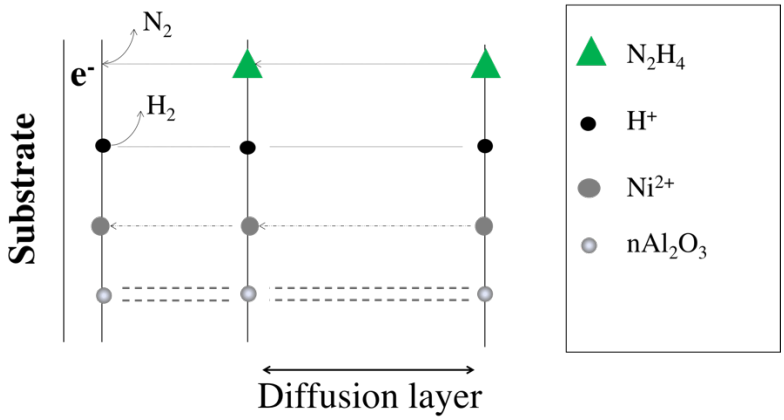

Figure 4.16: *Deposition Mechanism. Diffusion layer can transport the nanoparticles to the substrate and then embedded them into the matrix*

The nanoparticles, when introduced into aqueous solution, are able to charge superficially by creating an electric-double layer with the ions in solution. The intensity of this electrostatic field is defined by the Z potential. Depending on the pH of the solution in which this double layer of ions is found, the repulsion of two adjacent particles can be favored: if repulsion is favored, it will be said to be a stable suspension. If the Z potential is not sufficiently high, the particles will tend to agglomerate and superficial modifications will be required to ensure the stability of the suspension.
Figure 4. shows the trend of the Z potential of α-Al_2O_3 particles in aqueous solution. Given the high potential in the range of pH at which the depositions take place (pH between 10.9 and 10.3), it was decided not to functionalize the nanoparticles.

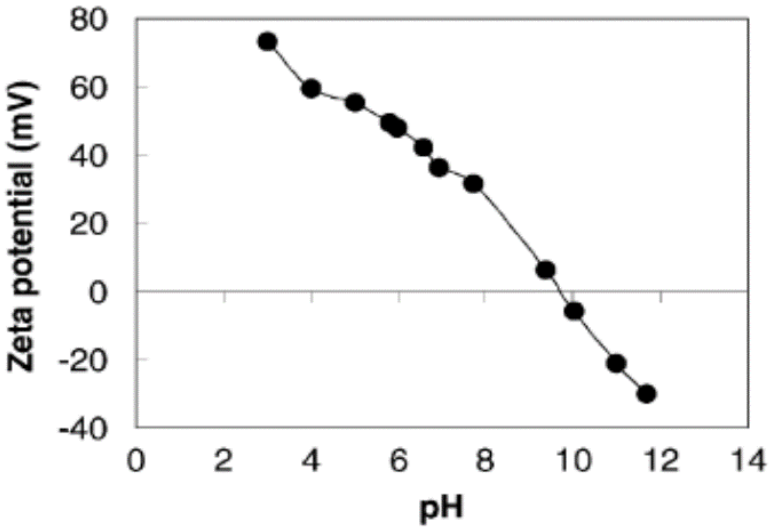

Figure 4.17: *Z potential vs pH for* α-Al_2O_3 *in water solution [26]*

The 50 nm diameter nanoparticles were purchased by Io-Li-tec and presented in anhydrous form. The powder was then put into an aqueous solution at concentrations ranging from 25 to 37.5 g / l and sonicated with a Fisher Scientific 505 tip ultrasonic sonicator with 20% intensity for 10 minutes before introduction into the plating solution. In this way, by exploiting the cavitation generated by the ultrasound, the agglomerates are broken and a homogeneous suspension is formed. Once the dispersions were prepared, 20 ml of this dispersion per liter of solution was added to the plating

solution so that the starting solution was not excessively diluted. In order to obtain the nanocomposite onto the superficial part of the coating, the nanoparticles suspension was added after a certain time of pure nickel deposition.

4.3 Slurry aluminization

The reactivity of the nickel deposited by electroless plating during phase 2 was tested using the slurry aluminization technique. Before the heat treatment, Al slurry was air-sprayed on top of the substrate and the quantity, in terms of mg/cm^2, was optimized in order to obtain a thickness of bond coat comparable to the coatings obtain during phase 1 (20 µm of β-NiAl).

Aluminum microparticles (Hermillion, France - 5 µm of diameter; Figure 4.) were mixed with a binder before to being air-sprayed.

The water-based binder is composed of 90 wt.% of ultra-pure water (R=18.2 M .cm-1) and the remaining 10 wt.% of polyvinyl alcohol (PVA) produced by MERCK (CAS n°: 9002-89-5). The water soluble PVA powder was added to water with some drops of EtOH in order to increase the solubility. Then the solution was heated (85°C, close to the glass-transition temperature of PVA) under magnetic stirring to allowing the polymer to dissolve faster. Thereafter, the Al particles (load agent) was added to the cold binder, in a pill box with the proportions of 50:50, and finally shaken mechanically for obtaining the homogeneity.

The slurry was, then, sprayed on top of the substrates by the use of an aerograph and the slurry was dried leaving the samples exposed to air (Figure 4.).

Figure 4.18: *Aluminum microparticles purchased from Hermillion (France) on the left; aerograph on the right*

In order to achieve a high reproducibility for the quantity of slurry coated on top of the substrates, the sprayings were conducted by the use of a rotator disc: the pressure (1 bar), the rotation speed and the

diameter of the nozzle were optimized to obtain 5 ± 1 mg/cm^2 of aluminum microparticles on top of the substrates.

This treatment is composed of three temperature steps, which allow the removal of the binder (400°C), the Al inward diffusion (700°C) and finally, the topcoat consolidation and the homogenization of the intermetallic phases of the substrate enriched in Al (1050°C).

Before the aluminization of the electroless nickel samples, the heat treatment procedure was studied for pure nickel samples. This has allowed to obtain a temperature profile that would allow the formation of an optimal bond coat without lengthening the diffusion times of aluminum.

The complete heat treatment is carried out in a quartz tubular furnace under flowing Ar(g) atmosphere (300 ml/min), which contains enough oxidizing species (2 ppm H_2O) to oxidize the aluminum material. In addition, evaporation of the binder shall lead to H_2O vapour and CO_2 that may also oxidize the Al particles. Before treating the samples, a pump allows to realize a partial vacuum (2.10-1 mbar) before filling the chamber with Ar(g).

References

[1] S. Bose, et al.: High temperature Coatings, Rensselaer Polytecnic Hartford, CT, 2007

[2] M. Okazaki, Sci. Technol. Adv. Mater., vol. 2, no. 2, pp. 357–366, 2001.

[3] X. Peng, T. Li, and W. P. Pan, vol. 44, pp. 1033–1038, 2001.

[4] X.Peng, Y. Guan, Z. Dong, C. Xu, and F. Wang, Corros. Sci., vol. 53, no. 5, pp. 1954–1959, 2011.

[5] X. Tan, X. Peng, and F. Wang, Surf. Coatings Technol., vol. 224, pp. 62–70, 2013.

[6] Z. D. Xiang and P. K. Datta, J. Mater. Sci., vol. 38, no. 18, pp. 3721–3728, 2003.

[7] Y. bo Zhou, H. yu Chen, H. jun Zhang, and Y. dong Wang, Trans. Nonferrous Met. Soc. China (English Ed., vol. 18, no. 3, pp. 598–602, 2008.

[8] A. Brenner and G. E. Riddell, J. Res. Natl. Bur. Stand. (1934)., vol. 37, no. 1, p. 31, 1946.

[9] G. O. Mallory, J. B. Hajdu, A. Electroplaters, S. F. Society, and K. (Firm), Int. Bus., 2000.

[10] G. O. Mallory and J. B. Hajdu. (1990), AESF.

[11] C. R. K. Rao and D. C. Trivedi, Coord. Chem. Rev., (2005) vol. 249, no. 5–6, pp. 613–631.

[12] M. Schlesinger and M. Paunovic, (2010) vol. 4, no. 3. wiley.

[13] J. E. A. M. Van Den Meerakker, J. Appl. Electrochem., (1981), vol. 11, no. 3, pp. 395–400,.

[14] Chen, H., Xu, C., Chen, C., Zhao, G. & Liu, Y. Mater. Res. Bull. (2012), 47, 1839–1844.

[15] Park, J. W. et al.. Mater. Chem. Phys (2006). 97, 371–378.

[16] Djokić, S. S. & Djokić, N. S., J. Electrochem. Soc., (2011) 158, D204–D209.

[17] Djokic., J. Electrochem. Soc, (1997), 144, 6–11

[18] Genova, V., Marini, D., Valente, M., Marra, F. & Pulci, G, Chem Eng Trans. (2017), 60, 73–78.

[19] Arai, S., Kobayashi, M., Yamamoto, T. & Endo, Solid-State Lett. (2010) 13, D94.

[20] Haag, S., Burgard, M. & Ernst, B. Surf. Coatings Technol. (2006), 201, 2166–2173.

[21] Cheng, Y. S. & Yeung, K. L, J. Memb. Sci. (2001), 182, 195–203.

[22] Bulasara, V. K., Thakuria, H., Uppaluri, R. & Purkait, M. K. Desalination, (2011), 268, 195–203.

[23] Bulasara, V. K., Thakuria, H., Uppaluri, R. & Purkait, M. K. Desalination, (2011), 275, 243–251.

[24] S. N. Jenq, H. W. Yang, Y. Y. Wang, and C. C. Wan, Mater. Chem. Phys., (1997), vol. 48, no. 96, pp. 10–16,.

[25] S. N. Jenq, H. W. Yang, Y. Y. Wang, and C. C. Wan, J. Power Sources, (1995), vol. 57, no. 1–2, pp. 111–118,.

[26] F. Tang, T. Uchikoshi, K. Ozawa, and Y. Sakka, Mater. Res. bullettin, (2002),vol. 37, pp. 653–660,

CHAPTER 5

Experimental results

5.1 Oxidation and hot corrosion resistance

5.1.1 Samples obtained with NH_4F as activator salt

In Figure 5.1 is reported the weight gain, normalized for each sample surface, for the specimens obtained by VPA with NH_4F as activator salt. Contrary to what was expected, in the deposition called NF2, weight gain is lower than the NF1 deposition despite a higher quantity of activator salt.

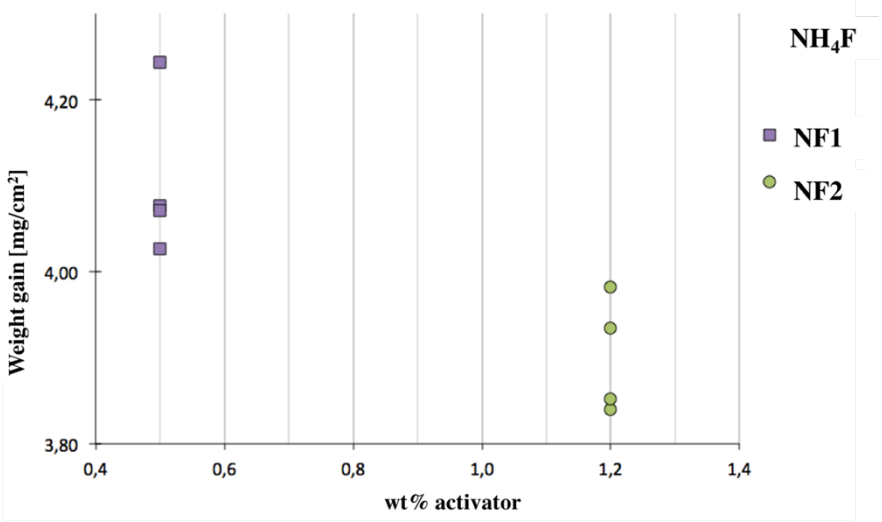

Figure 5.1: *Weight gain, normalized for the samples surfaces, for specimens aluminized by VPA with NH_4F as activator salt*

Cross-section SEM analysis have confirmed the different weight gain: the thickness, measured directly by SEM images, is different for the two samples and, as expected, is higher in the case of NF1 sample, as shown in Figure 5.2. With "thickness" is considered the total of β-NiAl+IDZ

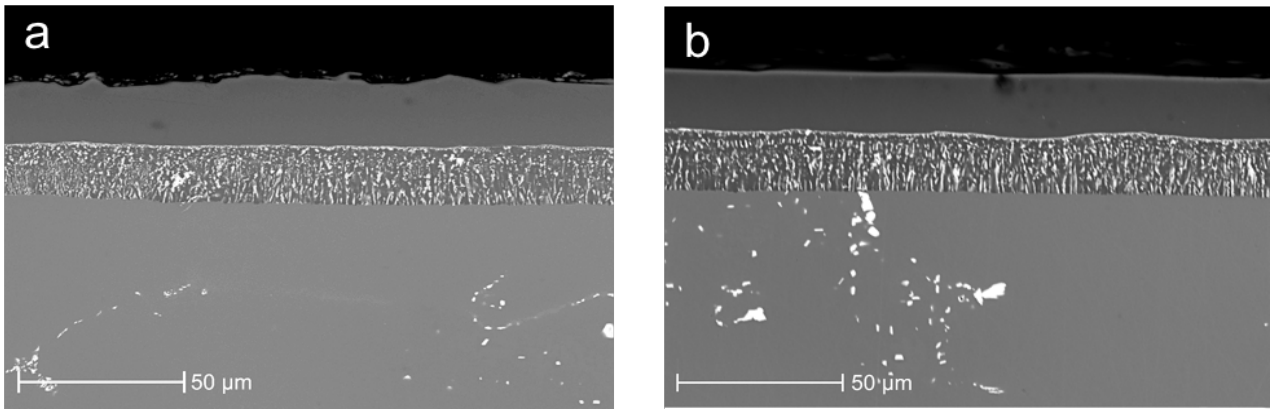

Figure 5.2: *Cross-section SEM images of samples obtained by VPA with NH_4F as activator salt. a) NF1; b) NF2*

In Tabe 5.1 are collected the features, in terms of thickness, for the samples obtained by aluminization with NH_4F as activator salt.

Table 5.1: *Features obtained from depositions with NH_4F as activator salt*

Deposition	β-NiAl thickness [µm]	IDZ thickness [µm]
NF1	23 (±1.0)	21 (±0.9)
NF2	20 (±0.6)	19 (±0.7)

Top-view SEM analysis has revealed the typical polyhedral structure of β-NiAl lattice (Figure 5.3). As it is possible to observe in the pictures, there are no great differences between NF1 sample and NF2 sample (except for the different grain size dimension).

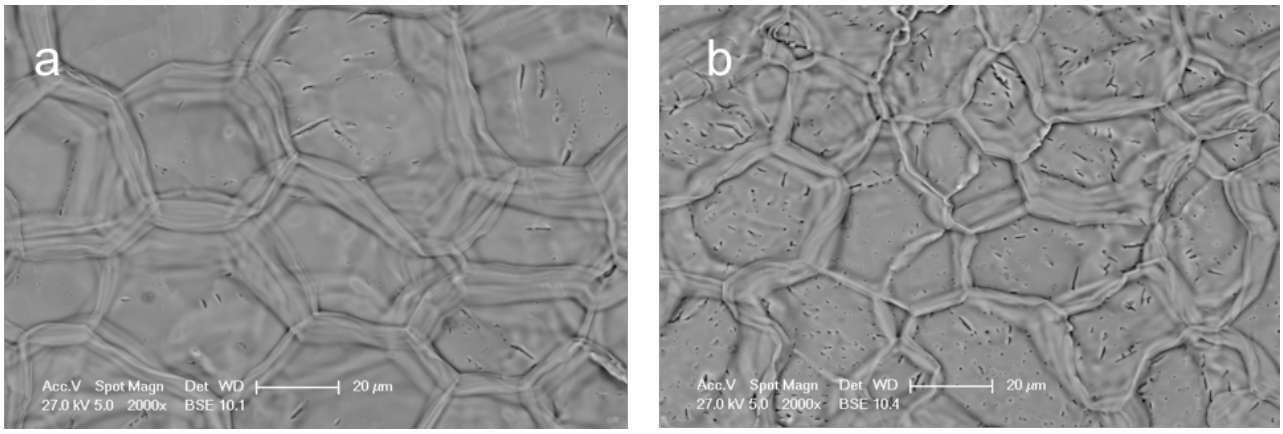

Figure 5.3: *Top-view SEM images of samples obtained by VPA with NH_4F as activator salt. a) NF1; b) NF2*

XRD analysis has confirmed the presence of β-NiAl phase as the only crystalline structure onto the coating surface. The only two peaks in the pattern can be indexed as the (1 1 0) and (1 1 1) planes of the cubic phase NiAl with lattice constant a = 2,8770 Å, which is comparable with the literature data (JCPDS No. 20-0019, a = 2,8870). Furthermore, it is clear that the relative intensities of the face (1 1 1) to the face (2 0 0) is higher than the conventional value. This is probably due to the epitaxial growth of the (1 1 1) phase onto a substrate which already had a high orientation (the superalloy was directionally solidified)

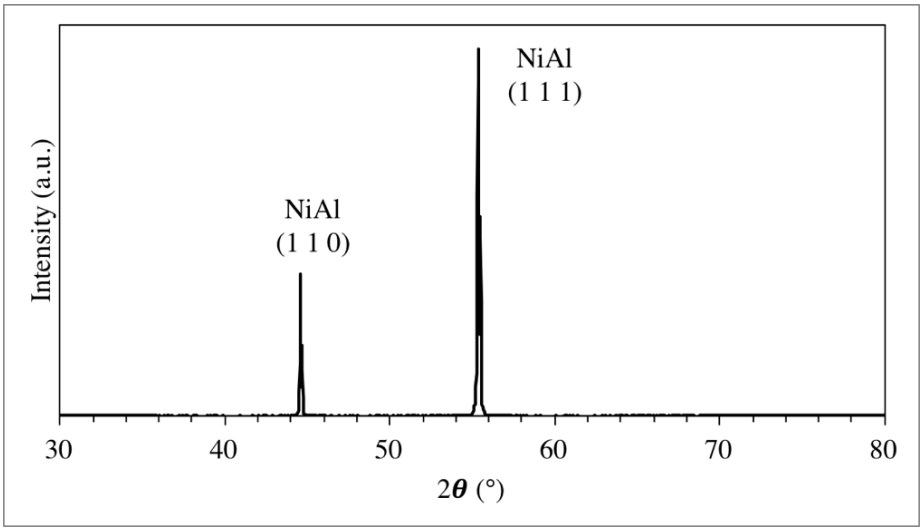

***Figure 5.4**: XRD pattern for the sample NF1*

5.1.2 Samples obtained with AlF_3 as activator salt

In Figure 5.5 is reported the weight gain, normalized for each sample surface, for the specimens obtained by VPA with AlF_3 as activator salt. It is notable that the weight gain is higher than the NF samples (about 5 mg/cm^2 for the AlF1, the sample with lower quantity of activator salt).

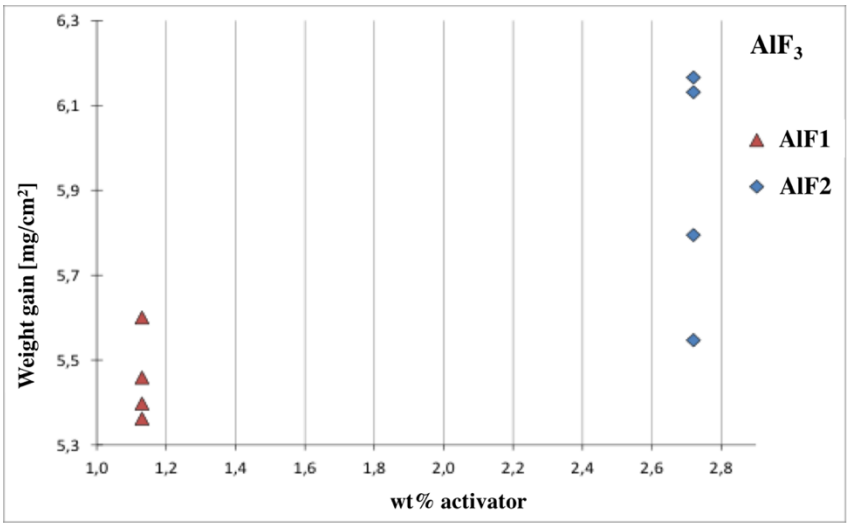

Figure 5.5: *Weight gain, normalized for the samples surfaces, for specimens aluminized by VPA with AlF_3 as activator salt*

The different weight gain is confirmed by thickness measurement performed with cross-section SEM analysis for the AlF samples, reported inFigure 5.6. The coating thickness, in terms of β-NiAl+IDZ, is higher for the sample AlF2.

This result can be explained by considering the different quantities of aluminum available on the super-alloy surface as diffusion occurs. Ammonium fluoride sublimes at 100°C and form ammonia and fluoridric acid. Then the HF can react with aluminum to form the fluoride. In the case of aluminum fluoride, the reactions are different: Menz et al.[1] has shown that AlF_3 loses water traces up to 600°C. As a result of the hydrolysis not only HF, but also gaseous HF-AlF_3 complexes are formed. Therefore, aluminum on the super-alloy surface can derive from packs and from activator salts as well. This can explain why, in the case of AlF_3, the β-NiAl and the IDZ layers are thicker respect to the NH_4F diffusion coatings despite of the same deposition procedure and parameters.

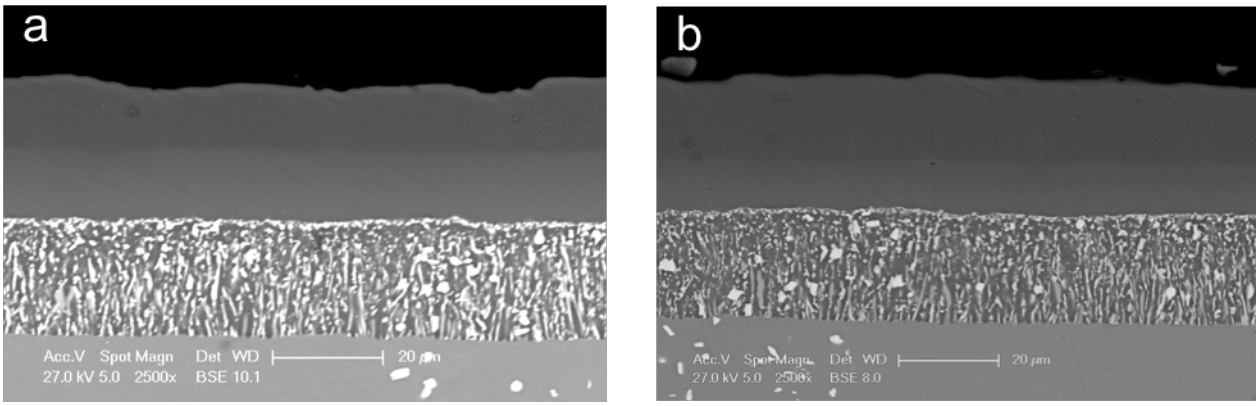

Figure 5.6: *Cross-section SEM images of samples obtained by VPA with AlF_3 as activator salt. a) AlF1; b) AlF2*

In Table 5.2 are collected the features, in terms of thickness, for the samples obtained by aluminization with NH_4F as activator salt.

Table5.2: *Features obtained from depositions with AlF_3 as activator salt*

Deposition	β-NiAl thickness [μm]	IDZ thickness [μm]
AlF1	27 (±1.2)	24 (±0.9)
AlF2	30 (±0.9)	25 (±0.8)

Top-view SEM analysis, also in this case, has revealed the the typical polyhedral structure of β-NiAl lattice (Figure 5.7). The difference with the NF samples lies in the presence of homogenously dispersed particles onto the coating surface. These products were characterized by EDS analysis which has identified that these residuals are actually Cr and AlF_3 crystallities.

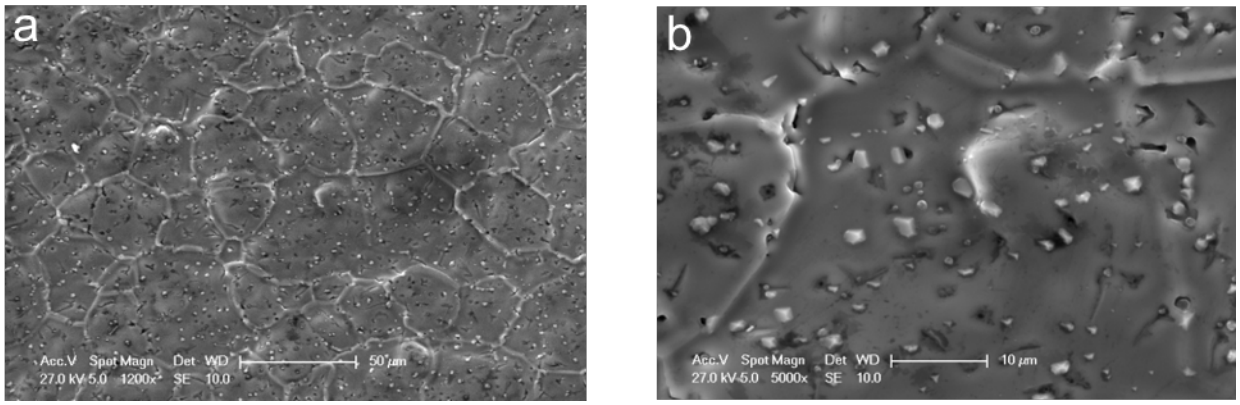

Figure 5.7: *Top-view SEM images of the samples AlF1: a) homogeneous dispersed deposited particles b) detail at higher magnification (5000X) for the deposited particles*

5.1.3 Isothermal oxidation

Isothermal oxidation test at 1050 ° C was carried out on the samples of the NF and AlF series, as described in Section 4.4.1. Besides the four coatings produced was also included in the test a sample of the substrate, to verify the difference in terms of useful life of the guaranteed by aluminides component.

Figure 5.8 shows the result of the test, which shows that the substrate is characterized by a linear oxidation kinetics that, after 25 hours, results in catastrophic oxidation. After 50 hours, there is a loss of structural material of the component. The aluminized samples instead have a parabolic kinetics of oxidation, thus forming a protective oxide scale on the surface.

Excluding the substrate from the graph, in Figure 5.9 is observed in detail the different behavior of the standard aluminide coatings in oxidation.

In both deposition families, where a higher activating salt concentration is used, a better oxidation behavior is observed. Moreover, it is noticed that the NF samples behave considerably better than the AlF, exhibiting a slower oxidation kinetics.

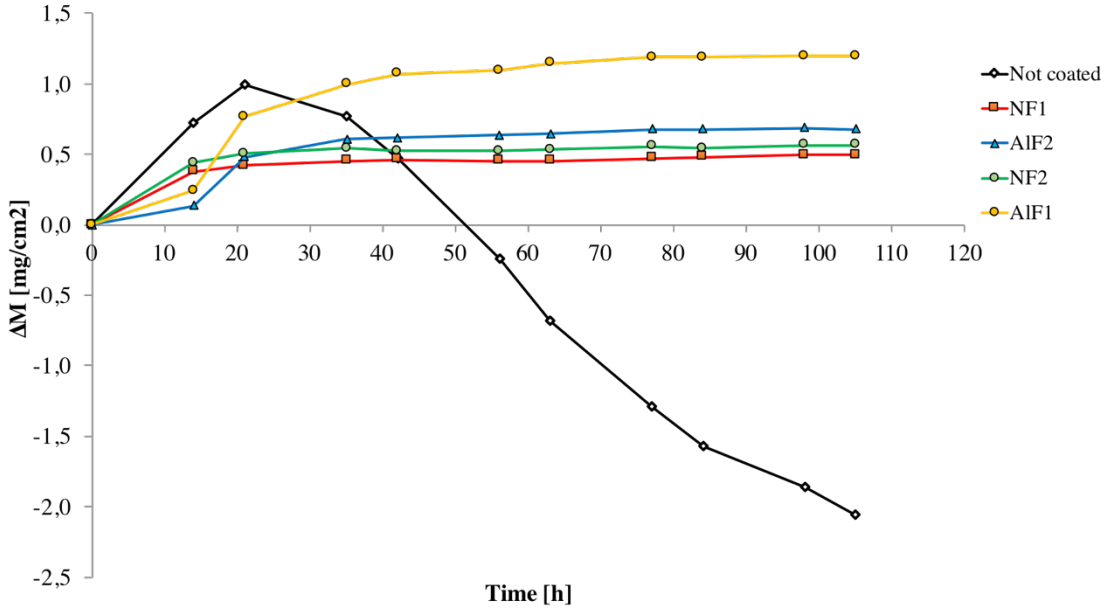

Figure 5.8: *Isothermal oxidation (1050°C) for NF and AlF series. "Not coated" refers to a simple substrate.*

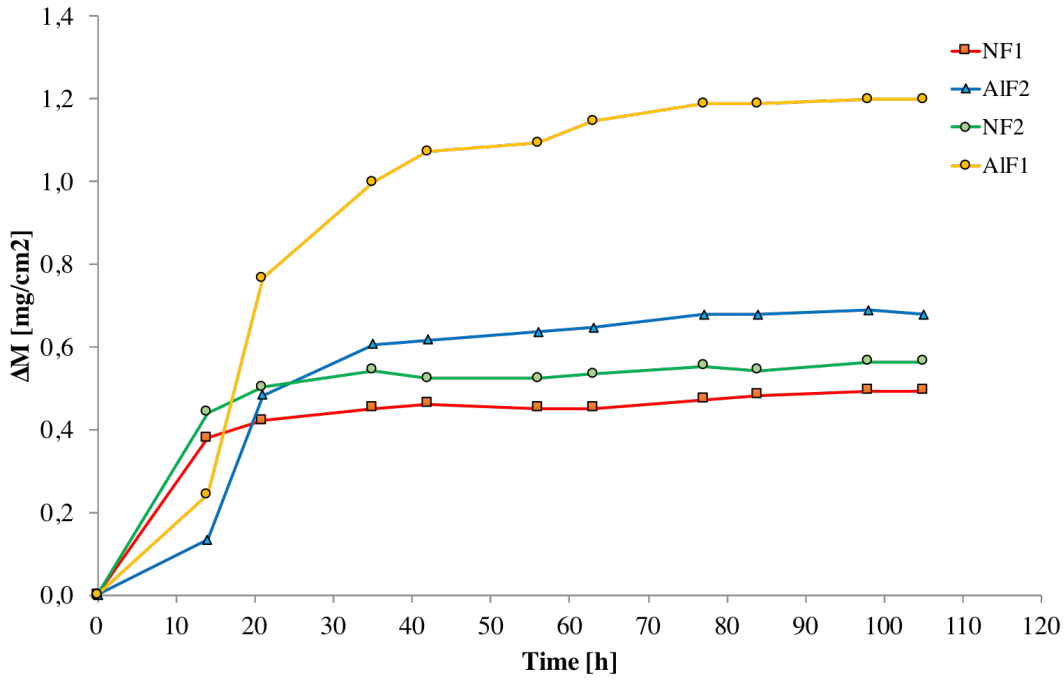

Figure 5.9: *Isothermal oxidation (1050°C) for NF and AlF series.*

The reasons for the oxidation behavior of the coatings are to be found in the features of the Al_2O_3 scale formed superficially. SEM micrographies shown in Figure 5.10 show the differences between the various protective oxides scales.

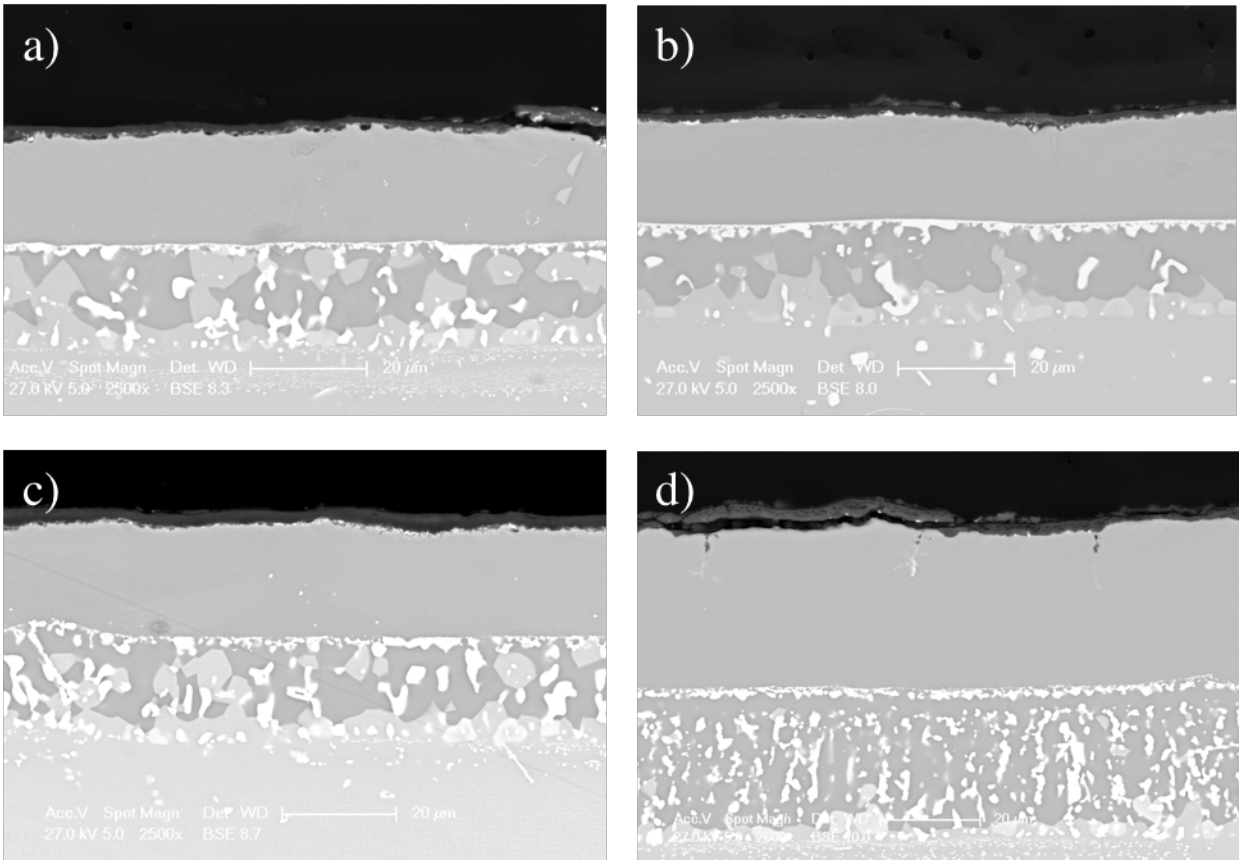

Figure 5.10: *Cross-section SEM micrographs for the sample after 105h of isothermal oxidation (1050°C): a) NF1; b) NF2; c) AlF1; d) AlF2*

All coatings have a thick oxide layer of about 2 μm. The NF1 and AlF2 coatings show a continuous oxide scale, but it is not adherent on the entire surface of the sample; furthermore, in AlF2 there is also the presence of a series of zones where oxygen is percolated through the scale, causing the internal oxidation of the β-NiAl and consequent depletion of such zones in Al.

The NF2 and AlF1 coatings exhibit the formation of an adherent and continuous oxide scale; is the clear difference in thickness to determine the different oxidation behavior of the two coatings. Therefore, it is apparent that the Al_2O_3 layer formed by the AlF1 coating has a higher permeability by the O_2.

In any case, the oxide scale formed by the NF1 coating, the best in terms of gain weight in oxidation, shows undesirable characteristics. Oxide, in fact, is adherent, cohesive and continuous, but on its surface has small aggregates of Al_2O_3, probably detached during cooling or residues of transitional

oxides. Finally, Figure 5.10 also shows how IDZ changes as a result of the heat treatment due to the diffusion between Ni and Al.

EDS analysis of the cross-section of oxidized coatings was performed on all samples. Figure 5.11 shows the map performed on the NF2 coating after 105 hours of oxidation at 1050 ° C; the elemental distribution is also representative for the other analyzed compositions.

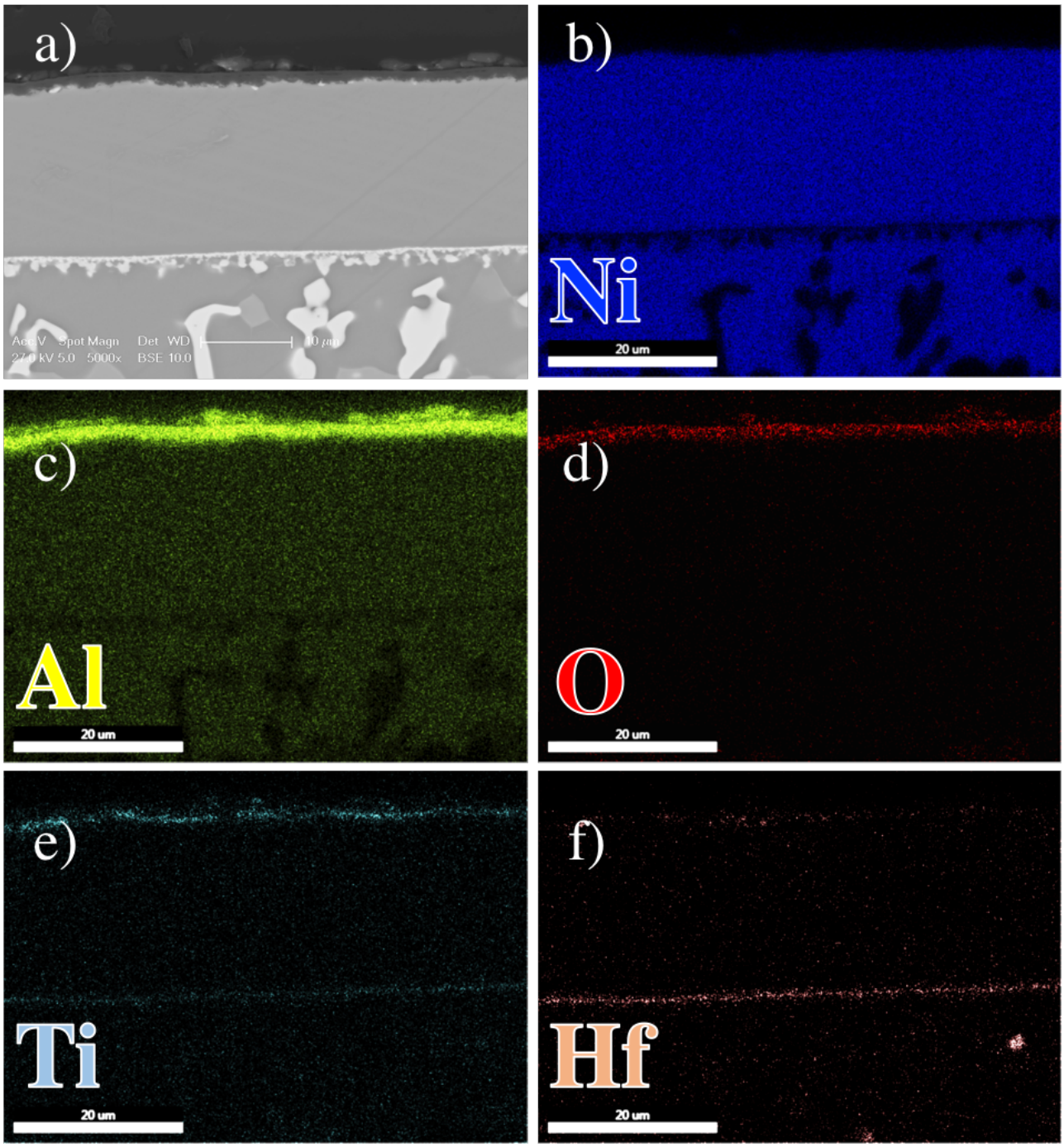

Figure 5.11: *EDS maps of the sample NF2 after 105h of oxidation at 1050°C; a) cross-section micrograph of the investigated area; b) Ni; c) Al; d) O; e) Ti; f) Hf*

At the top of the sample, at the oxide scale, a rich area of Al and O is observed (Figure5.11-d), confirming the presence of Al_2O_3. The EDS also reveals the presence of a rich Ti area and, in much smaller amounts, of Hf at the bottom of the Al_2O_3 scale (Figure 5.11e-f): this zone is the result of the outward diffusion of these two elements of alloy from the substrate to β-NiAl.

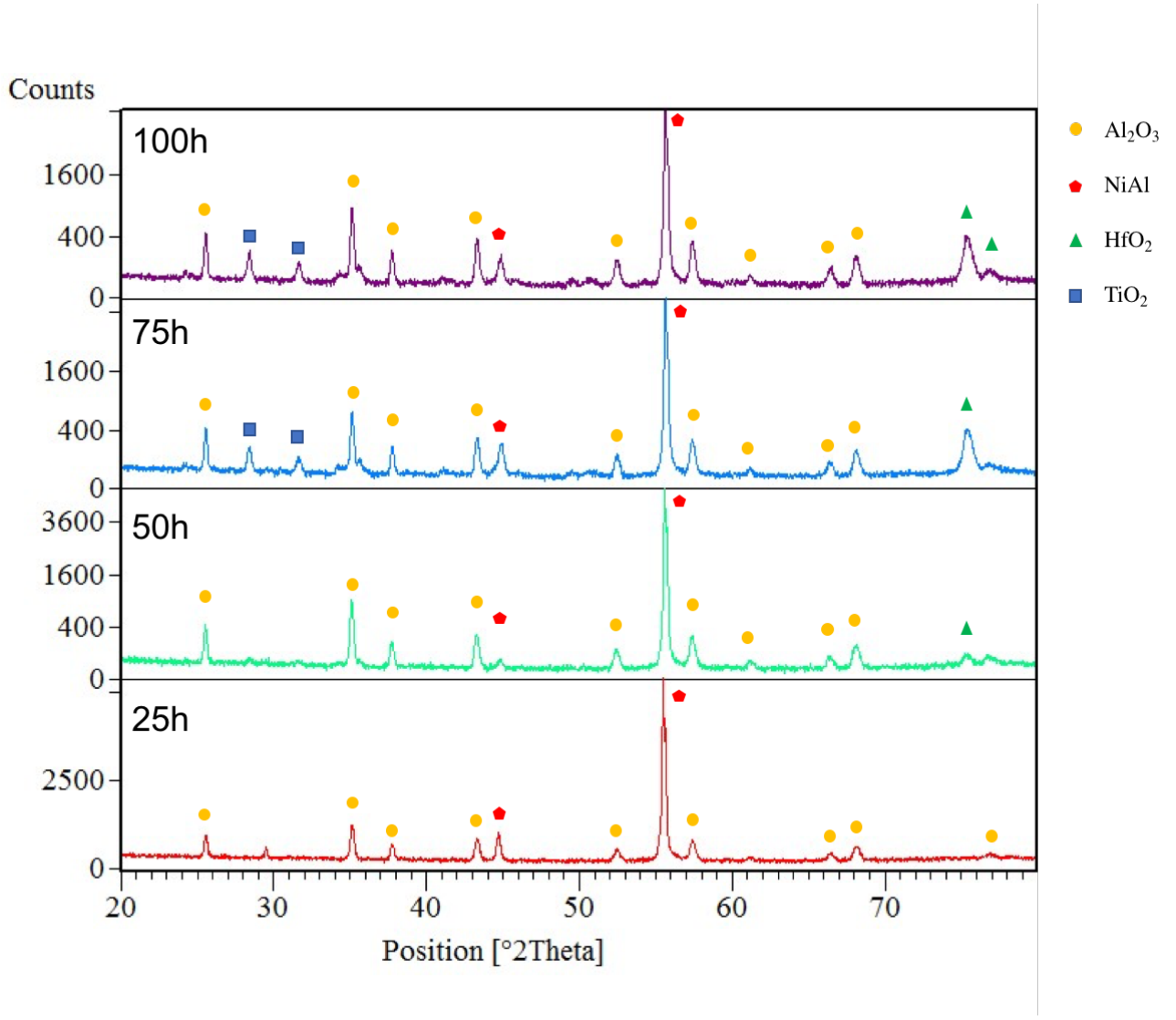

Figure 5.12: *Surface structure evolution during oxidation for NF2 sample: after 25h (red spectrum), 50 h (green spectrum), 75h (blue spectrum) and 105h (purple spectrum)*

Figure 5.12 shows the surface structure evolution during oxidation for NF2 sample. XRD spectra confirms the results obtained by EDS with the presence of the stable phase of α-Al_2O_3. Thanks to this analysis, it was possible to understand the kinetic of diffusion for the heavier element in the superalloy. It is observed, in fact, that the Ti and Hf diffuse into the surface already after 50h of high temperature treatment. In Figure 5.13 is presented the zoom for the most intense peak of NiAl (refers

to (1 1 1) phase. It is evident that the formation of the oxide scale causes the NiAl peak to shift to higher degrees

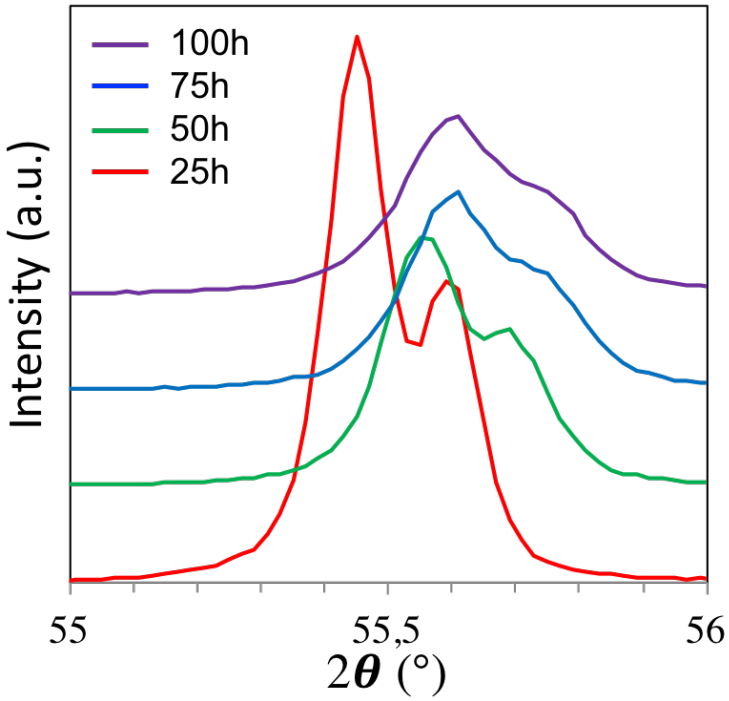

Figure 5.13: *Zoom of the NiAl most intense peak for the XRD spectrum of NF2 sample.*

Surface micrographies of oxidized coatings show the presence of cavities on the oxide layer that covers the samples. These are generated during cooling, as the thermomechanical stresses occurring at the ceramic oxide interface and intermetallic coatings are such as to cause the release of protective oxide zones. Figure 5.14 shows the presence of a cracked and discontinuous oxide.

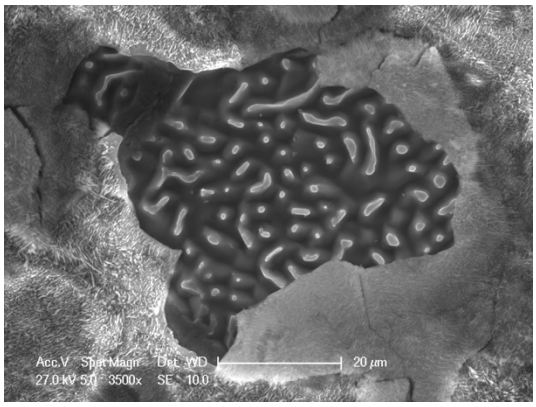

Figure 5.14: *SEM micrograph of a cavity on the NF2 coating*

The EDS map in Figure 5.15 confirms that these zones are oxide cavities that expose the underlying β-NiAl oxidation.

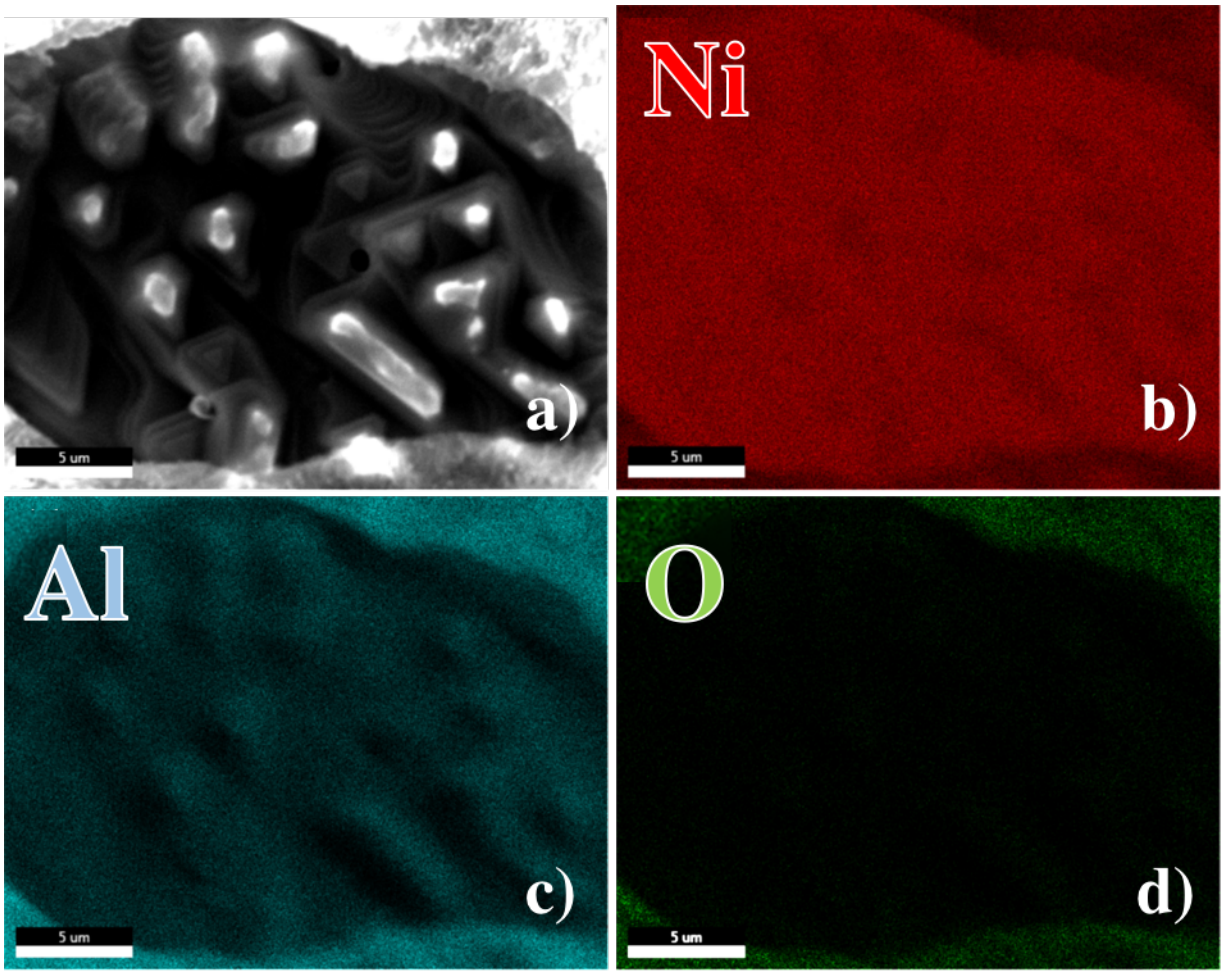

Figure 5.15: *EDS maps of the NF2 coating after 25 hours of oxidation at 1050 ° C: a) SEM micrograph of the investigated area; b) Ni; c) Al; d) O*

With the progress of oxidation these cavities are closed thanks to the formation of new oxide and thickening of the layer. Figure 5.16 shows the surface appearance of the NF2 coating at 25-hour oxidation intervals.

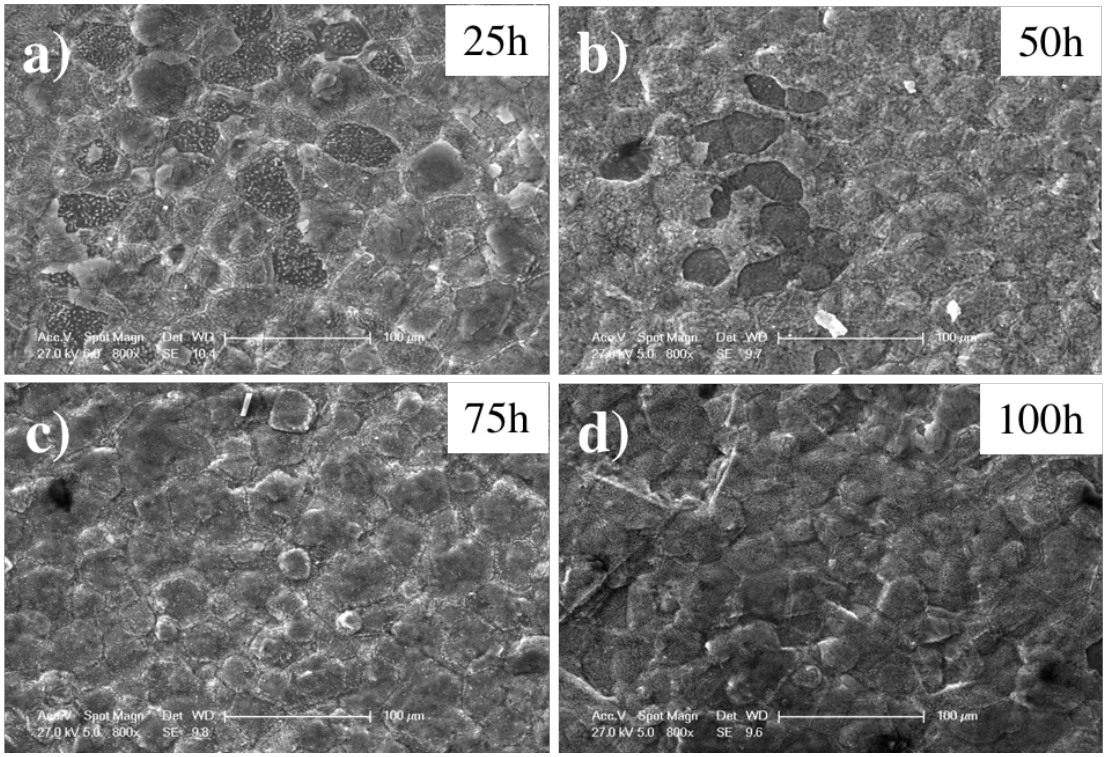

Figure 5.17: *Surface micrographs of the NF2 coating after oxidation at 1050 ° C: a) appearance after 25 hours; b) after 50 hours; c) after 75 hours; d) after 105 hours.*

Coatings obtained with NH_4F as an activators salt exhibit better oxidation behavior; in particular, NF2 has an increase in weight below NF1, with a more protective oxide scale. It was then chosen to carry out a further coating with a higher activator salt concentration in order to see if an increase in this process parameter would also improve the oxidation resistance. In Table 5.3 is reported the concentration of activator salt present in depositions NF2 and NF3.

Table 5.3: *Concentrations of activator salt for the deposition NF2 and NF3*

Deposition	wt% of activator salt	mol of activator salt
NF2	0.75	0.0201
NF3	1.00	0.0273

The NF3 sample was subjected to an isotermal oxidation test at 1050 ° C. Figure 5.18 shows the comparison between NF3 and NF2.

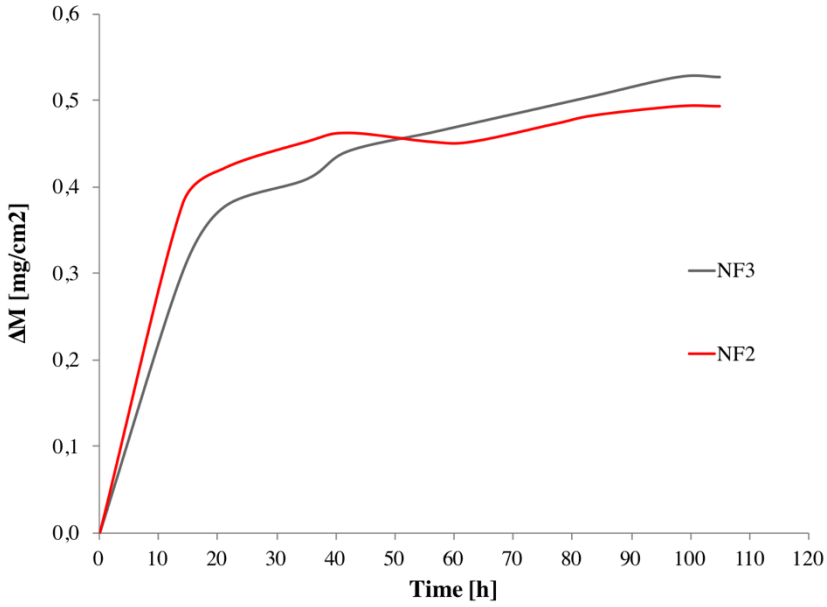

Figure 5.18: *Isothermal oxidation at 1050°C for the sample NF2 and NF3*

It is noted that the increase in concentration of activator salt has no benefit in terms of oxidation performance; it is concluded that there is a concentration threshold of the activating salt beyond which the benefits of the high temperature oxidation coating reach a plateau.

5.1.4 Oxidation kinetic

The thermally grown alumina is a dense, protective oxide layer, whose growth is controlled by the diffusion of anions and cations through the layer itself. Its growth kinetics is therefore parabolic, ie the oxidation time is proportional to the square of the sample weight gain.

Generally, the model used to describe the oxidation kinetics of these samples is the Wagner model. Wagner's theory describes the growth of an oxide scale on a metal, where ion and electron diffusion controls the speed of the whole process, with the equation:

$$\frac{dx}{dt} = \frac{k'}{x}$$

where x is the thickness of the oxide or the weight of the material and k 'is the parabolic constant of growth (cm^2/s or mg^2/s), correlated with the diffusion rate of species in the oxide layer. The integrated form of the equation is:

$$x^2(t) - x^2(t_0) = 2k'(t - t_0)$$

where t_0 is the time at which diffusion control begins.

However, this model hypothesizes the oxidation of a purely metallic sample without the presence of a surface oxide. In practice, there is always a layer on the surface of the -NiAl, which is formed by passivation of the material at the end of the deposition process or by thermal growth during oxidation. A kinetic model that takes into account all of these aspects is that proposed by Monceau [5.2], in which the independent variable becomes the weight gain of the material (or thickness of the oxide). This model is described by the equation:

$$t = A + Bx + \frac{1}{k_P}x^2$$

where parameters A and B contain information about the initially oxide layer (t = 0), while the coefficient k_P is the parabolic growth constant (cm^2/s or mg^2/s). A regression of experimental data has been made with both models in order to assess which of the two follows them more accurately (Figure 5.19-Figure 5.28).

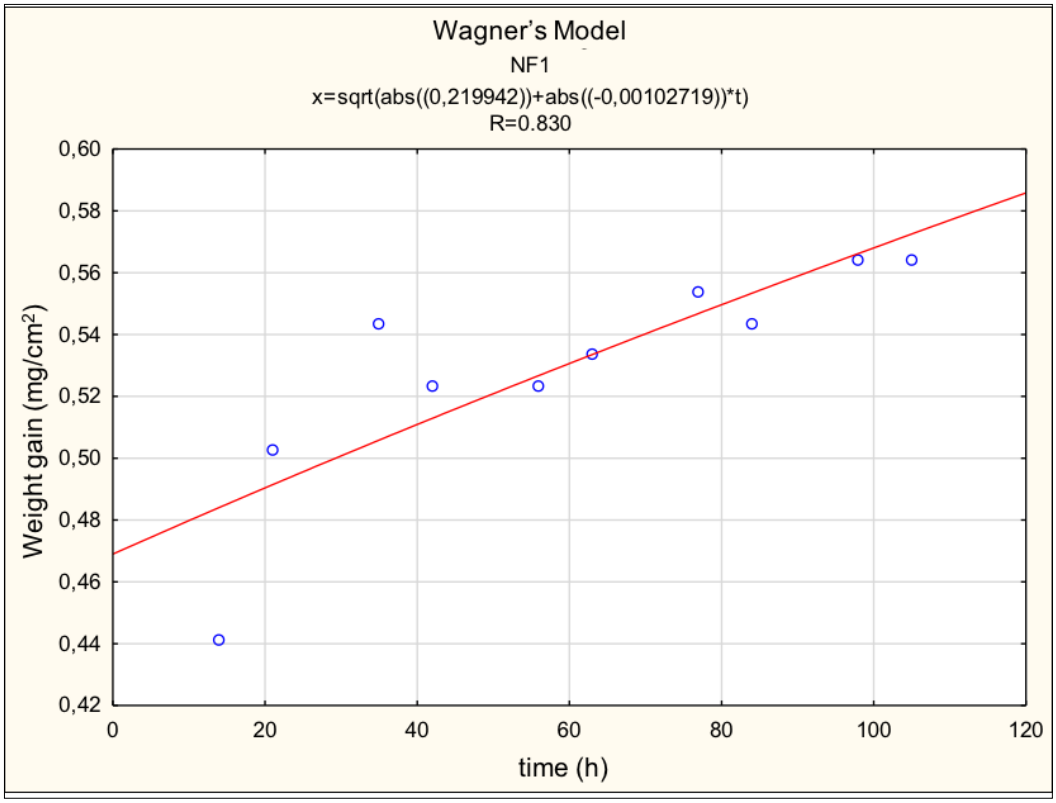

Figure 5.19: *Sample NF1 – oxidation kinetic, regression with Wagner's parabolic model*

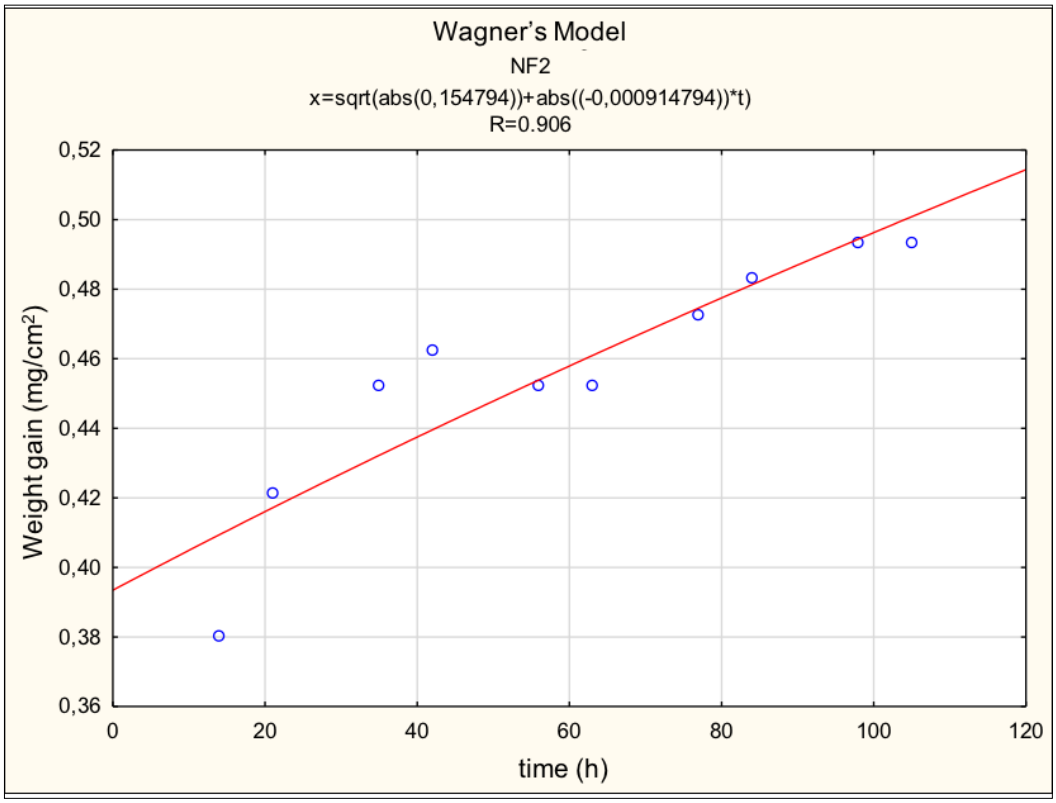

Figure 5.20: *Sample NF2 – oxidation kinetic, regression with Wagner's parabolic model*

.

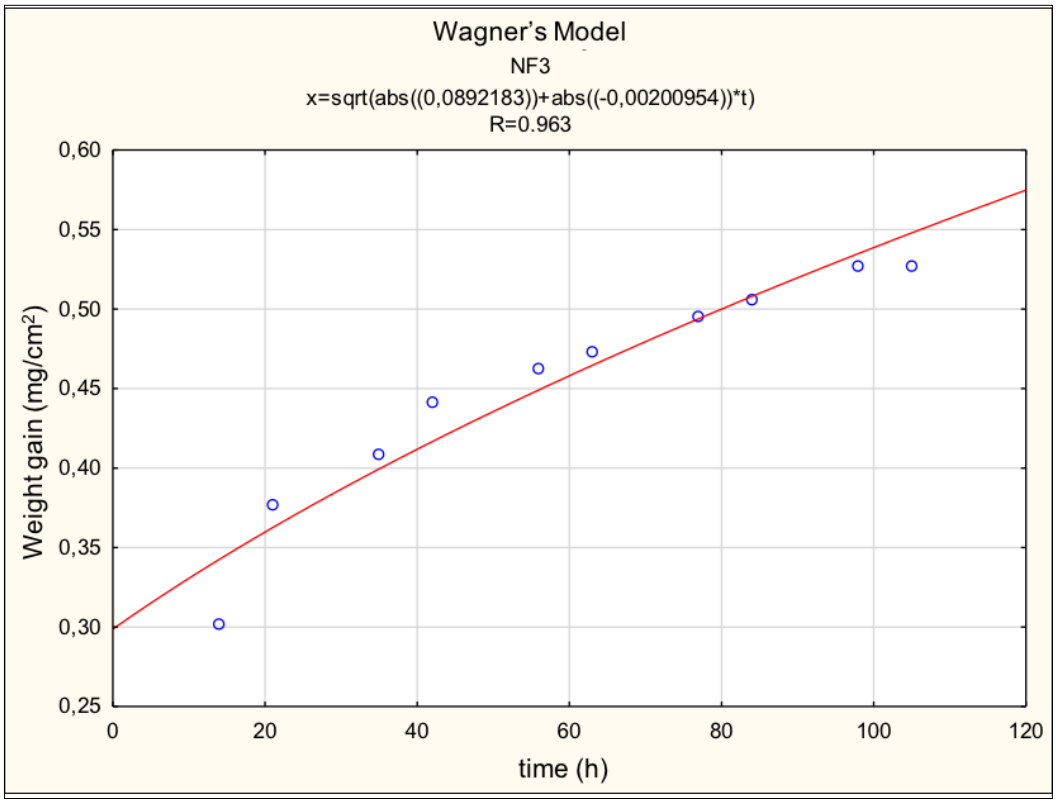

Figure 5.21: *Sample NF3 – oxidation kinetic, regression with Wagner's parabolic model*

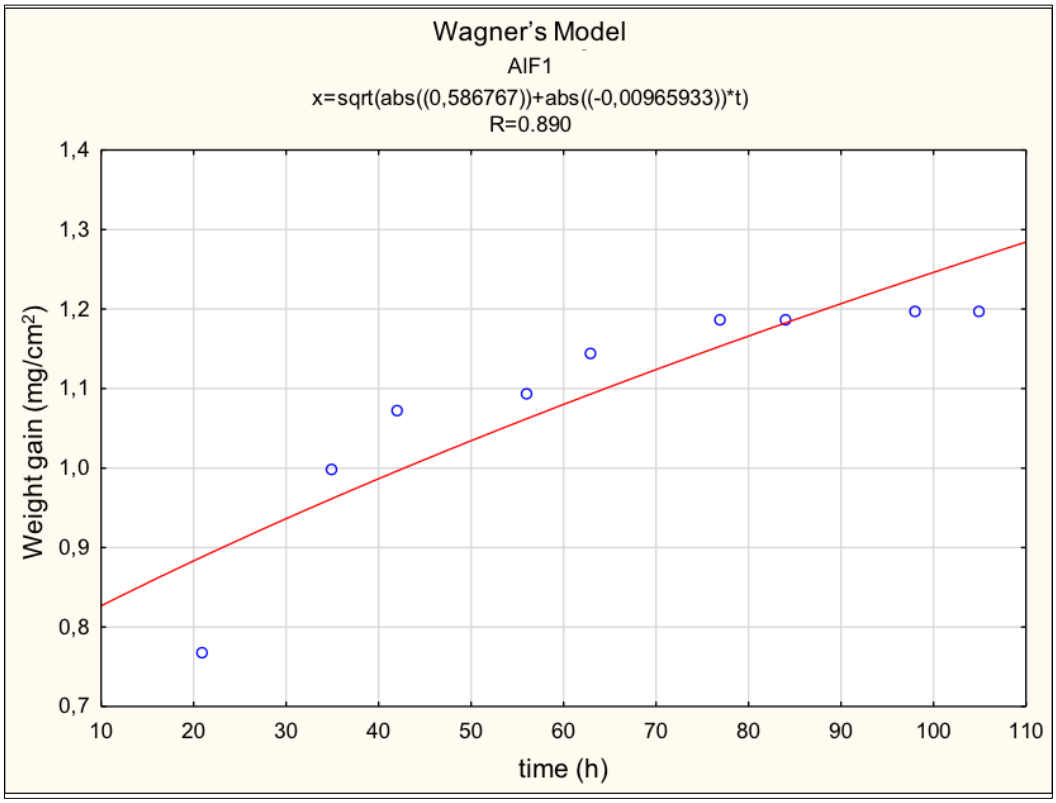

Figure 5.22: *Sample AlF1 – oxidation kinetic, regression with Wagner's parabolic model*

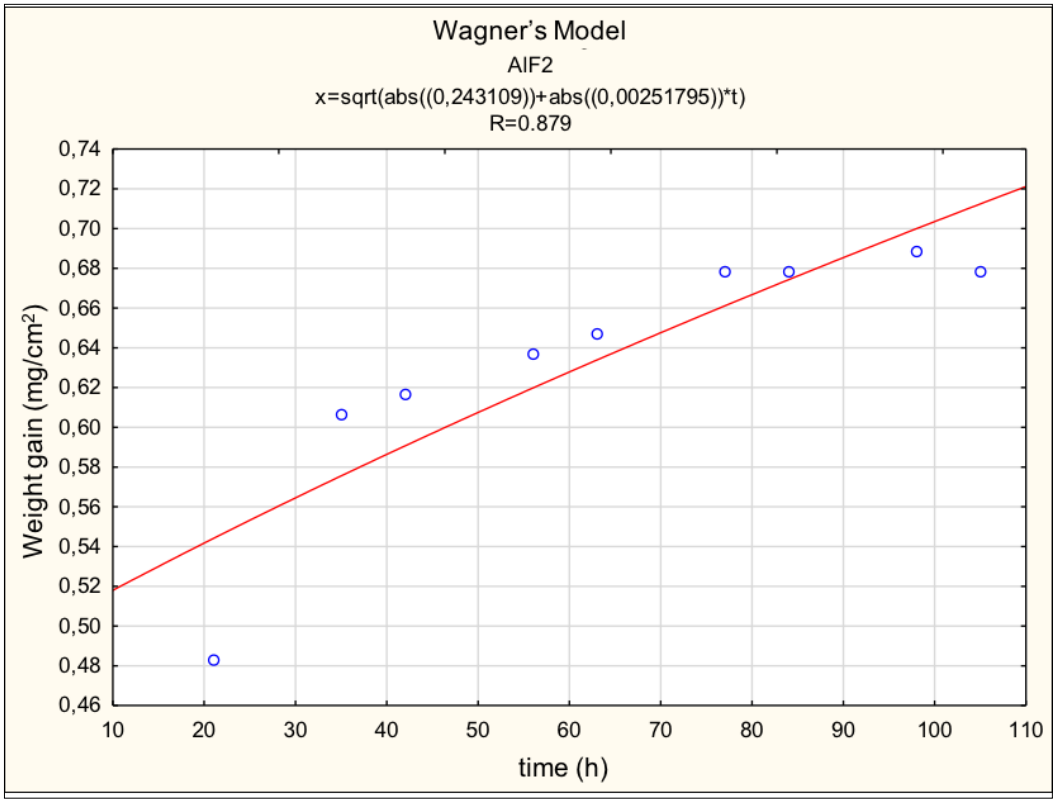

Figure 5.23: *Sample AlF2 – oxidation kinetic, regression with Wagner's parabolic model*

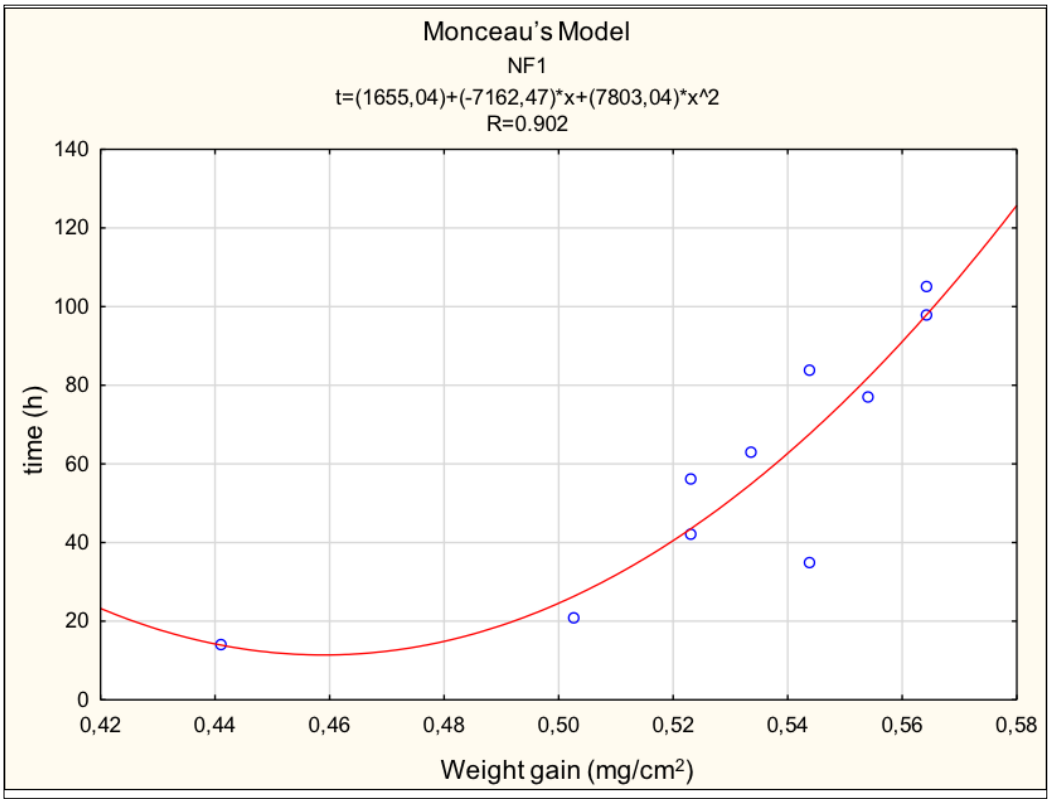

Figure 5.24: *Sample NF1 – oxidation kinetic, regression with Monceau's parabolic model*

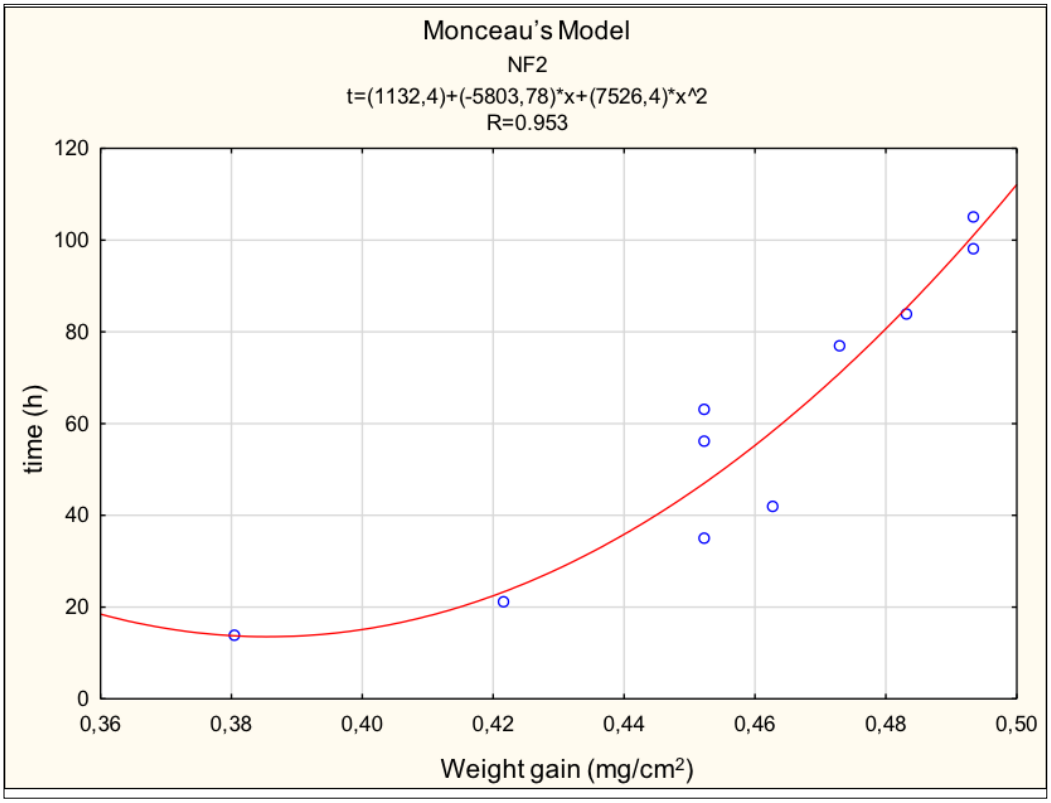

Figure 5.25: *Sample NF2 – oxidation kinetic, regression with Monceau's parabolic model*

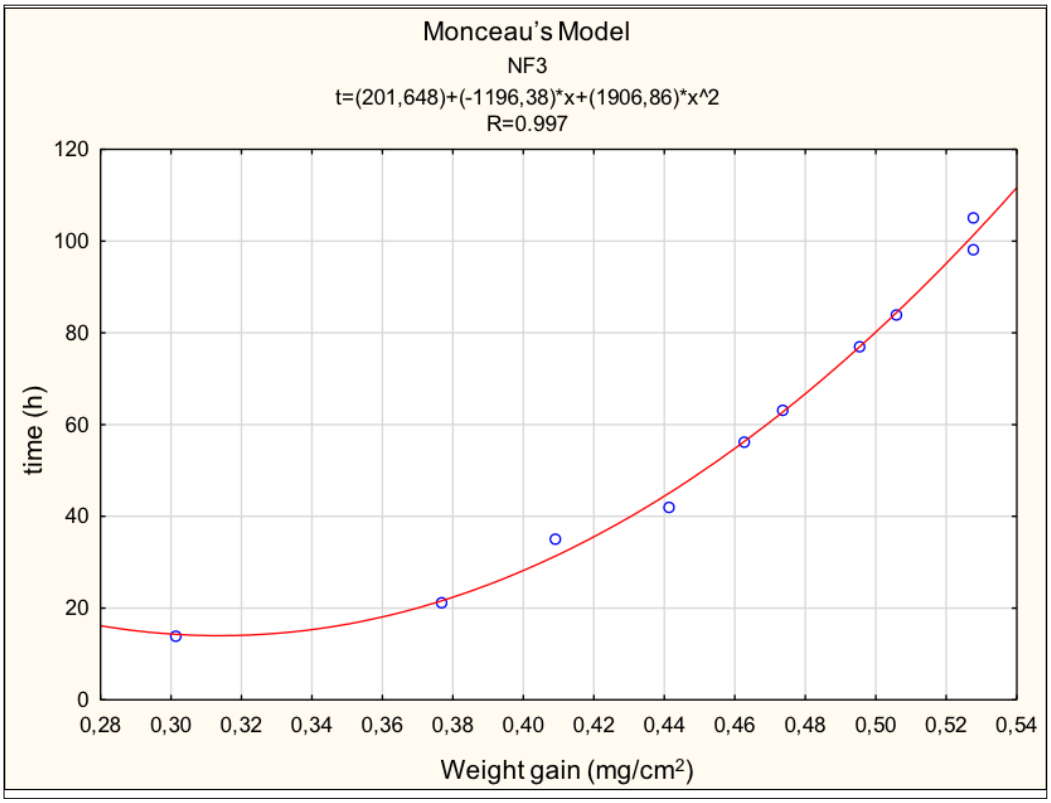

Figure 5.26: *Sample NF3 – oxidation kinetic, regression with Monceau's parabolic model*

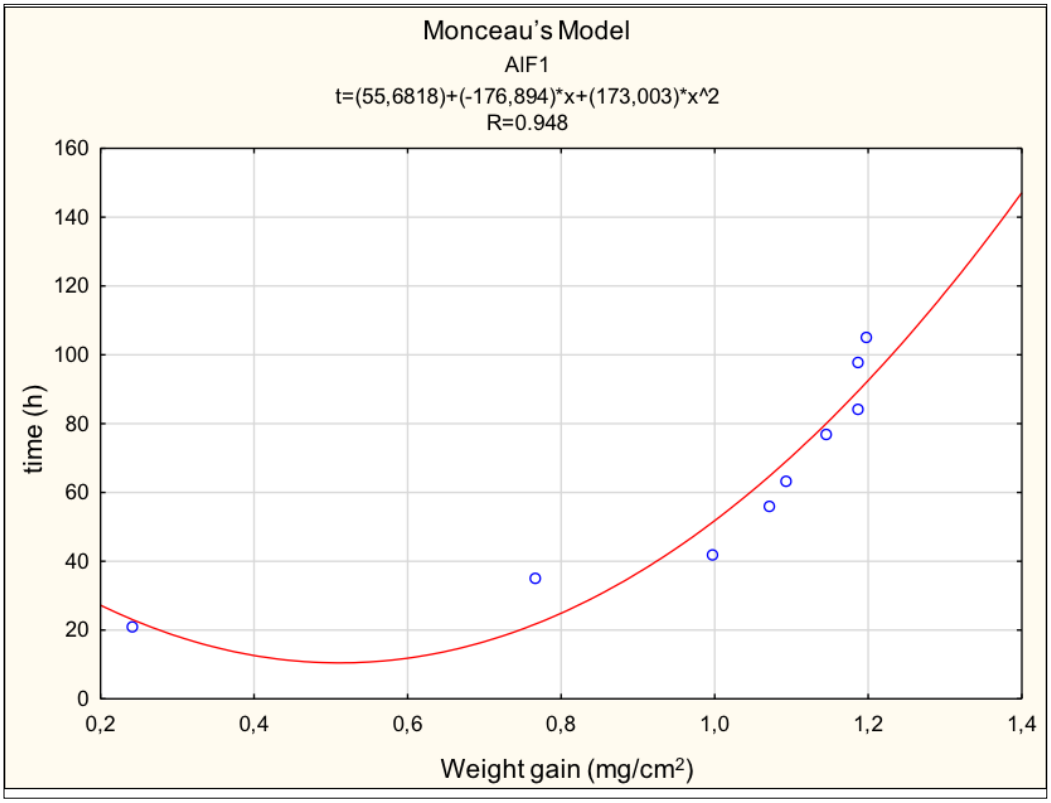

Figure 5.27: *Sample AlF1 – oxidation kinetic, regression with Monceau's parabolic model*

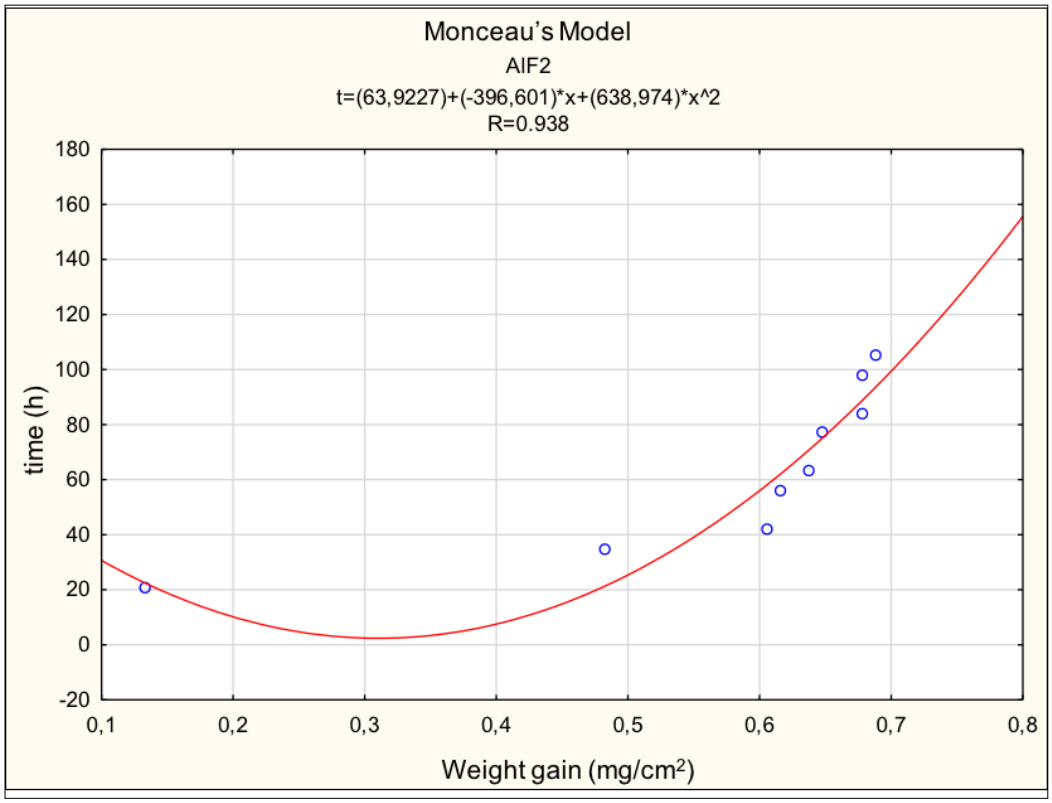

Figure5.28: *Sample AlF2 – oxidation kinetic, regression with Monceau's parabolic model*

To effectively compare the two models, Figures 5.29-Figure 5.33 show the regressions with the Monceau parabolic model with inverted axes.

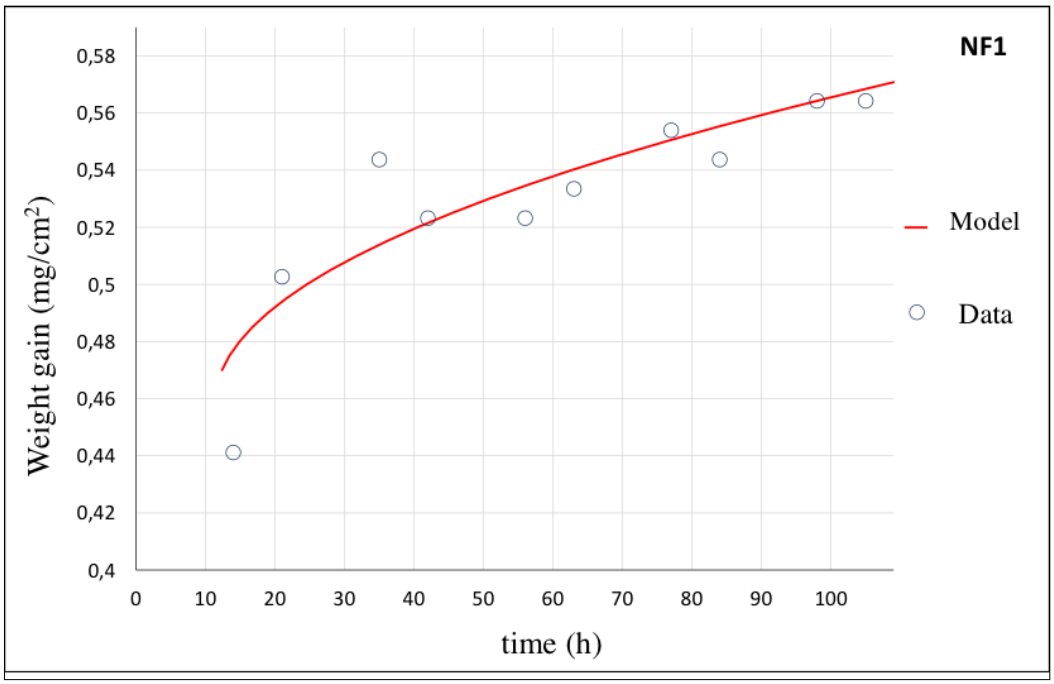

Figure 5.29: *Sample NF1 – oxidation kinetic, regression with Monceau's parabolic model with inverted axes*

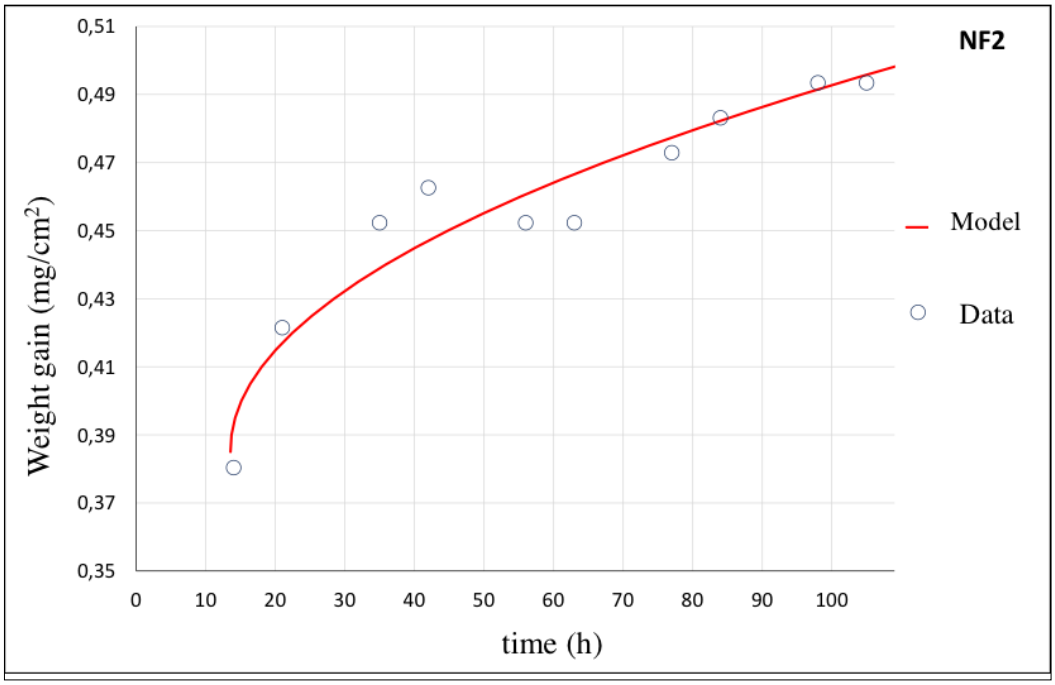

Figure 5.30: *Sample NF2 – oxidation kinetic, regression with Monceau's parabolic model with inverted axes*

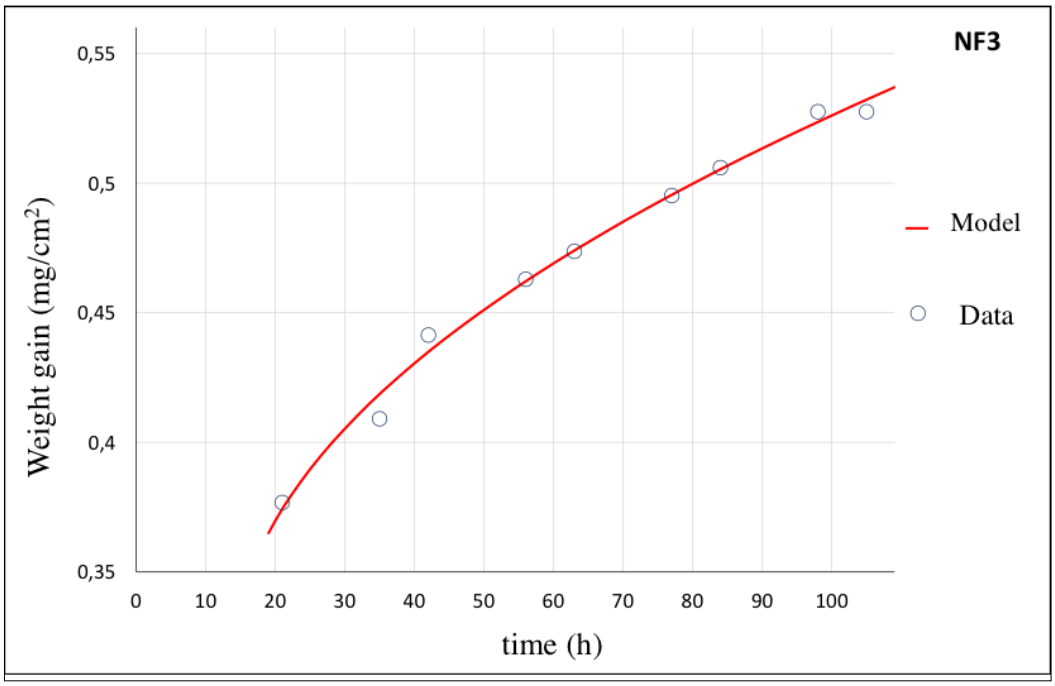

Figure 5.31: *Sample NF3 – oxidation kinetic, regression with Monceau's parabolic model with inverted axes*

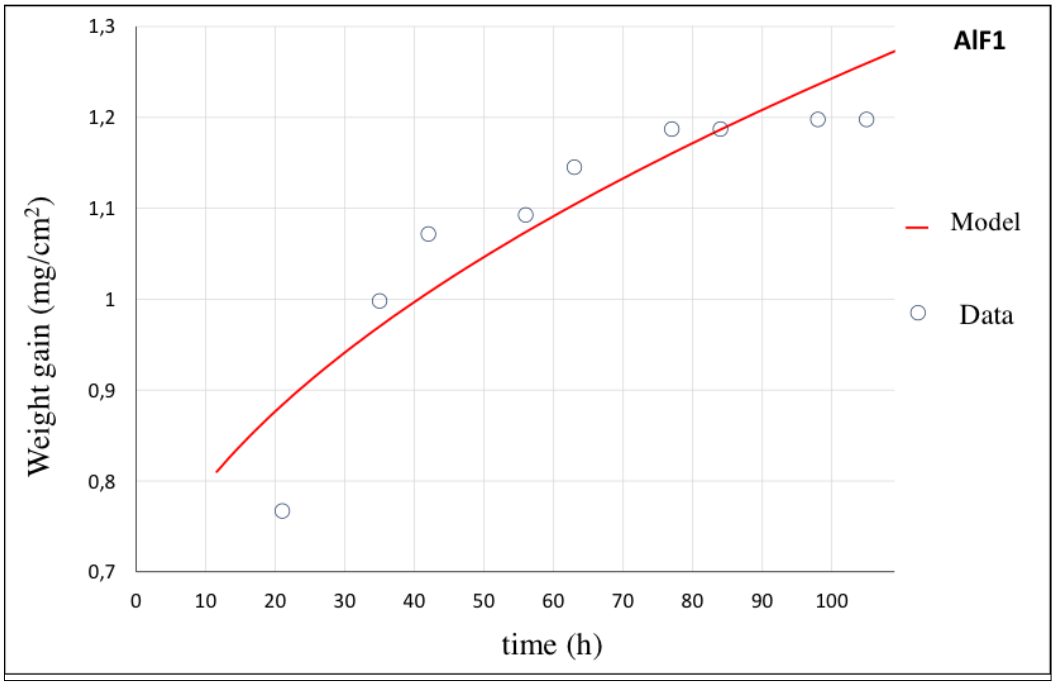

Figure 5.32: *Sample AlF1 – oxidation kinetic, regression with Monceau's parabolic model with inverted axes*

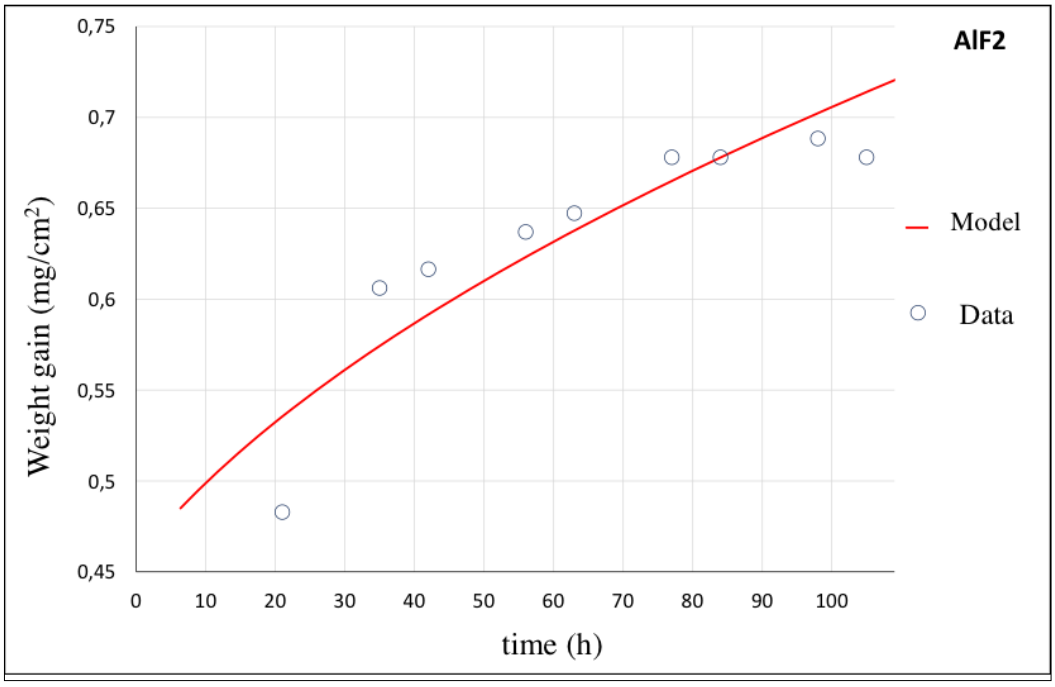

Figure 5.33: *Sample AlF2 – oxidation kinetic, regression with Monceau's parabolic model with inverted axes*

The regression curves obtained with the Monceau parabolic model have R correlation coefficients greater than 0.9 and therefore seem more suitable for the description of the experimental data. Table 5.5 shows the parabolic constraints extracted from this model.

Table 5.4: *parabolic constants growth for the samples of the series NF and AlF*

Deposition	k_P [mg^2/s]	R^2
NF1	3.55×10^{-8}	0.81
NF2	3.69×10^{-8}	0.91
AlF1	1.30×10^{-6}	0.88
AlF2	3.52×10^{-7}	0.87

The k_P calculated with this model roughly approximate the oxidation kinetics; it is noted, in fact, that the NF coatings exhibit a parabolic constant growth an order of magnitude less than the AlF coatings.

5.1.5 Hot corrosion

Samples were subjected to hot corrosion tests at 900 ° C, as described in Section 4.4.1. Besides the four coatings produced was also included in the test a sample of the substrate, to verify the difference in terms of useful life of the guaranteed by aluminides component.

Figure 5.34shows the result of the test in which the substrate is observed after 200 hours undergoing a loss of structural material. Aluminized samples, on the other hand, exhibit significantly greater corrosion resistance due to the formation of a protective oxide scale on the surface.

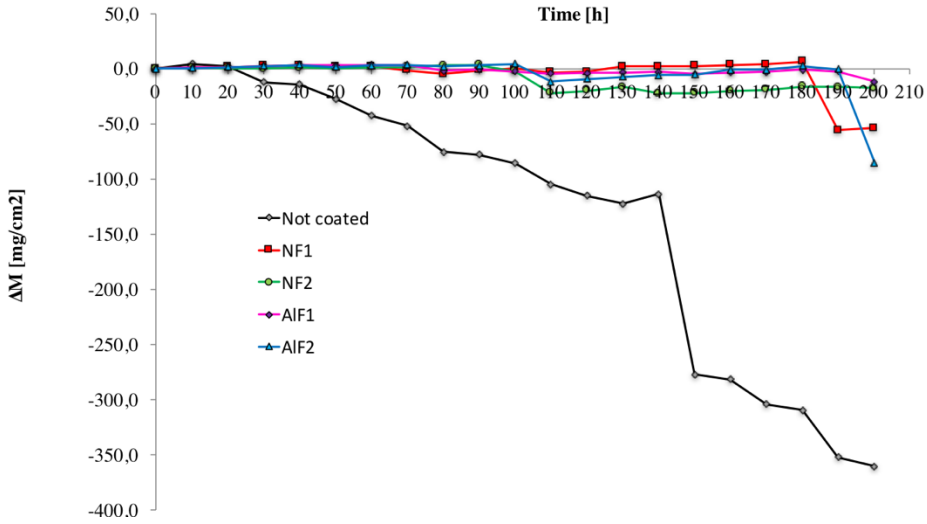

Figure 5.34: *Hot corrosion test at 900°C for 100h for the series NF and AlF. "Not coated" refers to a substrate not aluminized*

Figure 5.35 shows the first 100 hours of the test, in which the substrate was excluded from the graph. For the first 50 hours, a slower oxidation kinetics is observed for the NF2 coating; however, all specimens exhibit an alternation between increases and losses in weight, due to the localized attack of corrosion salts. In fact, they insist on a very small area of the sample, greatly accelerating the oxidation phenomenon. This causes a very high increase in the protective scale, which is unstable after a few hours of testing.

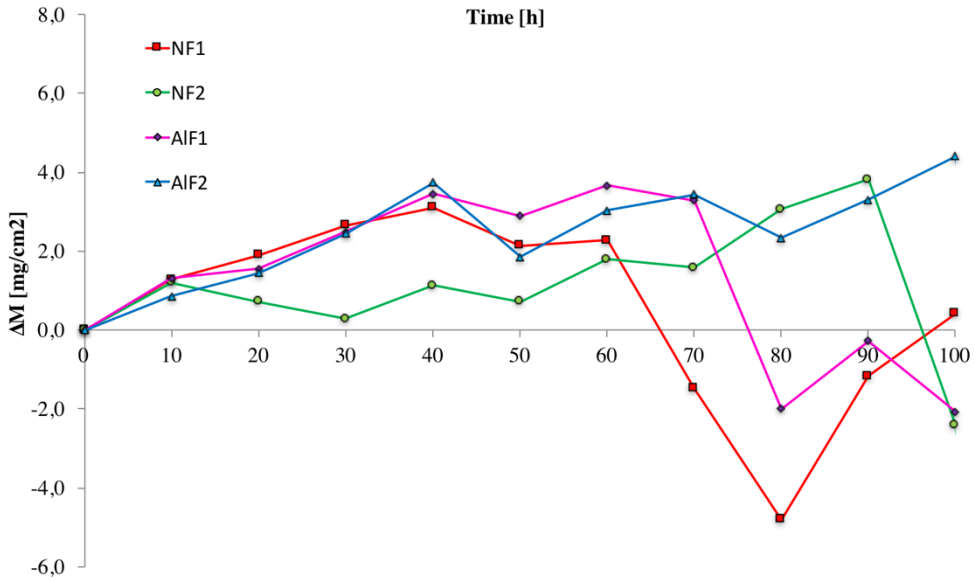

Figure 5.35: *Hot corrosion test at 900°C for 105h for the series NF and AlF*

Figure 5.36 shows the XRD analysis performed after 100 hours of testing at 900 ° C

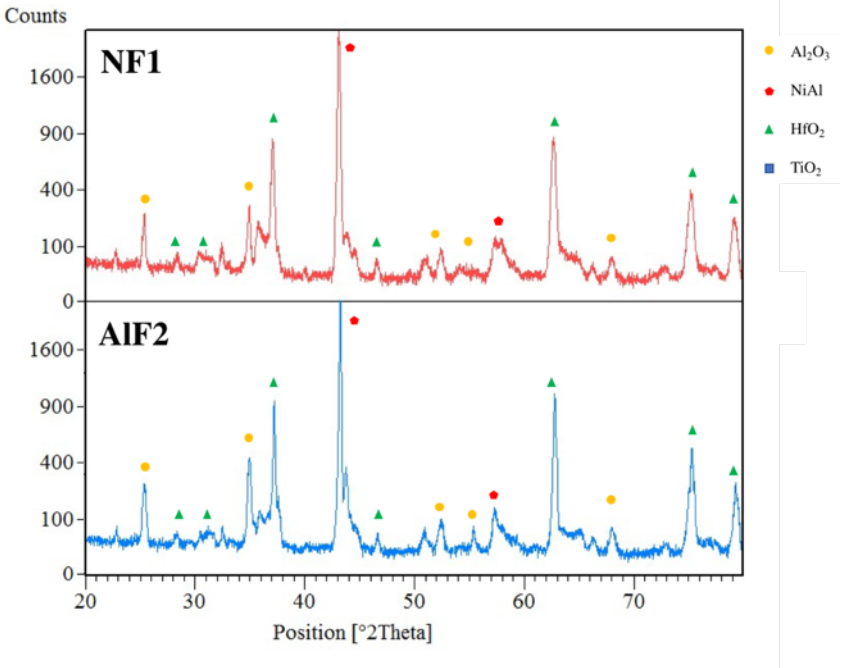

Figure 5.36: *XRD spectra after 100h of hot corrosion test for the samples NF1(red) and AlF2 (blue)*

From the spectra, it can be noticed the absence of peaks corresponding to the initial composition of the corrosion salts, meaning that the salt mixture is fully reacted according to a very fast reaction kinetics. The presence of some peaks due to corrosion products, in particular Ni_2S, is observed, which results in a high surface deterioration. The presence of Ni_3Al denote the depletion of Al of the phase β and subsequent phase transformation: therefore, corrosion, after 100 hours, is already in advanced stage. Figure 5.37 shows the first 150 hours of the test. At 100 hours, the only coating that has not suffered material losses is AlF2. However, in the next cycle there is a sharp loss of material, as well as the NF2. From 110 and 150 hours onwards all samples maintain a roughly stable weight

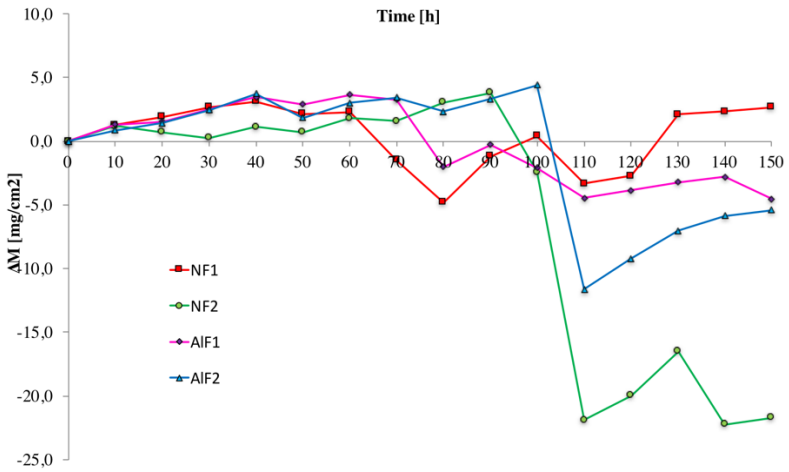

Figure 5.37: *Hot corrosion test at 900°C for 150h for the series NF and AlF*

Figure 5.38 shows the full test run. The NF1 and ALF2 samples suffer a loss of structural material, a symptom of the end of the coating life. The NF2 and AlF1 coatings have a stable weight, but below the starting weight, meaning that the coating has been subjected to substantial oxidation and subsequent release of oxide, but it is still protective.

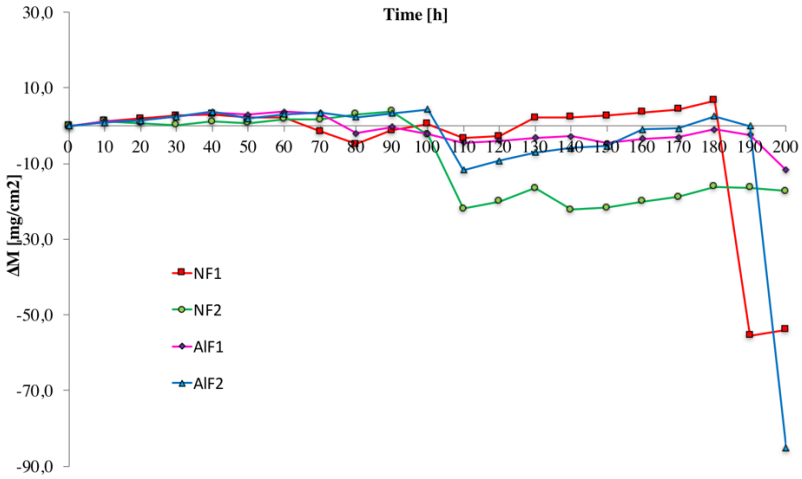

Figure 5.38: *Hot corrosion test at 900°C for 100h for the series NF and AlF*

To investigate the consequences of the lack of homogeneity of the distribution of corrosion salts on the surface of the sample, superficial EDS analysis were performed to the center and to the external zone of the sample. Figure 5.39 shows the center of the sample, the area where the coating has undergone a more intense attack.

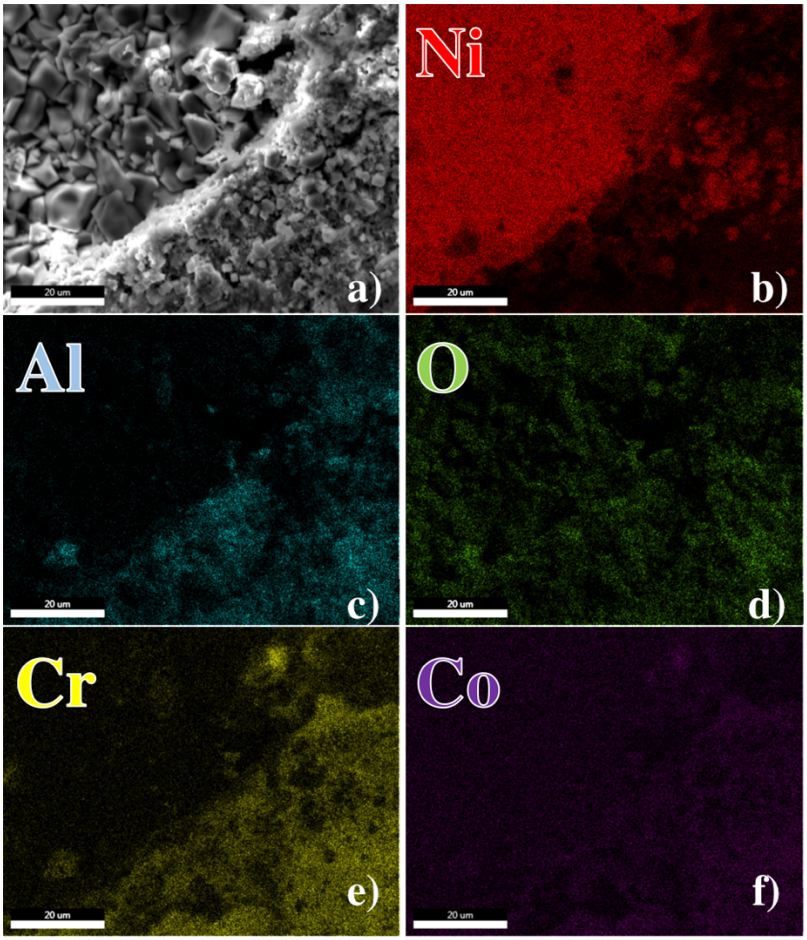

Figure 5.39: *EDS maps in the attacked zone (centre of the sample) after 100h at 900°C; a) SEM micrograph of the investigated area; b) Ni; c) Al; d) O; e) Cr; f) Co*

Figure 5.39b-d denotes the presence of a cavity at the center of the sample, where the Ni substrate has been exposed to the attack and is bonded to the O: the cubic NiO formations appear in the center of the sample. Al_2O_3 is present only in the external zone. Alloy Co and Cr are widespread on the surface and reacted with oxygen (Figure 5.39e-f).

Figure 5.40shows EDS analysis of the sample external zone, the area where the coating has suffered a blander attack from the corrosion salts.

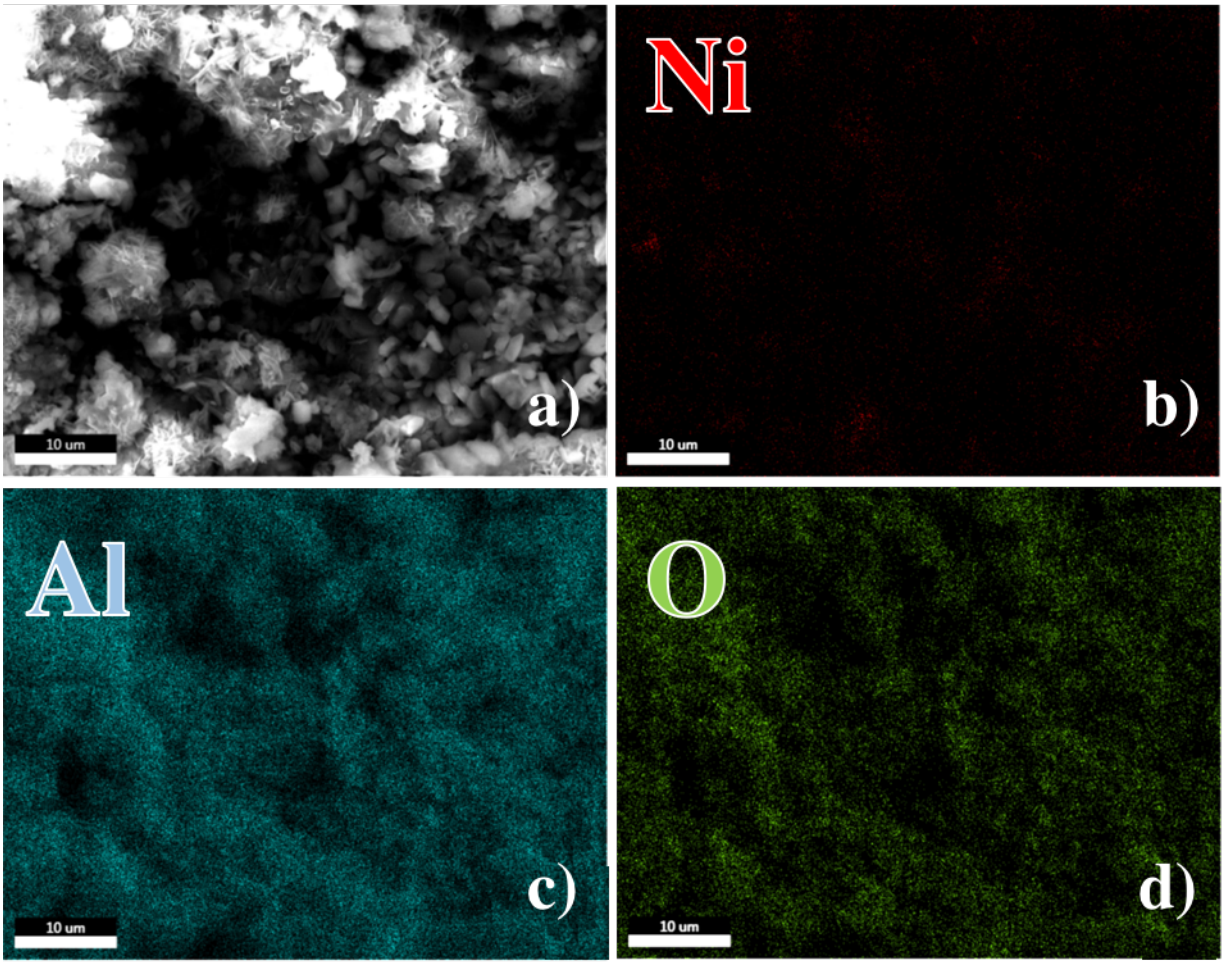

Figure 5.40: *EDS maps of the external zone for the sample NF2 after 100 h of hot corrosion at 900 °C: a) SEM micrograph of the investigated area; b) Ni; c) Al; d) O.*

Figure 5.40b-d shows a continuous layer of α-Al_2O_3, with the absence of Ni on the surface. This evidence confirms what it was assumed seen the trend of the weights of the samples during the test: the samples undergo an inhomogeneous attack of the surface, accelerating to an appreciable extent the detachment of the protective oxide scale (Figure 5.40e-f).

In conclusion, the diffusion coatings obtained with NH_4F as the activator salt show a better oxidation behavior than those obtained with AlF_3; in particular, NF2 has an increase in weight after 105 hours of oxidation lower than all other samples, characterized by a more protective oxide scale. Through the Monceau model, the parabolic constants of k_P growth have been calculated: NF coatings exhibit a parabolic growth constant of an order of magnitude less than the AlF coatings. There is also an activator salt concentration threshold beyond which the oxidation benefits of the coating do not change.

During the cooling following the oxidation test, the release of protective oxide zones is due to the different thermal expansion coefficient of the oxide and the undercoat.

The hot corrosion test has generated a very accelerated and inhomogeneous oxidation on the surface of the sample. This is due to the restriction area on which the corrosion salts insist, causing a very high increase in thickness of the protective scale, which is unstable after a few hours of testing; such loss of surface material is not found in the external zone of the samples.

5.1.6 Modified aluminide coating with Zr

Modified coatings were obtained using a NH_4F / ZrF_4 mixed activator salt, in which the concentration of NH_4F (0.75 wt%) was maintained constant while the concentration of ZrF_4 was varied in each deposition, as reported in Table 5.5.

Table 5.5: *Concentrations of activator salt for the deposition of ZrF series*

Deposition	wt% of activator salt	mol of activator salt
ZrF1	0.121	0.0072
ZrF2	0.145	0.0087
ZrF3	0.165	0.0100
ZrF4	0.335	0.0201
ZrF5	0.670	0.0402

Table 5.6 summarizes the features of the product coatings. From this table, it is possible to see how modified coatings are considerably thicker than conventional ones, which implies a direct involvement of ZrF4 in the deposition process.

Table 5.6: *Features obtained from depositions with NH_4F/ZrF_4 mixture as activator salt*

Deposition	β-NiAl thckness [μm]	IDZ thickness [μm]
ZrF1	35 (±0.8)	24 (±0.9)
ZrF2	39 (±1.2)	27 (±1)
ZrF3	27 (±1.1)	19 (±0.9)

ZrF4	32 (±1.8)	24 (±1.2)
ZrF5	32 (±0.8)	24 (±0.5)

Beyond the thickness, the coatings are very similar to each other, as shown in Figure 5.41. In addition, there are no particular differences compared to the conventional coatings obtained during the first phase of the experiment.

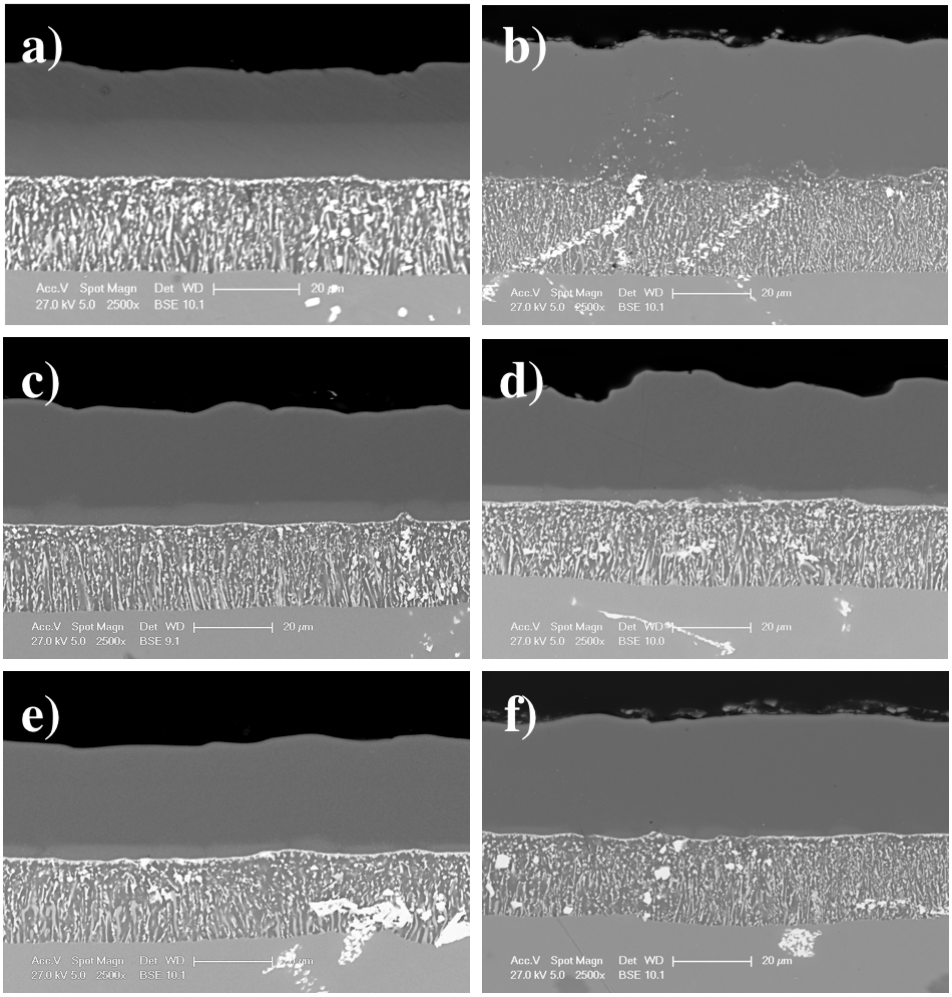

Figure 5.41: *Cross-section SEM micrographies for coatings obtained with the NH_4F/ZrF_4 mixture as activator salt - a) ZrF1; b) ZrF2; c) ZrF3; d) ZrF4; e) ZrF5.*

The quantity and distribution of Zr present within the coating was studied by GDOES technique. The concentration profiles in weight of the ZrF3 coating are shown in Figure 5.42
; the elemental distribution is also representative of the other analyzed compositions.

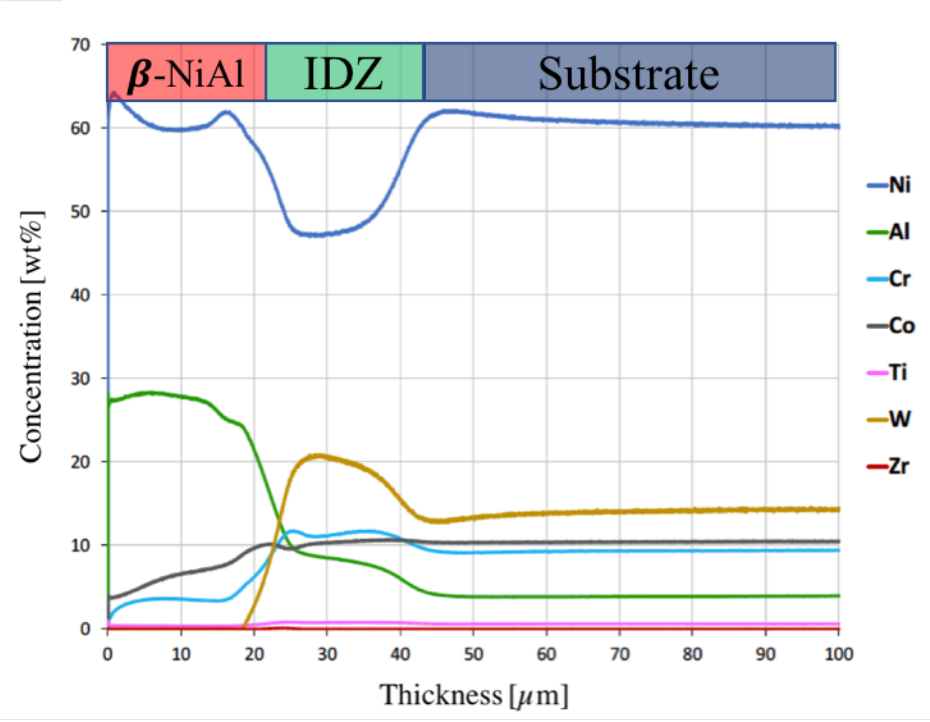

Figure 5.42: *Concentration profile obtained through GDOES of the main elements in the ZrF3 coating*

Figure 5.42 shows the presence of about 25 m of β-NiAl, followed by 20 m of IDZ, as found in SEM micrographies. In this area, the intensity of W is too high compared to alloy concentration; this experimental error is due, probably, to the fact that there are some optical interferences with other elements (such as Hf and Ta, which possess a very similar atomic weight). Thus, a concentration is obtained that is the overlap of the three elements. Considering the low concentration of Zr, it is necessary to modify the y-axis scale to find the peak of the reactive element taken into account.

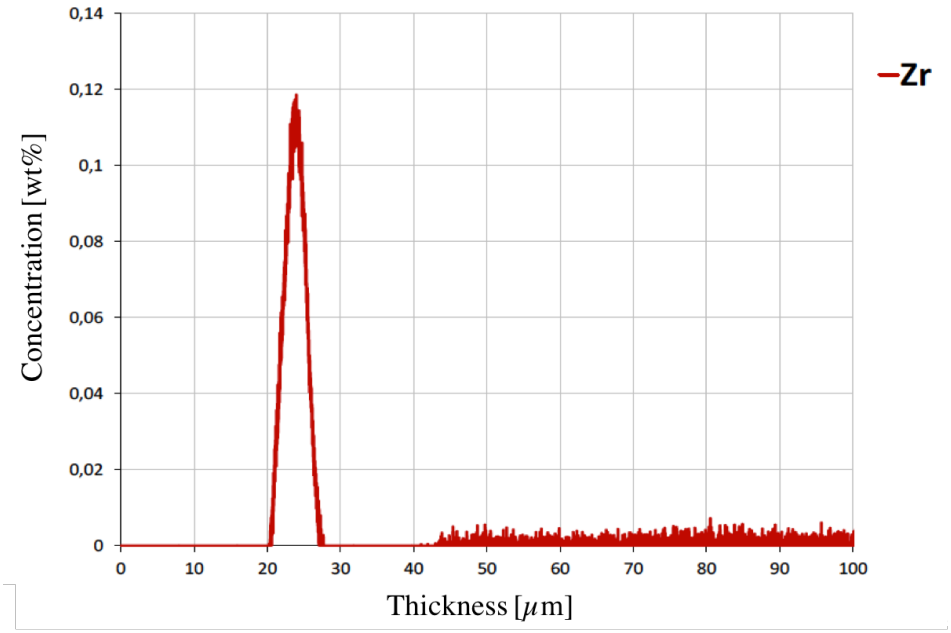

Figure 5.43: *Concentration profile obtained through GDOES of the Zr in the ZrF3 coating*

The concentration profile of Zr (Figure 5.43) highlights how it is located at the interface between β-NiAl and IDZ, finding results with literature [1].

Top-view SEM analysis did not show any difference from the coatings obtained during the first phase of the experimentation: in fact, all the specimens show the polyhedral structure of the β-NiAl. Except for the ZrF5 deposition, where it is possible to observe the presence of macroscopic crystals on top of the surface of some specimens of the same batch (Figure 5.44).

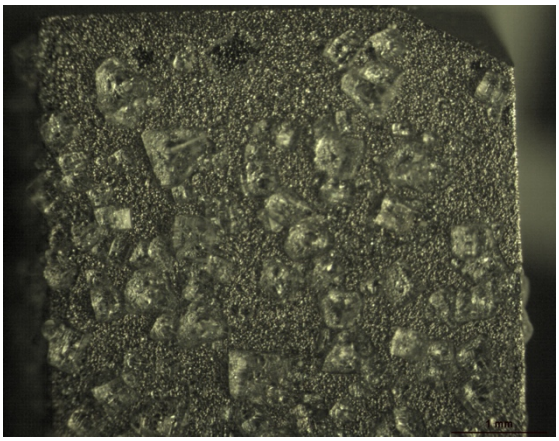

Figure 5.44: *Surface optical microscope image of a sample from the ZrF5 deposition.*

EDS analysis were performed to investigate the chemical compositions of those crystals (Figure 5.45 – Figure 5.46)

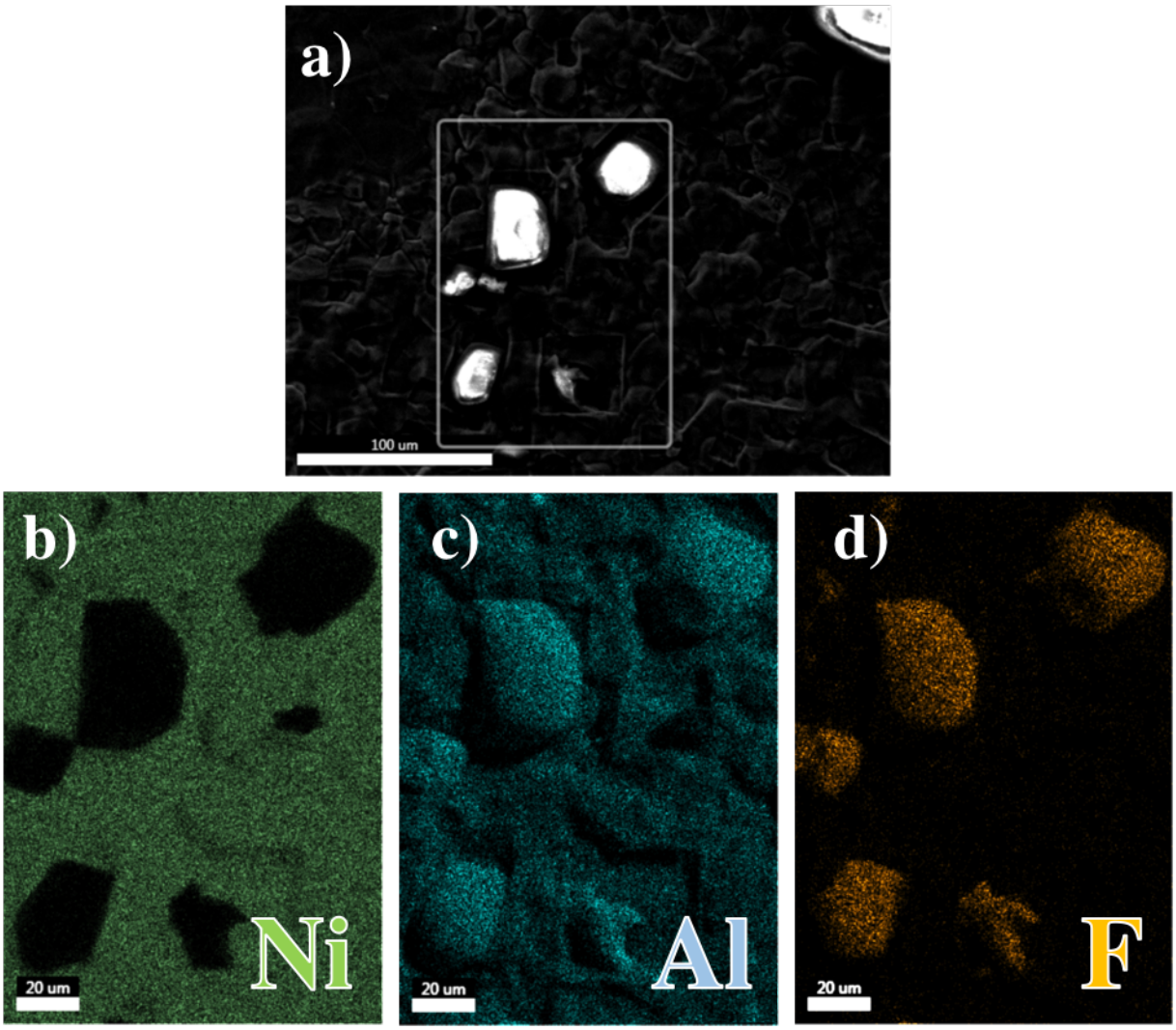

Figure 5.45: *EDS maps of the coating ZrF5, top-view – a) SEM micrograph of investigated area; b) Ni; c) Al; d) F*

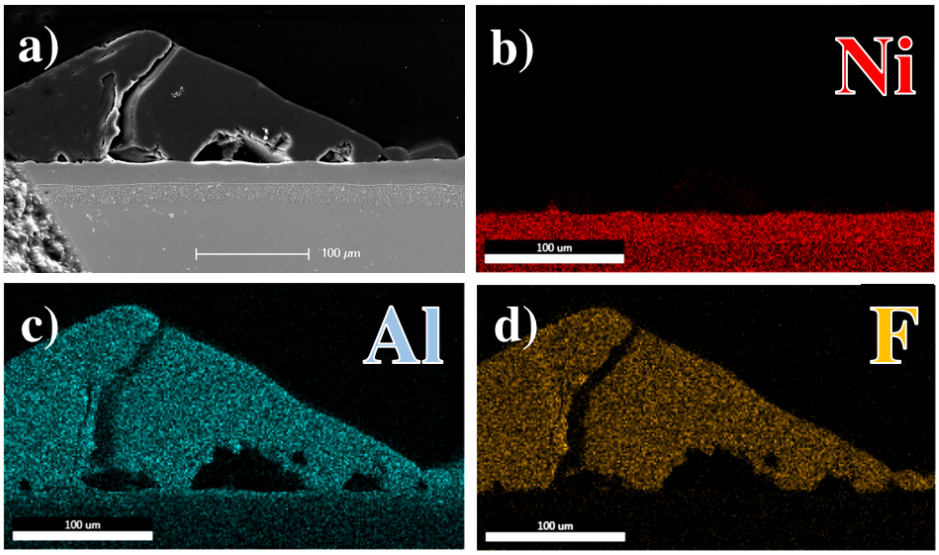

Figure 5.46: EDS maps of the coating ZrF5, cross-section–a) SEM micrograph of the investigated area; b) Ni; c) Al; d) F

It was hypothesized that these deposits were linked to excessive production of AlF vapors during the process, which accumulate near the substrate. In fact, the stage determining the deposition rate is the solid state diffusion of the Al into the substrate; consequently, an excess of halydes of Al causes the deposition of solid AlF_3 near the surface, which at the end of the process remains mechanically anchored to the surface. The same situation was observed for the sample aluminized with AlF_3 as activator salt. In the case of ZrF_4, however, the concentration of gaseous Al halydes is high enough to prevent the completely diffusion of Al within the coating with a consequent re-crystalization of AlF_3on top of the substrate. It is concluded that for an efficient deposition of the coating the gas phase produced must be accurately proportioned to the diffusion velocity within the superalloy.

5.1.7 Isothermal oxidation

Isothermal oxidation test at 1050 ° C was carried out on the samples of the ZrF series, as described in Section 4.4.1. Besides the four coatings produced was also included in the test a sample of the substrate, to verify the difference in terms of service life of the aluminides component.
Figure 5.47 shows the result of modified coatings compared to the best specimen of standard diffusion coatings. From the Figure 5.46 is possible to see that all modified coatings have a parabolic oxidation kinetics and after 105 hours they show a better oxidation resistance then the standard coating.

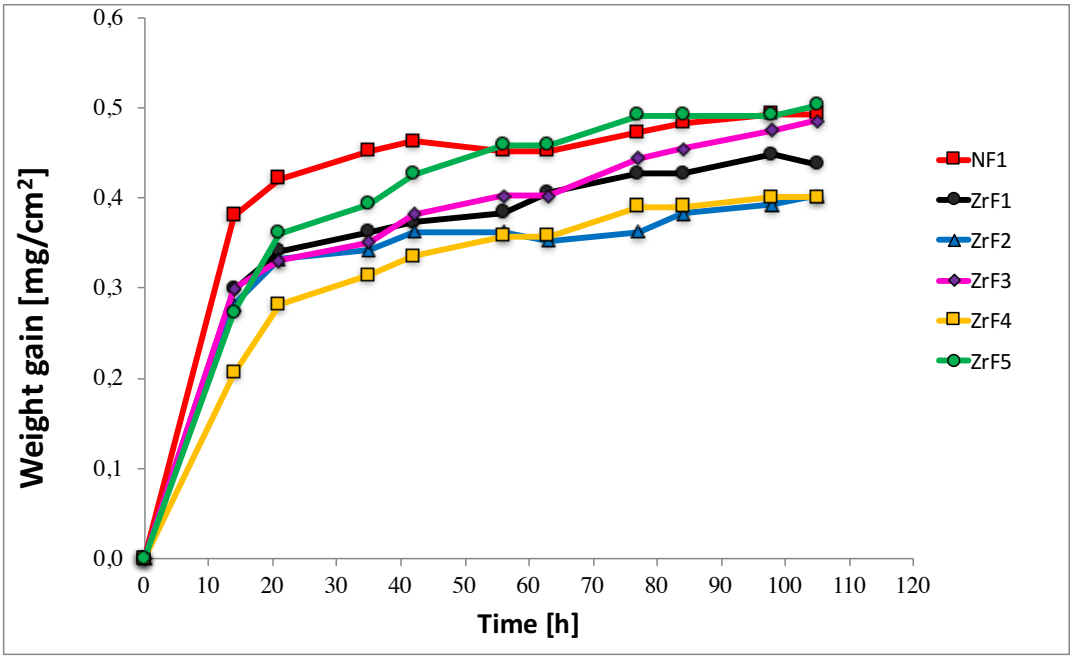

Figure 5.47: *Isothermal oxidation (1050°C) for ZrF series.*

From the previous figure, it is shown how the ZrF1 and ZrF5 coatings, which have respectively the minimum and maximum amount of starting activators, are those that are a higher weight amount

between the modified diffusing coatings. However, it is noted that their oxidation kinetics is in any case is comparable to that of NF1. Figure 5.48 shows ZrF coatings which show a higher oxidation resistance than NF1. It is noticed that adding a reactive element in the right amount leads to a decrease in weight gain by almost 20%.

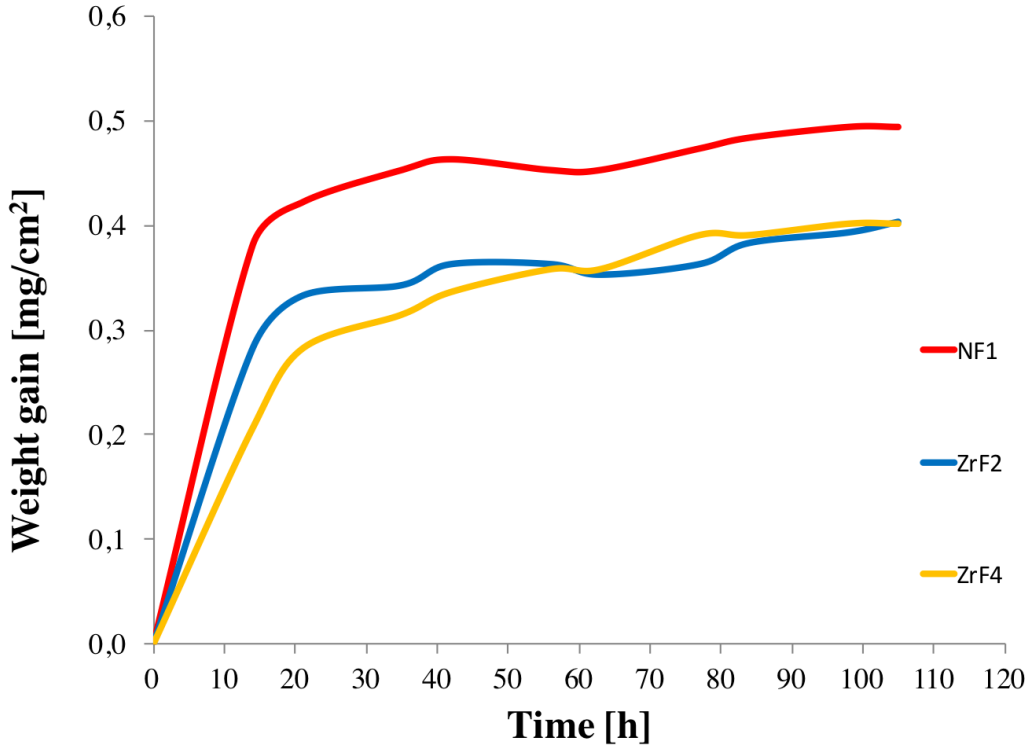

Figure 5.48: *Isothermal oxidation (1050°C) for ZrF2, ZrF4 in comparison with NF1*

Figure 5.49 shows SEM micrographs after 100 hours of isothermal oxidation of ZrF3, ZrF4 and ZrF5 coatings. There is a clear note of the presence of a protective oxide scale of α-Al_2O_3 and the differences between the various protective oxides formed can be observe.

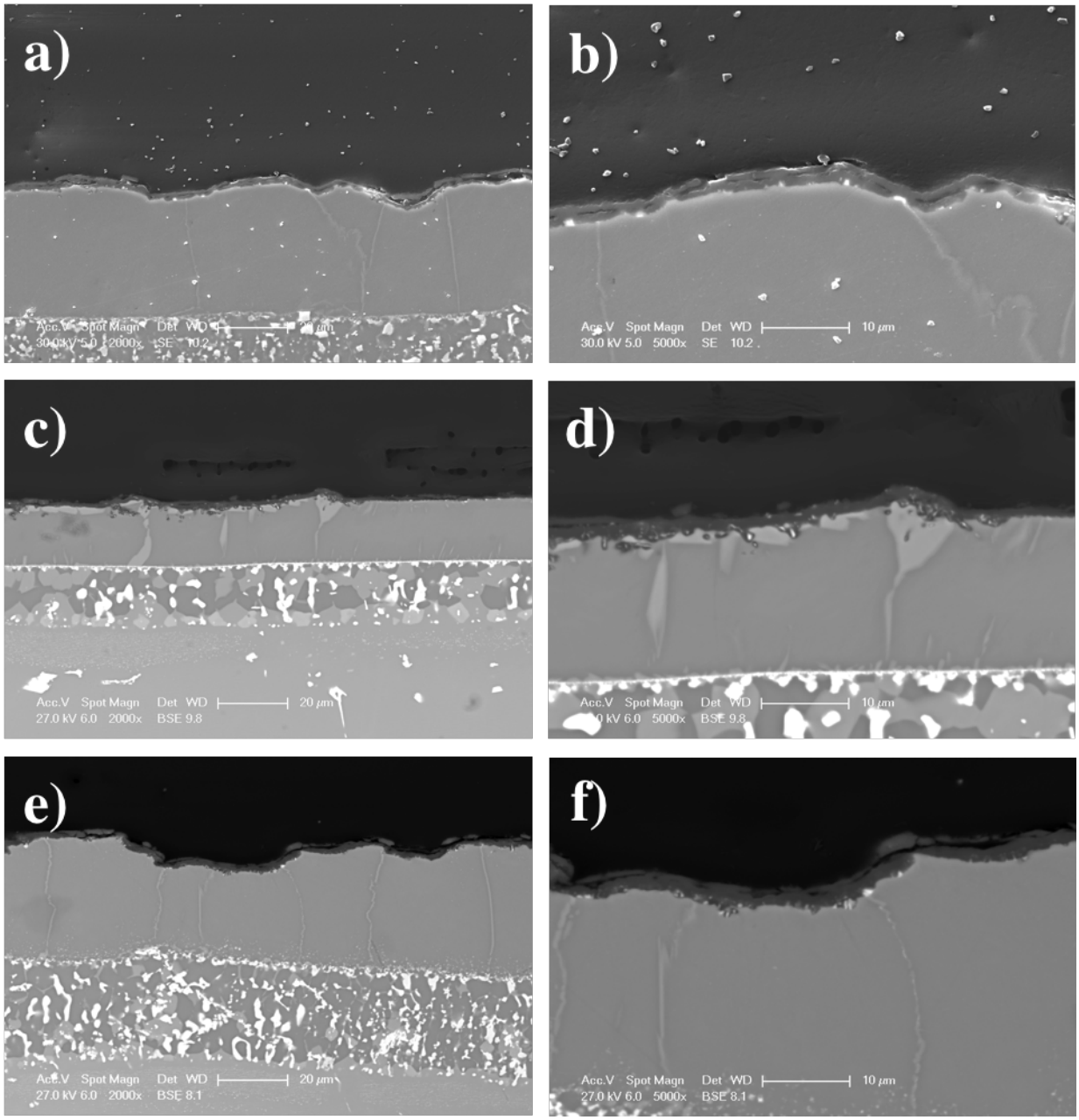

Figure 5.49: *Cross-section SEM micrographs for the sample after 105h of isothermal oxidation (1050°C): a) ZrF3 2000X; b) ZrF3 5000X; c) ZrF4 2000X; d) ZrF4 5000X; e) ZrF5 2000X; f) ZrF5 5000X*

The difference between the three coatings is in the thickness of oxide formed: the ZrF 4 (Figure 5.49c-d), which shows the best oxidation resistance, after 105 hours is covered with an oxide layer of about 1.5 microns. The ZrF5 (Figure 5.49e-f), on the other hand, is characterized by a 2.7 µm protective oxide, which makes it the coating that gain more weight at the end of the test. Finally, the ZrF3 (Figure 5.49a-b), which exhibits an intermediate behavior between the two, has a protective oxide scale of about 2.3 µm.

EDS analysis of the cross-section of oxidized coatings was performed on all samples. Figure 5.50 shows the maps for the oxidized ZrF5 coating for 105 hours at 1050 ° C; in particular, the presence

of heavy elements around the scale is observed, diffused by the IDZ trough the bond coat and up to the oxide scale. Zr seems to have the same role of the RE already present in the chemical composition of the super alloy. As is known[2], the reactive elements increase the resistance to oxidation by increasing the adhesion of the protective scale. The dynamic segregation theory states that the diffusion mechanism of the reactive elements takes place through the grain boundaries of the oxide scale up to the interface with the gaseous phase. In this case, it was seen that Zr can play a different role in terms of oxidation resistance: in fact, before to reach the interface between the bond coat and the oxide scale, the Zr has blocked the oxygen path through the scale, by avoiding the penetration inside the bond coat.

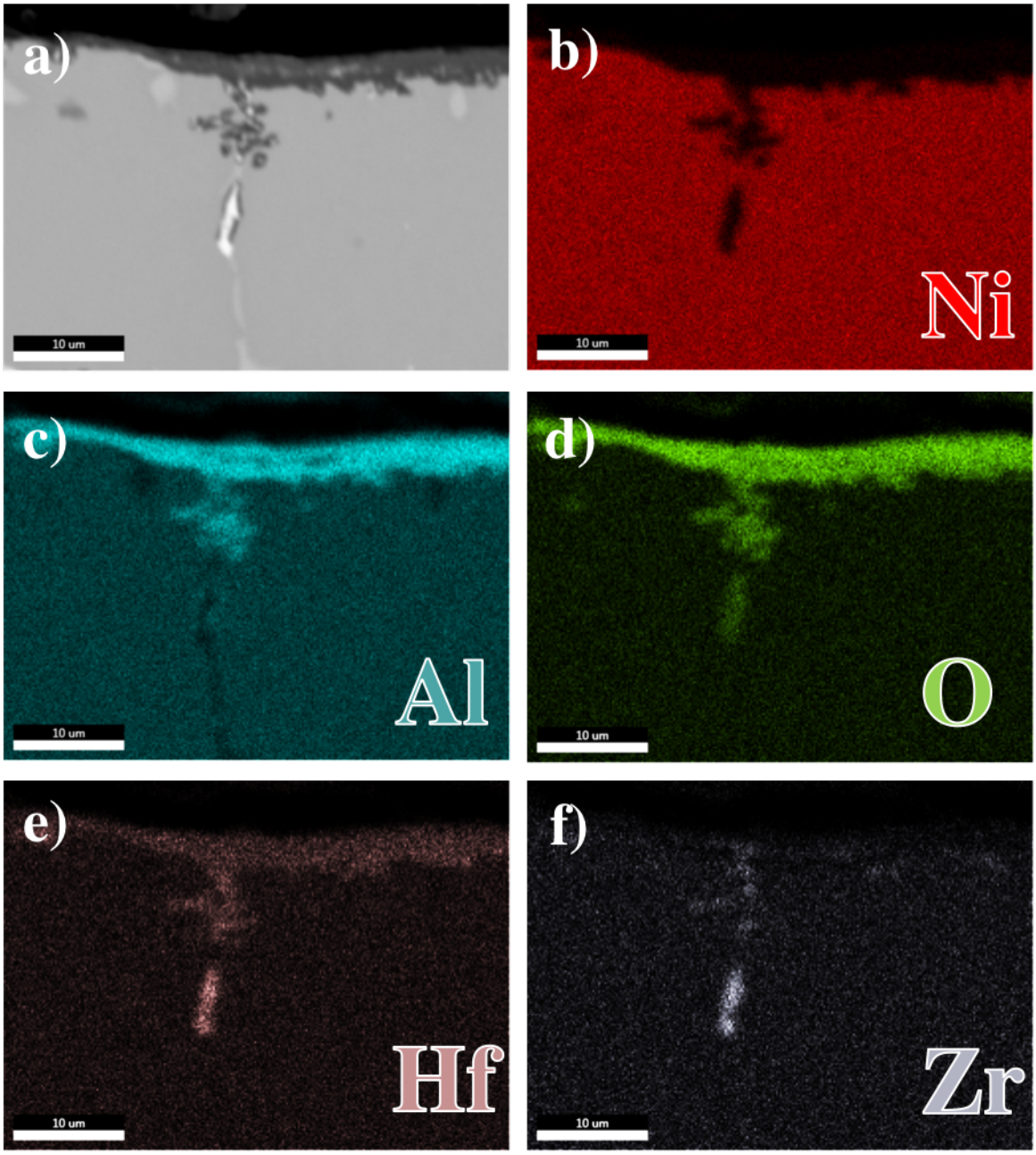

Figure 5.50: EDS maps of the coating ZrF5, top-view, after 105h of oxidation test – a) SEM micrograph of investigated area; b) Ni; c) Al; d) O; e) Hf; f) Zr

Zr increases the oxidation resistance of modified coatings. The hypothesis is that Zr limits the release of protective oxide during cooling, suppressing the formation of Kirkendall's voids at the interface. According to the Kirkendall mechanism, the selective oxidation of Al causes a depleted area of this element to the oxide-metal interface, which induces opposite atomic flows: the Ni present in this area diffuse to the superalloy and while the Al diffuse to this depleted area. Since Ni is characterized by a higher diffusion velocity than Al, reticulate vacations are generated which, by coalescence, form void in the oxide-metal interface, which reduce the adhesion of the scale. Figure 5.51-Figure 5.52 shows EDS spectra of NF2 and ZrF4 coatings; it is highlighted that in both cases

there is the presence of heavy element (reactive element) aggregates on the oxide-coating interface. In the case of NF2, the presence of Hf is observed, while ZrF4 also has Zr, confirming the interaction between this element and the diffusion of Al, Ni and O.

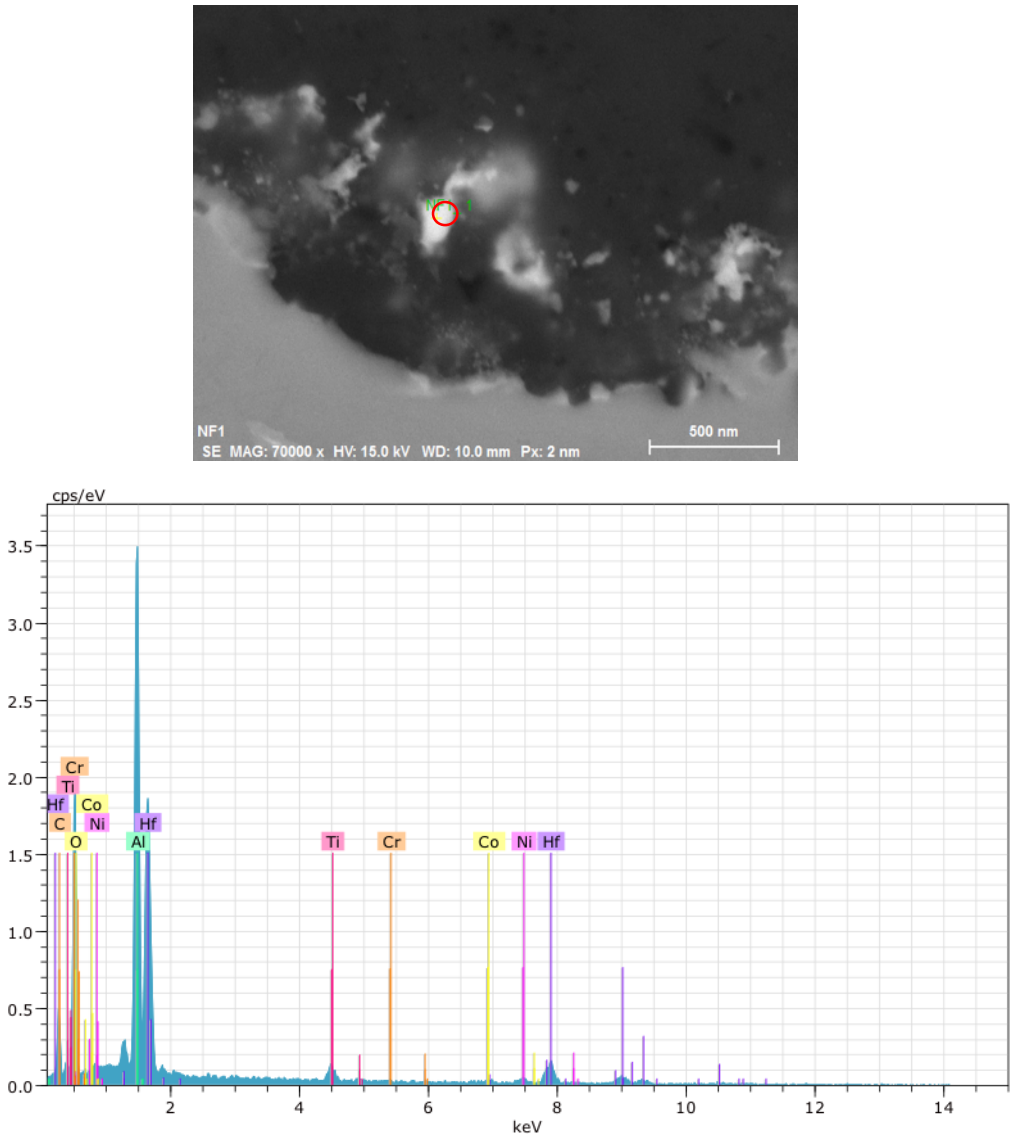

Figure 5.51: *EDS spot analysis on NF1 sample after 100h of oxidation. SEM micrograph of the investigated area*

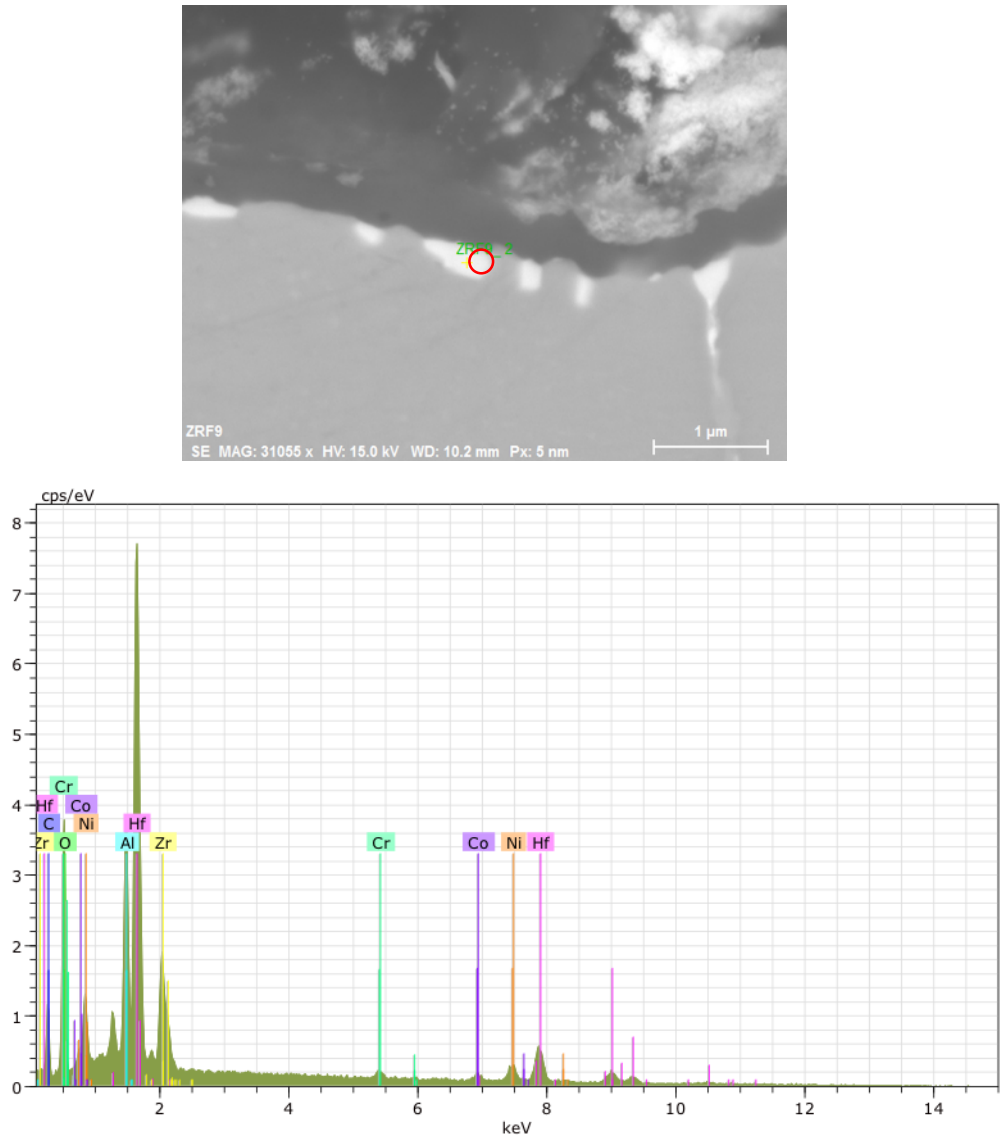

Figure 5.52: *EDS spot analysis on AlF1 sample after 100h of oxidation. SEM micrograph of the investigated area*

Figure 5.53 shows the surface structure evolution during oxidation for ZrF5 sample. XRD spectra confirm the results of the EDS maps. As it was seen for the standard coatings, after 50 hours of oxidation at high temperature, Hf and Ti diffuse trough the bond coat to the surface.

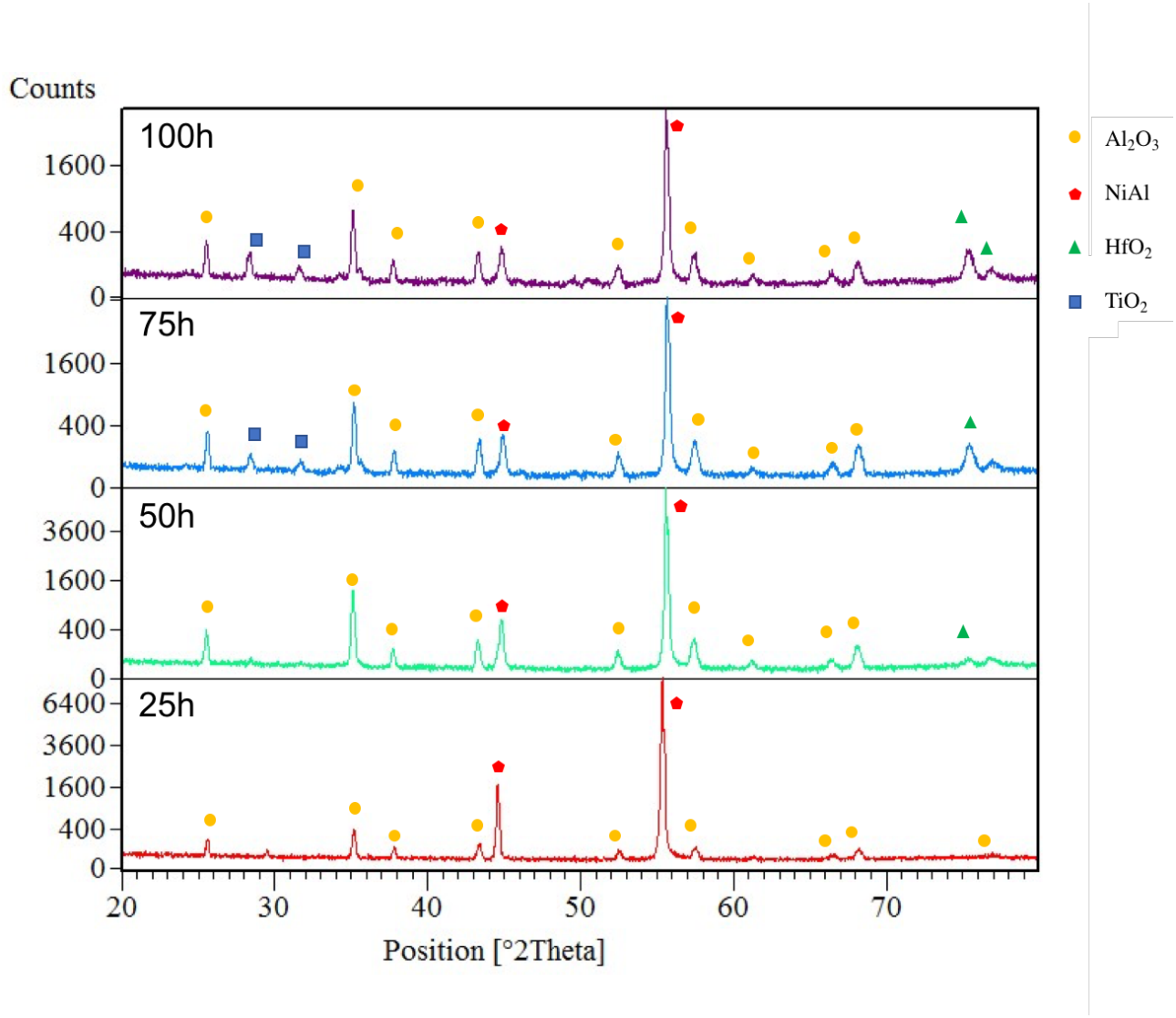

Figure 5.53: *XRD Surface structure evolution during oxidation for ZrF5 sample: after 25h (red spectrum), 50 h (green spectrum), 75h (blue spectrum) and 105h (purple spectrum)*

As it was seen for standard diffusion coatings previously tested, surface micrographs show the presence of cavities on the oxide layer generated during cooling. Figure 5.54 shows the presence of cracked and discontinuous oxide.

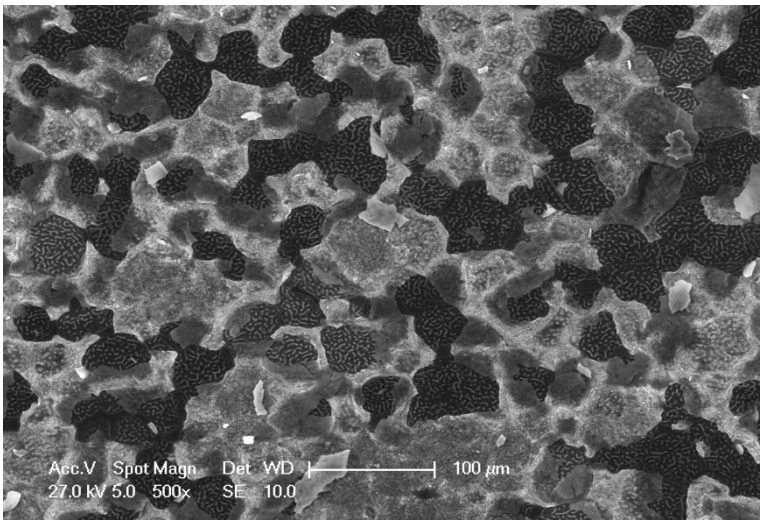

Figure 5.54: *SEM micrograph of a cavity on the ZrF5 coating*

Also in the case of Zr-doped coatings, the oxidation process allows these cavities to close. Figure 5.55 shows the change in the surface appearance of the ZrF coating at 25-hour oxidation intervals.

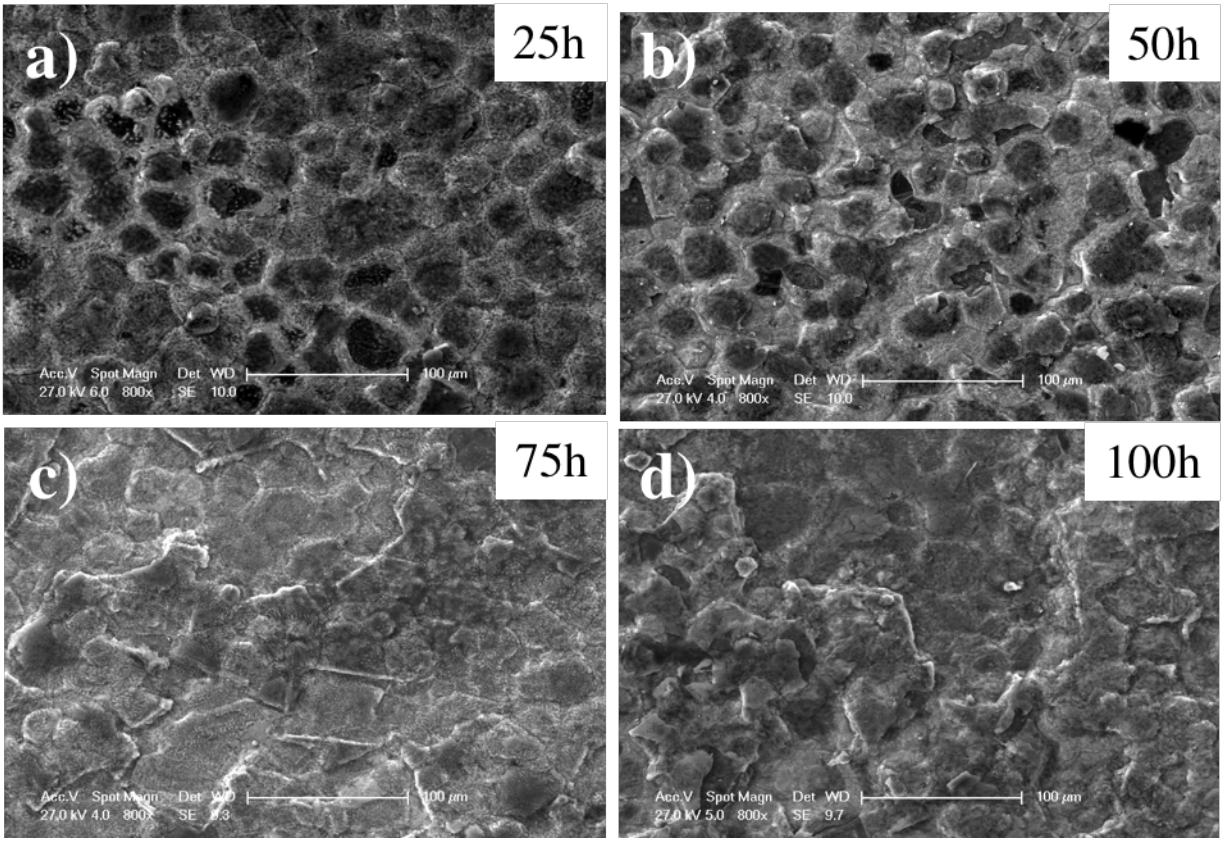

Figure 5.55: *Surface micrographs of the ZrF5 coating after oxidation at 1050 ° C: a) appearance after 25 hours; b) after 50 hours; c) after 75 hours; d) after 105 hours.*

During oxidation tests, modified coatings show the oxidation resistance depending by the activator salts concentrations (Figure 5.56).

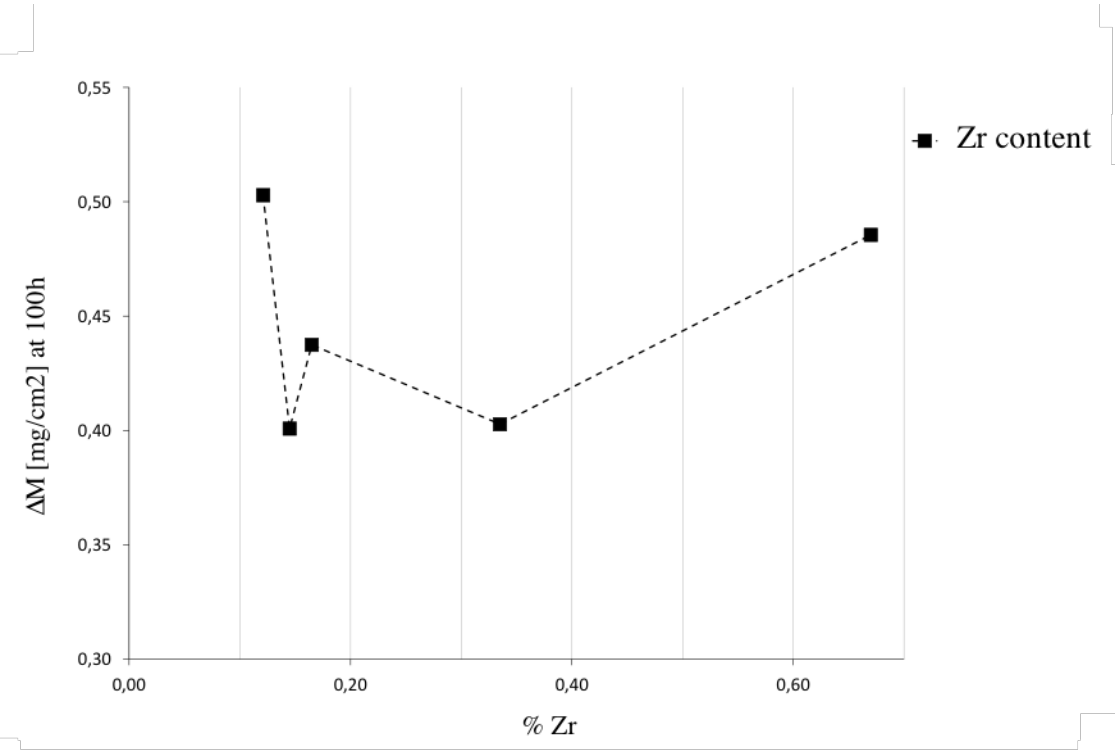

Figure 5.56: *Weight gain in oxidation tests as a function of Zr content for modified aluminide coatings*

Thus, a range of concentrations has been identified within which the addition of Zr improves the performance of the standard coating. For concentrations lower than the optimum values, the effects generated by the presence of the reactive element are invalid or minimal; in fact, the ZrF1 coating has the same performance as NF2. For addition above the optimum values, the oxidation rate increases as the reactive element reactor formed oxides allow a faster diffusion of the oxygen into the bulk and / or determine heterogeneous interfaces within the oxide scale where the diffusion velocity of the oxygen can be higher. The ZrF2, ZrF3 and ZrF4 coatings have a kP parabolic constants of magnitude smaller than ZrF1 and ZrF5.

5.1.8 Oxidation kinetic

Also for Zr-doped coatings a regression of experimental data was made with the models of Wagner and Monceau. The regressions obtained are shown in Figure 5.57-Figure 5.66.

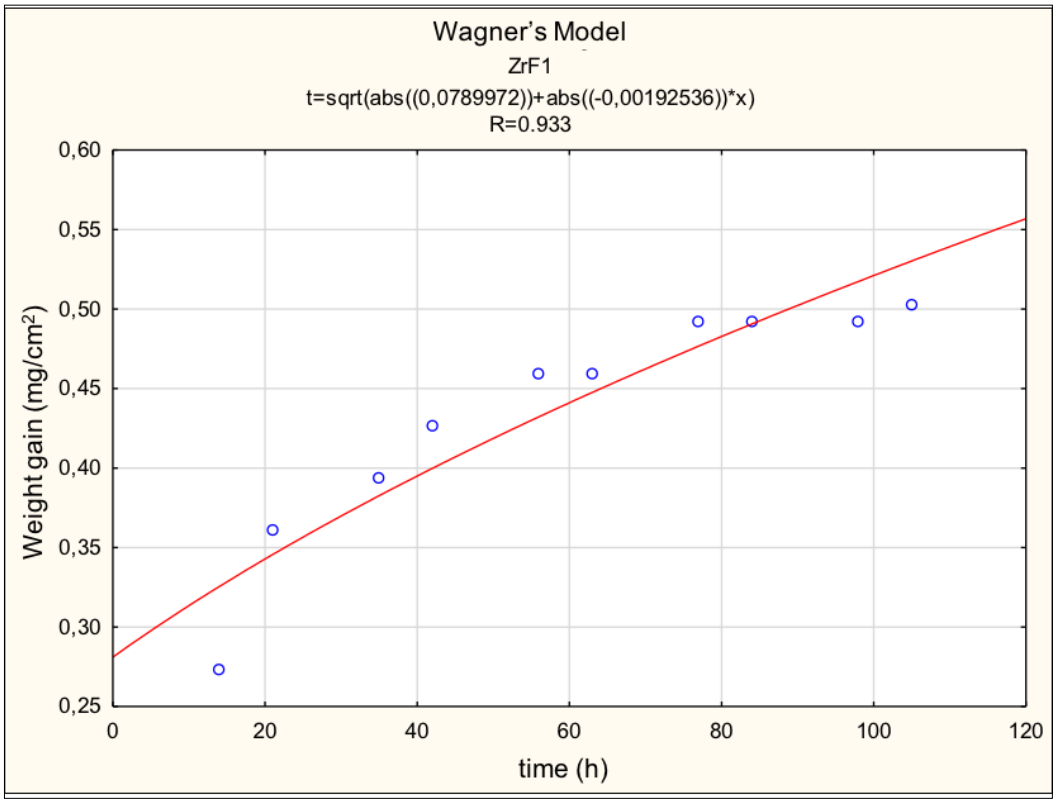

Figure 5.57: *Sample ZrF1 – oxidation kinetic, regression with Wagner's parabolic model*

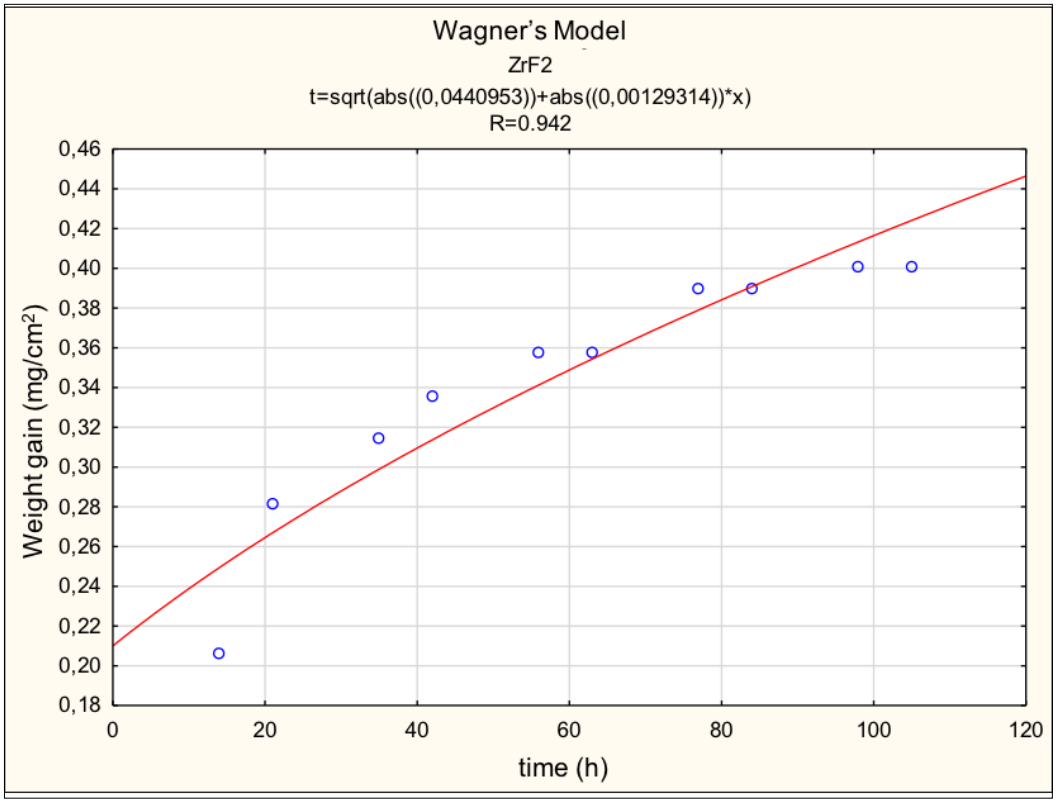

Figure 5.58: *Sample ZrF2 – oxidation kinetic, regression with Wagner's parabolic model*

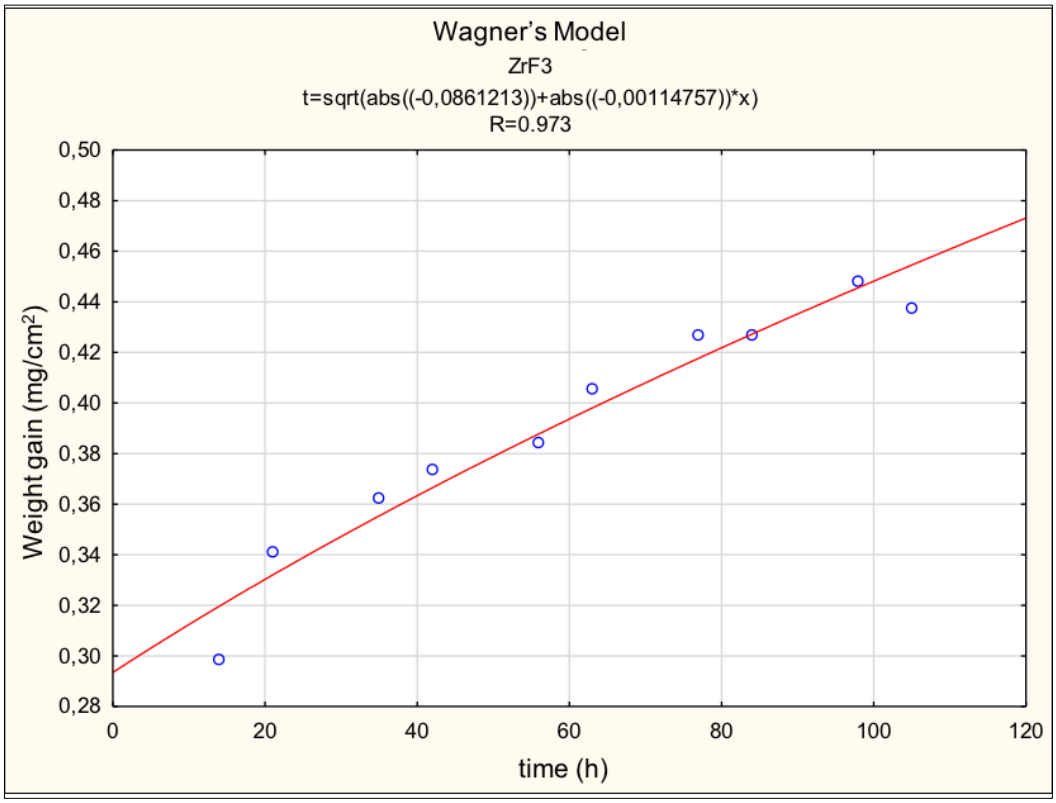

Figure 5.59: *Sample ZrF3 – oxidation kinetic, regression with Wagner's parabolic model*

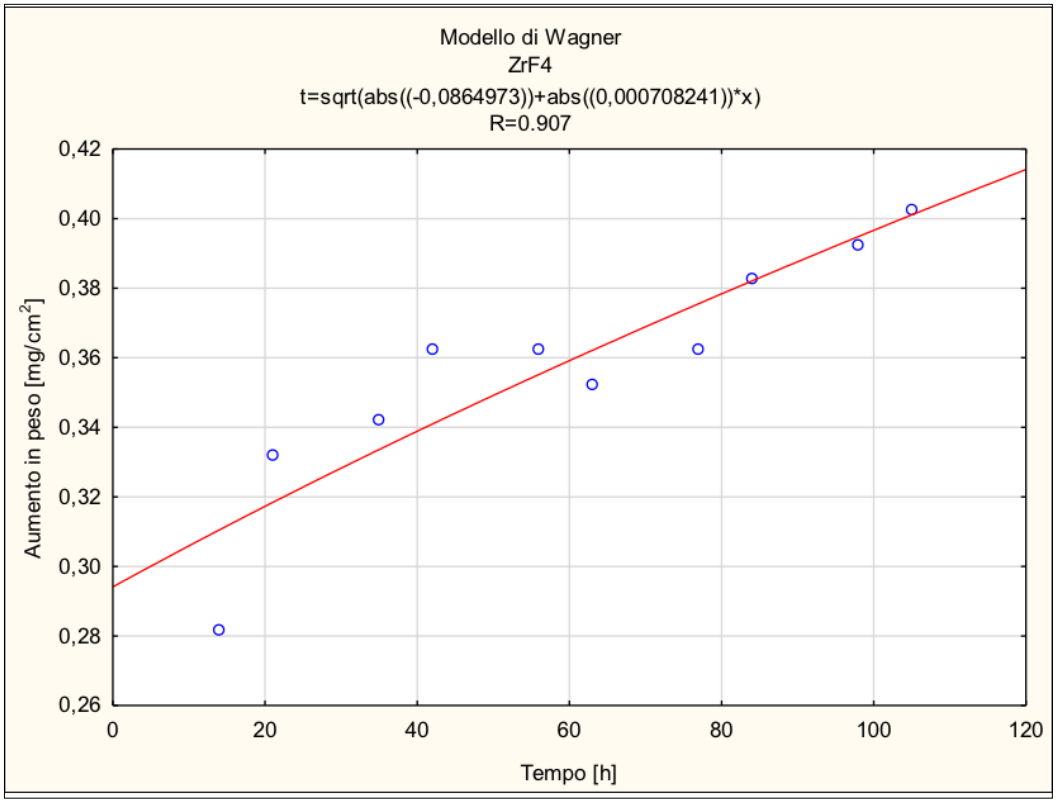

Figure 5.60: *Sample ZrF4 – oxidation kinetic, regression with Wagner's parabolic model*

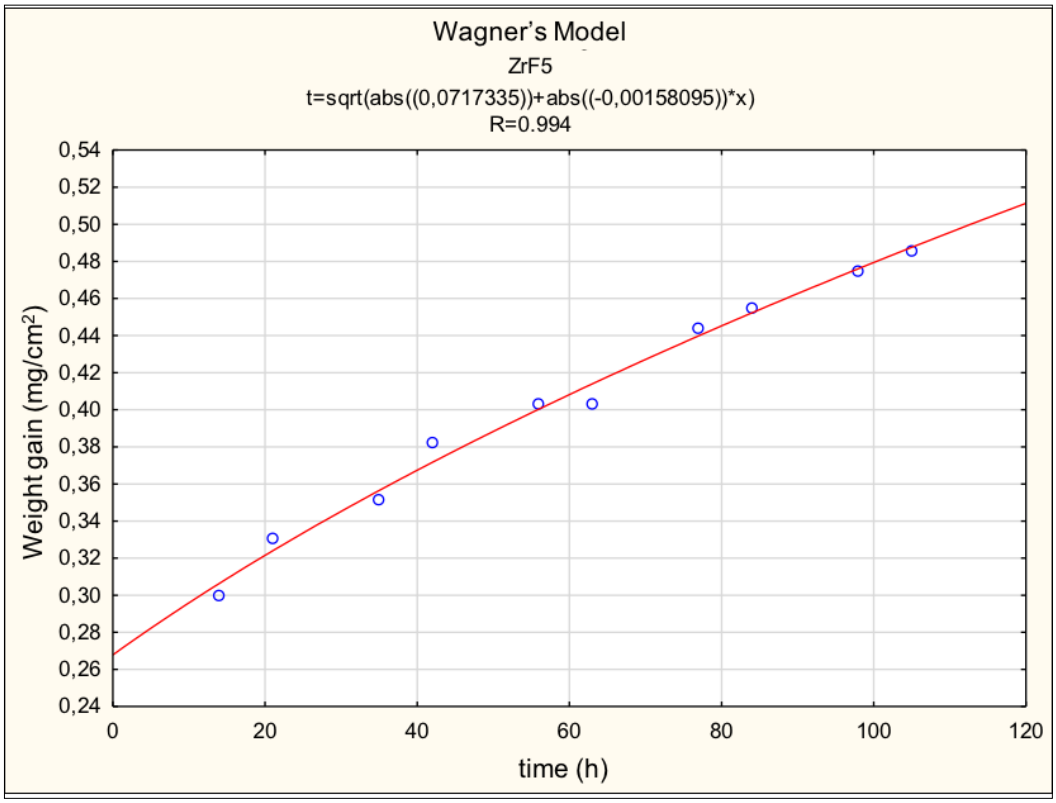

Figure 5.61: *Sample ZrF5 – oxidation kinetic, regression with Wagner's parabolic model*

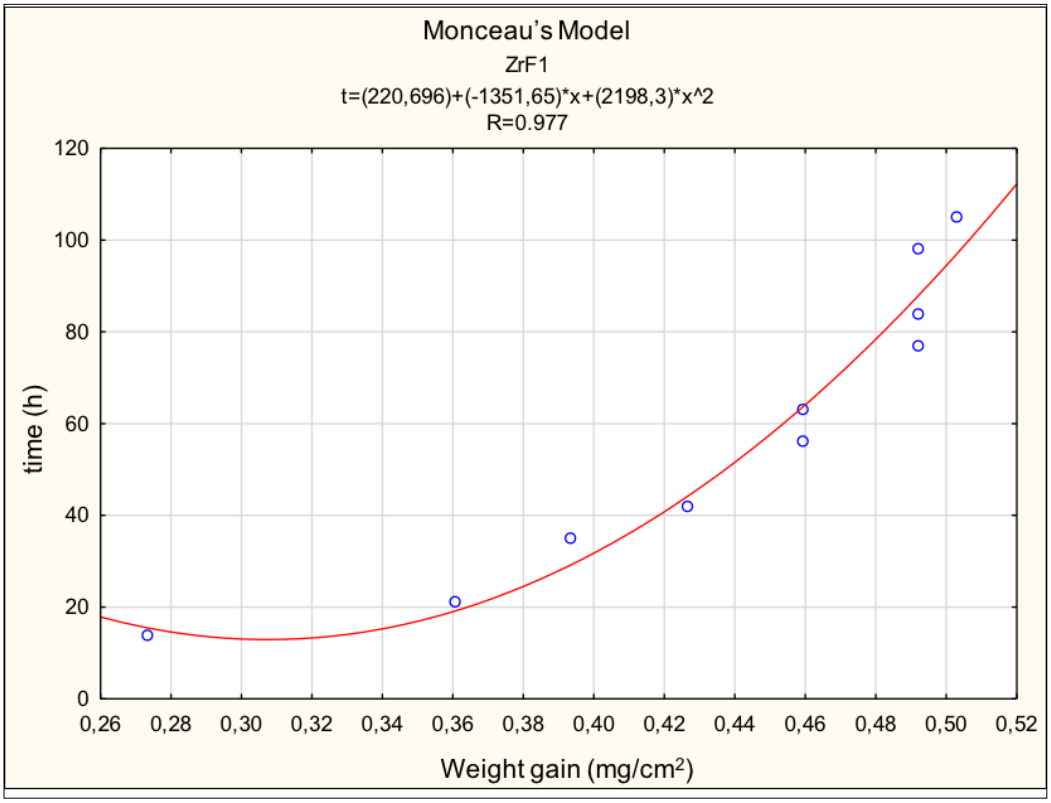

Figure 5.62: *Sample ZrF1 – oxidation kinetic, regression with Monceau's parabolic model*

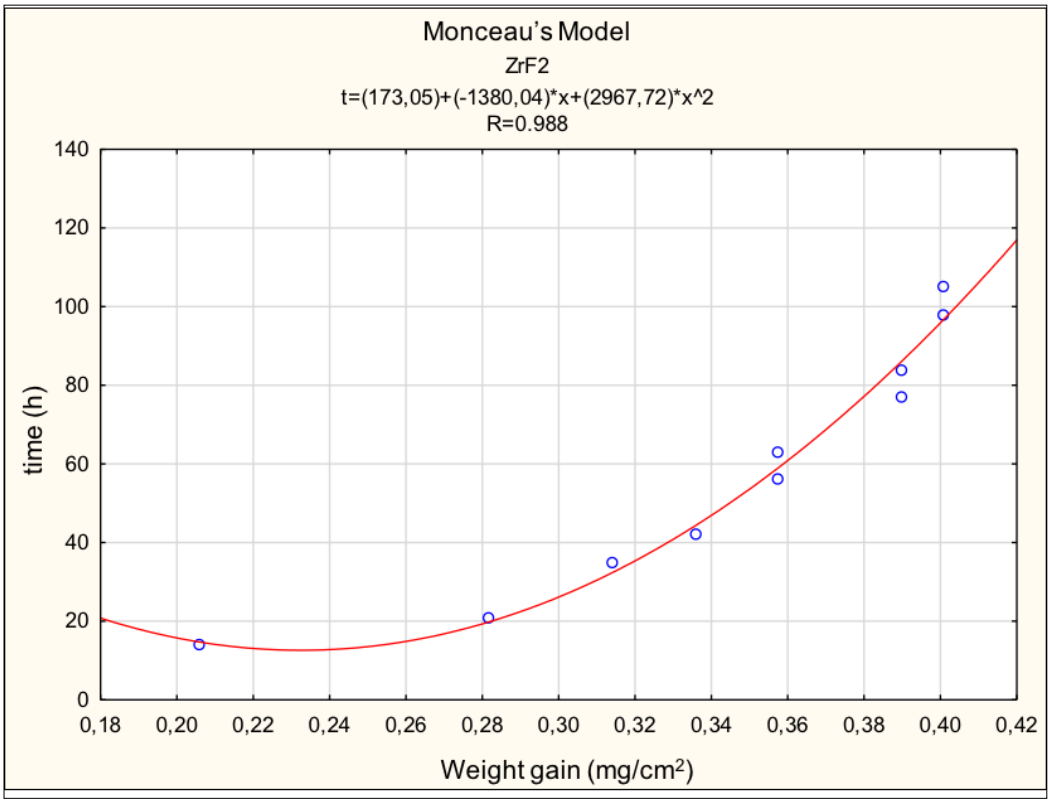

Figure 5.63: *Sample ZrF2 – oxidation kinetic, regression with Monceau's parabolic model*

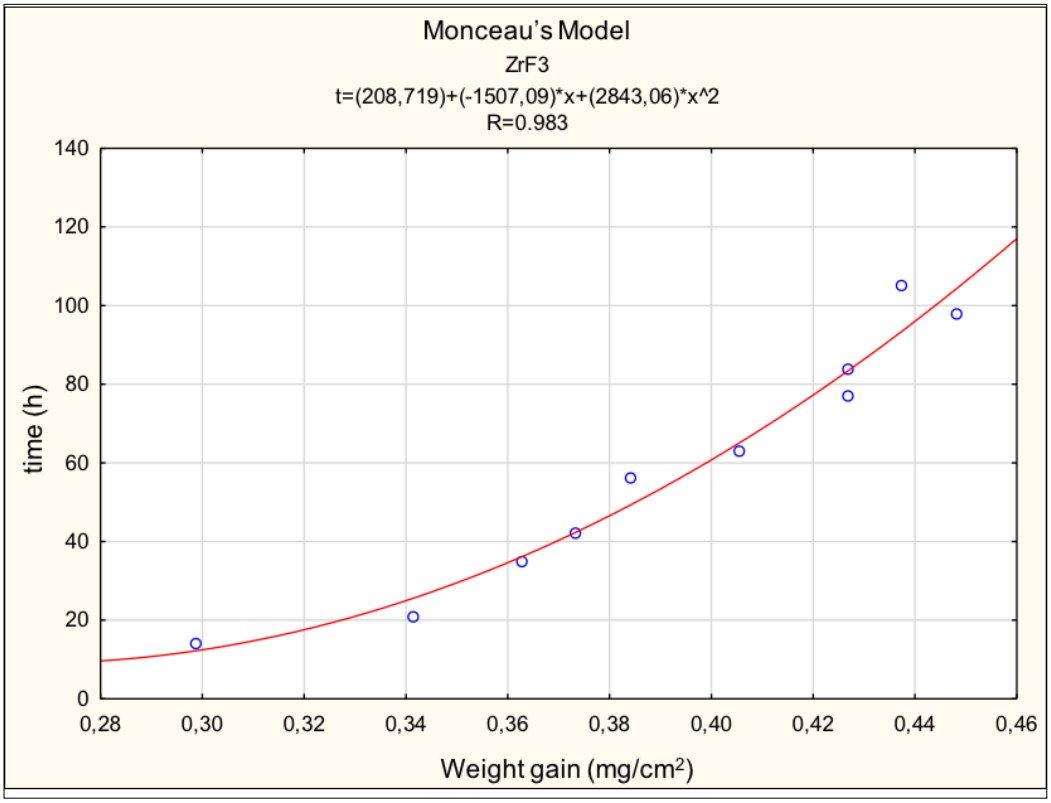

Figure 5.64: *Sample ZrF3 – oxidation kinetic, regression with Monceau's parabolic model*

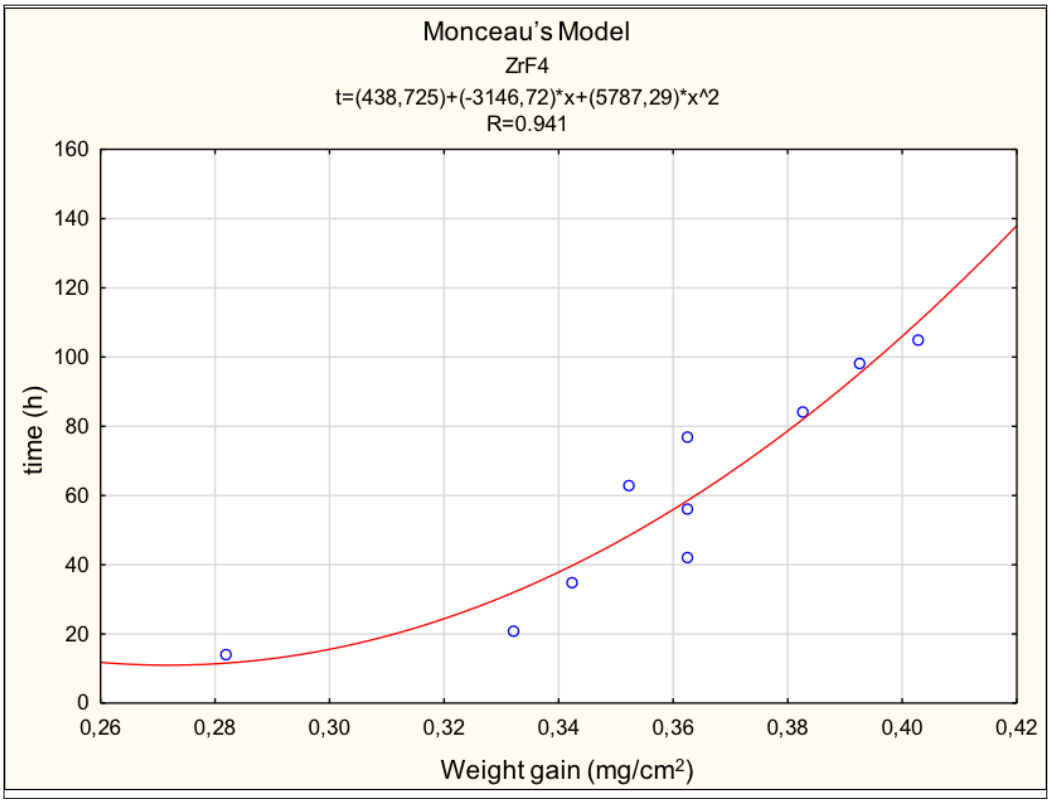

Figure 5.65: *Sample ZrF4 – oxidation kinetic, regression with Monceau's parabolic model*

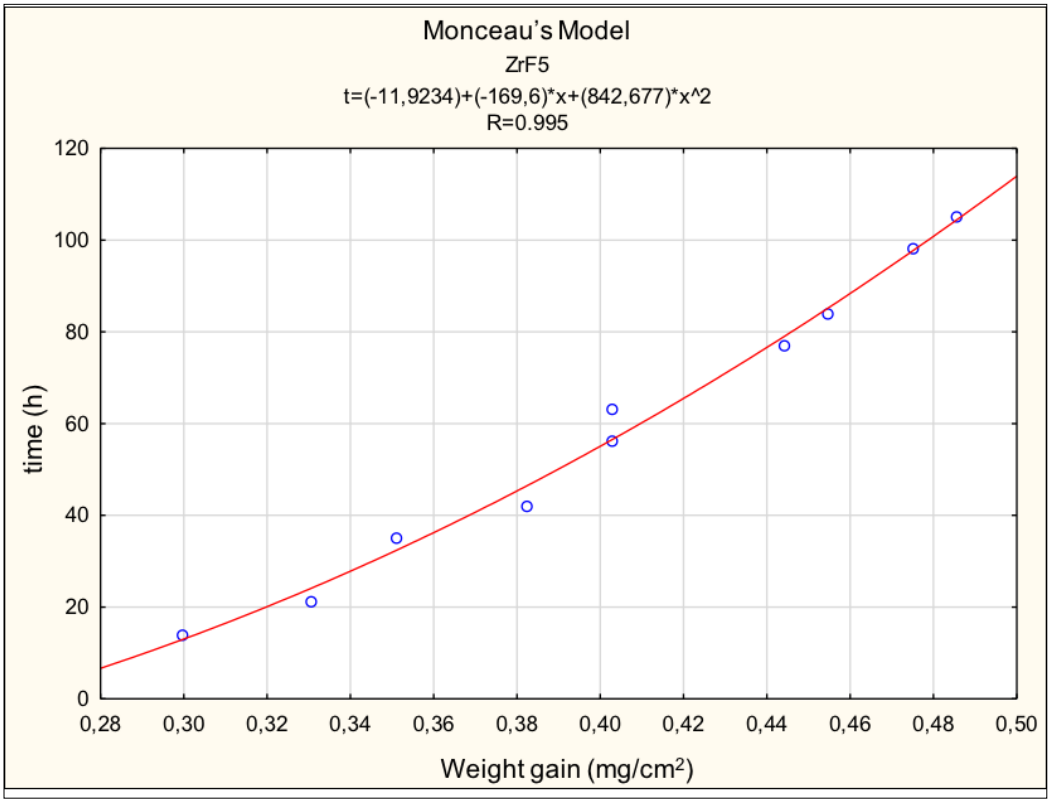

Figure 5.66: *Sample ZrF5 – oxidation kinetic, regression with Monceau's parabolic model*

To effectively compare the two models, Figure 5.67- Figure 5.71 show regressions with Monceau parabolic model with inverted axes.

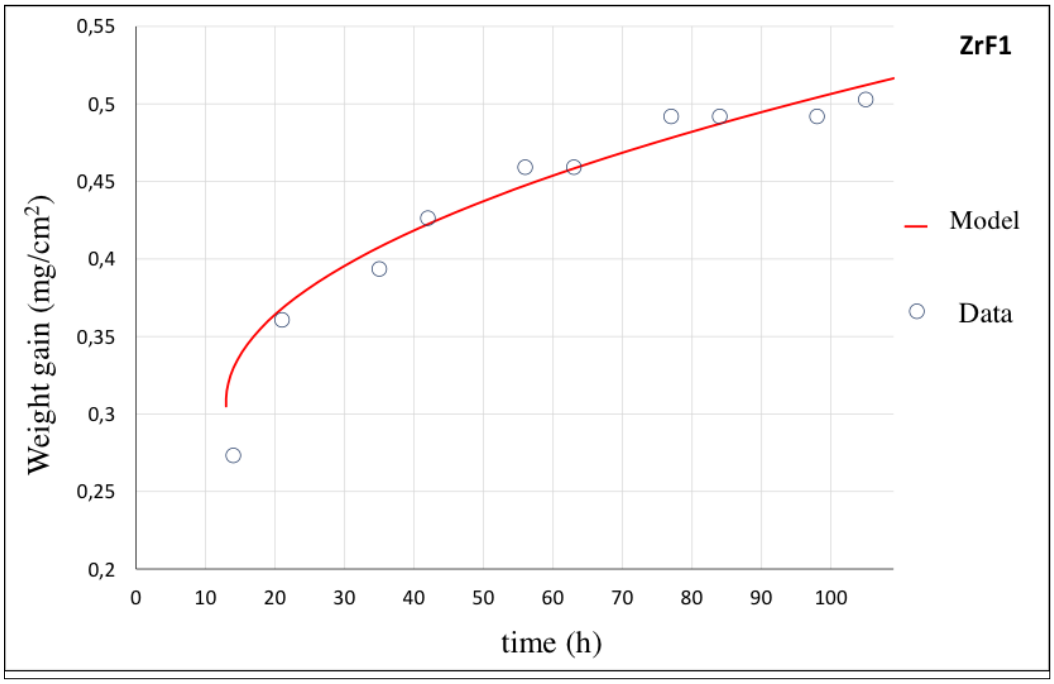

***Figure 5.67: Sample** ZrF1 – oxidation kinetic, regression with Monceau's parabolic model with inverted axes*

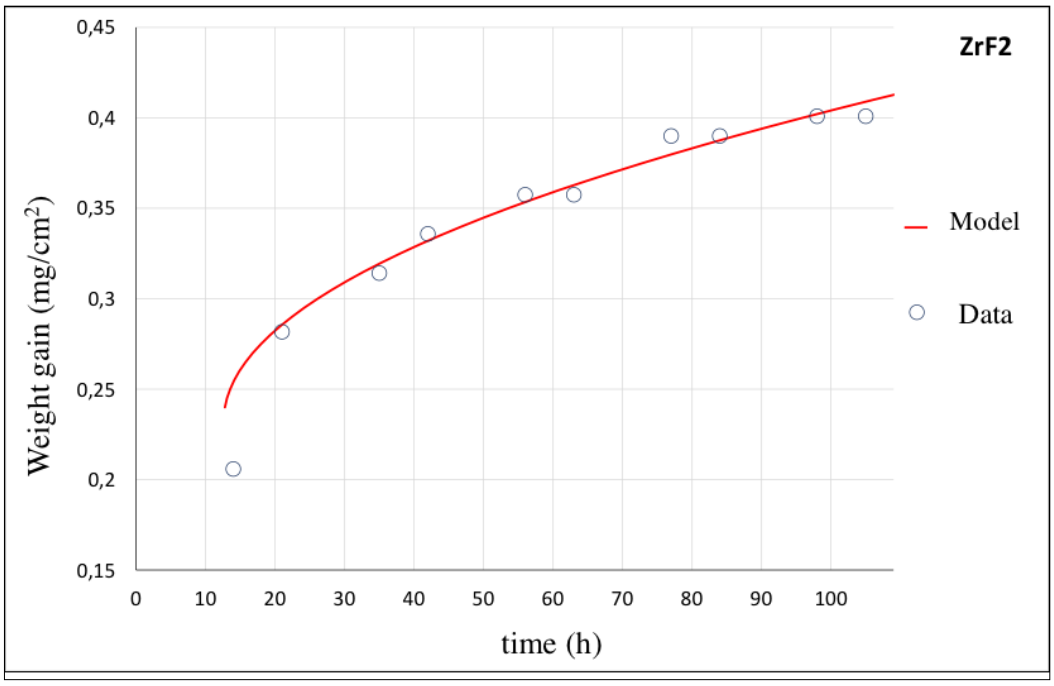

***Figure 5.68:** Sample ZrF2 – oxidation kinetic, regression with Monceau's parabolic model with inverted axes*

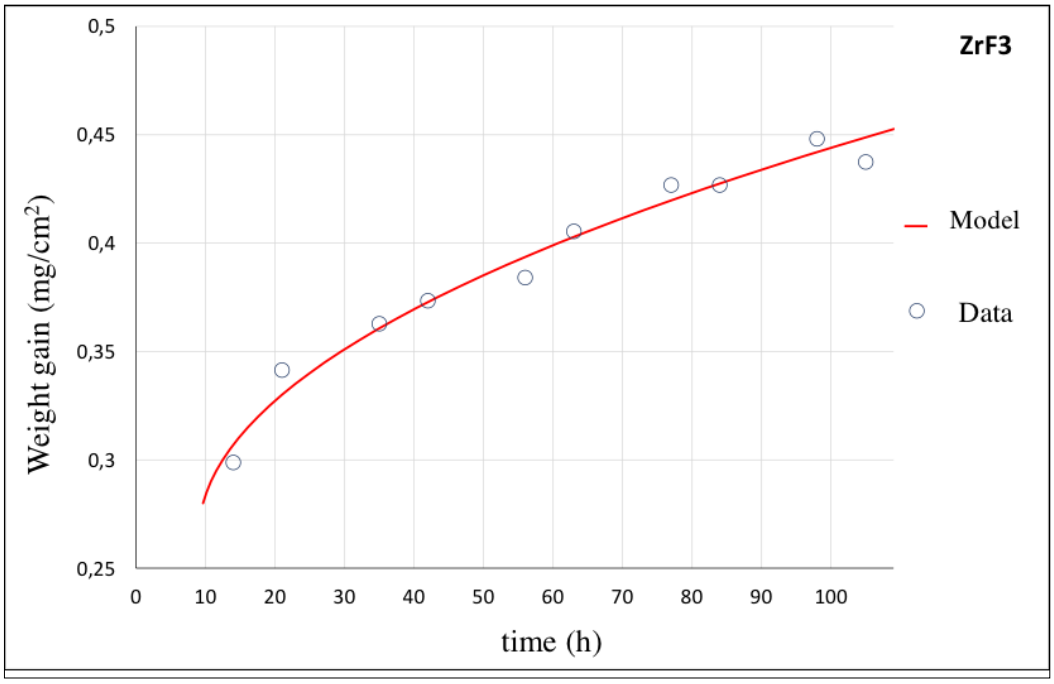

Figure 5.69: *Sample ZrF3 – oxidation kinetic, regression with Monceau's parabolic model with inverted axes*

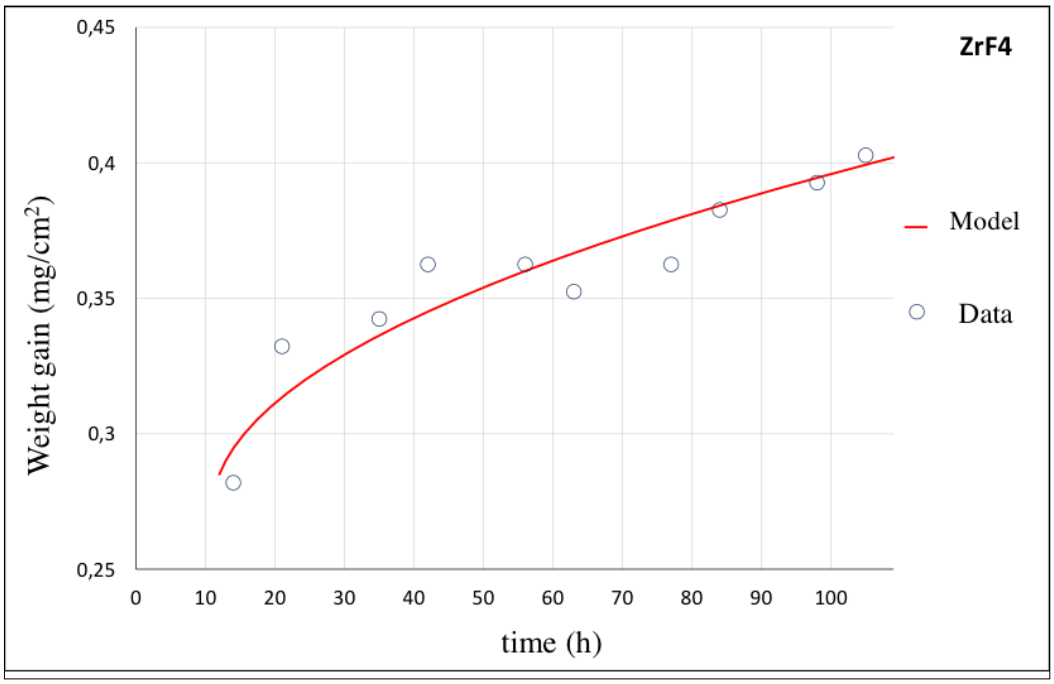

Figure 5.70: *Sample ZrF4 – oxidation kinetic, regression with Monceau's parabolic model with inverted axes*

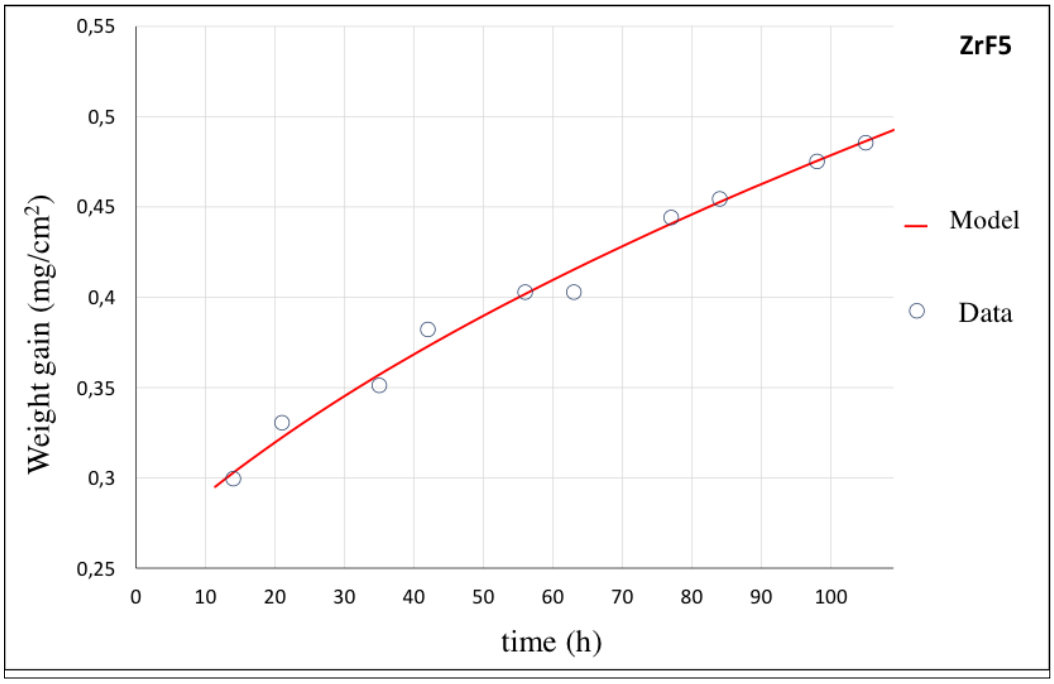

Figure 5.71: *Sample ZrF5 – oxidation kinetic, regression with Monceau's parabolic model with inverted axes*

The regression curves obtained with both models have R correlation coefficients greater than 0.9; however, for each data set, Monceau's parabolic model is characterized by greater R than the Wagner model, and therefore it is more appropriate to describe the experimental data. Table 5.6 shows the parabolic constants extrapolated from the Monceau's model. For completeness, k_P is compared with the NF2 sample.

Table 5.6: *Parabolic constants growth for the samples of the series ZrF compared with the NF2 sample*

Deposition	k_P [mg^2/s]	R^2
NF2	3.69×10^{-8}	0.91
ZrF1	1.26×10^{-7}	0.95
ZrF2	9.35×10^{-8}	0.98
ZrF3	9.77×10^{-8}	0.97
ZrF4	4.79×10^{-8}	0.89
ZrF5	3.29×10^{-7}	0.99

The k_P calculated with this model roughly approximate the oxidation kinetics; it is noted that ZrF2, ZrF3 and ZrF4 coatings have a parabolic constant growth rate of 10-^{8} mg2 / s, while ZrF1 and ZrF5

coatings, which have shown lower oxidation performance than these three, are characterized by a kP of the order of 10^{-7} mg2 / s. The growth constants of the three modified coatings with the best oxidation performance are of the same order of magnitude, meaning that oxygen permeates the oxide scale at the same speed.

5.1.9 Hot corrosion

Samples were subjected to hot corrosion tests at 900 ° C, as described in Section 4.4.1. Besides the five coatings produced was also included in the test a sample of the substrate, to verify the difference in terms of useful life of the guaranteed by aluminides component as done for the standard coatings. Even in the case of doped coatings, significant weight loss is observed after 100 hours of hot corrosion. This is definitely due to the fact that the amount of salt is added as a refill every 14-hour cycle, as described in the paragraph (reference). This creates a very corrosive environment that allows to make predictions on the durability of coatings in less extended time.

Figure 5.72 shows the result of the test for the first 100h. The weight gain, as expected, is similar to the standard coatings because reactive element doping doesn't influence positively but neither negatively the corrosion resistance.

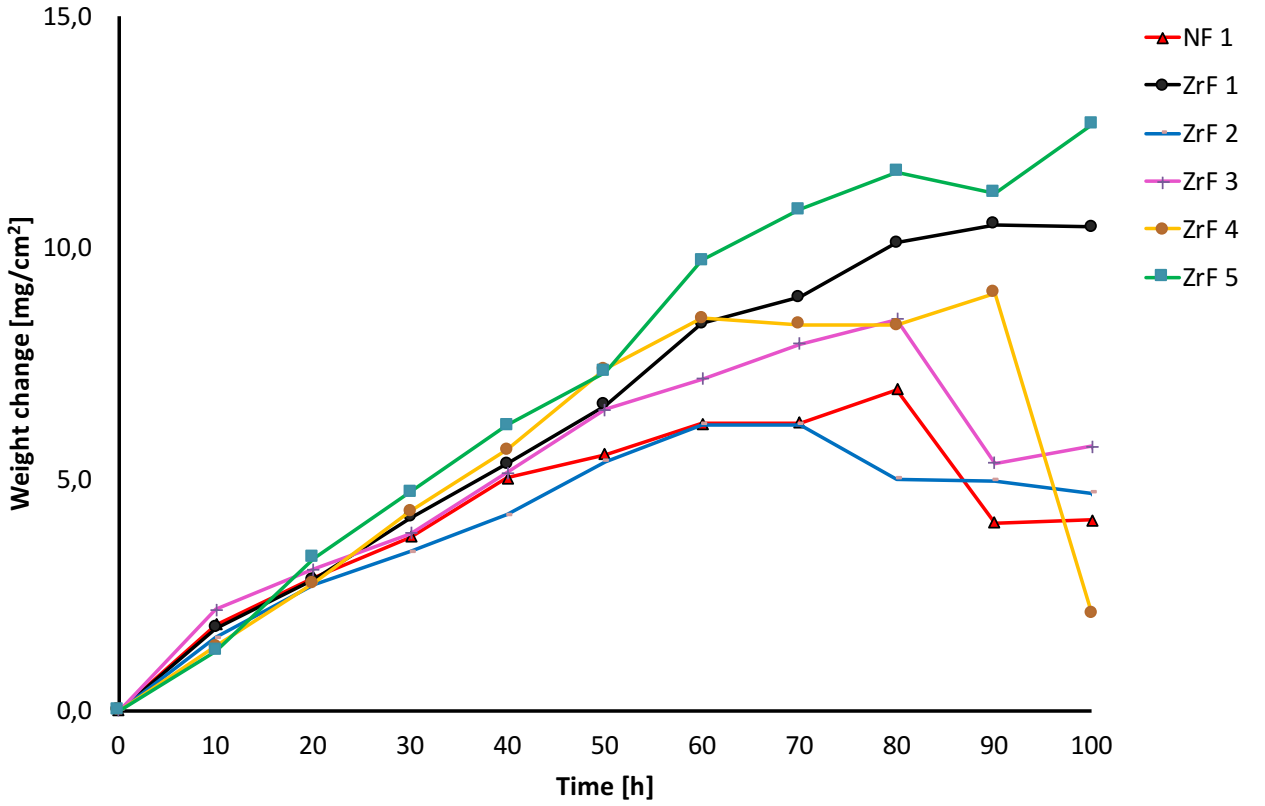

Figure 5.72: *Hot corrosion test for sample of the ZrF series; to compare the results with phase 1, the results for NF1 were added*

5.2 Phase 2: Electroless pure nickel plating

The results of the phase 2 are presented in this section. The aim was to obtain an external pure nickel layer by electroless nickel plating technique. SEM analysis were carried out by a FEG-SEM ZEISS (Carl Zeiss Microscopy, Oberkochen, Germany) Auriga 405 Scanning Electron Microscope coupled with its energy dispersive spectrometer. Samples were mounted in epoxy resin, cut and polished with SiC papers and diamond suspension up to 1 μm.

X-Ray diffractometry (XRD) was performed with a Philips X'Pert device (PANalytical B.V., Almelo, The Netherlands) on the samples in order to analyze the phase structure and the purity of the coatings after deposition. The XRD device operated at 40 KV and 40 mA with CuKα_1 radiation ($\lambda_{K\alpha1}$ = 1.540598 Å, $\lambda_{K\alpha2}$= 1.544426 Å) with a scan range of 30-80° (2θ), step size of 0.02° and counting time of 2 sec.

The formation of the nickel complex was studied by Fourier-transform infrared (FTIR) analyses and carried out with a Bruker Vertex 70 spectrometer (Bruker Optik GmbH) equipped with a single reflection Diamond ATR cell. The ATR-FTIR spectra were recorded with 256 scans in the mid infrared range (400–4000 cm^{-1}) at a resolution of 4 cm^{-1}.

5.2.1 Solution A

Chemical composition of solution A is reported in Table 5.7

Table 5.7: *Chemical composition for solution A*

		g/l (mol(l)
Nickel acetate	$Ni(OCOCH_3)_2$	21,2 (0,08)
Hydrazine	N_2H_4	20,02 (0,4)
Na_2EDTA	Na_2EDTA	5,62 (0,016)
Lactic acid	$C_3H_6O_3$	13,5 (0,15)
Sodium hydroxide	NaOH	9,87 (0,247)

Starting from the solution A, a highly stressed coating was produced that tends to detach, especially near the edges of the sample, as can be seen in Figure 5.73 and as reported by the SEM micrograph in Figure 4.2 .

Figure 5.73: *As-coated sample plated with the solution A*

Following the analysis of the cross-section, we measured the thickness of the coating, in the order of 5 μm, obtained with 1 h of deposition.

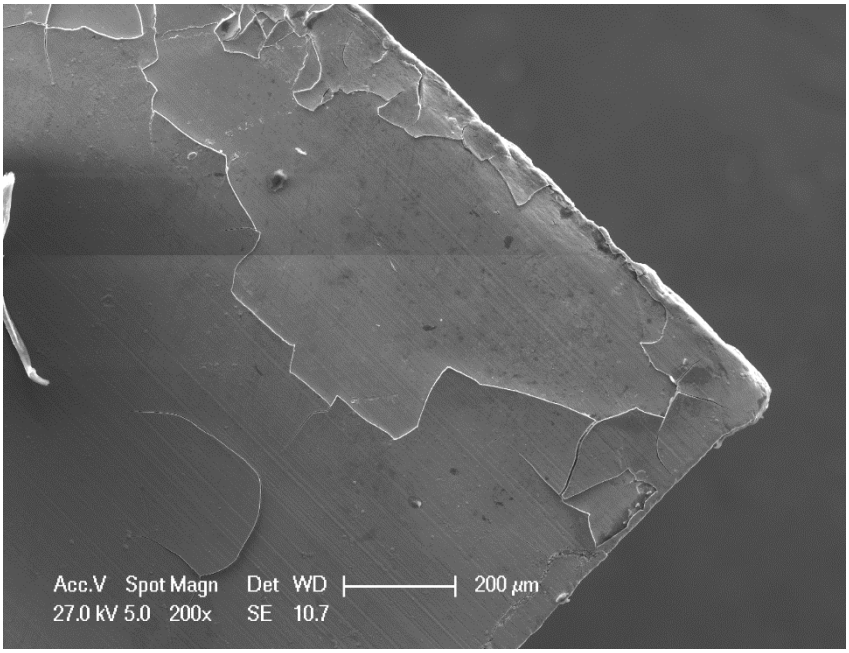

Figure 5.74: *Top-view SEM micrographs of a sample plated with the solution A*

Also, as shown in Figure 5.74, there are some cracks that pass through the thickness of the sample and porosity to the metal-coating interface, a sign of poor adhesion and detachment following the polishing process.

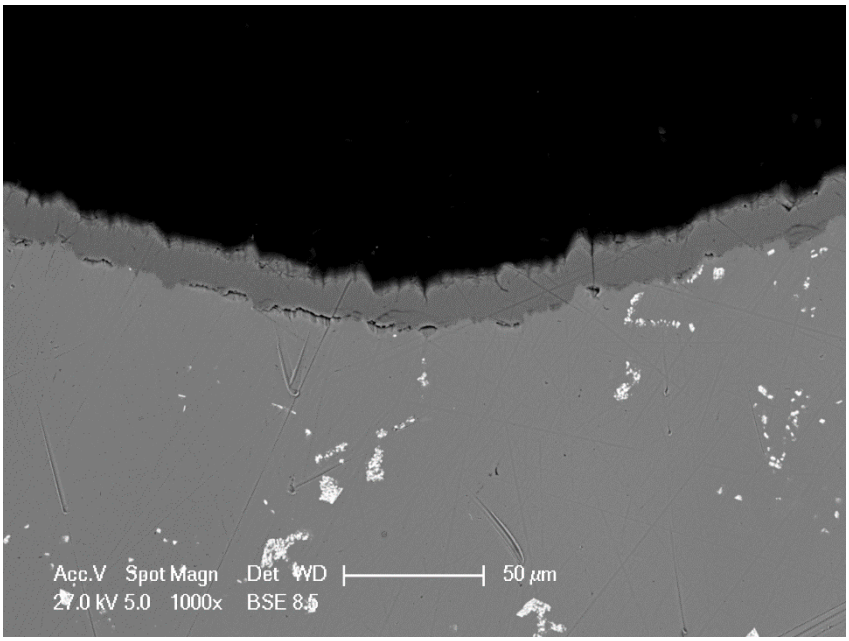

Figure 5.75: *Cross-section micrograph for a sample obtained with the solution A*

Considering the poor adherence of the coating, reagent concentrations were varied to obtain a more adherent and less stressed coating: at first the amount of NaOH was increased so as to increase the pH of the solution to a value of 9.2. In contrast to what was reported in the literature, the increase in pH did not increase deposition rate but rather a decrease in this. Thus, the degree of Ni^{2+} ions complexation was varied by acting on the concentrations of the complexes so as to decrease the nickel reduction rate with the aim of decreasing the internal stress. In fact, considering the complexes present in excess of nickel, the free Ni^{2+} ions concentration can be obtained from the nickel complexation equilibrium:

$$Ni^{2+} + EDTA \leftrightarrow NiEDTA$$

with a stability constant given by:

$$K_{Ni-EDTA} = \frac{[Ni - EDTA]}{[Ni^{2+}][EDTA]}$$

Thus, the concentrations of Ni^{2+} ions are:

$$[Ni^{2+}] = \frac{[NiEDTA]}{K_{NiEDTA}[EDTA]} = \frac{[Ni^{2+}]_0}{1 + K_{NiEDTA}[EDTA]}$$

Where $[Ni^{2+}]_0$ is the initial concentration of nickel ions, which can be considered as the concentration of nickel salt dissolved in the solution. Having in the solution two distinct complexes, four different trials of 2.5 h were performed, each with a molar concentration of the complexes increased by 15 wt% or 30 wt%. Table 4.2 shows all changes to the starting solution. Variations in the concentration of the reagents of the solution did not produce appreciable results from the point of view of the

internal stresses: the coatings continue to exhibit detached areas as well as poor adhesion as can be seen in Figure 5.76.

Table 5.8: *Experimental matrix for the solution A. "PN_A" stands for "Pure Nickel_solution A"*

Samples	Nichel acetate [mol/l]	Hydrazina [mol/l]	Na2EDTA [mol/l]	Lactic acid [mol/l]	NaOH [mol/L]	Deposition rate [$\mu m/h$]
PN_A_03	0,12	0,4	0,016	0,15	0,18	5 ±0,43
PN_A_10	-	-	-	-	0,24	4 ±0,47
PN_A_13	-	-	-	0,172 (+15%)	0,24	4.54 ±0.51
PN_A_14	-	-	-	0,195 (+30%)	0,24	-
PN_A_15	-	-	0,018 (+15%)	-	0,24	2.9 ±0.54
PN_A_16	-	-	0,021 (+30%)	-	0,24	-
PN_A_03	0,12	0,4	0,016	0,15	0,18	5 ±0,43

The depositions carried out with a higher complexing increases did not produce coatings suitable: the solution with + 30% of lactic acid has produced a very porous coating, while the prepared solution with + 30% Na_2EDTA is precipitated after 2 hours.

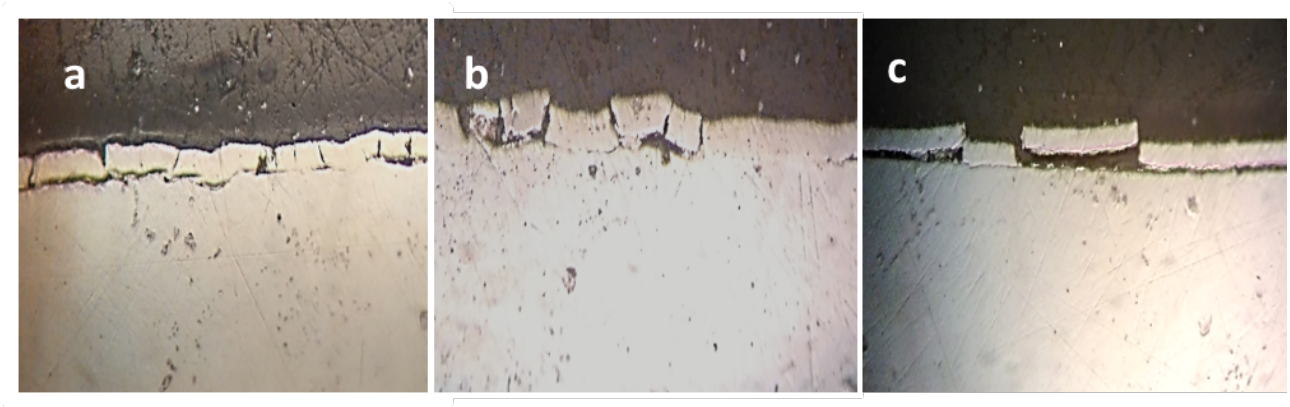

Figure 5.76: *Optical microscopy photographs for the sample of the series PN_A. All the variation has no lead to a good coating in terms of adhesion – a) PN_A_10; b) PN_A_13; c) PN_A_03*

The modifications made to the composition of the solution did not produce consistent improvements in coating quality. The production of stressed coatings, which is not homogeneous and porous with this particular composition, was also found in other papers available in literature [2]. It seems that the

production of these stressed coatings is due to the strategy of using a very strong complexing agent (EDTA) with a weaker one (lactic acid). Always according to Muench better results are obtained by adopting a single complexing agent from the constant of intermediate stability between EDTA and lactic acid.

5.2.2 Solution B

Solution B provides the use of only one complexing agent which at the same time also acts as a reducing agent: the bath composition is reported in Table 5.9. The coatings obtained with solution B showed excellent adhesion and absence of internal stresses and higher deposition rate than in case of solution A. It was possible to produce coatings up to 20 μm with 2 hours of deposition with no impurities.

Table 5.9: *Chemical composition for solution A*

		g/l (mol(l)
Nickel chloride	$NiCl_2$	23,76 (0,1)
Hydrazine	N_2H_4	32,56 (0,65)
Potassium carbonate	K_2CO_3	69,1 (0,5)
Potassium hydrogen carbonate	$KHCO_3$	45 (0,45)
Potassium phosphate	K_3HPO_4	87,1 (0,45)
Sodium hydroxide	KOH	9,78 (0,3)

According to the principle of electroless plating, Ni ions reacts in stoichiometric quantities with the reducting agent (hydrazine, in this case) by giving metallic nickel onto the autocatalytic surface. As already known[2], under alkaline conditions, hydrazine is a stronger reducting agent with a potential of 1.16 V (referring to the semiconducting cell reaction). This could lead, if the reactivity is not controlled, to the precipitation of $Ni(OH)_2$ and the consequent decomposition of the plating solution. Theoretically, the formation of the nickel complex allows to create an "in-situ redox reactor" where the Ni^{2+} ions and the hydrazine lie in the same molecular structure. This could be the way to obtain a controlled reduction of the nickel and to avoid the formation of products that can decompose the

plating solution. The crystal structure of the complex reveals that the Ni^{2+} ions are coordinated by three ligands of hydrazine carboxylate[3]. The hydrazine carboxylate coordinates the nickel ions in a chelating system with the atom of N and O represented by the bold curves in Figure 5.77 (the arcs structure is $N'H_2$-NH-COO). The presence of this high spin complex is confirmed by the peculiar blue color of the plating solution.

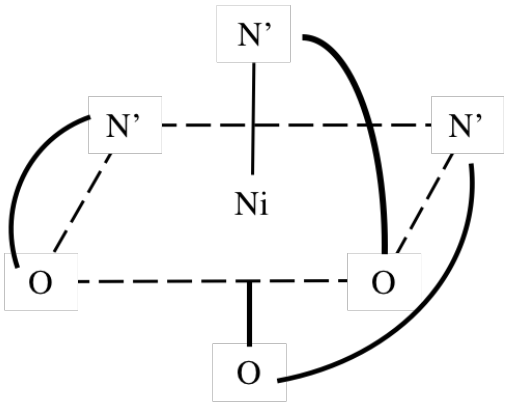

Figure 5.77: *Structure of tris(hydrazine carboxylato-N',O) nickelate(1-)[3]*

The formation of the nickel complex was confirmed by FTIR analysis. It is notable in Figure 5.78 that the presence of the water (dashed red line) does not allow to observe the characteristic peaks of the nickel complex, preventing its interpretation. For this reason, concentrated plating solution, prepared as described in the previous paragraph, was left in vacuum drying in order to obtain a solid. In Figure 5.78 is reported the FTIR spectrum (solid line) for the solid nickel complex salt.

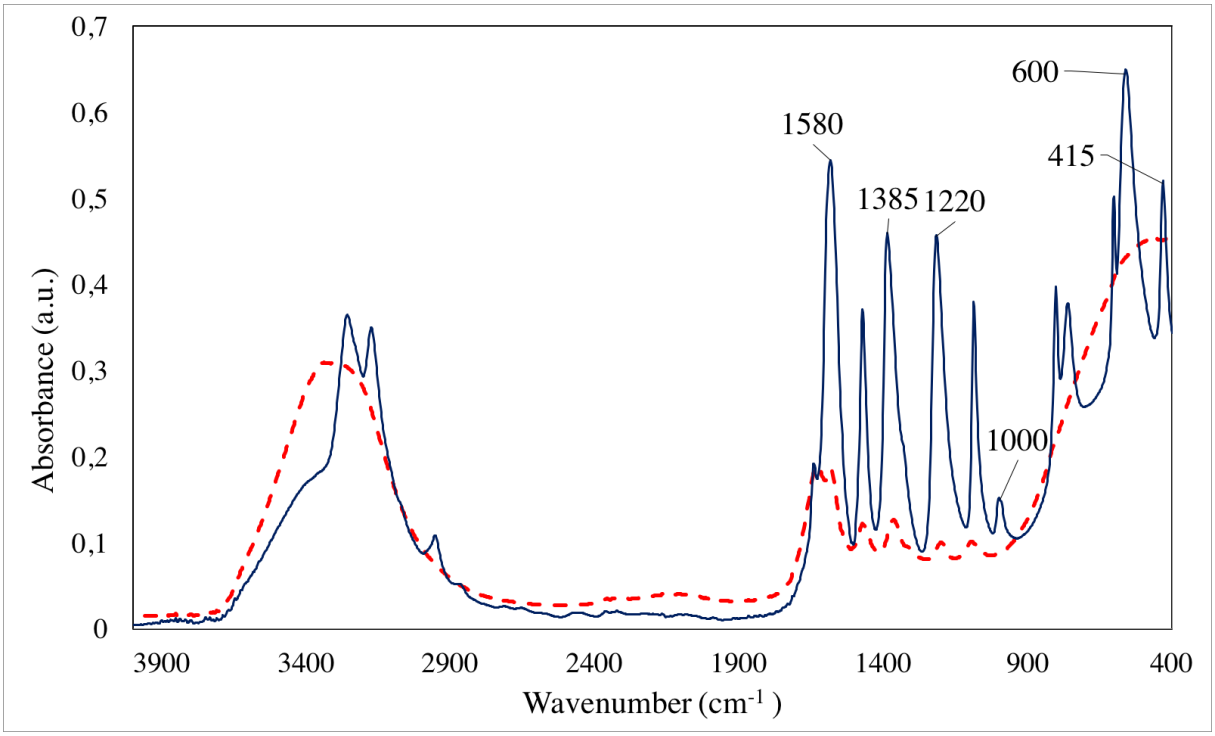

Figure 5.78: *FTIR spectrum of tris(hydrazine carboxylato-N',O) nickelate(1-) salt. Comparison between the water solution (dashed red line) and the precipitated salt (solid blue line)*

The stretching vibrational mode (N—N) of hydrazine is shifted to 1000 cm-1 because the hydrazine radical H2N'-NH- is attached to a conjugate system[3]. The presence of characteristic peaks, such as the Ni-N stretching (415 cm-1), the rocking vibration (600 cm-1) and the symmetric distortion of the ligands in the complex (region between 1000 and 1600 cm-1) are consistent with the values reported in earlier literature[4],[5],[6],[7]. The characteristic peaks for the nickel complex are listed in Table 5.10

Table 5.10: *Characteristic peaks for the nickel complex salt*

Assignment	Wavenumber (cm^{-1})
Stretching (N-H)	3335
Stretching (COO^-)	1385
Stretching (N_2H_3-)	1580
Rocking (N_2H_3-)	1220

Stretching (N-N)	1000
Rocking (N-N)	600

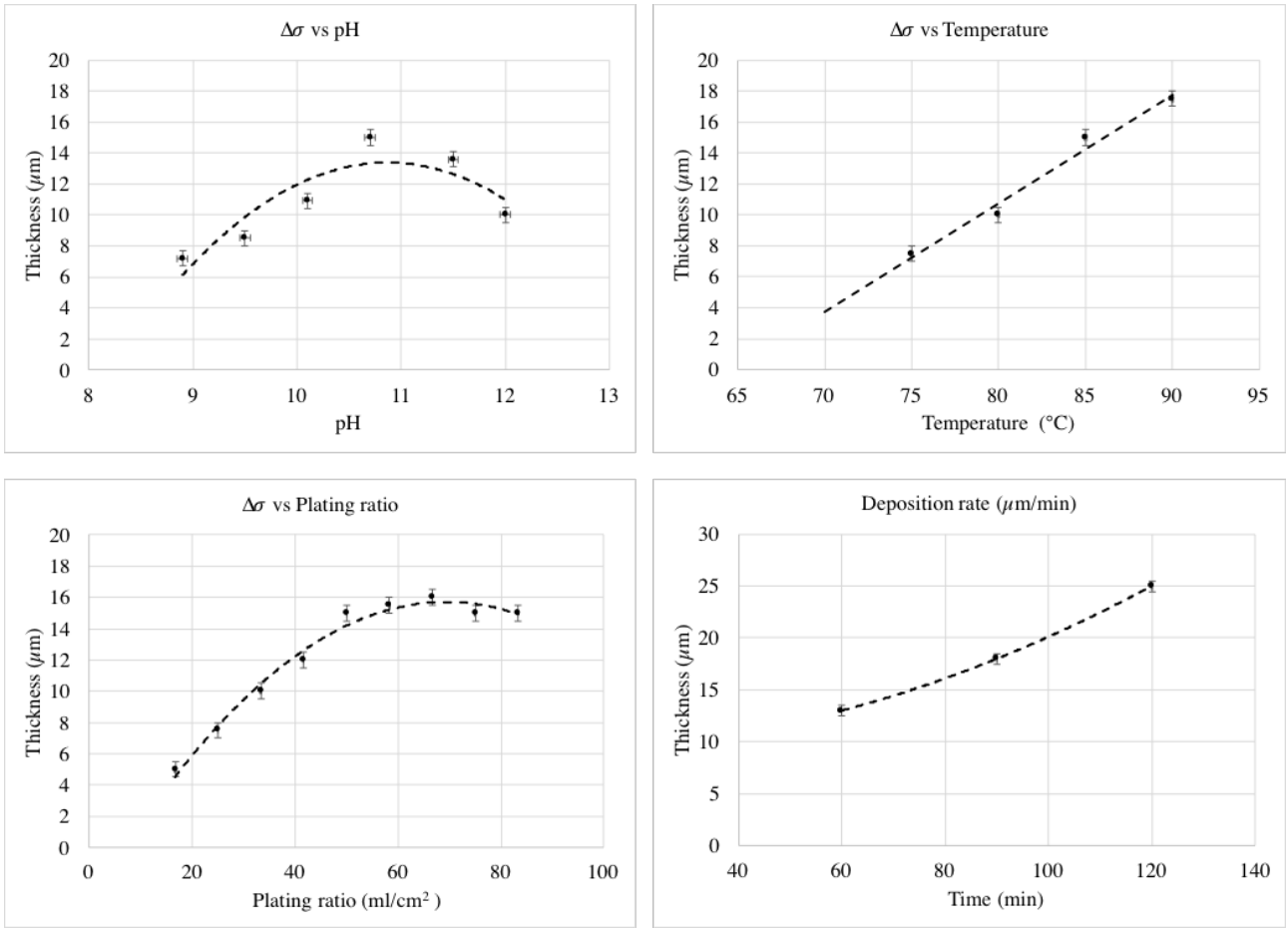

Figure 5.79: *Evaluation of thickness for different parameters: pH (a); temperature (b); plating ratio (c). Deposition rate for the best parameters (d)*

The formation of the complex nickel has allowed to control the deposition and to study the deposition rate. Three different plating parameters were investigated to optimize the plating rate (temperature, pH and plating ratio). pH was controlled by varying the quantity of KOH in the solution preparation and the chosen range was 9-12. Higher temperature value for the selected range (70-90°C) was chosen in order to avoid the concentration of the solution by the solvent evaporation. Plating ratio (PR) is referred to the quantity of solution per sample surface area (ml/cm^2). All the depositions were conducted with the same composition for the plating solution (except for pH investigations) and for the same time (60 min). As expected hydrazine reactivity is strongly influenced by the pH. Despite this, the results presented in Figure 5.79a show that after a pH of 11 the formation of $Ni(OH)_2$ is relevant and it prevents the reduction of nickel. Temperature influences the reduction of the nickel

not only in terms of deposition rate but also on the surface microstructure. In fact, after 85 °C the coating is thicker but the surface morphology is negatively affected. The fast and not controlled reduction of the nickel ions involves the formation of a porous coating. Finally, the quantity of nickel ions in terms of volume solution seems to have a negative influence just for small quantity of volume. This was predictable but the investigation of PR for a large quantity of plating solution shows that the surface has a catalytic role for the deposition as expected from the theory [8]. It was seen that after a threshold (60 ml/cm^2 for one sample) the plating solution is more efficient in terms of coating thickness by increasing the surface available for the deposition. The optimized parameters selected for the characterization analysis are presented in Table 5.11.

Table 5.11: *Optimized parameters for plating solution*

Parameters	Best value
pH	11
Temperature (°C)	85
Plating ratio (ml/cm^2)	50
Deposition rate (μm/60min)	15

The purity and the structure of the as-coated samples were analyzed by XRD (Figure 5.80). The only three peaks in the pattern can be indexed as the (1 1 1), (2 0 0) and (2 2 0) planes of the fcc cubic phase Ni with lattice constant a = 3.525 Å, which is comparable with the literature data (ICDD No. 04-0850, a = 3.524 Å). Furthermore, the relative intensity ratio for the face (1 1 1) to the face (2 0 0) is higher than the conventional value. This was already seen [9] as the consequence of a preferential orientation of the (1 1 1) crystallographic plane. XRD pattern does not reveal the presence of impurities such as nickel oxides or hydroxides and confirms that the deposition correctly allows to a metallic pure nickel coating.

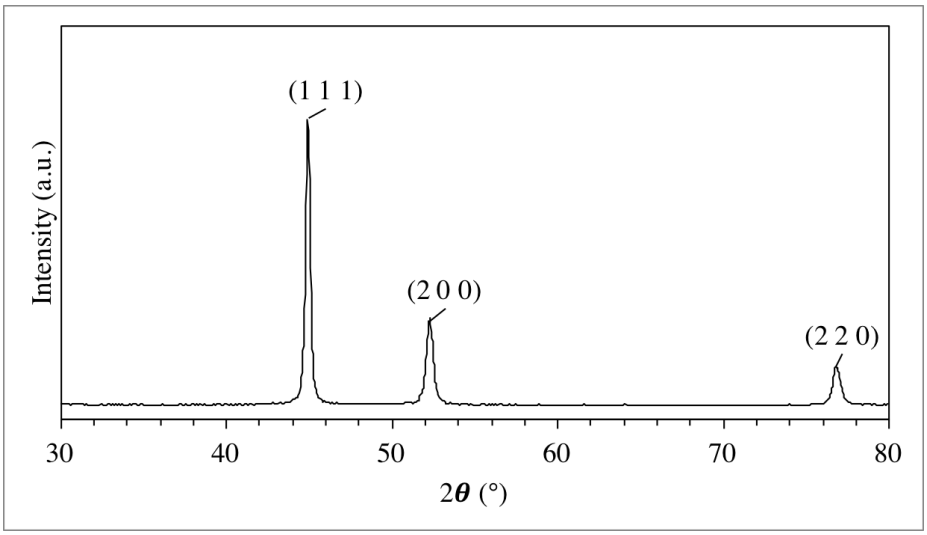

Figure 5.80: *XRD pattern of the electroless nickel coating.*

The surface microstructure was investigated by SEM analysis. Cross-section analysis has allowed to obtain the direct measurement of the thickness for each sample. Furthermore, as it is shown in Figure 5.81, the cross-section micrographies has revealed a good interface between the substrate and the coating. Typical top-view morphologies of nickel coating obtained by electroless plating is shown in Figure 5.82. The surface presents a hierarchical microstructure that goes from the cauliflower-like structure (Figure 5.82a,b), typical for the electroless coating [10], to a nanoarchitecture made by pine cone-like shape (Figure 5.82c,d) with an average diameters of 2 μm. Further SEM analysis at higher magnifications has revealed that this nickel flowers were made by nickel nano-spike with the average size of 150-200 nm.

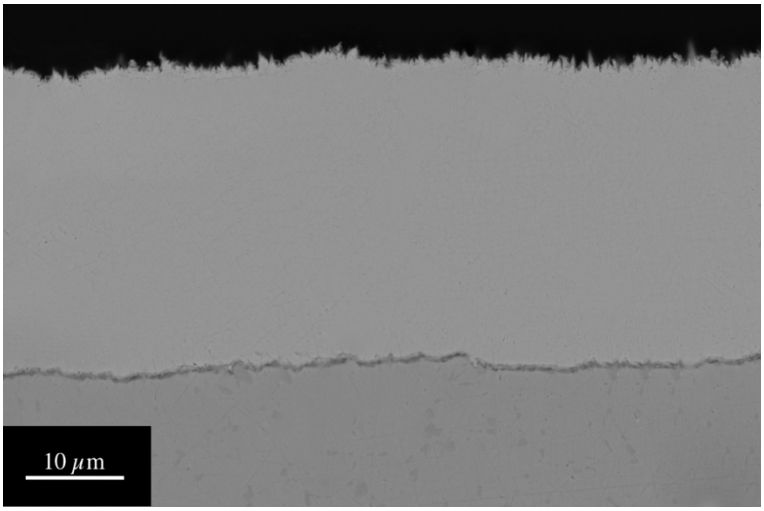

Figure 5.81: *Cross-section SEM micrograph of electroless pure nickel plating in 2 hours*

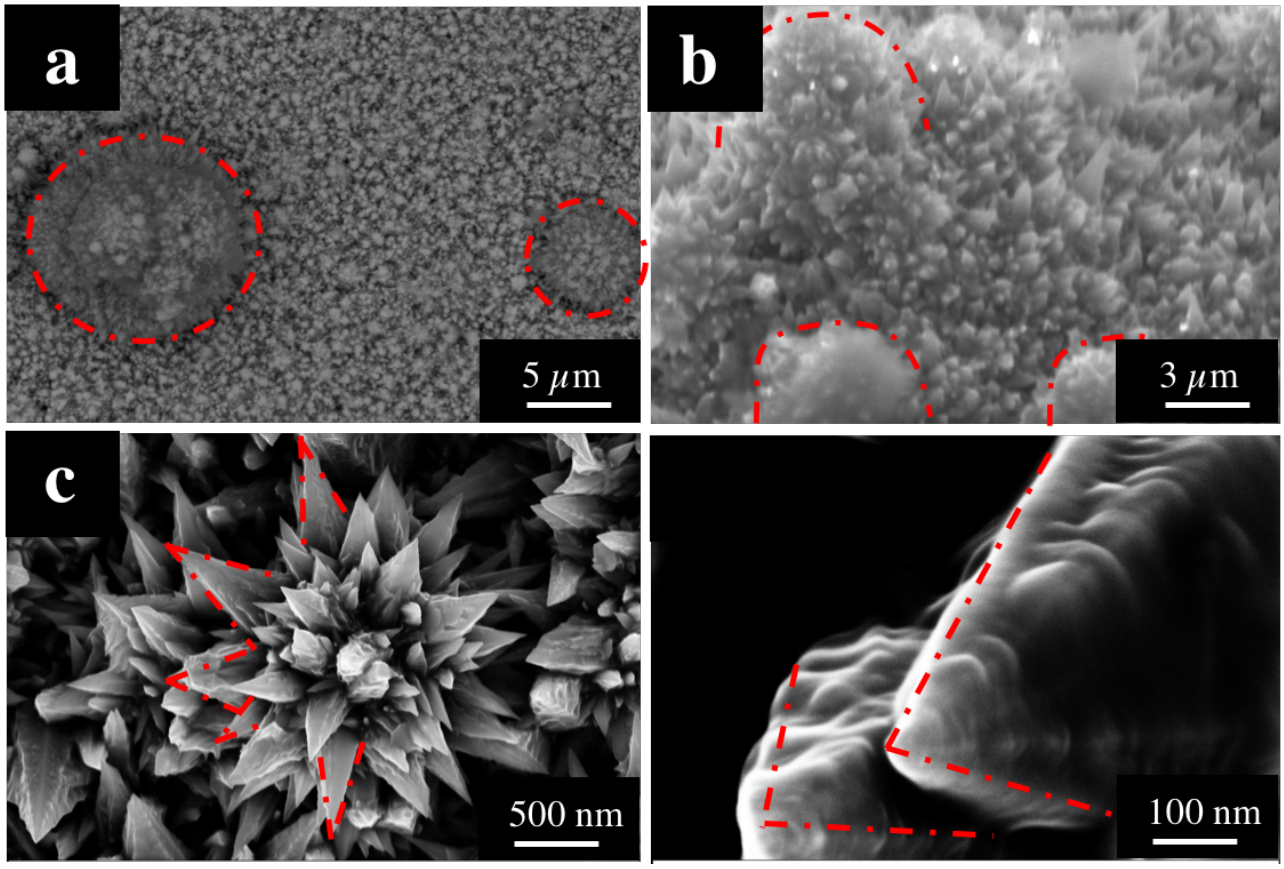

Figure 5.82: *Surface microstructure of as-coated electroless nickel with increasing magnification (from a to d).*

Specific tests were conducted in order to understand if the formation of this peculiar nano structure came from the first step of the reaction. Three different plating time (1 min, 5 min and 10 min) were studied to understand the growing mechanism of the coating. SEM micrographs have shown that for the first minute of reaction, nickel grows as domain onto the surface (Figure 5.83). It has been demonstrated [9] by combined HRTEM and SEAD analysis that the single nano-spike of nickel grows along the preferential orientation (1 1 1) of the nickel phase structure. So, theoretically, this should mean that the domains, formed in the first minute of the plating deposition, must have time to coalesce in a layer.

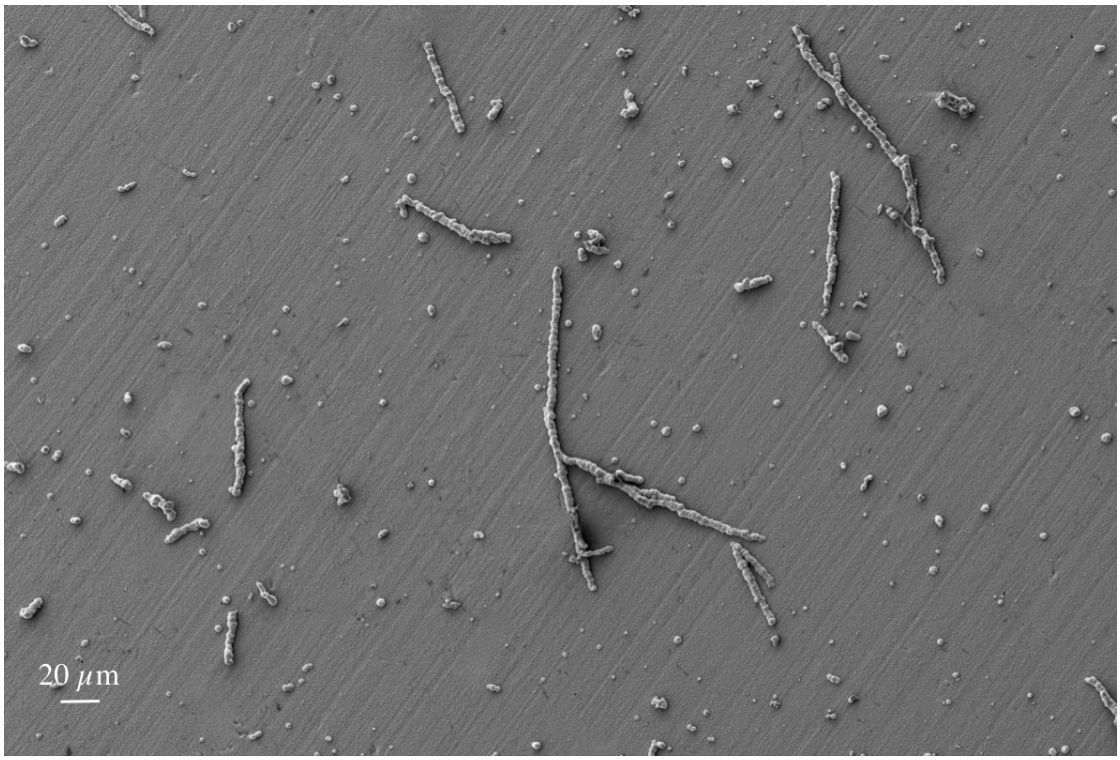

Figure 5.83: *SEM micrograph for a sample plating in 1 minute*

The microstructure for 2 and 5 minutes of plating deposition have confirmed this theory. As it is possible to see in Figure 5.84 the nano-spike are growing in the sense of the arrows to form the layer of the coating. The results obtained by the SEM analysis have allowed to confirm the theory of the growing mechanism as "nickel domain" already formulate in a previous work [11].

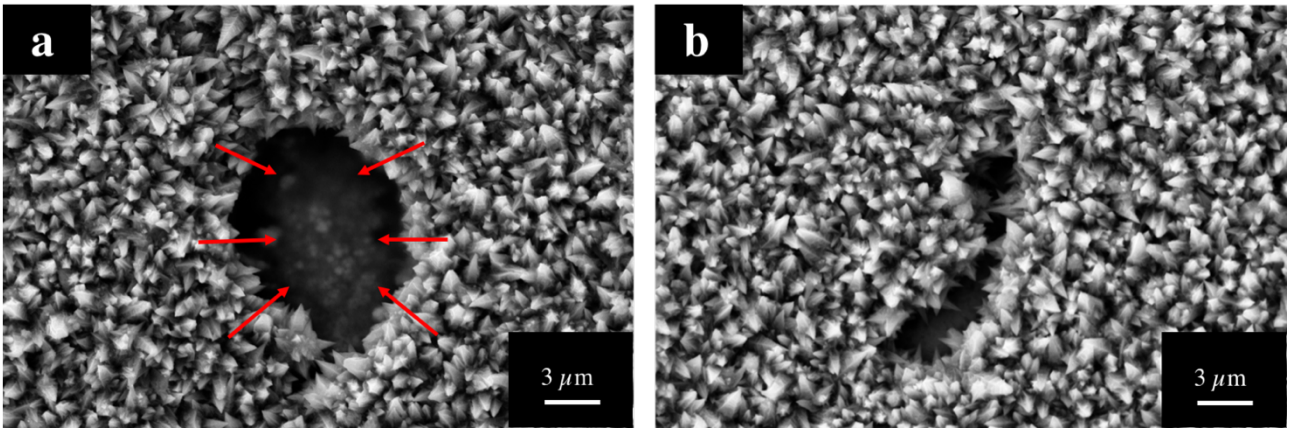

Figure 5.84: *SEM micrographs for the samples coating in 5(a) and 10(b) minutes. In the figure is possible to see the coalescence of the micro-flower in a single layer.*

The peculiar nanoarchitecture obtained with electroless plating has shown a super hydrophilic behavior for the sample as-coated. In order to understand the roughness influence on the wettability of the coating, photographs of water droplet on coating electroless plating with and without polishing are compared in Figure 5.85. The as-coated electroless plated sample shows a super-hydrophilicity

with a water CA <5° (Figure 5.85a). The Ni coating could be described by the Wenzel's model [12], according to which the surface roughness should increase the hydrophilicity if the smooth material is hydrophilic itself. To valuate this, a sample was polished with a 4000 SiC paper to eliminate the nanostructure obtained with the plating. The sample has shown a water CA of 58,27°, confirming the hypothesis.

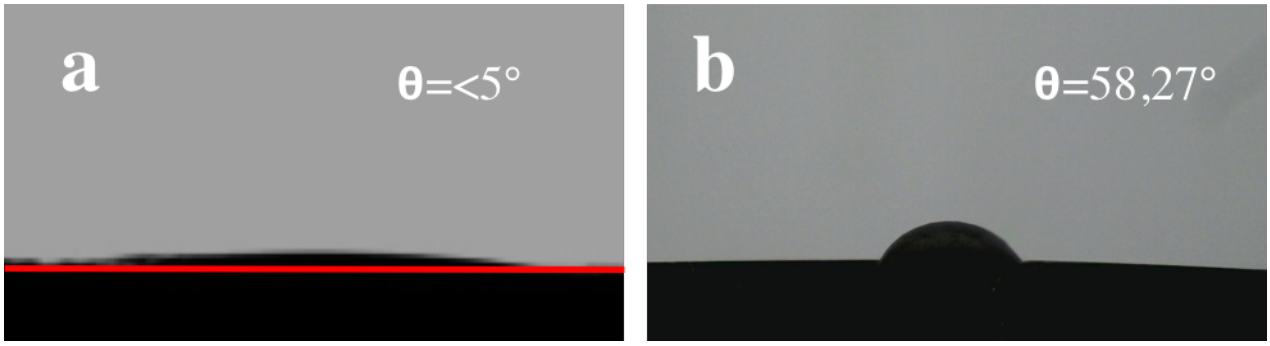

Figure 5.85: *Photographs of the contact angle for the samples: a) electroless pure nickel plated as-coated; b) electroless pure nickel plated polished with P4000 SiC paper*

The Ni-coatings became super hydrophobic after being exposed in ambient air for two weeks. The wetting transition phenomenon was studied by measuring the water contact angle as a function of the air exposition time. In Figure 5.86 it can be clearly noticed that the evolution of contact angles at different air exposition time can be divided into three different regions: for the first 24 hours, the samples are substantially superhydrophilic with contact angle <5° and can be described by the Wenzel's model [12]. The water contact angle drastically increase to higher values and reach the values of about 100° after 100 hours; this means a transition from the super-hydrophilic state (for the freshly coated) to a hydrophobic state that can be described by the Cassie-Baxter's model [13]. Then, after more than 200 hours, the surface of the nickel coating became super-hydrophobic (with contact angle = 150°) with an excellent water repellent properties. This transition was already seen in literature for different systems: Ni and Ni-Co electroplated surface [14], [15] that grow with the same superficial structure and exhibit the same wetting transition after approximately the same time (about 200h). This phenomenon, then, could be theoretically attributed not only to the surface roughness nanostructure but also to the nature of coating. However, the same transition was observed for different chemical nature systems: boron nitride nanotubes (BNNTs) [16], aluminum surface [17] and ZnO nanorod [18], for example.

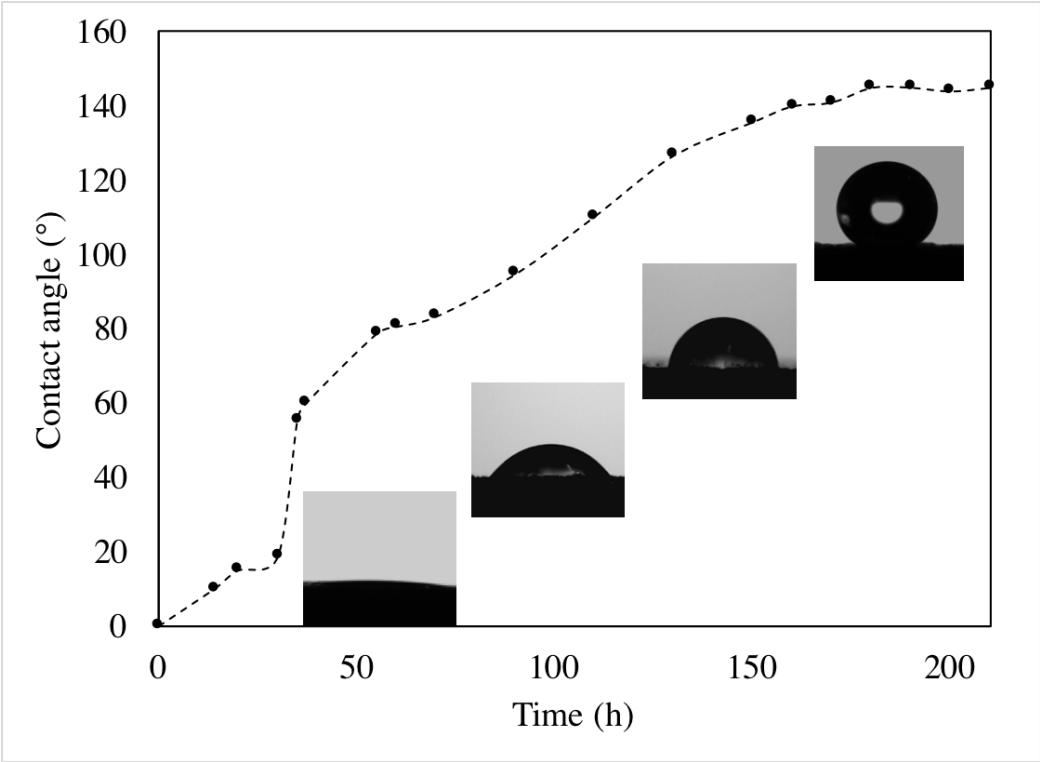

Figure 5.86: *Time-dependent evolution of water contact angle for sample coated with electroless pure Ni and exposed to ambient air*

The nature of wetting transition can be attributed to a surface morphological modification or chemical variation. As described for similar surface roughness1, the simple exposition to the air can't afflict the surface morphology in any way. This was confirmed by comparison surface roughness obtained with AFM analysis (Figure 5.87). Surface roughness can be compared (220 nm for the super-hydrophilic sample and 234 nm for the super-hydrophobic sample) and there is no evidence of morphological modifications.

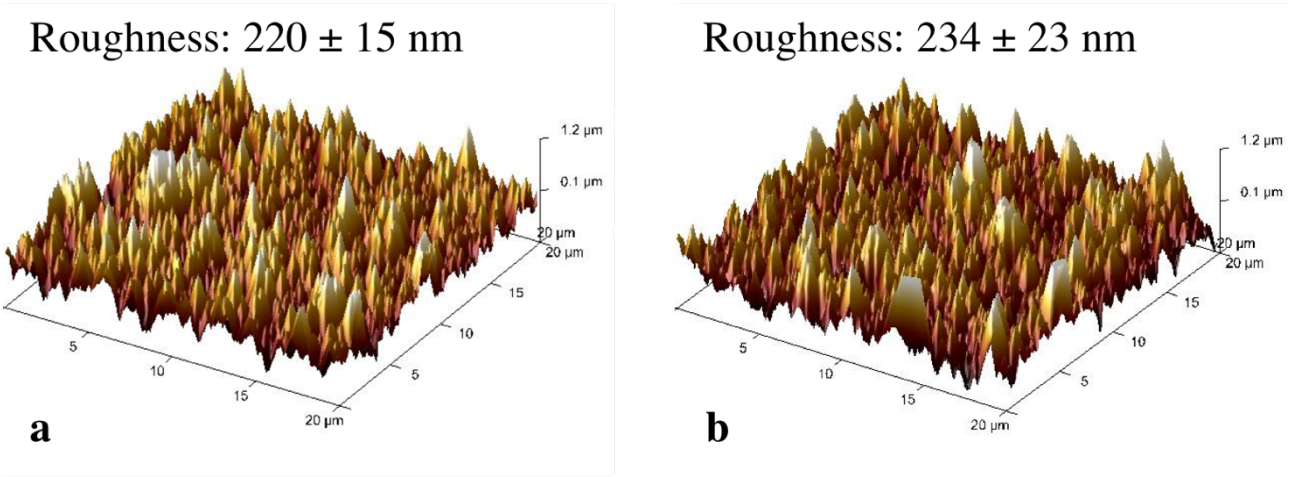

Figure 5.87: *AFM images of the as-coated electroless super-hydrophilic sample (a) and the same sample after 200h of air exposition(b)*

The chemical modifications of the surface seem to be the only phenomenon that can modify the wettability. Although it was reported that the surface layer of nickel film went through a process of oxidation and nickel oxide is formed by exposing the film in air [19], the hydrophobicity of NiO can't be attributed as the cause of wetting transition because the presence of oxides onto the surface wasn't observe during surface characterizations. Another reason for the hydrophobic state of nano-structured coating has been related to adsorption of organic molecules [16]. This phenomenon is in accordance with thermodynamic because the adsorption of molecules onto the surface can decrease the total free energy of the system by diminishing the surface energy part. So, if the electroless nickel surface has a great surface energy (given by the super-hydrophilic state), a wetting time dependent transition can be well explained as a consequence of decreasing surface energy by chemisorption or physisorption of adsorbates. The super-hydrophobic stability tests have partially demonstrated this theory. In order to remove chemically adsorbed contaminants onto the surface, all the samples were washed into several organic solvents. To demonstrate the presence of the organic airborne hydrocarbons as adsorbates, the solvents were chosen with different and increasing polarity. All the samples have kept the hydrophobic state without any drastically change for all the solvents except for the ethanol. The coating washed in ethanol returns to the super-hydrophilic state after 10 min of washing treatment. The water CA measurements as a function of time performed before and after washing in ethanol are presented inFigure 5.88. As expected, after the physico-chemically removal of the hydrophobic adsorbates, the coating state returns to the originally super-hydrophilic and the wetting transition occurs with the same time-conditions before the washing.

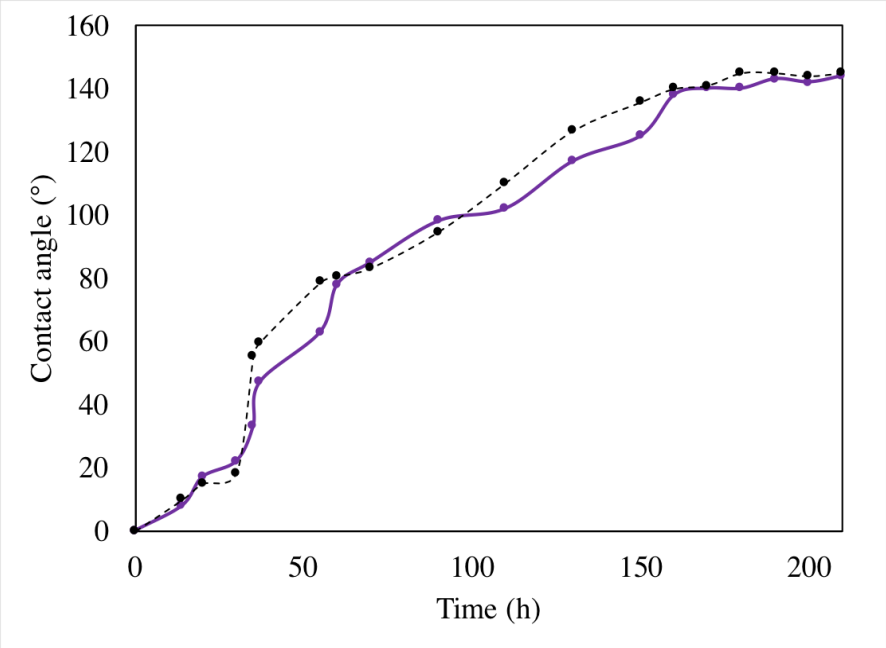

Figure 5.88: *Time-dependent evolution of sample water contact angle before (dashed line) and after (solid line) washing in ethanol at room temperature for 10 minutes.*

5.2.3 Nanocomposite Ni-nAl_2O_3

Once the parameters of solution B were optimized, the Ni-αAl_2O_3 nanocomposite was studied by introducing a water dispersion of nanoparticles into the plating solution. In Table 5.12 are summarized the different concentrations studied in this phase of the work

Table 5.12: *α-Al_2O_3 concentrations, in terms of water solution*

Samples	α-Al_2O_3 Water solution [g/l]	α-Al_2O_3 Volume in solution [g/l]
PN_Al_B_09	25	0,5
PN_Al_B_10	37,5	0,75
PN_Al_B_16	30	0,6

The deposition time for all samples containing alumina was 2 hours, and the nanoparticles were added after an hour of pure Ni deposition. In all cases, the coatings produced have a thickness similar to that obtained without nanoparticles: this is an indication that the deposition rate is not changed.
In low concentrations (0.5 g / l), a good dispersion was observed, although the number of particles that can be detected is very low. In fact, as can be seen from Figure 5.89 a,b the particles embedded in the coating are few, not sufficient to achieve the desired effects. On the contrary, increasing the concentration up to a value of 0.75 g / l the particles are agglomerated, with dimensions reaching 200 nm. This agglomeration can be seen in Figure 5.89 c,d.
It was then chosen to work with an intermediate concentration of 0.6 g / l of Al_2O_3 per liter of solution, resulting in a good compromise between dispersion and the amount of particles embedded in the coating, as can be seen in Figure 5.89 e,f.
The presence of Al_2O_3 was confirmed by EDS analysis.

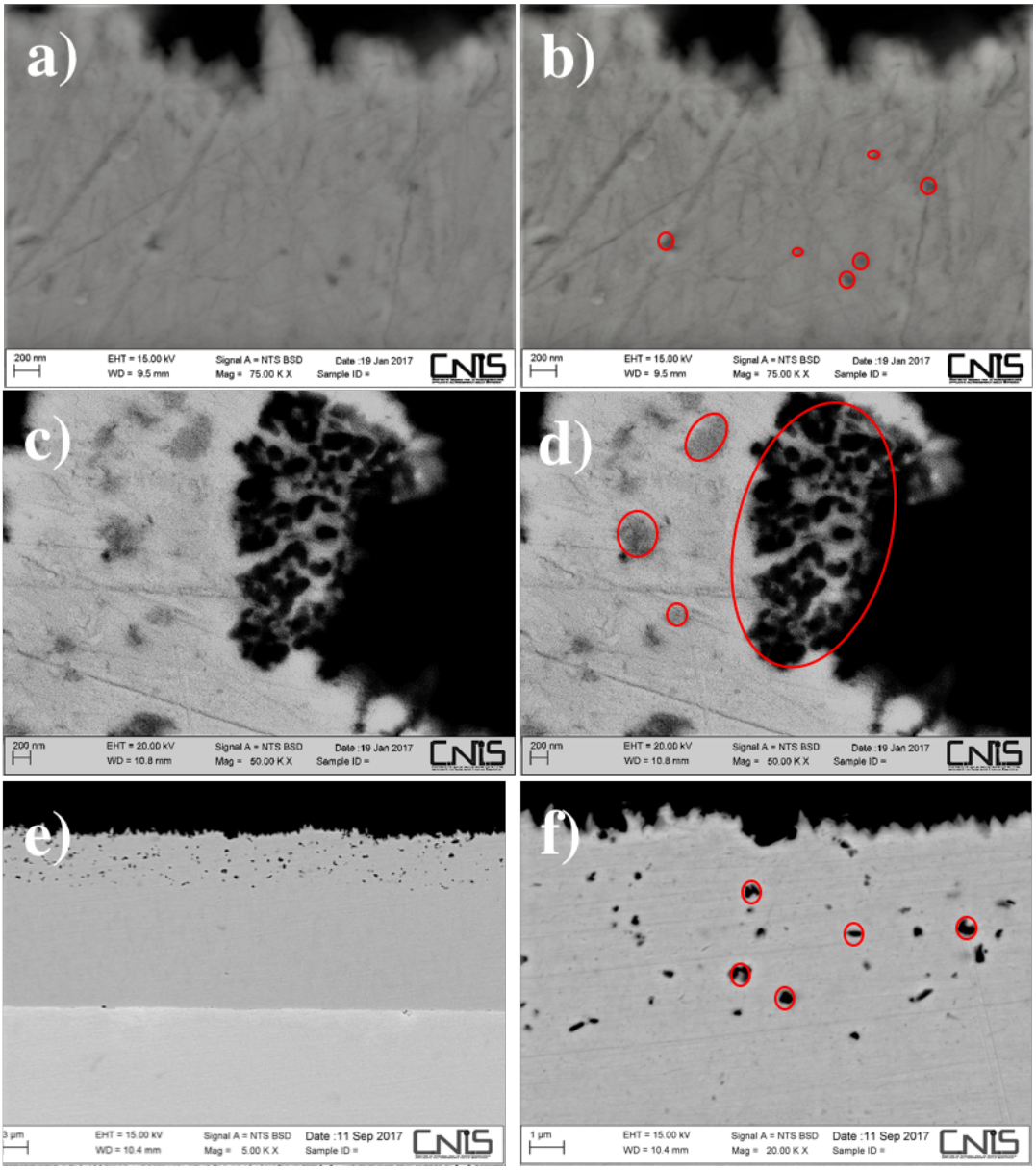

Figure 5.89: *Cross-section SEM micrographs of the Ni-αAl_2O_3 nanocomposite –a,b) PN_Al_B_09; c,d) PN_Al_B_10; e,f) PN_Al_B_16*

5.3 Phase 3: Slurry aluminization of Electroless pure nickel samples

Firstly, heat treatment parameters were optimized by performing slurry aluminization on nickel (purchased by GoodFellows inc.) samples. In Table 5.13 are reported the temperature profile selected for the aluminization.

Table 5.13: *Heat treatment parameters selected for the pure nickel (Good Fellows)*

Samples	dT/t (RT-650°C)	t_1 (650°C)	dT/t (650-1050°C)
Ni_1	5 K/min	1h	10 K/min
Ni_2	5 K/min	1.5h	10 K/min
Ni_3	5 K/min	1h	5 K/min

The fixed parameters selected for the aluminization were the first plateau at 650°C to allow the melting of aluminum and its consequent diffusion within the substrate and the plateau at 1050°C to homogenize the β-NiAl phase on top of the substrate.

The SEM micrographs (Figure 5.90, Figure 5.91, Figure 5.92) show the cross-section for the sample of the Ni series.

On the sample 2 and 3 it is possible to see the formation of three different zones:

One, on top of the coating, zone of Al-rich β-NiAl; the second one, less thick and more bright at BSE, is compositional Ni-rich β-NiAl. The third one is the "interdiffusion zone" Ni_3Al phase, formed by the inward diffusion of the Al and the outward diffusion of Ni. Of course, the is no precipitation of heavier element because we are considering a Ni pure sample.

In the sample Ni_1 seems that the Ni-rich zone is less pronounced but, above all, there is a sharp decrease in the amount of Al at the β-NiAl phase and Ni_3Al interface. For this reason, this heat treatment was selected for the aluminization on electroless pure nickel plating. Aluminization on pure Ni samples has allowed to optimize the heat treatment parameters depending on the amount of slurry deposited on the surface of the sample (5mg / cm2). It should be remembered, however, that the objective is to obtain a coating with the same thickness as the coatings obtained in phase 1 (20 μm of b-NiAl). For this reason, heat treatment 1 has been preferred to others as it allows to obtain a b-NiAl layer of the required thickness and with a rather satisfactory composition.

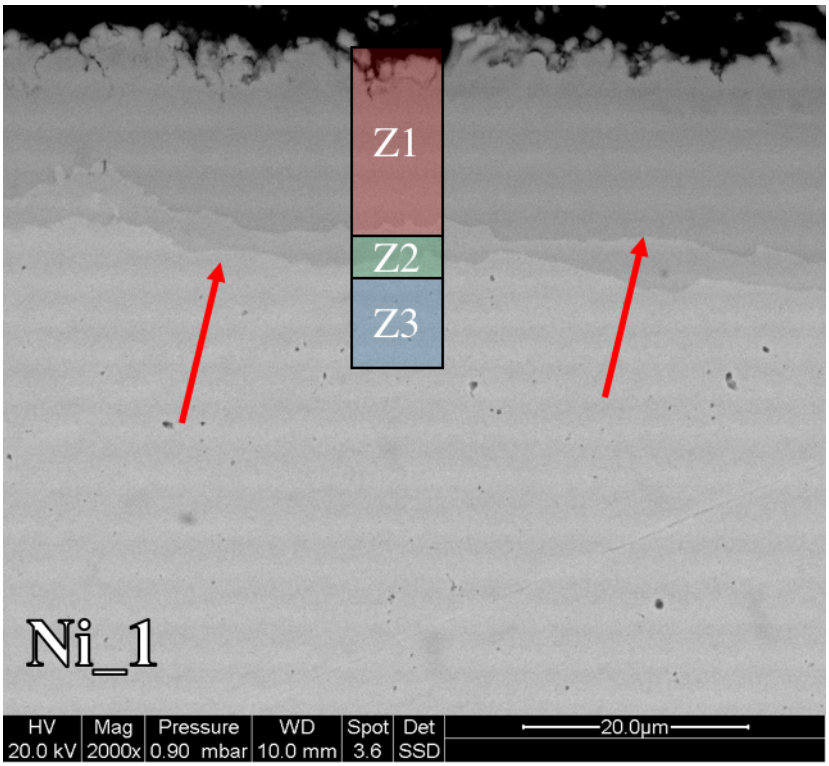

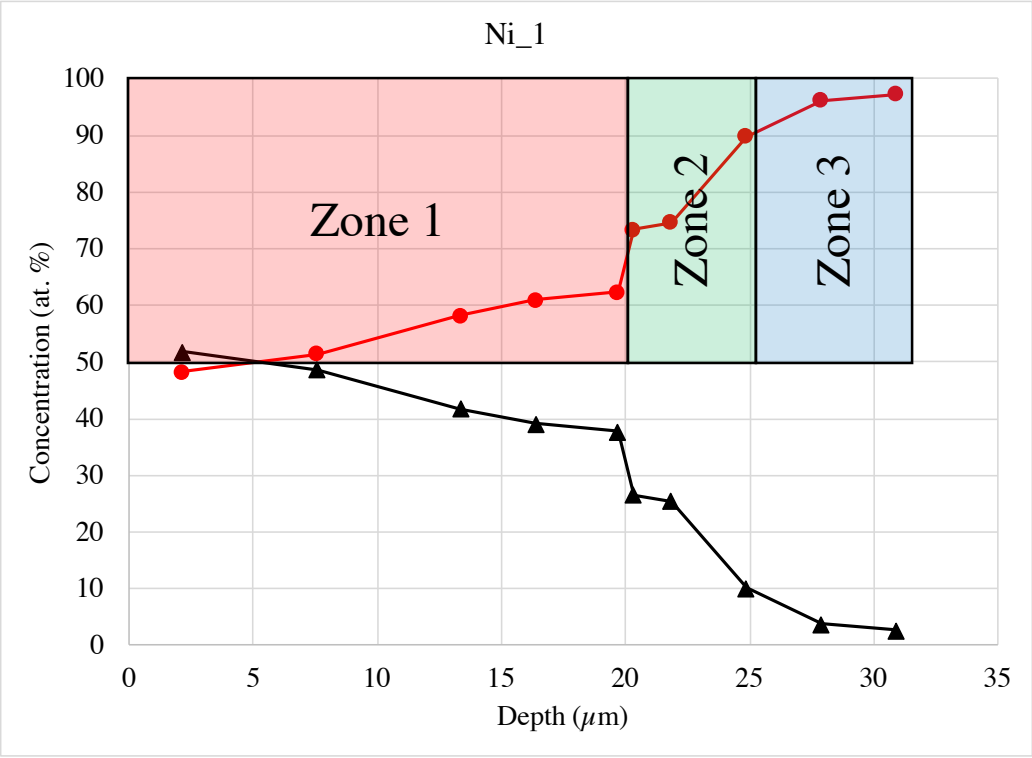

Figure 5.90: *Cross-section SEM micrograph for the samples Ni_1 with the relative diffusion profile obtain by EDS*

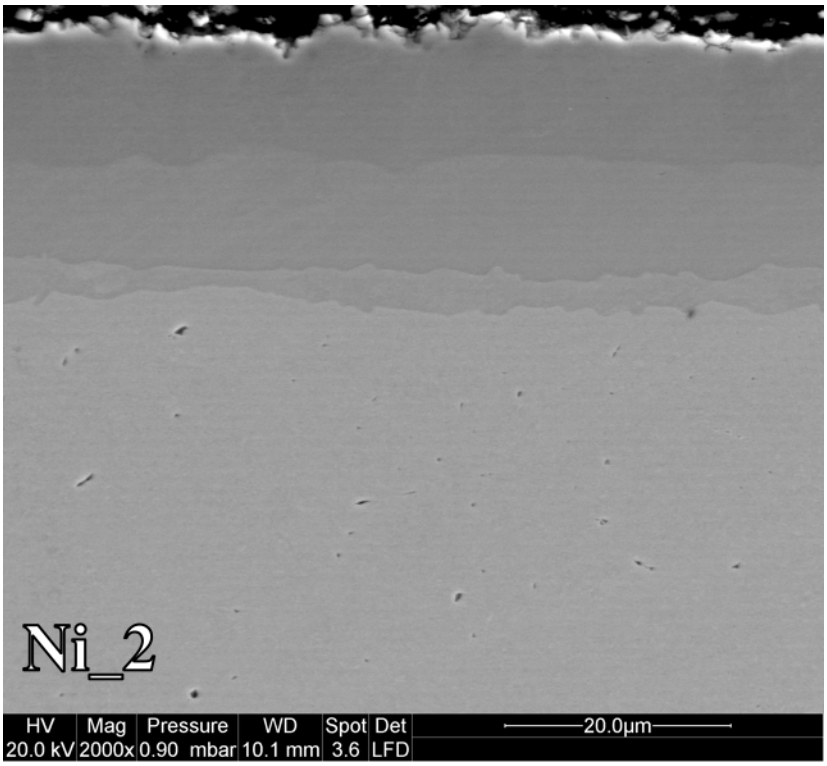

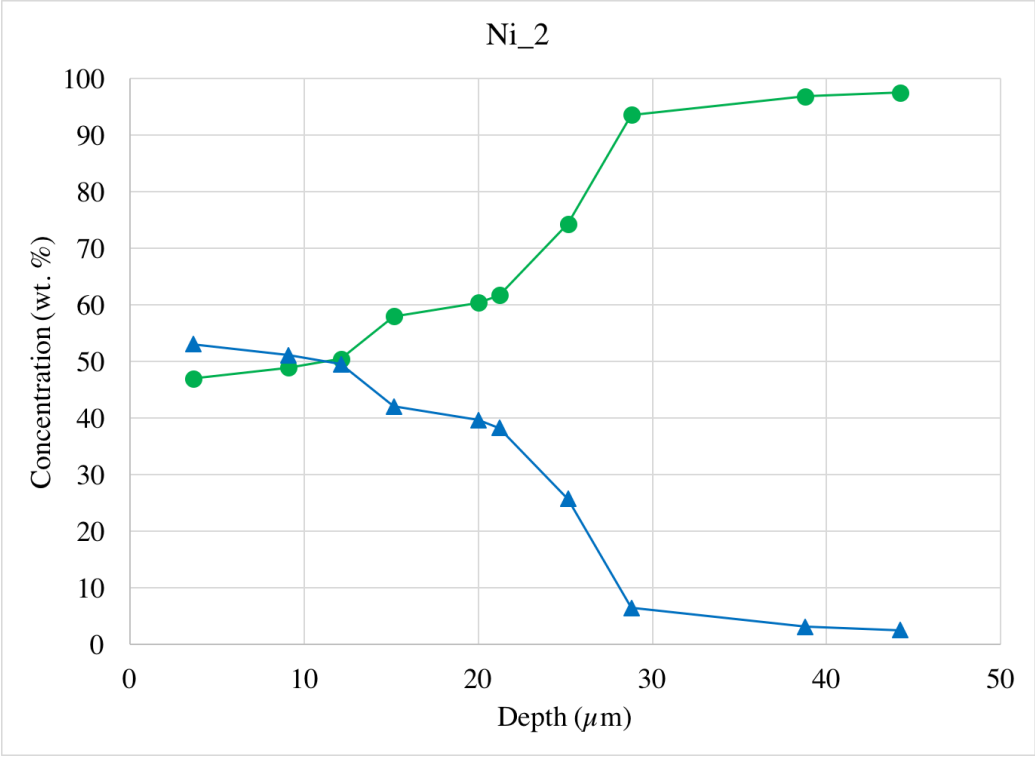

Figure 5.91: *Cross-section SEM micrograph for the samples Ni_2 with the relative diffusion profile obtain by EDS*

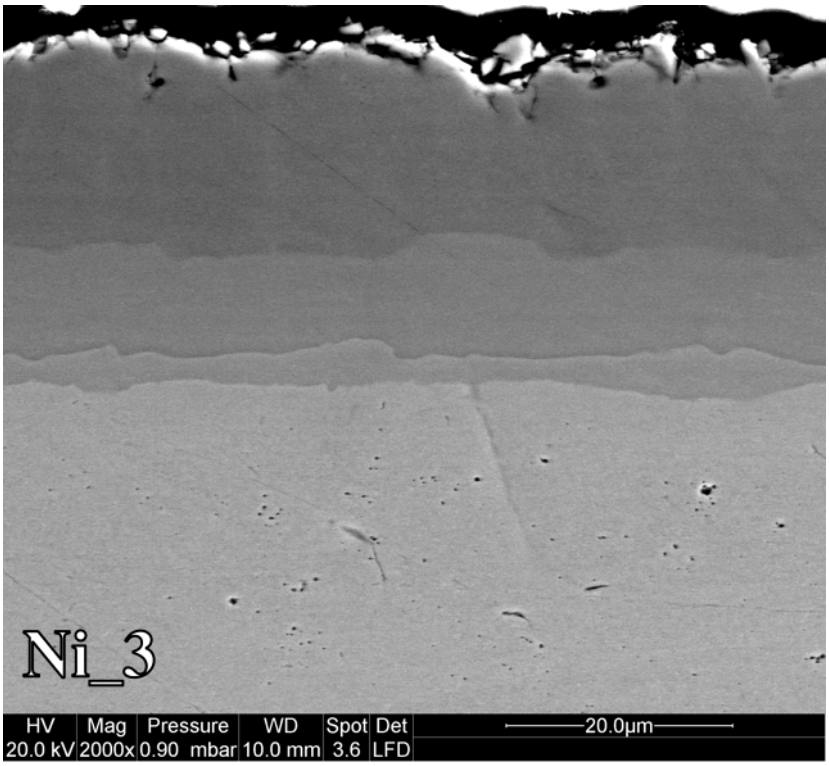

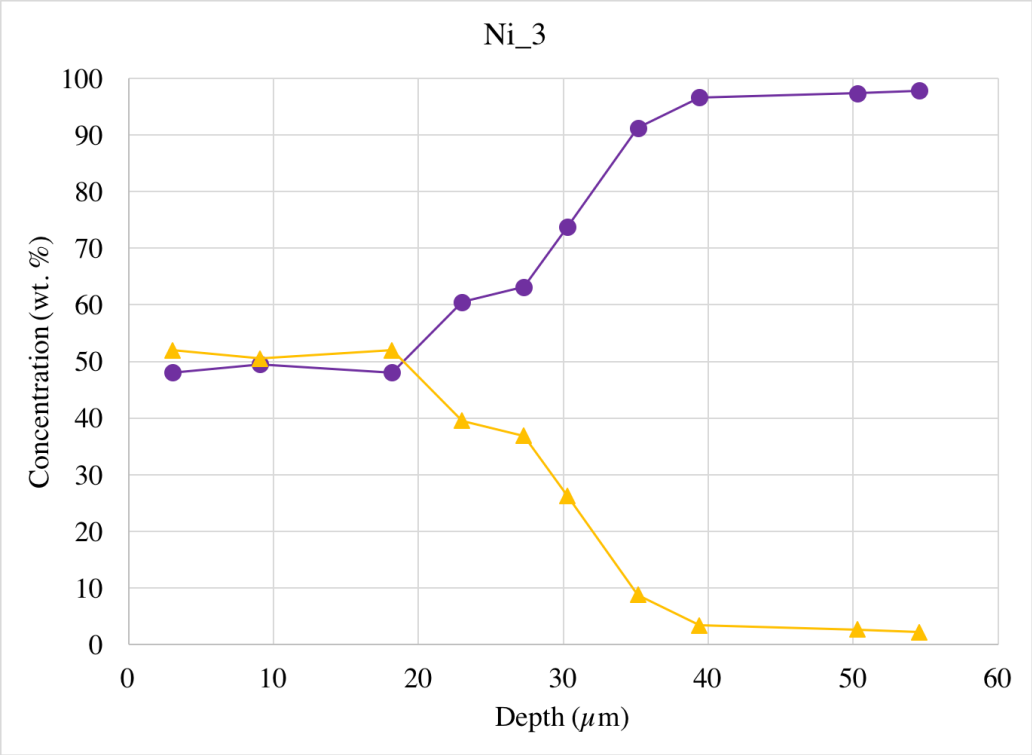

Figure 5.92: *Cross-section SEM micrograph for the samples Ni_3 with the relative diffusion profile obtain by EDS*

The aluminization were carried out on the electroless pure nickel sample with the heat treatment selected and reported in Table 5.14.

Table 5.14: *Heat treatment selected for the slurry aluminization of the electroless nickel samples*

Samples	dT/t (RT-650°C)	t_1 (650°C)	dT/t (650-1050°C)
Ni_1	5 K/min	1h	10 K/min

In order to study the influence of the ENL on the aluminide coating oxidation resistance, the same aluminization was carried out on a superalloy not coated. In Figure 5.93 the cross-section SEM micrographs show the influence of the ENL on the aluminization: there is no difference, in thickness and microstructure, on the edges of the sample. This is due to the homogeneity of the ENL but also to its wettability: the super-hydrophilicity of the surface, given by the nano-roughness, allow the water-based slurry to cover all the sample surface.

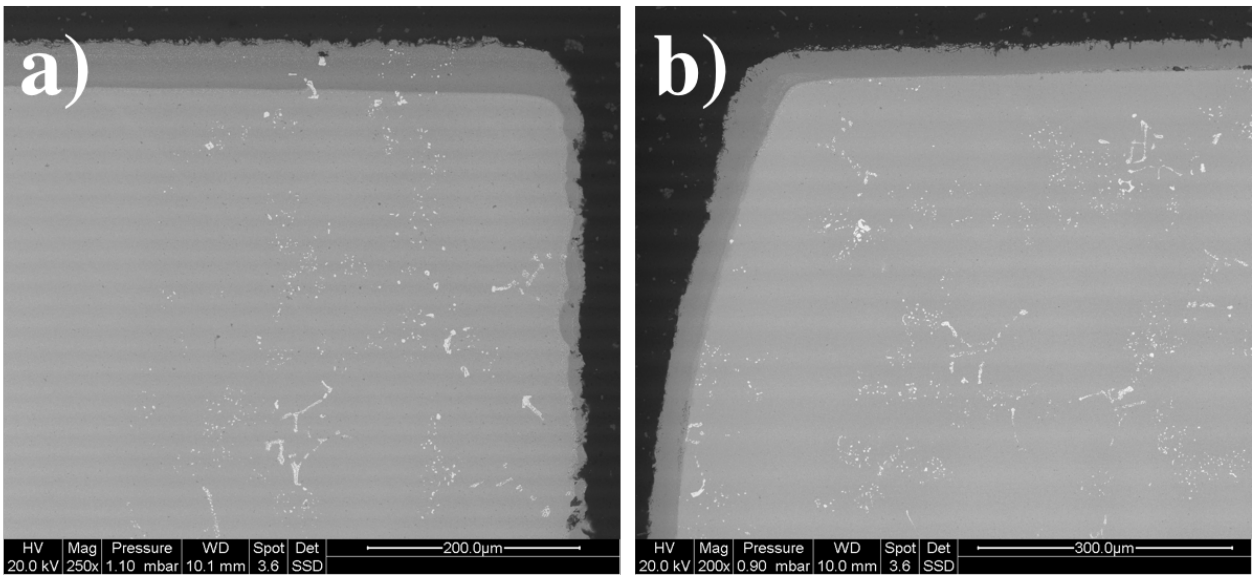

Figure 5.93: *Cross-section SEM micrographs for slurry aluminization on René 108DS(a) and electroless pure nickel plating sample (b)*

The thickness of the ENL was 16 µm before the aluminization. In Figure 5.94 the cross-section SEM micrograph of the electroless pure nickel sample is shown. The bond coat formed is uniform, has a good thickness but, despite the expectations, there is the formation of a small IDZ at the interface between the bond coat and the substrate. This is due, probably, to a diffusion of the heavier elements inside the ENL during the heat treatment.

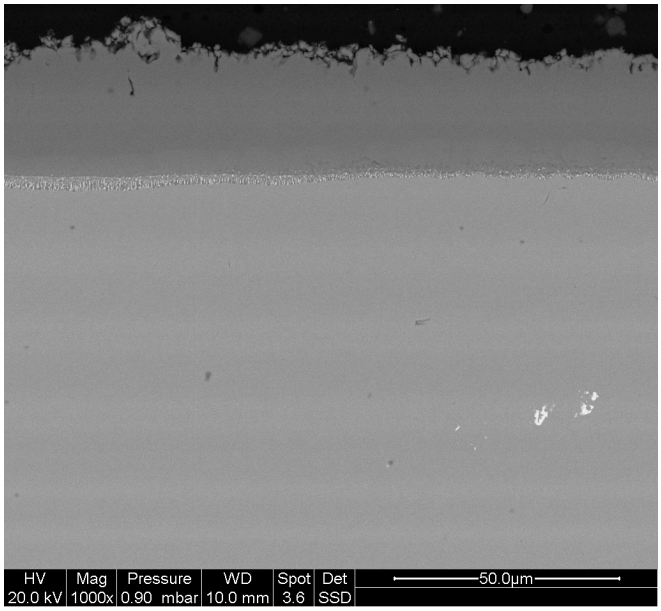

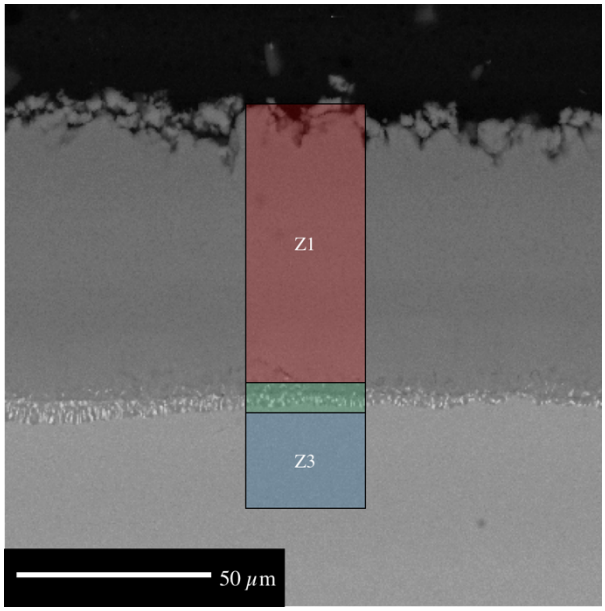

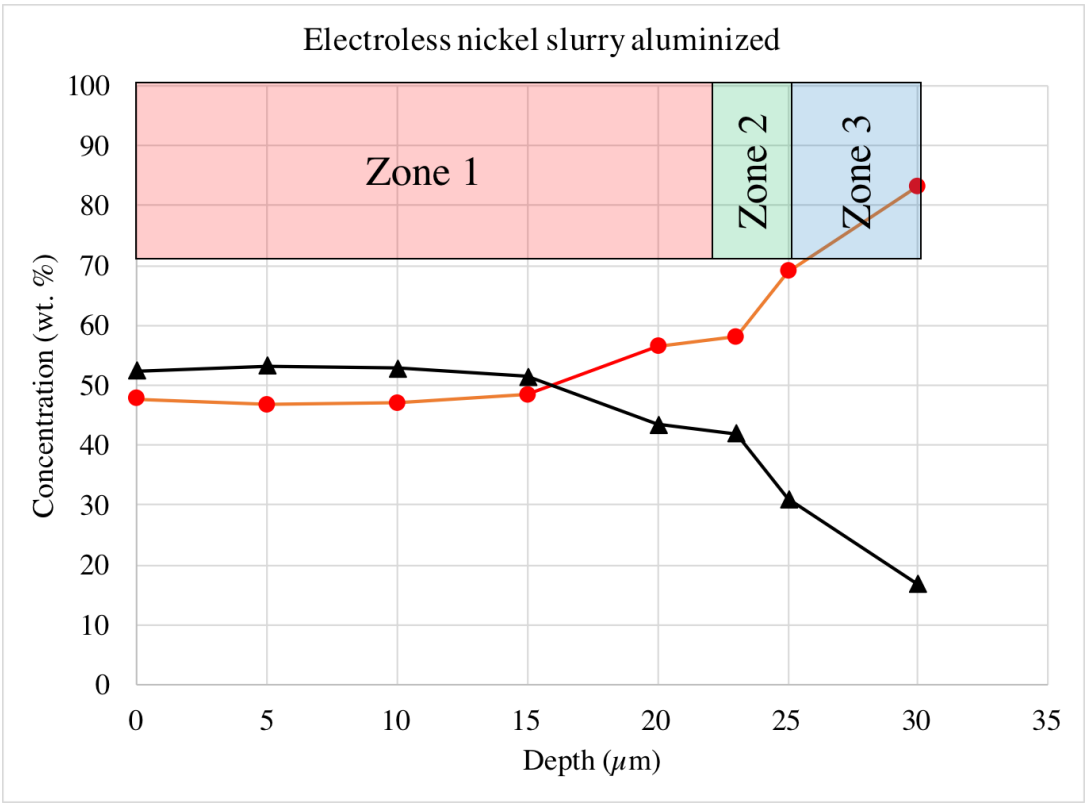

Figure 5.94: *Electroless nickel sample cross-section SEM micrograph aluminized with slurry with the relative diffusion profile obtained by EDS*

For comparison, a sample of René 108DS was aluminized by slurry with the same heat treatment. The cross-section micrograph is shown in Figure 5.95. The microstructure resulted from the aluminization is the typical Low Temperature High Activity with the precipitation included in the bond coat.

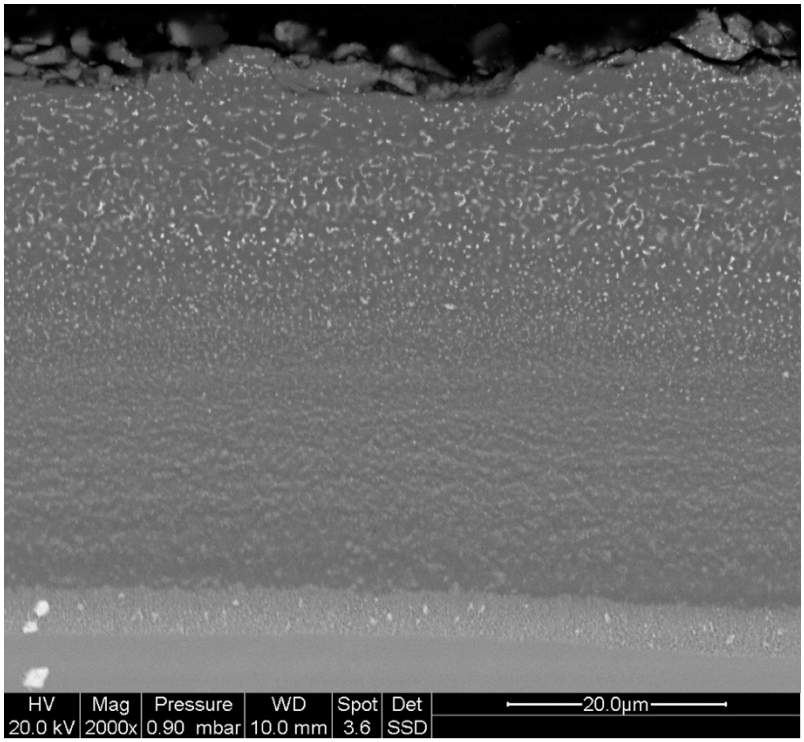

Figure 5.95: *René 108DS cross-section SEM micrograph aluminized by slurry*

Preliminary isothermal oxidation was carried out on the electroless sample aluminized by slurry in the same conditions of phase 1. The results are shown inFigure 5.96: the curve relative to the electroless nickel sample show a not expected mass gain with a consequent loss after 30 hours of heat treatment. Evidently the aluminization has not brought to equilibrium intermetallic phase which is, therefore, unstable and continues its diffusion during oxidation at high temperature. The oxidation of the bond coat seems not to be selective; this is probably because the aluminum diffuses to the substrate and thus subtracts itself from the oxidation phenomena. On the contrary, Ni, tends to diffuse outwardly making it more available to the oxidation. This would explain, in part, the total absence of formation of a protective oxide scale with a spalling phenomenon that occurs only after 30 hours of high temperature testing.

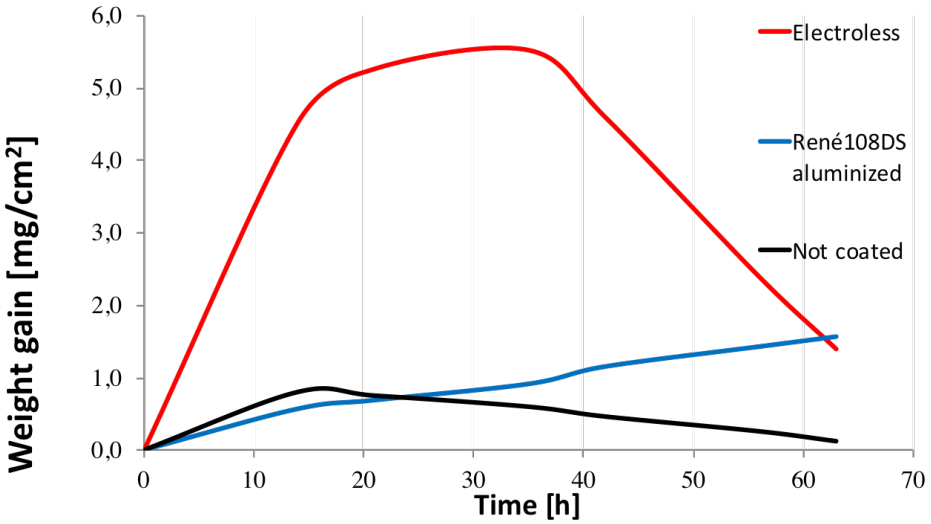

Figure 5.96: *Isothermal oxidation (1050°C)*

XRD spectrum (Figure 5.97) has confirmed this theory. As it was said, these are the preliminary test on this sample. It is evident that the β-NiAl phase formed after aluminization needs a further heat treatment to reach the final equilibrium and allows to the Al to oxidize in a protective way.

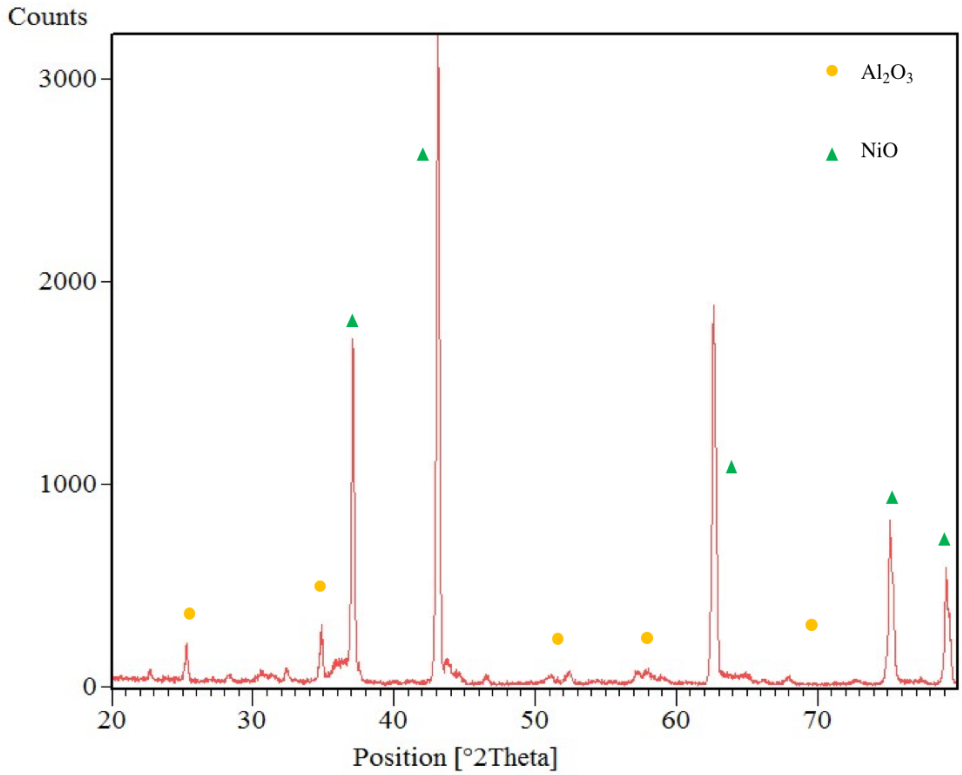

Figure 5.97: *XRD spectrum of the electroless nickel plating sample aluminized by slurry after 25h of isothermal oxidation test at 1050°C.*

Although the isothermal oxidation test did not yield a satisfactory result, the aluminization obtained by slurry deposition showed an interesting result. As expected, adding an external layer of nickel involves a variation of the aluminization mechanism: the substrate does not participate in the deposition mechanism. The only result is the formation of a small IDZ that can be considered as a reinforcing mechanism in adhesion between the substrate and the external nickel layer. Thus, the typical microstructure of a deposited HTLA coating has been obtained with the times and especially the most contained parameters of a LTHA aluminization.

References

[1] S. Hamadi et al., Surface & Coatings Technology 204, 756–760, 2009.

[2] Mallory, G. O., Hajdu, J. B., Electroplaters, A., Society, S. F. & (Firm), Int. Bus. (2000).

[3] Cheng, Y. S. & Yeung, K. L., Memb. Sci. (2001), 182, 195–203 (2001).

[4] Braibanti, A., Dallavalle, F., Nghelli, M. A. P. & Leporati, E., Inorg. Chem. (1968), 7, 1430–1433.

[5] Haag, S., Burgard, M. & Ernst, B. Surf. Coatings Technol., (2006), 201, 2166–2173.

[6] Patil, K. C. & Rattan, T. M., (2014).

[7] Park, J. W. et al., Mater. Chem. Phys. (2006), 97, 371–378

[8] Mallory, G. O., Fundam. Appl., (2009), 69; 71; 72

[9] Chen, H., Xu, C., Chen, C., Zhao, G. & Liu, Y. Mater. Res. Bull. (2012), 47, 1839–1844.

[10] Baskaran, I., Narayanan, T. S. N. S. & Stephen, A. Mater. Chem. Phys. (2006), 99, 117–126.

[11] Genova, V., Marini, D., Valente, M., Marra, F. & Pulci, G., Ch. Eng. Trans., (2017), 60, 73–78.

[12] Wenzel, R. N., (1936), Ind. Eng. Chem. 28, 988–994.

[13] Cassie, B. D. Of porous surfaces, (1944), 546–551.

[14] Khorsand, S., Raeissi, K., Ashrafizadeh, F. & Arenas, M. A. Chem. Eng. J. (2015), 273, 638–646.

[15] Khorsand, S., Raeissi, K. & Ashrafizadeh, F. Appl. Surf. Sci. 305, (2014), 498–505.

[16] Boinovich, L. B. et al. Langmuir 28, (2012), 1206–1216.

[17] Zheng, S. et al. Surf. Coatings Technol. (2015), 276, 341–348.

[18] Guo, M., Diao, P. & Cai, S. Thin Solid Films, (2007), 515, 7162–7166.

[19] Geng, W., Hu, A. & Li, M. Appl. Surf. Sci., (2012), 263, 821–824.

CONCLUSIONS

Diffusion aluminide coatings are used on turbine blades, both as a single coating and as a bond coat in a Thermal Barrier Coating System (TBC), to ensure its protection against oxidation and hot corrosion. Their protective function is achieved through the selective oxidation of the aluminum present in the coating; this process leads to the formation of a Thermally Grown Oxide (TGO).
In this work, the diffusion coatings corrosion resistance was studied and the modification of the standard aluminide coating with the aim of improving its high temperature performance was carried out by studying different techniques.

In the first part of the work, the process of VPA (Vapour Phase Aluminizing) was optimized, varying the concentration of the two deposition salts, NH4F and AlF3. The diffusion coatings obtained with NH4F show better oxidation resistance than those obtained with AlF3. In particular, the coating with a higher concentration of ammonium fluoride has a weight gain after 100 hours of oxidation lower than all others.
For the description of experimental oxidation data, Monceau's parabolic model seems more suitable than the Wagner's model.
During the hot corrosion test all coatings exhibit an alternation between increases and losses by weight, as a high amount of corrosion salt is applied on a very narrow area of the surface. This greatly accelerates the oxidation phenomenon: there is a very high localization of the protective scale, which becomes unstable after a few hours of testing.
Once the optimal NH4F concentration has been selected, five coatings in -NiAl doped with Zr were produced using a mixed NH4F / ZrF4 activator salt. The Zr is deposited on the interface between the superalloy and the interdiffusion zone, and during oxidation diffuse to the surface to the oxide scale. A range of concentrations was identified within which the addition of Zr improves the performance of the conventional coating. For concentrations lower than the optimum values, the effects generated by the presence of the reactive element are zero or minimal; for higher concentrations, the internal oxidation of the reactive elements is observed, which results in an increase in oxygen permeability and hence the rate of oxidation.
Experimental evidence shows that zirconium has the effect of increasing the adhesion of the oxide scale to the substrate. This may be essentially due to two reasons, both of which are explained in the segregation of Zr at the interface between coating and oxide during oxidation. The first hypothesis is that Zr reduces the rate of transient oxidation: -Al_2O_3 is characterized by a rapid growth driven by the cationic diffusion of the Al towards the outside. Zr would thus slow the diffusion of Al, favoring the

nucleation of -Al_2O_3. The second hypothesis is that Zr limits the release of protective oxide during cooling, suppressing the formation of Kirkendall's voids at the interface.
The experimental data produced in the second phase of the experiment also confirm that Monceau's parabolic model seems more suitable for the description of the oxidation kinetics than the Wagner model.
From preliminary considerations on the hot corrosion test of the doped samples, it is assumed that modification of the coatings with Zr does not give rise to substantial benefits in the resistance to this degradation phenomenon. Samples with conventional and doped coatings, in fact, have a comparable increase in weight.

In the second part of the work, electroless pure nickel plating was selected as technique to deposit an ENL on top of the substrate before the aluminization process. This modification of the standard coating was conducted in order to reduce the formation of the IDZ that can influence the mechanical properties of the turbine blade. Furthermore, the deposition technique allows to introduce Al_2O_3 nanoparticles inside the coating in order to increase the oxidation resistance by promoting the nucleation of the protective oxide scale on top of the bond coat.
The study of several plating parameters (pH, T, P_R etc.) has allowed to obtain a thicker (20 μm), homogeneous, continuous pure nickel layer on top of the superalloy. Well dispersed nanoparticles were embedded inside the Ni matrix and the quantity of α-Al_2O_3 nanoparticles inside the plating solution was studied and optimized.

The electroless pure nickel plating sample were aluminized by slurry deposition, in order to study the reaction of the ENL, plated directly onto the Ni-based super alloy, to the aluminization heat treatment. Once the aluminization heat treatment was optimized, isothermal oxidation was carried out for the samples that showed the best microstructure after slurry aluminization. Preliminary results have shown that the heat treatment selected for the slurry aluminization doesn't allow the formation of a stable β-NiAl on the top of the substrate with a consequent diffusion to equilibrium that occur during oxidation heat treatment. Future test of annealing after aluminization will carried out in order to rebalance the bond-coat superficial structure.
Despite this, the most important result is that the typical microstructure of a deposited HTLA coating has been obtained with the times and especially the most contained parameters of a LTHA aluminization.